

Title	Optically injected dual state quantum dot lasers
Authors	Dillane, Michael
Publication date	2022-04-14
Original Citation	Dillane, M. 2022. Optically injected dual state quantum dot lasers. PhD Thesis, University College Cork.
Type of publication	Doctoral thesis
Rights	© 2022, Michael Dillane. - <a href="https://creativecommons.org/licenses/by-nc-sa/4.0/">https://creativecommons.org/licenses/by-nc-sa/4.0/</a>
Download date	2025-07-17 05:20:09
Item downloaded from	<a href="https://hdl.handle.net/10468/13210">https://hdl.handle.net/10468/13210</a>

# Optically injected dual state quantum dot lasers

Thesis

Michael Dillane



NATIONAL UNIVERSITY OF IRELAND, CORK

SCHOOL OF SCIENCE

DEPARTMENT OF PHYSICS

**Thesis submitted for the degree of  
Doctor of Philosophy**

14 April 2022

Head of Department: Prof. John McInerney

Supervisors: Dr. Bryan Kelleher

# Contents

List of Figures . . . . .	iv
List of Acronyms . . . . .	xxiv
List of Publications . . . . .	xxv
Acknowledgements . . . . .	xxix
Abstract . . . . .	xxxii
<b>1 Introduction</b>	<b>1</b>
1.1 Photonic computing . . . . .	1
1.1.1 Photonic computing and non-linear dynamics . . . . .	1
1.1.2 Computing architectures . . . . .	2
1.1.2.1 Biological inspiration . . . . .	2
1.1.2.2 Artificial neuron . . . . .	3
1.1.3 Excitability . . . . .	4
1.2 Fundamentals of lasers . . . . .	5
1.2.1 Band structure . . . . .	5
1.2.2 Recombination . . . . .	5
1.2.3 Quantum dot lasers . . . . .	6
1.2.3.1 Fabrication . . . . .	6
1.2.3.2 Dual state emission . . . . .	7
1.2.3.3 Phase Amplitude coupling . . . . .	8
1.2.3.4 Relaxation oscillations . . . . .	8
1.3 Optical injection . . . . .	9
1.4 Excitability in optically injected lasers . . . . .	11
1.5 Brief history of optically injected QD lasers . . . . .	12
1.5.1 Single mode . . . . .	13
1.5.2 Multi-mode . . . . .	14
1.6 Outline of the Thesis . . . . .	14
<b>2 Square wave excitability</b>	<b>16</b>
2.1 Introduction . . . . .	17
2.2 Experimental setup . . . . .	18
2.3 Noise induced excitable square wave trains . . . . .	19
2.3.1 Square wave onset . . . . .	19
2.3.2 Statistical Analysis . . . . .	20
2.4 Periodic square wave trains . . . . .	22
2.5 Optothermal measurement . . . . .	23
2.5.1 Intrinsic detuning sweep measurement . . . . .	26
2.5.2 Phase measurement . . . . .	29
2.6 Deterministic triggering . . . . .	32
2.7 Class A theoretical model . . . . .	35
2.7.1 Inclusion of the optothermal effect and the evolution of the region of excitability . . . . .	36
2.7.2 Bifurcation analysis . . . . .	39
2.7.3 Deterministic triggering . . . . .	40
2.8 Quantum dot laser model . . . . .	41

2.8.1	Bifurcation analysis . . . . .	43
2.8.1.1	Subcritical Hopf . . . . .	43
2.8.1.2	Reduction to Canard Explosion . . . . .	44
<b>3</b>	<b>History of dual state optical Injection</b>	<b>48</b>
3.1	A brief history in dual state dynamics . . . . .	49
3.2	Bistability and state switching . . . . .	50
3.3	Boundary dynamics . . . . .	56
3.3.1	Intrinsic Q-switching . . . . .	56
3.3.2	Two-colour bursting . . . . .	59
3.4	Where is the chaos? . . . . .	62
<b>4</b>	<b>Locking Maps</b>	<b>64</b>
4.1	Introduction . . . . .	65
4.2	Experiment . . . . .	67
4.2.1	Stability maps . . . . .	69
4.2.2	Bistability . . . . .	72
4.2.3	Slow Oscillations . . . . .	75
4.3	Theory . . . . .	79
4.3.1	First optothermal effect . . . . .	83
4.3.2	Second optothermal effect . . . . .	84
4.4	Discussion . . . . .	86
<b>5</b>	<b>Noise induced dual state excitability</b>	<b>88</b>
5.1	Introduction . . . . .	89
5.2	Experimental setup . . . . .	89
5.2.1	Phase measurement . . . . .	91
5.3	Model . . . . .	93
5.4	Discussion . . . . .	95
<b>6</b>	<b>Dual state excitability with two asymmetric thresholds</b>	<b>99</b>
6.1	Introduction . . . . .	100
6.2	Experiment . . . . .	101
6.2.1	Dual threshold . . . . .	103
6.2.2	Delay time . . . . .	105
6.3	Model . . . . .	107
6.4	Discussion . . . . .	109
6.4.1	Phase measurement . . . . .	109
<b>7</b>	<b>Dual state excitability neuromorphic capabilities</b>	<b>115</b>
7.1	Refractory Periods . . . . .	115
7.1.1	Small amplitude anticlockwise perturbations and refrac- tory periods . . . . .	116
7.1.2	Large amplitude perturbations and refractory periods . .	121
7.1.2.1	Anticlockwise perturbations . . . . .	122
7.1.2.2	Clockwise perturbations . . . . .	125
7.2	Subthreshold perturbation integration . . . . .	130

7.2.1	Setting new thresholds . . . . .	130
7.2.2	Measurement of large thresholds . . . . .	130
7.2.3	Integrate and fire mechanism . . . . .	132
7.3	Image edge detection . . . . .	135
7.3.1	Binary . . . . .	137
7.3.1.1	2×1 kernel . . . . .	137
7.3.1.2	2×2 kernel . . . . .	138
7.3.2	4 level system . . . . .	140
<b>8</b>	<b>Conclusion</b>	<b>143</b>
8.1	Overview of the results presented . . . . .	143
8.2	Future work . . . . .	145
8.2.1	Optothermal . . . . .	145
8.2.2	Neuromorphic . . . . .	146

## List of Figures

- 1.1 Schematic of typical leaky integrate and fire neuron found in the brain.  $x_j$  are the input signals, each spike has a weight  $\omega_j$  and a delay  $\tau_j$ . The signals are joined at the stoma and then the signal  $I_{app}$  is sent to the axon hillock. If the inputs exceed a threshold the activation function is fired. There is some rest time before the neuron can fire again. . . . . 4
- 1.2 Schematic showing some of the different ways carriers can scatter between a quantum dot and the wetting layer.  $B^w$  is the rate at which carriers fall from the wetting layer into the ES. The carriers can then fall to the GS at a rate of  $B$ . The carriers that scatter out of the GS and into ES do so at a rate of  $C$  and the rate of scattering from the ES to the wetting layer is  $C^w$ . The occupation probabilities of the GS ( $n^g$ ) and ES ( $n^e$ ) and the carrier density in the wetting layer ( $n^w$ ). The subscripts indicate if the densities relate to electrons  $e$  or holes  $h$  [46]. Carriers can radiatively recombine from from either the GS or the ES. . . . . 7
- 1.3 Common bifurcations observed in laser systems. Black dots represent stable points and white dots represent unstable points. The top panel shows Type I excitability and the bottom shows Type II. The dashed lines represent perturbations and the solid lines are excitable trajectories and the arrows show the direction of rotation [64]. . . . . 11
- 1.4 Analytic stability diagram for an optically injected QD laser using QD rate equations.  $\Gamma$  is the normalised injection strength and  $\Delta$  is detuning. The saddle-node and Hopf bifurcation points are denoted by SN and H, respectively. The shaded region corresponds to region of steady-state bistability. The dots indicate where where Hopf and SN bifurcation lines merge to create are fold-Hopf points. The inset shows a stability diagram for an injected Class A laser [71]. . . . . 14
- 2.1 Basic setup of an optically injection experiment. A QD laser is acting as the secondary laser (SL). The primary laser (PL) is a tunable laser source. A polarisation controller (PC) is used to maximise coupling. A circulator shines light from the PL into the SL, the light that is emitted from the SL into the circulator is sent to a 12 GHz detector connected to an oscilloscope (OSC). . . . 18
- 2.2 Extracts taken from 20 ms timetraces. (a) shows randomly separated pulses at -6.4 GHz detuning. (b) shows periodic squares at -4.8 GHz detuning and (c) shows square dropouts appearing randomly at -3.4 GHz detuning. The bottom row zooms in on a square event from the top row. . . . . 20

2.3	Heat map of (a) 2016 pulses and (b) 1818 dropouts plotted on top of each other. The pulses/dropouts are taken from same 20 ms timetraces as the squares shown in Figure 2.2 (a) and (c) at -6.4 GHz and -3.4 GHz detuning, respectively. The pulse widths are extremely regular and approximately $0.4 \mu\text{s}$ long. A deterministic trajectory appears to be responsible for these square events. . . . .	21
2.4	Histograms of the interpulse/dropout times taken over 20 ms with detuning values of -6.4 GHz and -3.4 GHz. (a) shows the interpulse time distribution of 2016 pulses shown in Figure 2.2. The exponential shape indicates that these pulses are randomly separated and induced by noise. (b) shows the distribution for 1818 dropouts. Again, the exponential shape is evidence that the dropouts are noise-induced random events. The Kramer's escape times were approximately $6.9 \mu\text{s}$ and $6.6 \mu\text{s}$ respectively. The insets are the persistence plots of 100 pulses/dropouts. . . . .	21
2.5	Histograms showing (a) the distribution of upper intensity state lifetimes, (b) the distribution of lower intensity state lifetimes and (c) a persistence plot of 100 pulses. The histograms correspond to the time traces in Figure 2.2 (b) at detuning of -4.8 GHz. The narrow distribution shown in (a) and (b) emphasises a deterministic cycle is in fact being undertaken. . . . .	23
2.6	Heat map of periodic square wave train at detuning of -4.8 GHz, corresponding to the extracts taken from 20 ms timetraces shown in Figure 2.2 (b). The pulse widths are approximately $0.6 \mu\text{s}$ long, with a tight distribution. This is a limit cycle and are not noise induced square pulses. . . . .	23
2.7	Cartoon describing the optothermal effect. (a) and (b) show the optical spectrum of the QD laser. The blue lines represent the subthreshold modes. The red line represents the lasing frequency of the QD laser, which remains fixed as the QD laser is phase locked to the constant TLS $\omega_P$ . The grey dashed line, $\omega_S$ , is the longitudinal mode that would lase in this single mode laser, in the absence of optical injection. Detuning is defined as $\omega_P - \omega_S$ . The bottom panels show timestraces of the square wave train. The circles indicate what part of the cycle the top panel is describing. As shown in (c) the system has just began emitting from the lower intensity section. This increases the temperature, decreasing the frequency of the longitudinal modes and $\omega_S$ , as indicated by the arrows. Over the duration of the lower intensity section the detuning has increased from -4 Ghz to -2 Ghz. . . .	24

- 2.8 Cartoon describing the optothermal effect. (a) and (b) show the optical spectrum of the QD laser. The blue lines represent the subthreshold modes. The red line represents the lasing frequency of the QD laser, which remains fixed as the QD laser is phase locked to the constant TLS  $\omega_P$ . The grey dashed line,  $\omega_S$ , is the longitudinal mode that would lase in this single mode laser, in the absence of optical injection. Detuning is defined as  $\omega_P - \omega_S$ . The bottom panels show timestraces of the square wave train. The circles indicate what part of the cycle the top panel is describing. As shown in (c) the system has just began emitting from the upper intensity section. This allows the temperature of the device to decrease. As indicated by the arrows, this increases the frequency of the longitudinal modes and  $\omega_S$ . Over the duration of the upper intensity section the detuning has decreased from -2 GHz to -4 GHz. . . . . 26
- 2.9 Experimental setup of an optically injected laser, where the secondary laser (SL) is a QD laser. The primary laser (PL) is a tunable laser source (TLS). A polarisation controller (PC) is used to maximise coupling. A circulator shines light from the PL into the SL, the light that is emitted from the SL into the circulator is then sent into a 50/50 splitter. 50% of light is sent directly to a 12 GHz detector connected to an oscilloscope (OSC). The other 50% is sent to a 90/10 coupler, where it is mixed with light from a second TLS. A polarisation controlled is used to maximise the amplitude of the beat signal. 90% of the beat signal is sent to a 12 GHz detector connected to an oscilloscope and the remaining 10% is sent to an optical spectrum analyser (OSA). . . . . 27
- 2.10 Cartoon describing the measurement of the optothermal effect, similar to Figure 2.7. (a) and (b) show the optical spectrum of the QD laser. The blue lines represent the subthreshold modes. The red line represents the lasing frequency of the QD laser, which remains fixed at  $\omega_P$  as the QD laser is phase locked to the constant TLS. The grey dashed line,  $\omega_S$ , is the longitudinal mode that would lase in this single mode laser, in the absence of optical injection. The green line labelled  $\omega_{TLS}$  is a second TLS and is used as a probe laser. When a subthreshold longitudinal mode happened to receive more gain during the low intensity section of the square wave train, as shown in (a), a beating tone is observed showing the frequency difference between the sweeping longitudinal mode and  $\omega_{TLS}$ . It changes from -12 GHz to -10 GHz over the duration of the lower intensity section as indicated by the timestraces in (c) and (d). The circles indicate what part of the cycle the top panel is describing. . . . . 28

- 2.11 (a) The resulting intensity after a square wave train is mixed with and a second TLS (with frequency of approximately 12 GHz from the side mode). The longitudinal mode did not have sufficient power in the upper intensity section to create a beat signal. In the lower intensity section there was enough power from the longitudinal mode to create a beat tone that could be detected. The power of the longitudinal mode decreased over the duration of the lower intensity section and thus the amplitude of the beat tone can also be seen to decrease. (b) 10 ns windows were taken and the FFT was calculated for each window. The resulting frequencies are plotted in a heat map. The frequency recorded is the frequency of the second TLS minus that of the subthreshold longitudinal mode under investigation. These values are arbitrarily set but it's important to note that the QD laser undergoes a 2 GHz sweep due to an optothermal effect. . . . . 29
- 2.12 The basic setup shown in Figure 2.1 is repeated but more components are added before detection. Experimental setup of an optically injected QD laser acting as the secondary laser (SL). Light from the primary laser (PL) which is a tunable laser source (TLS) is split. 10% is sent into one arm of a  $3 \times 3$  coupler for an interferometric phase measurement technique. 90% is sent to a circulator and is then injected into a QD laser. A polarisation controller (PC) is used to maximise coupling. The light emitted from the SL into the circulator is sent to another arm of the  $3 \times 3$  coupler. The third arm is left empty. Polarisation controllers are used to maximise the interference of the  $3 \times 3$  coupler input signals. All 3 outputs of the  $3 \times 3$  coupler are connected to 12 GHz detectors connected to an oscilloscope (OSC). . . . . 30
- 2.13 (a) Timetrace of a noise induced excitable pulse at approximately [Pleaseinsertintopreamble]6.6 GHz detuning. (b) The phase associated with the timetrace from (a). The phase undergoes a change of 2.4 rad at the onset of a square pulse and over the duration of the pulse the phase undergoes a slow change of approximately 1.4 rad before jumping back to the lower intensity section. . . . . 31
- 2.14 Phasor diagram for the secondary laser field, corresponding to the pulse seen in Figure 2.13. The long stretched out part corresponds to the square pulse and the more concentrated section in the lower intensity section. . . . . 31
- 2.15 (a) Intensity trace of periodic square wave train. (b) The phase corresponding to (a). During the upper intensity section the phase undergoes a slow 1 rad change. During the lower intensity section there is a slow 0.4 rad change of phase. . . . . 32

2.16	The basic setup shown in Figure 2.1 is repeated but a LiNbO <sub>3</sub> phase modulator (MOD) is introduced after the primary laser (PL). The PL is a tunable laser source (TLS). The modulator is driven by a pulse generator. This modulates the light being injected into the QD secondary laser (SL). A polarisation controller (PC) is used to maximise coupling. A circulator shines light from the PL into the SL, the light that is emitted from the SL into the circulator is sent to a 12 GHz detector connected to an oscilloscope (OSC). . . . .	33
2.17	(a) and (b) show the output from the secondary laser. (c) and (d) show the electric pulses of different amplitudes that were sent to the phase modulator in order to perturb the injected light. (a) is a successfully triggered optical square pulse and was triggered by the electrical pulse (c) with an amplitude of 3.82 V. The smaller perturbation (d) with an amplitude of 1.67 V, fails to excite a square pulse as shown in (b). . . . .	34
2.18	Efficiency curve for deterministically triggered square pulses. There is a threshold at approximately 2.3 V. If the strength of the perturbation is greater than this then there is a 50 % probability that a pulse would be fired. . . . .	34
2.19	Numerical pulse/dropout trains. (a) shows the intensity at a detuning of $-0.955$ ; (b) shows the intensity at a detuning of $-0.9225$ ; and (c) shows the intensity at a detuning of $-0.89$ , $K$ is $0.7056$ . . . . .	37
2.20	Zoomed in traces of the pulse/dropout trains shown in Figure 2.19. (a) shows the intensity at a detuning of $-0.955$ ; (b) shows the intensity at a detuning of $-0.9225$ ; and (c) shows the intensity at a detuning of $-0.89$ , $K$ is $0.7056$ . . . . .	37
2.21	The distribution of the interpulse times is shown in (a) and the inset is a persistence plot of 100 consecutive pulses plotted on top of each other illustrating the regular pulse width. (b) shows the distribution for the square dropouts with a persistence plot inset. The control parameters match those in Figure 2.19. . . .	38
2.22	(a) shows the distributions of the duration of the high intensity plateaus. Similarly (b) shows the distributions of the low intensity lifetimes. The narrow distributions indicate a consistent and reproducible square wave train. (c) is a persistence plot of 100 consecutive pulses plotted on top of each other illustrating the regular pulse width. . . . .	38
2.23	Bifurcation diagram using the Class A model. The blue curve shows the saddle node structure of the bare system (no optothermal coupling, $c = 0$ ). The solid lines represent stable solutions and the dotted lines represent unstable solutions. There is a clear bistability. The red curve shows the trajectory of Figure 2.24 (b) obtained at $\Delta = -0.9540124775$ with a finite optothermal coupling, $c = 0.1$ and $\gamma = 5 \times 10^{-6}$ . For both cases $K = 0.7104$ . . .	39

- 2.24 Bifurcation diagram showing the new Hopf bifurcation created by the optothermal coupling. The Hopf point  $\Delta_H = -0.95401276$  is shown with a blue dot. Examples of small and large amplitude cycles at  $\Delta = -0.95401248$  and  $\Delta = -0.9540124775$  are shown in insets (a) and (b), where their amplitudes are approximately 0.004 and 0.86 respectively. Zero corresponds to constant output. Inset (c) zooms in on the canard explosion and the associated region of small amplitude oscillations.  $K = 0.7104$  throughout. 40
- 2.25 Two examples of perturbed trajectories. In the black dashed trace a perturbation of  $\delta\phi = 0.0011$  was applied at  $t = 1000$  yielding a short trajectory back to the steady state behaviour. In the red trace a perturbation of  $\delta\phi = 0.0012$  was applied yielding an excitable trajectory.  $K = 0.7104$ ,  $\Delta = -0.9541$ . The inset zooms in on the perturbation. . . . . 41
- 2.26 (a) Noise induced excitable squares pulses found for  $K = 0.04$ ,  $\Delta = -0.029525$ ,  $D = 0.01$ ,  $\gamma = 5 \times 10^{-6}$  and  $\eta = 2 \times 10^{-3}$ . (b) shows the associated phasor trajectory. . . . . 43
- 2.27 Near the subcritical Hopf bifurcation point a bistability is creating and the two solutions are shown above. The solution the system evolves into depends on the initial conditions. Initial conditions for the constant trace are  $R = 0.735$ ,  $\phi = 1.560$ ,  $n = 2.06$  and  $\omega = 0.016$ . For the square trace the initial conditions are  $R = 1.08$ ,  $\phi = 0.667$ ,  $n = 0.795$  and  $\omega = 0.028$ . The operating parameters are the same for both.  $K = 0.04$ ,  $\Delta = -0.02929$ ,  $\eta = 2 \times 10^{-3}$ ,  $\gamma = 5 \times 10^{-6}$  and  $D = 0$ . . . . . 44
- 2.28 Bifurcation diagram using the QD model. The blue curve shows the saddle node structure of the bare system (no optothermal coupling,  $c = 0$ ). The solid lines represent stable solutions and the dotted lines represent unstable solutions. There is a clear bistability. The red curve shows the trajectory shown in Figure 2.29 (b) for  $\Delta = -0.02931155$  with finite optothermal coupling,  $c = 0.03$  and  $\gamma = 5 \times 10^{-6}$ . For both cases  $K = 0.04$ ,  $D = 0$  and  $\eta = 2 \times 10^{-3}$ . . . . . 45
- 2.29 Bifurcation diagram for the supercritical Hopf case showing the amplitude of the cycle versus the detuning. (Thus, zero corresponds to constant output.) Small amplitude oscillations are obtained just after the Hopf point (blue dot)  $\Delta_H = -0.0293118$ . A canard explosion then leads to the creation of a large amplitude cycle. The insets show two characteristic examples of the output.  $K = 0.04$ ,  $D = 0$ ,  $\eta = 0.03$ ,  $c = 0.03$  and  $\gamma = 5 \times 10^{-6}$  throughout. The insets show  $\Delta = -0.0293116$  and  $\Delta = -0.02931155$  for the small amplitude and large amplitude cycles with amplitudes of 0.01 and 0.43 respectively. . . . . 45
- 2.30 Noise induced square pulses for the supercritical Hopf case.  $K = 0.04$ ,  $\Delta = -0.0304$ ,  $\gamma = 5 \times 10^{-6}$ ,  $\eta = 0.03$ ,  $D = 0.01$ . . . . . 46

3.1	Basic optical injection set up. Light from a primary laser (PL), typically a tunable laser source, is injected into a circulator and then into the cavity of the secondary laser (SL), the QD laser. A polarisation controller (PC) maximises coupling. A filter is used to separate the ground state (GS) and excited state (ES), so each state can be monitored independently by detectors connected to an oscilloscope. . . . .	50
3.2	(a) the LI curve of a two colour device used in [132] that demonstrates the typical features observed in most devices discussed here. (b) shows the emission spectra of the device and correspond to 3 distinctive lasing regions: (i) There is the GS threshold beyond which only GS light is emitted. (ii) At the ES threshold, both the ES and GS last simultaneously. (iii) At higher pump currents the GS is quenched and only the ES lases. Reprinted with permission from [132] © The Optical Society. . . . .	51
3.3	(a) the ES and (b) GS spectra before and after optical injection into the GS. Initially the device is pumped so as to emit from the ES only and all the GS modes are subthreshold (black). Injecting close to a GS mode the ES turns off and the GS turns on (red). Figures reprinted with permission from [132] © The Optical Society.(c) shows three line width measurements. The blue shows the line width of the GS when the laser is pumped to emit from GS only. The black shows the very narrow linewidth of the primary laser, the TLS. The red shows the linewidth of the QD laser after injection. Phase locking is verified as the QD laser has adopted a similar line width to the primary laser. Reprinted with permission from [46] © The Optical Society. . . . .	51
3.4	Hysteresis cycle analyses using Equations 6.1-3.5. The QD laser is biased to emit from the ES when free-running. The panels show the effect of changing $\beta$ . (a) $\beta = 3$ , (b) $\beta = 2.5$ , and (c) $\beta = 1$ . For $\beta > 2$ the experimentally observed bistability is reproduced. Reprinted with permission from [132] © The Optical Society. . . . .	53
3.5	Experimental optical switching between a bistability. A Mach Zehnder Modulator is connected to a pulse generator that produces square pulses, the insets in (b) and (c) show the electrical signals. During a short square pulse GS light injects into the QD laser that is free running in the ES. The ES quickly turns off and the GS quickly turns on until the Mach Zehnder Modulator switches off the injected light again. Reprinted with permission from [132] © The Optical Society. . . . .	55

- 3.6 (a) Experimental and (b) numerical periodic pulse trains of GS dropouts accompanied by sharpened ES pulses. The small ringing oscillations at the minima of each GS dropout correspond to oscillations around a saddle focus. By experimentally varying the detuning the frequency of the train can be tuned between 0.3 and 1.3 GHz. In the bottom panel time is in units of photon lifetime. Figures reprinted with permission from [136] © The Optical Society. . . . . 57
- 3.7 Bifurcation diagram of the GS (red) and ES (blue) intensities vs detuning using the rate equations from [136]. Continuous (dashed) lines correspond to stable (unstable) branches. *LP* denotes a homoclinic bifurcation point. Other models [134, 137] also produce a homoclinic bifurcation point at the negative detuning boundary. Reprinted with permission from [136] © The Optical Society. Note that the sign of the detuning in this figure is the opposite of that used in the rate equations presented in this Chapter . . . . . 58
- 3.8 Left panel: Periodic switching between a quiet state and a bursting state. During the quiet state the GS is the dominant frequency and during the bursting state the ES is dominant. Right Panel: A zoom of an individual bursting state. The intensity of both states oscillate in antiphase, the amplitude and the frequency of the oscillations continuously grow until there is a state switch back to the quiet state. An optothermal effect is responsible for an intrinsic detuning sweep and slow passage through bifurcation points. Figures reprinted from [78]. . . . . 60
- 3.9 Bifurcation diagrams showing the intensity of the GS vs detuning. Stable and unstable branches are shown by full and dotted lines, respectively. An optothermal effect is included and the black bursting cycle is reproduced. The points LP1 and H mark a limit point of steady states and a Hopf bifurcation point, respectively. Right: A branch of periodic solutions represented by the maximum intensity is emerging from H and snakes with various stability changes until it reaches the unstable steady state branch at a homoclinic bifurcation point (HOM). The figure shows that the bursting oscillations follow a stable branch of periodic solutions until it reaches a limit-point of limit-cycles (LP2). Reprinted figure from [78]. Note that the sign of the detuning in this figure is the opposite to that used in the rate equations presented in this Chapter. . . . . 61

- 3.10 Maps comparing a single-colour laser (a) and a two-state laser (b) under optical injection using the microscopic model. There are regions of chaos near the unlocking boundaries of the single-colour laser map. However there is no chaos or even multi-frequency dynamics observed in the map for the two-state laser. Reprinted with permission from [139], S. Meinecke, B. Lingnau and K. Lüdge, in *Physics and Simulation of Optoelectronic Devices XXV*, Vol. 10098, International Society for Optics and Photonics (SPIE, 2017). . . . . 62
- 4.1 Schematic representing the experimental set up. A unidirectional injection experiment similar to the one shown in Figure 2.12 is setup, where the secondary laser (SL) is a QD laser and the primary laser (PL) is a tunable laser source (TLS). The main difference is that a filter is added to separate the GS emission from the ES emission. Light from the (PL) is sent to a circulator and is then injected into a QD laser. A polarisation controller (PC) is used to maximise coupling. The light emitted from the SL is sent into the circulator and then to a filter where the ES and GS light are separated. The ES light is sent directly to a 12 GHz detector. The GS light goes into a 90/10 splitter, 10% is sent to a power meter (PM) and the remain goes to a detector connected to an oscilloscope. The red lines represent light at approximately 1300 nm close to the GS emission, the blue is ES only and the purple is both GS and ES. The black are high speed electrical cables. . . . . 68
- 4.2 Experimental stability map. The top panels show results when the injection strength,  $K$ , is swept from low to high. The bottom panels show the results when injection strength is swept from high to low. The average ES and GS intensities are calculated for 20  $\mu$ s long measurements. The phase locked region is identified as the bright yellow/cyan area in (a) and (c), where the GS has high output intensity. This corresponds to a quenched ES, shown as dark blue in (b) and (e). The ES variance is shown in (c) and (f), green is where oscillatory behaviour is observed and dark blue corresponds to constant output. The speckled area on the positively detuned boundary of (a) and (c) is related to very slow oscillations. A more detailed stability map of this boundary is shown in Figure 4.7. . . . . 69

- 4.3 Qualitative behaviours observed for various injection strengths during an up-sweep, the detuning remains fixed at -6.9 GHz. The lower panels zoom into the dynamics shown in the corresponding upper panels. The title on top of the subplots show the injection strength value. The colour of the font corresponds to the colour of dots in Figure 4.4. The dots mark the location on the map where the timetraces were recorded. (a) shows a periodic cycle where the GS and ES intensities oscillate in antiphase, with a period in the order of a nanosecond. (b) there is a quiet state between long periods of oscillations. (c) a periodic square wave emerges with large amplitude oscillations at the start and end of bursting state. (d) oscillations at the beginning of the bursting state become damped, but growing amplitude oscillations still appear before there is a switch back to the quiet state. (e) all fast oscillations are strongly damped and a square wave train is observed. . . . . 71
- 4.4 The same experimental stability maps of average GS and ES intensities, and ES variance, previously shown in Figure 4.2. Here markings have been added to make our discussion easier. The injection strength is swept up in (a)-(c) and down in (d)-(f). The coloured dots correspond to the timetraces in Figure 4.3. For a more obvious identification of a hysteresis the boundary of oscillating dynamics observed in the down-sweep is plotted on top of the up-sweep data as a red line. Similarly the boundary of oscillating dynamics seen in the up-sweep is plotted as a white line on top of the down sweep map. Hysteresis is evident in (f) where the region of oscillating dynamics extends beyond the white line, which marks the boundary observed (c). . . . . 72
- 4.5 Timetraces from an up-sweep in the region of hysteresis at -8.2 GHz detuning. The corresponding down-sweep timetraces are shown in Figure 4.6. Initially the QD laser is unlocked and as injection strength is increased the intensity of the regenerated GS slowly increases and the ES intensity decreases. Small oscillations are visible in the GS intensity at  $K=0.645$  before a sudden change in behaviour. When  $K > 0.651$  short quiet regions appear between long bursting states. As  $K$  is increased the length of time spent in the bursting state decreases. . . . . 73

- 4.6 Timetraces from a downsweep in the region of hysteresis at -8.2 GHz detuning. These subfigures correspond to the same  $K$  levels in Figure 4.5 but the direction of the injection strength sweep starts at (l) and then moves in reverse. In the bottom row the duration of the quiet and bursting states is very similar to that of Figure 4.5. But as  $K$  is decreased below 0.645 the QD laser continues to operate in an oscillatory regime, whereas in Figure 4.5 continuous dual state emission is observed. The time between quiet states becomes larger as  $K$  is decreased. The top line then zooms in on the traces to show the fast oscillations that become the dominant behaviour. When  $K = 0.611$  no quiet state is detected over the course of a  $20 \mu\text{s}$  time window on the oscilloscope. When injection strength is decreased below 0.605 the QD laser suddenly moves to a dual state continuous emission regime. . . . . 74
- 4.7 Experimental maps of the positively detuned side of the unlocking boundary. The top row shows an upsweep and the bottom shows a downsweep. The timetraces used to build this map were 1 second long. Three regions are visible in (a) and (b). The large yellow region with high GS intensity extending all the way from the negatively detuned unlocking boundary is a phase locked region. The blue region extending from the right is the unlocked region with low GS intensity and dual state emission. The narrow green region in the middle is where there are slow oscillations between the high and low GS intensity solutions and thus the average intensity lies somewhere in the middle. (b) and (e) show a completely quenched ES with dark blue when the laser is phase locked. The region of slow oscillations is represented by the slightly lighter shade of dark blue. For positive detuning values dual state emission is clear. The variance shows the region where slow oscillations occur more clearly, (c) and (f). There is a small hysteresis cycle of one to two pixels at both sides. The white line marks corresponds to the timetraces shown in Figure 4.8. . . . . 76
- 4.8 Slow oscillations observed during an upsweep at -0.6 GHz, near the positively detuned side of the unlocking boundary. The sweep is marked by a white line in Figure 4.7. Comparing (a) and (l), there are two very different GS amplitudes at either side of the region of oscillations. The slow oscillations are between these two underlying intensities, suggesting there is a bistability. . . . 77

- 4.9 Experimental maps of the positively detuned side of the unlocking boundary. The top row shows an upsweep and the bottom shows a downsweep. (a) and (d) show the average period of the GS oscillations, and are always approximately 40 ms. (b) and (e) show the average lifetime of the higher intensity GS state which is longer lived closer to the centre locking region. (c) and (f) show the average lifetime in the lower intensity GS section and it is longer lived at the more positively detuned boundary. . . . . 78
- 4.10 Experimental maps of the positively detuned side of the unlocking boundary. The top row displays the results from an upsweep and the bottom displays results from a downsweep. These maps show the variance of the data used to calculate the averages in Figure 4.9. (a) and (d) show the variance of the period of the GS oscillations, the variance is greatest at the boundary suggesting noise may have more of an influence there. (b) and (e) show the variance of the time spent in the higher intensity GS state. It is largest at the negative side of the slow oscillation region. This corresponds to a low variance for time spent in the lower GS intensity region, (c) and (f). The opposite is true at the positively detuned side of the slow oscillation region. Here there is a large variance in the time spent in the low intensity section but low variance in the time spent in the higher intensity section. . . . . 79
- 4.11 Stability maps in the absence of any optothermal effects. The upper panel shows the results for the upsweep and the lower panel shows the corresponding downsweep. Bistability 1, the bistability between the phase-locked output and the regenerated two state output can be seen by comparing the top left corners of (a) and (c) at high injection strengths near  $K = 5$ . Bistability 2, the bistability between the phase-locked output and the oscillating two state output is clear when looking at the top left corners of the variance plots, (c) and (f). Bistability 3, the bistability with lowest injection strength between phase-locked/pulsing regime and regenerated two state output can be seen in (c) and (f). . . . . 82
- 4.12 Simulated stability map with one optothermal effect. The top panel shows the results from an upsweep and the lower panel shows the corresponding downsweep. (a) and (d) are the average GS intensity and (b) and (e) are the average ES intensity. The region of high ES variance, (c) and (f), is much larger than in Figure 4.11 as Bistability 1 is broken and is replaced with a square wave regime.  $\gamma_1 = 40 \mu\text{s}^{-1}$ ,  $c_1 = 3 \text{ ns}^{-1}$ . . . . . 83

- 4.13 1D bifurcation diagrams showing the bistabilities. The many diagonal lines are brought about by the bursting phenonema, where the amplitude is growing even though the input parameter for detuning remains fixed. (a) only one optothermal effect is included. A bistability is created on the positive unlocking boundary. At the negative unlocking boundary, there is a large cycle between the remnants of a bistability, with some of the bistability remaining in tact. (b) both optothermal effects are included. Figure 4.15 shows the evolution of the time traces during a sweep. The bistability at the positive boundary is now a limit cycle. In both cases  $K = 4.5$ . . . . . 84
- 4.14 Simulated map with two optothermal effects. Top panel shows the results from the upsweep and the lower panel shows the corresponding the downsweep.  $c_1$  is different because the second optothermal effect counteracts the first one. In order to get the same overall shape  $c_1$  must change.  $\gamma_1 = 40 \mu\text{s}^{-1}$ ,  $c_1 = 4.5 \text{ ns}^{-1}$ ,  $\gamma_2 = 4 \mu\text{s}^{-1}$ ,  $c_2 = 0.7 \text{ ns}^{-1}$  . . . . . 85
- 4.15 Time series progression for Figure 4.13 (b). There is an increased number of bursting oscillations when going from positive to negative detuning.  $\gamma_1 = 40 \mu\text{s}^{-1}$ ,  $c_1 = 4.5 \text{ ns}^{-1}$ ,  $\gamma_2 = 4 \mu\text{s}^{-1}$ ,  $c_2 = 0.7 \text{ ns}^{-1}$  . . . . . 85
- 4.16 Simulated maps showing the number of maxima in log scale when no optothermal effect is included, (a) and (d), when the non-radiative optothermal effect is included, (b) and (e), and when both the non-radiative and light reabsorption optothermal effects are included (c) and (f). The top panel shows the results from the upsweep and the lower panel shows the corresponding downsweep. Chaos is not present for any case. . . . . 86
- 5.1 Setup for unidirectional optical injection experiment where the secondary laser (SL) is a QD laser and the primary laser (PL) is a tunable laser source (TLS). Light from the (PL) is split; 10% is sent into one arm of a  $3 \times 3$  coupler for an interferometric phase measurement technique. 90% is sent to a circulator and is then injected into a QD laser. A polarisation controller (PC) is used to maximise coupling. The light emitted from the SL is sent into the circulator and then to a filter where the ES and GS are separated. The GS light goes into another arm of the  $3 \times 3$  coupler and the ES light is sent directly to a 12 GHz detector. The third arm of the  $3 \times 3$  coupler is left empty. Polarisation controllers are used to maximise the interference of the  $3 \times 3$  coupler input signals. All 3 outputs of the  $3 \times 3$  coupler are connected to 12 GHz detectors and each detector is connected to the oscilloscope (OSC). The red lines represent light at approximately 1300 nm close to the GS emission, the blue lines represent ES only and the purple is both GS and ES. The black are high speed electrical cables. . . . 90

5.2	Timetrace of dual state excitability. (a) shows the 300 ps GS drop out, (b) shows the 80 ps ES pulse and (c) is the phase of the GS.	91
5.3	Phasor diagram showing the real and imaginary parts of the electric field. The steady state is at approximately (0.6,0). When noise triggers a pulse it results in a bounded trajectory that does not go around the origin. The spiral close to the origin suggests the presence of a saddle focus. . . . .	92
5.4	A 3 dimensional figure showing the phase and the GS and ES intensities. When the ES turns on it pulls the phase away from the origin, stopping a $2\pi$ rotation. The saddle focus has 2 oscillations as in Figure 5.3 but it is not visible from this reference angle. .	92
5.5	Numerical bifurcation diagram. (a) shows the GS (red) and ES (blue) intensities vs $\varepsilon$ . (b) shows the phase of the GS vs $\varepsilon$ , the injection strength. Continuous (dashed) lines correspond to stable (unstable) branches. $LP$ and $H$ denote limit points and Hopf bifurcation points, respectively. $BP$ denotes an unstable bifurcation point. $LP1$ denotes a SNIC bifurcation and arises at $\varepsilon = 4.4373$ . The fixed parameters are: $\eta = 0.01$ , $\Delta = 0$ , $\alpha = 3$ , $\beta = 2.4$ , $g_0^g = g_0^e = 0.55$ , $J = 56$ , $B_{e,h} = B_{e,h}^w = 100$ , $C_e^w = 0$ , $C_h^w = 10^2$ , $C_e = B_e \exp(-2)$ , $C_h = B_h$ . $I_g$ is normalised by its value ( $I_g = 223.83$ ) at $\varepsilon = 8$ . . . . .	95
5.6	Numerically obtained noise induced excitable events ( $D = 0.5$ ). (a) shows the GS (red) and ES (blue) intensities. (b) shows the corresponding phase evolution. The parameters are the same as in Figure 5.8, where the vertical line indicates the point of operation. . . . .	96
5.7	Simulated 3D plots. (a) has a low noise level ( $D = 0.5$ ) and consequently displays many rotations in the spiral. (b) has a more realistic noise level ( $D = 1$ ) and is in close agreement with the experimental results in Figure 5.4. . . . .	96
5.8	Zoom of Figure 5.5 (b). Where $LP1$ denotes the limit point which is a SNIC bifurcation. The blue dot labelled SF represents the saddle focus. The green dotted line marks the operating injection strength where the noise induced events in Figure 5.6 and Figure 5.7 are found. The dashed lines are unstable branches and the solid lines are stable. The same operating parameters described in Figure 5.6 are used here. . . . .	97
6.1	Spectra of the ES (a) and (c) and the GS (b) and (d) before and after optical injection. While Free running at 75 mA the strongest ES mode is 42.5 dB greater than the strongest GS mode which is visible due to amplified spontaneous emission. After optically injecting into a GS mode the ES is quenched and the GS mode increased by 52.6 dB. . . . .	101

- 6.2 A unidirectional optical injection experiment similar to the one shown in Figure 5.1 is set up, where the secondary laser (SL) is a QD laser and the primary laser (PL) is a tunable laser source (TLS). The main difference is a  $\text{LiNbO}_3$  phase modulator (MOD) driven by a pulse generator (PG) is introduced between the PL and SL, which perturbs the injected light. After modulation, light from the (PL) is split; 10% is sent into one arm of a  $3 \times 3$  coupler for an interferometric phase measurement technique. 90% is sent to a circulator and is then injected into a QD laser. A polarisation controller (PC) is used to maximise coupling. The light emitted from the SL is sent into the circulator and is then to a filter where the ES and GS are separated. The GS light goes into another arm of the  $3 \times 3$  coupler and the ES light is sent directly to a 12 GHz detector. The third arm of the  $3 \times 3$  coupler is left empty. Polarisation controllers are used to maximise the interference of the  $3 \times 3$  coupler input signals. All 3 outputs of the  $3 \times 3$  coupler are connected to 12 GHz detectors and each detector is connected to the oscilloscope (OSC). The red lines represent light at approximately 1300 nm close to the GS emission, the blue is ES only and the purple is both GS and ES. The black are high speed electrical cables. . . . . 103
- 6.3 (a) Experimental efficiency curves for anticlockwise and clockwise perturbations. The thresholds, defined at 50% efficiency, are at approximately 2 rad and -3.5 rad respectively. (b) The corresponding theoretical efficiency curves with thresholds at 0.975 rad for anticlockwise perturbations and at -1.7 rad for clockwise, where  $\sigma = 1$ . . . . . 104
- 6.4 The response of the secondary laser to phase perturbations. (a) and (b) are for anticlockwise perturbations of 1 and 4.2 rad. (c) and (d) are for clockwise perturbations of -3 and -4.2 rad. The left panels show unsuccessful perturbations and the right show successfully triggered excitations. . . . . 104
- 6.5 Heatmap showing delay times; the time a pulse is fired after the system has been perturbed. The left panel is for clockwise and the right is for anticlockwise. The efficiency curves are also plotted. The delay time is largest when the efficiency is below 100%. 106
- 6.6 Numerically generated sample responses to an above threshold (a) anticlockwise perturbation where  $d = 1.7$  and (b) clockwise perturbation where  $d = -2$ . The longer response time for clockwise perturbations is partially due to the positive and non-zero  $\alpha$ . The fixed parameters are  $\eta = 0.01$ ,  $\Delta = 0$ ,  $\alpha = 3$ ,  $\beta = 1.5$ ,  $g_0^g = g_0^e = 0.55$ ,  $J = 5$ ,  $B_{e,h} = B_{e,h}^w = 100$ ,  $C_e^w = 0$ ,  $C_h^w = 100$ ,  $C_e = B_e e^{-2}$ ,  $C_h = B_h$ ,  $\varepsilon = 0.327$ . . . . . 108

- 6.7 (a) Intensity traces from a QD laser. (b) A zoom in on the intensities where the QD laser is emitting pulses after clockwise and anticlockwise perturbations were applied. (c) The phase of the TLS with respect to CW QD laser and the phase of the QD laser light with respect to CW TLS light. The phase perturbation amplitude can be measured, 5.7 rad. (d) To see what the QD laser is doing with respect to the TLS while it is perturbed, the two must be aligned and subtracted. . . . . 110
- 6.8 (a) intensity timetraces of the GS and ES after successful clockwise and anticlockwise perturbation. (b) the phase measurement is shown in a rainbow plot. The colour of the line changes in time for easy comparison to the phasor plot (d). (c) shows the phase of the TLS, the perturbation is 5.7 rad. (d) the phasor diagram showing the phase of the QD laser. Initially there is a large kick brought about by the clockwise perturbation. The trajectory turns around and completes a bounded rotation. After the anticlockwise perturbation the initial trajectory is not present, but the bounded trajectory is the same. (e) shows the phasor diagram corresponding to the TLS perturbation in (c).<sup>1</sup> . . . . . 112
- 6.9 (a) intensity timetraces of the GS and ES after successful clockwise and anticlockwise perturbation. (b) the phase measurement is shown in a rainbow plot. The colour of the line changes in time for comparison to the phasor plot (d). (c) shows the phase of the TLS, the perturbation is 3.5 rad. (d) the phasor diagram showing the phase of the QD laser. The clockwise perturbation is not as large as it was in Figure 6.8 so the initial trajectory is not as far. The trajectory still turns around and completes a bounded rotation. After the anticlockwise perturbation the initial trajectory is not present, but the bounded trajectory is the same. (e) shows the phasor diagram corresponding to the TLS perturbation in (c).<sup>1</sup> 113
- 7.1 A second LiNbO<sub>3</sub> phase modulator is added in series to the setup shown in Figure 6.2. Again the secondary laser (SL) is a QD laser and the primary laser (PL) is a tunable laser source (TLS). The LiNbO<sub>3</sub> phase modulators are driven by a pulse generator (PG). A 50:50 power splitter sends a similar signal to each modulator (MOD). A variable electrical delay line (VDL) is added to adjust the time between two perturbations. A polarisation controller (PC) is used to maximise coupling. The light emitted from the SL is sent into the circulator and then to a filter where the ES and GS light are separated and are sent directly to 12 GHz detectors connected to an oscilloscope (OSC). The red lines represent light at approximately 1300 nm close to the GS emission, the blue is ES only and the purple is both GS and ES. The black are high speed electrical cables. . . . . 116

7.2	(a) Timetraces close to the absolute refractory period, the second pulse can have long escape times. (b) Perturbations separated by 0.85 ns. There is a narrow distribution as the first dropout is interrupted. (c) Perturbations are separated by 1.22 ns, there is a large distribution of delay times because a relaxation oscillation increases the threshold. (d) The system has returned to steady state when the second perturbation is applied and the relative refractory period has passed. The two small GS negative spikes at approximately 2 ns are the location of the subthreshold clockwise perturbations. . . . .	117
7.3	(a) (Blue) Average time between two ES pulses after two perturbations were applied vs the time between two perturbations. Each data point is the average of 1000 sets of perturbations. The first perturbation was always successful. The absolute refractory period was 0.62 ns. (Red) Efficiency of the second perturbation. The first perturbation was always 100 % successful. (b) (Blue) the normalised average times between two ES pulses after two perturbations were applied vs the time between perturbations. The average is of 1000 sets of perturbations. (Red) standard deviation of the times between two ES pulses. (b) The average peak intensity of the second ES pulse vs the time between perturbations. (Red) The standard deviation of the peak intensities vs the time between perturbations. . . . .	118
7.4	The normalised times between two ES pulses after two perturbations were applied, shown in Figure 7.3 (a), have been normalised to the time between perturbations. The first perturbation was always successful. . . . .	119
7.5	Heat map showing the ES peak intensity (top) and the intensity of GS dropout troughs (bottom) vs the time between ES pulses. . . . .	121

7.6	A unidirectional optical injection experiment similar to the one shown in Figure 7.1 is set up, where the secondary laser (SL) is a QD laser and the primary laser (PL) is a tunable laser source (TLS). Two LiNbO <sub>3</sub> phase modulators, driven by a pulse generator (PG), are placed between the PL and SL, which perturbs the injected light. A variable delay line (VDL) is used to adjust the time between perturbations. After modulation, light from the (PL) is split; 10% is sent into one arm of a 3×3 coupler for an interferometric phase measurement technique. 90% is sent to a circulator and is then injected into a QD laser. A polarisation controller (PC) is used to maximise coupling. The light emitted from the SL is sent into the circulator and then to a filter where the ES and GS light are separated. The GS light goes into another arm of the 3×3 coupler and the ES light is sent directly to a 12 GHz detector. The third arm of the 3×3 coupler is left empty. Polarisation controllers are used to maximise the interference of the 3×3 coupler input signals. All 3 outputs of the 3×3 coupler are connected to a 12 GHz detectors which are connected to an oscilloscope (OSC). The red lines represent light at approximately 1300 nm close to the GS emission, the blue is ES only and the purple is both GS and ES. The black are high speed electrical cables. . . . .	122
7.7	Blue line shows the efficiency of the first perturbation. It always excites a pulse. The red line shows the efficiency of the second perturbation. 0.42 ns marks the end of the absolute refractory period, if the second perturbation arrives 0.42 ns after the first, a second pulse can be observed, timetrace shown in Figure 7.8. After 0.63 ns the second perturbation always triggers a pulse. Between 0.56 ns and 0.90 ns two perturbations can produce three pulses, timetrace shown in Figure 7.9. . . . .	123
7.8	Timetrace showing two anticlockwise perturbations applied 0.42 ns apart and both trigger a pulse. This marks the absolute refractory time. . . . .	124
7.9	(a) Timetrace showing two pulses arising from two perturbations, the time between the two perturbations is 0.72 ns. (b) Timetrace showing three pulses arising from two perturbations with the same time between them as in (a). There is an 95% probability of three pulses occurring for this perturbation separation. . . . .	124
7.10	(Blue) the average time between two ES pulses after two anticlockwise perturbations are applied. (Red) the standard deviation of the times between two ES pulses. . . . .	125
7.11	Timetrace showing that a second clockwise perturbation can inhibit the first perturbation if it arrives close enough in time. In this case the perturbations are separated by 0.22 ns. . . . .	126

7.12	Four different behaviours are observed when the time between two clockwise perturbations is between 0.47 and 0.93 ns. This figure shows examples of each behaviour when the perturbations are separated by 0.84 ns. (a) the second perturbation inhibits an ES pulse that would have been triggered by the first perturbation. (b) there is a small increase in ES intensity but not enough to deem it a pulse. (c) the peak ES intensity is large enough and is considered a pulse. (d) the first perturbation does not trigger a pulse as the second perturbation acted as an inhibitory signal. But a pulse is triggered after the second perturbation. . . . .	127
7.13	Efficiency curves for the first clockwise perturbation (blue) and the second clockwise perturbation (red) given that the first perturbation has already triggered a pulse. . . . .	128
7.14	(Blue) the average time between two ES pulses after two clockwise perturbations are applied. (Red) the standard deviation of the times between two ES pulses. . . . .	129
7.15	Two clockwise perturbations with similar amplitudes are summed together (green line). The amplitude of the perturbations are coupled to each other as the signal from the pulse generator is split 50/50. Thus the amplitude of both are varied simultaneously. The green line shows the efficiency curve for their total effective amplitude. The clockwise threshold is at -5.6 rad. The same experiment was done using two anticlockwise perturbations and the efficiency curve is represented by the black line. The anticlockwise threshold is 5.2 rad. . . . .	131
7.16	Timetraces that show two sets of perturbations from two electrical square signals, four perturbations in total. The perturbations are shown in the first 19 ns of (b). The subsequent 20 ns shows the lasers response, similar to the figures shown in Chapter 5. (a) shows the intensity traces of the GS and ES. No ES pulses are triggered, confirming that these perturbations are indeed sub-threshold. . . . .	132
7.17	(a) ES and GS intensities when a pulse has been successfully triggered. The time between two anticlockwise perturbations is 0 ns. (c) shows the effective perturbation amplitude from two anticlockwise perturbations summed together. When the time between perturbations is increased to 320 ps the efficiency of a pulse being triggered decreases to 0.991. (b) is an example of the intensities after two perturbations summed together are unsuccessful and (d) shows the phase has longer rise time when the time between perturbations is 320 ps. . . . .	133
7.18	The time between two anticlockwise perturbations is varied and an efficiency curve is plotted. . . . .	134

7.19	(a) ES and GS intensities when a pulse has been successfully triggered. The time between two clockwise perturbations is 0 ns. (c) shows the effective perturbation amplitude from two clockwise perturbations summed together. When the time between perturbations is increased to 120 ps the efficiency of a pulse being triggered decreases to 0. (d) is an example of the intensities after two clockwise perturbations summed together are unsuccessful and shows the effective phase perturbation. . . . .	134
7.20	(a) ES and GS intensities when a clockwise perturbation is applied 200 ps after an anticlockwise perturbation, a pulse is not triggered. (c) shows the effective perturbation amplitude, there is a small dip related to the anticlockwise perturbation, but when the clockwise perturbation is applied they effectively cancel each other out. (b) shows the ES and GS intensities when a clockwise perturbation is applied and then an anticlockwise one is applied 40 ps later. (d) shows the effective perturbation applied and similar to (c), the two opposing perturbations essentially cancel out.	135
7.21	An example of a matrix multiplication when applying the Roberts Kernel to an image. . . . .	136
7.22	A 256 level greyscale image of two elephants. The image is converted into a 4 level image and a binary image. Prewitt and Canny edge detection techniques are applied on the greyscale image and are compared to the $2 \times 1$ kernel photonic neural network. . . . .	137
7.23	$G_x$ and $G_y$ show the output matrix after the Roberts filter was applied to a binary image. 0 is represented by grey pixels, +1 are white and -1 are black. High (+1) and low (-1) thresholds are applied to both $G_x$ and $G_y$ , where +1 and -1 perturbations that are sent to the photonic neuron trigger a pulse. The conventional magnitude is compared to the approximated $G_x + G_y$ , that is built into the dual threshold system. . . . .	139
7.24	$G_x$ and $G_y$ show the output matrix after the Roberts filter was applied to a binary image. The values range from +3 to -3. +3 are white and -3 are black and integers in between are represented by different shades of grey. A high and low thresholds of (1) are applied to both $G_x$ and $G_y$ . The conventional magnitude is compared to the approximated $G_x + G_y$ , that is built into the dual threshold system. . . . .	141

## List of Acronyms

<b>ASE</b>	Amplified Spontaneous Emission
<b>CPU</b>	Central Processing Unit
<b>CW</b>	Continuous Wave
<b>ES</b>	Excited State
<b>FFT</b>	Fast Fourier Transform
<b>GS</b>	Ground State
<b>LIF</b>	Leaky Integrate and Fire
<b>MMO</b>	Mixed Mode Oscillation
<b>PC</b>	Polarisation Controller
<b>PG</b>	Pulse Generator
<b>PL</b>	Primary Laser
<b>QD</b>	Quantum Dot
<b>QDL</b>	Quantum Dot Laser
<b>QW</b>	Quantum Well
<b>RF</b>	Radio Frequency
<b>RO</b>	Relaxation Oscillation
<b>SL</b>	Secondary Laser
<b>SNIC</b>	Saddle-node on invariant cycle
<b>SNIPER</b>	Saddle-node on infinite period
<b>TLS</b>	Tunable Laser Source
<b>VCSEL</b>	Vertical Cavity Surface Emitting Laser
<b>WL</b>	Wetting Layer

## List of Publications

### Publications:

*Square wave excitability in quantum dot lasers under optical injection*

M Dillane, B Tykalewicz, D Goulding, B Garbin, S Barland and B Kelleher,  
Optics letters **44** (2), 347-350 (2019).

*Excitable interplay between lasing quantum dot states*

M Dillane, I Dubinkin, N Fedorov, T Erneux, D Goulding, B Kelleher and EA  
Viktorov,  
Physical Review E **100** (1), 012202 (2019).

*Neuromorphic dynamics with optically injected quantum dot lasers*

M Dillane, J Robertson, M Peters, A Hurtado and B Kelleher,  
The European Physical Journal B **92** (9), 197 (2019).

*Multimode dynamics and modeling of free-running and optically injected  
Fabry-Pérot quantum-dot lasers*

B Lingnau, M Dillane, J O'Callaghan, B Corbett and B Kelleher,  
Physical Review A **100** (6), 063837 (2019).

*Asymmetric excitable phase triggering in an optically injected semiconductor laser*

M. Dillane, B. Lingnau, E. A. Viktorov, I. Dubinkin, N. Fedorov, and B. Kelleher,  
Optics letters **46**, 440-443 (2021).

*Optical information processing using dual state quantum dot lasers: Complexity  
through simplicity*

B Kelleher, M Dillane and EA Viktorov,  
Light: Science Applications **10** (1), 1-15 (2021).

*Mapping the Stability and Dynamics of Optically Injected Dual State Quantum  
Dot Lasers*

M Dillane, B Lingnau, EA Viktorov and B Kelleher,  
Photonics **9** (2), 101 (2021).

**Conference publications**

*Non-Adler excitable interplay between lasing quantum dot states*

M Dillane, D Goulding, N Fedorov, I Dubinkin, T Erneux, EA Viktorov and B Kelleher,

Semiconductor Lasers and Laser Dynamics VIII 10682, 106820C (2018).

*Control of neuromorphic dynamics in two state quantum dot lasers*

M Dillane, I Dubinkin, N Federov, T Erneux, D Goulding, B Kelleher and EA Viktorov,

The European Conference on Lasers and Electro-Optics, jsi p9 (2019).

*Type II excitability with quantum dot lasers: Canards, bistabilities and more*

M Dillane, J Robertson, D Goulding, A Hurtado and B Kelleher,

European Quantum Electronics Conference, jsi p8 (2019).

**Conference oral presentations**

*Phase locked bistability of quantum dot lasers under high optical injection strengths*

Photonics Ireland, Galway 2017.

*Non-Adler excitable interplay between lasing quantum dot states*

Society of Photo-Optical Instrumentation Engineers (SPIE) Photonics Europe, Strasbourg 2018.

*The neuromorphic dynamics of quantum dot lasers under optical injection*

Photonics Ireland, Cork 2018.

*Type II excitability in optically injected quantum dot lasers*

European Semiconductor Laser Workshop (ESLW), Cork 2019.

*Type II optothermal excitability in optically injected quantum dot lasers*

International Symposium on Physics and Applications of Laser Dynamics (IS-PALD), Metz 2019.

*Dual threshold excitability*

European Semiconductor Laser Workshop (ESLW) virtual conference, 2020.

**Conference poster presentations** *Intensity and phase dynamics of optothermal instability in quantum dot lasers*

Photonics Ireland, Galway 2017.

*Canard explosion in the optically injected semiconductor laser*

Society of Photo-Optical Instrumentation Engineers (SPIE) Photonics Europe, Strasbourg 2018.

*Control of neuromorphic dynamics in two state quantum dot lasers*

The European Conference on Lasers and Electro-Optics (CLEO) Europe, Munich 2019.

*Type II excitability with quantum dot lasers: Canards, bistabilities and more*

The European Conference on Lasers and Electro-Optics (CLEO) Europe, Munich 2019.

I, Michael Dillane, certify that this thesis is my own work and I have not obtained a degree in this university or elsewhere on the basis of the work submitted in this thesis.

*Michael Dillane*

## Acknowledgements

Firstly, I'd like to thank my supervisor Dr. Bryan Kelleher. I really enjoyed the time I spent working with Bryan during my PhD. Bryan gave me free reign to explore ideas that interested me. I never felt like I was told to do anything and always felt we were more like collaborators. Bryan always gave me great direction and was quick to respond when I had any questions. I have learned so much under his supervision, thanks for your all patience and teaching and the odd re-re-explanation.

Next I'd like to thank Dr. Benjamin Lingnau. One of the most intelligent people I have met and a wizard with Python. Ben sat beside me and had to put up with all my crackpot ideas as soon as they popped into my head. Thanks for taking the time to teach me and explain things in detail. Ben also helped me with Python and even though he left the group he was always quick to reply and willing to help. I hope someday you return to working with lasers but if not I know you'll be succesfull in whatever you do.

To Dr. Evgeny Viktorov and his group, Jenya was always enthusiastic and eager to collaborate. He was the driving force that helped us get over the line for some great publications. His blunt emails always made for enjoyable reading and efficient communication.

Next I'd like to thank my family. I would not be at this point today if wasn't for my Dad. He supported me and my education throughout my life for which I am incredibly grateful. When I was in school his mantra was always "stay in the books". My Mom always placed a strong emphasis on education, I know she would be beaming with pride with what I have achieved. My two sisters Catherine and Niamh, thanks for all the support and encouragement over the last few years. I'd like to thank Miriam who helped along the way and never lost patience for all the times I made her late dropping me to school.

To Sinéad, I genuinely don't think this thesis would be half as good if you weren't in my life. Thanks for always supporting me and particularly for reminding me that life can go back to normal after COVID and after writing this thesis. I would probably have developed scurvy if it wasn't for Sinéad cooking countless meals and taking me out for loops around the block and the old reliable walk around The Lough. Thank you for the sacrifices you have made for me over the last year, I really do appreciate it.

To Creamy, Rory, and Russell who came with me all the way from my undergrad, right through my PhD. Although we all worked in the same building we rarely ever talked about work, which was always a welcomed distraction. Thanks for the tea break chats about nonsense and more importantly for your friendship outside of work. All the pool and pints in the Mardyke, Costigans, Cissies and Coughlans where we also talked absolute nonsense were always so enjoyable along with so many trips; Amoi, beers for the boys in Thailand and being a part of Johann van Graans Red Army in

Edinburgh are just a few of the really great memories.

To my lunch group, Anya, Declan, Emma, Eoin, Louise, Ruaidhrí, Thomas, it was always great coming down into the canteen, again chatting nonsense. I don't think we will ever know if GOMAD would have been a success but strangely I am OK with that.

To Dan, Laura, Pearse, Phelan, Steve and Susanne, I was really lucky that you all had courses that finished after mine. Over the last 5 years I have enjoyed my time in Cork so much. Particularly, the early in my PhD, I basically had two more years of undergrad, I was amazingly fortunate! Thanks for all the nights out in Monday Club, house visits, games of Battlefield, FIFA, Fortnite and Rugby World Cup 2011 (basically anything with the dual entertainment system) and building snow sculptures. I would also like to thank Pearse for his excellent customer service when he worked in Riardans. I briefly had my own office in the Kane and was fortunate enough to have Susanne join me for so many lunches where we discussed a multitude of very serious topics. The flexibility to travel during my PhD was one of the main benefits and I don't think I could have asked for better friends to travel with. Thanks for the memories of inter-railing and the World Cup tour in Japan. Turning the screw on Pearse white water rafting, Sziget, Art's Hole, Valvasorjev Dom, the Shinjuku line, karaoke, hedgehog cafes, tiny bars and amazing toilets are just some of the highlights I'll never forget.

To Ayisha, Emma, Killian and Queelan my housemates in Bendemeer Park, I have really enjoyed living with you all over the last 3 years. You managed to make a world wide pandemic an enjoyable time. It was a much more boring version of Love Island but it was always great to come home to a buzzy house with such a great atmosphere.

To all my teachers in school who sparked my interest in science

Finally, to Coca-Cola, Haribo and whoever makes Squashies! The sheer volume of sugar consumed to fuel these last nine years has been both necessary and damaging. Couldn't have done it without you.

## Abstract

The spikes and pulses observed in biological neurons have similar characteristics to the excitable pulses seen in optically injected lasers. This thesis investigates the feasibility of optically injected dual state quantum dot lasers as artificial photonic neurons. Photonic waveguides are not as sensitive to centimetre long transmission lines as electronic circuits. This could be particularly advantageous for neural networks where one element, a neuron, must receive signals from many different other neurons. Having many lasers on a chip will inevitably lead to long spacings between neurons. With integrated photonic circuits, shorter pulses can be sent between distant neurons without having to worry about adverse RC dynamics. Therefore photonics offers a solution to the fan in and fan out bottleneck hindering the development of efficient hardware that can support an artificial neural network.

Quantum dot lasers are some of the most stable semiconductor lasers in optical injection configurations due to their highly damped relaxation oscillations. This stability introduces a bistability between two phase locked states. However, we show that this bistability is broken by an optothermal effect and is replaced by a deterministic cycle between the remnants of the two states. Excitable trajectories around this cycle can be triggered by noise and deterministically through phase perturbations.

Quantum dot lasers can lase from multiple energy states. The lower energy state, the ground state (GS), is achieved through low pump currents and the excited state (ES) is reached through higher pump currents. This dual state or two colour laser produces many unique dynamics, particularly when biased to emit from the ES and then optically injected near the GS, so as to turn off the ES and turn on the GS. A locking map is recorded for different injection strengths and injection frequencies. A hysteresis cycle is found along with optothermally induced square waves trains on the negatively detuned boundary. On the positively detuned boundary a second optothermal effect caused by the heating of the laser facet introduces a different square wave train, with a period of a tens of milliseconds.

Excitable GS dropouts with accompanying ES pulses are also observed close to the negative unlocking boundary. These events are shown to be noise induced or can be deterministically triggered. The events can display a true all or none

response, analogous to a leaky integrate and fire neuron. The dual state nature of the quantum dot laser introduces two excitable thresholds, one for each direction of phase perturbation around the phasor diagram. The thresholds, delay times and refractory periods of these pulses are investigated for each perturbation direction. An excitable interval is uncovered and an integrate and inhibit mechanism is observed. Not only this but an integrate and fire mechanism is also found. A prototypical photonic neuron is realised and is used in a rudimental image edge detection technique.

# Chapter 1

## Introduction

### 1.1 Photonic computing

#### 1.1.1 Photonic computing and non-linear dynamics

Photonics has been central to telecommunication over the last few decades but electronics has dominated computation. All-optical devices with ultra fast response times are necessary for the realisation of optical networks with transmission capacity exceeding a Tb/s. Applications in sensing and increased complexity of scientific and mathematical problems require faster processing speeds to warrant all optical processors, with their attractive bandwidth and noise performance [1]. Thanks to the recent advances in Photonic Integrated Circuits (PICs), researchers now have a toolbox with many functionalities to help create a compact computation unit. Understanding the non-linear dynamics of an optical element is vital if one is to integrate it with other elements. In fact there have been many instances where the observation of non-linear dynamics has been the inspiration for photonic computation elements, such as bistable dynamics which have been utilised to create all optical switches and flip flops [2]. More recently a form of non-linear dynamics known as excitability has gained attention because of the similarities between excitable pulses and the activation functions used in neural networks for artificial intelligence [3]. For neural networks to work as an effective computation tool they require hardware that can support many long interconnections between neurons. This requirement is where photonic circuits can excel over their electronic counterparts. PICs can send short pulses through centimetre long waveguides on chip with minimal distortion to the

signal, however, high speed electronics can be hampered by the inductance and skin effect of such long transmission lines [4]. Therefore optical computing is necessary for both logic based and neuromorphic computing.

### 1.1.2 Computing architectures

Von Neumann is currently the most common architecture and is used in logic based central processing units (CPUs) in all computers and smartphones. It works sequentially, where one process is done after another and memory is stored and called from elsewhere. However, a neural network is structured as the name suggests, where there is a broad network of many neurons connected to each other. Neurons operate in parallel and the interconnections combine memory elements with processing elements [3]. Each architecture has its own strengths: von Neumann is useful in performing calculations, whereas neural networks are better for tasks that can easily be performed by the human brain such as image processing and voice recognition. The key benefit of neural networks over von Neumann is that machine learning algorithms can be applied more efficiently, taking advantage of the parallelism. Machine learning has become increasingly popular over the last decade and it moves away from the von Neumann architecture where rules are programmed by the user [5]. For a more detailed review on photonic neuromorphic computing methods see [4]. The type of photonic neuron investigated in this thesis is a spiking leaky integrate and fire neuron, analogous to the neurons observed in the human brain.

#### 1.1.2.1 Biological inspiration

Neurons and neural networks were first discovered in nature. One of the earliest studies involved an Atlantic squid [6] and later researchers were drawn to the human brain. The brain is a complex system and to this day many mysteries still remain unanswered. On a basic level the brain is understood to be a vast network of approximately 86 billion neurons connected to each other. Each neuron is made up of three parts: dendrites, the axon, and the soma. A dendrite is the input channel of the neuron, where it receives information from other neurons. The signals from all dendrites are joined at the soma, the body of the neuron. The output channel of a neuron is called the axon. Synapses are the connections between the axon of one neuron and the dendrite of another. The axon hillock is located at the end of the

soma, before the axon. It sums together all the input signals and if they exceed an intrinsic threshold an electrical spike travels down an axon. Typically a neuron will have many inputs but only one output. Every output spike has the same amplitude and interestingly information can be encoded in the timing of a spike [7]. Such temporal coding schemes can be forgiving if the interconnects between neurons are lossy. Every neuron generates its own pulse rather than simply amplifying the input. This limits the effect of noise in a long a chain of neurons.

### 1.1.2.2 Artificial neuron

Realising the processing power and efficiency of the brain, the logical next step is to create an artificial neural network based on the architecture of the brain. At the moment neural networks are often simulated using conventional CPUs but this is not an energy efficient approach and the method is severely limited by the CPUs sequential processing. For neural networks to be truly successful the hardware must exist to support them. There are functional electronic neural networks [8–11], but as mentioned above, photonic neural networks [12–14] have their advantages. Figure 1.1 shows a basic example of how the leaky integrate and fire neuron in the brain is structured and will be the basis for our artificial neuron. There are several inputs and a weight is applied to each of them. The weights applied could be positive or negative (excitatory or inhibitory). There is an integrator that sums the weighted inputs. The effect of the input diminishes over time, hence it is a leaky integrator. When the stimulus is sufficient a nonlinear response such as a pulse (also called a spike or activation function) will be triggered which is broadcast to other neurons through synapses.

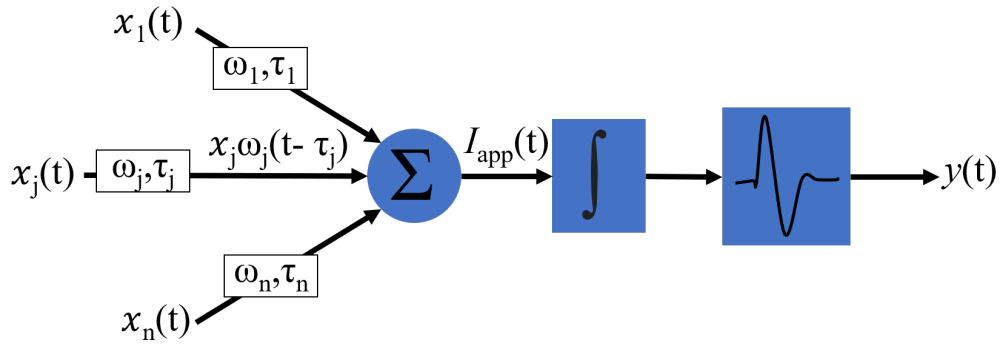


Figure 1.1: Schematic of typical leaky integrate and fire neuron found in the brain.  $x_j$  are the input signals, each spike has a weight  $\omega_j$  and a delay  $\tau_j$ . The signals are joined at the soma and then the signal  $I_{app}$  is sent to the axon hillock. If the inputs exceed a threshold the activation function is fired. There is some rest time before the neuron can fire again.

### 1.1.3 Excitability

The nonlinear activation functions observed in biological neurons are similar to excitable pulses observed in laser systems. Excitability is observed in many nonlinear dynamical systems and refers to the generation of large orbits in phase space following perturbations that exceed an intrinsic threshold [6, 15]. The threshold is the minimum perturbation amplitude required to trigger a pulse. Beginning with a dynamical system in a steady state, if the perturbation is sufficiently large and exceeds the threshold it will result in a nonlinear response, such as a long trajectory in phase space which usually has a corresponding intensity pulse. If the amplitude is below the threshold, the system relaxes adiabatically back to the steady state. A neuron that displays this relaxing behaviour in response to a subthreshold perturbation is called a leaky integrate and fire (LIF) neuron [16]. If two or more perturbations arrive closely in time they can be integrated together and exceed the threshold. If the second perturbation arrives too late, the system will have returned to a steady state and will have no memory of the initial perturbation.

The firing rate of the excitable pulses depends on the refractory periods [17]. The absolute refractory period is the time after a pulse is fired where it is impossible to trigger a second. The relative refractory period is the period of time where a second pulse can be triggered, but its amplitude is inhibited. After the relative refractory period has passed the second pulse resembles the first pulse.

As mentioned above, photonic neurons have real potential to be the core building block in creating a powerful neural network. In recent years, laser systems have proved to be rich sources of excitable phenomena [18–37]. Indeed, the emergence of neuromorphic photonic systems for novel information processing tasks has seen an increased interest in studies of excitability in coupled laser systems. In this thesis we discuss QD (Quantum Dot) lasers and how their unique characteristic and non-linear dynamics make them the ideal candidates for photonic neurons.

## 1.2 Fundamentals of lasers

### 1.2.1 Band structure

Atoms in a solid state crystal act differently to a single unbound atom. Electrons in individual atoms have discrete allowed energy states, but in a crystal the number of different energy levels depends on the number of atomic bonds. The energy levels are close to each other and act more like energy bands. The valence band is the group of energy levels that are filled with electrons (carriers) at 0 Kelvin, while for the same temperature the conduction band is at a higher energy and is empty. For higher temperatures carriers can have sufficient energy to move to the conduction band, vacating a hole in the valence band. The difference in energy between these two bands is known as the band gap energy ( $E_g$ ) [38]. Carriers can be electrically pumped from the valence band to the conduction band.

### 1.2.2 Recombination

In semiconductors when a carrier falls from the conduction band to the valence band it loses energy, and the electron is said to have recombined with a hole. The two main types of recombination are radiative, where electromagnetic radiation is emitted in the form of a photon and non-radiative, where the energy is transferred through phonons - discretised lattice vibrations. For an efficient laser, radiative recombinations are more desirable. These are more likely to occur if the conduction band and the valence band have a direct bandgap, where the lowest part of the conduction band and the highest part of the valence band occur at the same value of momentum space. When an electron drops down from the conduction band a photon is emitted. This photon has a small amount momentum and the carrier

loses some during the transition. The energy of the photon will be equal to the bandgap energy,  $E_g = hf$ , where  $h$  is Planck's constant and  $f$  is the frequency of the emitted photon. If the extrema of the bands don't occur at the same point in momentum space then there is an indirect band gap. Radiative recombination can still occur, but requires a large change in momentum through phonons before a photon can then be emitted. The probability of this occurring is low and thus indirect bandgap materials make inefficient lasers.

There are two ways in which a carrier can recombine radiatively. Spontaneous emission is where a carrier spontaneously drops from the conduction band to the valence band emitting a photon with a random phase and direction. Stimulated emission is where a photon perturbs a carrier in the conduction band, the carrier falls to the valence band and combines with a hole, emitting a photon with the same phase and direction as the incident photon. As the resulting photons are in phase they constructively interfere and provide the amplification necessary for a laser to overcome the losses and surpass the lasing threshold. Sometimes however, carriers in the valence band can absorb a photon and move to the conduction band.

### 1.2.3 Quantum dot lasers

#### 1.2.3.1 Fabrication

Quantum confinement of carriers in semiconductor material is responsible for many of the technological advances in modern technology, being central to the vast majority of semiconductor lasers in use worldwide. Quantum Well (QW) based devices are dominant but there are many reasons to believe that going beyond the one dimensional confinement could lead to technological advantages. Quantum dot semiconductor material offers the ultimate possible quantum confinement, with dimensions on the order of the de Broglie wavelength in all three spatial dimensions [39]. This means they have a delta like density of states, moving away from energy bands and closer to the discrete energy levels in atoms. When free-running, they offer advantages over conventional devices, with low pump threshold values [40–42] and excellent temperature insensitivity [43, 44].

Quantum dot lasers are often grown via the Stranski–Krastanov method [45]. When InAs is grown on a GaAs substrate a thin layer called the wetting layer first deposited across the entire substrate. By adding more InAs, small amounts

of InAs cluster into pyramidal shapes due to the strain from the lattice mismatch. These clusters are quantum dots. A layer of GaAs is grown on top and the dots are embedded. This layer of GaAs acts like another wetting layer, typically multiple layers of quantum dots are grown so as there is enough gain to overcome the losses and device can lase. When carriers are electrically pumped into the laser they first flow into the wetting layer. From there they fall into the first excited state (ES) then into the ground state (GS) at a rate of  $B^w$  and  $B$  respectively, see Figure 1.2. Out scattering is also possible where carriers can escape out of the GS into the ES or scatter out of the ES into the wetting layer at rates of  $C$  and  $C^w$  [46]. Scattering directly between the wetting layer and GS has also been predicted in some models. A limitation of the Stranski–Krastanov method is that there is little control over the size of the dots. The energy gap and therefore the frequency of light emitted depends strongly on the size of the dot, therefore each dot contributes to the broadening of the laser linewidth, this is known as inhomogeneous broadening.

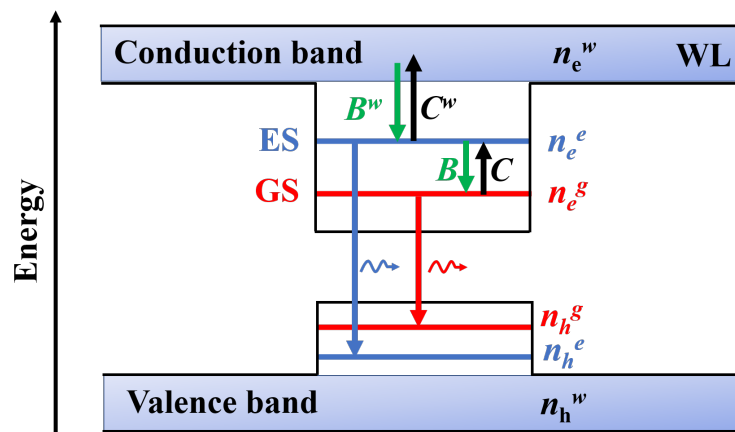


Figure 1.2: Schematic showing some of the different ways carriers can scatter between a quantum dot and the wetting layer.  $B^w$  is the rate at which carriers fall from the wetting layer into the ES. The carriers can then fall to the GS at a rate of  $B$ . The carriers that scatter out of the GS and into ES do so at a rate of  $C$  and the rate of scattering from the ES to the wetting layer is  $C^w$ . The occupation probabilities of the GS ( $n^g$ ) and ES ( $n^e$ ) and the carrier density in the wetting layer ( $n^w$ ). The subscripts indicate if the densities relate to electrons  $e$  or holes  $h$  [46]. Carriers can radiatively recombine from either the GS or the ES.

### 1.2.3.2 Dual state emission

Quantum well based lasers always emit at the frequency of the lowest energy transition (typically called the ground state - GS). This is not the case with InAs QD based lasers. For low pump currents the GS threshold can be reached

and the laser emits at 1300 nm. But an increase in current leads to the saturation of the GS and lasing can be obtained from higher energy transitions - the so-called excited states (ESs) [47]. In particular, lasing from the first ES is regularly obtained (1220 nm). By continuously increasing the electrical pumping beyond the GS threshold a second threshold is reached where ES emission arises and simultaneous GS and ES lasing is obtained. A further increase in pump current, quenches GS emission and the laser emits from the ES only [48–54].

### 1.2.3.3 Phase Amplitude coupling

The linewidth enhancement factor or the  $\alpha$  factor is a measure of the coupling between the amplitude of the electric field and its phase inside the laser cavity [55]. The phase of the electric field depends on the refractive index of the laser cavity. Refractive index in turn depends on the temperature and the carrier density of the semiconductor. Below threshold, the phase of light is strongly coupled to the carriers. Above threshold the gain is clamped and the majority of carriers are involved in radiative recombinations so the carrier density is almost fixed even if pump current is increased. But as mentioned, QD lasers can have multiple energy levels and the carrier density of each level will be coupled to the phase of the light, so  $\alpha$  alone is not sufficient. A microscopic model can be used to incorporate  $\alpha$  dynamically. Other methods introduce a second coupling term  $\beta$  that describes the coupling between the phase of the electric field the GS to the carriers of the ES [46]. This term also helps to compensate for inhomogeneous broadening caused by different dot sizes.

### 1.2.3.4 Relaxation oscillations

In laser models, very often light is treated classically via Maxwell's equations, while the carriers are treated semi-classically or even fully quantum mechanically. The polarisation induced in the medium by the electric field is expanded in the cavity eigenmodes. The amplitudes of each polarisation mode is calculated via the Bloch equations for a two state quantum system interacting with the corresponding single eigenmode of the electric field. The polarisation lifetime is the inverse of the decay rate arising in the Bloch equations. Lasers can be divided into several categories depending on the ratios of the carrier, photon and polarisation lifetimes [56]. If the photon and polarisation lifetimes are similar then the laser is known as a Class C laser. If

the polarisation lifetime is much shorter than the other timescales, then one has a Class B laser.

Most semiconductor lasers are Class B lasers (although recent research has shown that some semiconductor nanolasers may in fact be Class C). For Class B lasers, the typical response of the device to perturbations takes the form of damped, harmonic oscillations in the intensity and carriers. These oscillations are known as the relaxation oscillations (ROs) of the laser and they typically have a frequency of the order of a few GHz. Conventional semiconductor lasers display weakly damped ROs, and so there are many oscillations following a perturbation. Because of this weak damping, the ROs are also easy to excite and become self-sustained and this is a source of many instabilities when lasers are subject to feedback or coupling to other lasers.

The ROs of quantum dot lasers however are strongly damped. In fact, they appear to be close to critical damping. This increased damping means that they are more stable than conventional semiconductor lasers when undergoing feedback or when coupled to other lasers. Finally, lasers where the photon lifetime is much longer than the other timescales are known as Class A lasers, and they can be modelled using equations for the electric field only. In this case, there are no ROs at all and so these lasers are extremely stable when undergoing feedback or coupling to other devices. Gas and dye lasers are typically Class A. The high damping of quantum dot lasers mean that they operate in a somewhat middle ground and they display many phenomena that are more associated with Class A lasers than with conventional semiconductor lasers.

## 1.3 Optical injection

The idea of synchronisation dates back to 1665 when Christiaan Huygens noticed that if two pendulum clocks were attached to the same wooden board, they would eventually become frequency locked, where the frequency at which the pendulums oscillate would become the same, if their initial frequencies were similar [57]. This is an example of bidirectional coupling, where both oscillators influence each other. Unidirectional coupling will be the type of coupling described throughout this thesis. It is where one oscillator, referred to as the master or primary oscillator, influences the other, known as the slave or secondary. In this case the secondary has no influence on the primary.

An electric field inside the cavity of a laser can also be considered as an oscillator. Similar to the pendulum clocks, if light from a primary laser is injected into the cavity of the secondary laser it could influence the electric field. Under the right conditions the secondary laser could be forced to adopt the frequency of the primary and the phase difference between the two oscillators would remain fixed. This is known as phase locking or injection locking. The concept of synchronisation and phase locking was expanded by Van der Pol [58] and Adler [59], the Adler equation being used to describe the prototypical optical injection setup:

$$\frac{d\phi(t)}{dt} = -\Delta + K \sin(\phi(t)), \quad (1.1)$$

where  $\phi$  is the phase difference between the primary and secondary laser. This equation describes how the phase of the secondary laser is evolving in time with respect to the primary's.  $\Delta$  is the detuning, the frequency of the primary minus that of the secondary.  $K$  is the coupling strength (the ratio of the electric field amplitude of the injected light to that of the output light per unit time) and corresponds to how strongly the secondary laser's phase will be influenced by the primary laser. The Adler model is applicable when the injection strength (the ratio of the intensity of the primary laser, which enters the secondary laser's cavity to the intensity in the secondary laser's cavity in the injection-free case) is less than 0.01 [60], but can be adapted for higher injection strengths [61]. When phase locked, the phase difference between the primary and secondary lasers is constant, simply leading to  $\frac{d\phi(t)}{dt} = 0$ . Thus, for  $|\frac{\Delta}{K}| < 1$  phase locking can be achieved. These two parameters can be easily varied with a tunable laser source (TLS), a common piece of equipment in any modern photonics lab.

If the detuning between the primary and secondary lasers is very large, the two electric fields will not interact coherently and a simple beating tone will be observed, where the frequency is equal to the detuning. Phase locked CW (Continuous Wave) emission and beating are two very different qualitative behaviours. By varying either the detuning or injection strength, one can move from one of these behaviours to another by passing through a bifurcation point, the point at which these behaviours change qualitatively. There are different types of bifurcations that describe how different transitions are

undertaken. A saddle-node infinite period (SNIPER) bifurcation and a Hopf bifurcation are the two main types which will be mentioned throughout this thesis [62, 63].

## 1.4 Excitability in optically injected lasers

Excitability is usually found close to certain bifurcation points, more specifically, where there is a transition from a steady state (phase locked) to a limit-cycle resembling a train of excitable pulses. Depending on the underlying bifurcation structure, see Figure 1.3, and the resulting statistical properties of the pulse train, one generally speaks of Type I excitability or of Type II

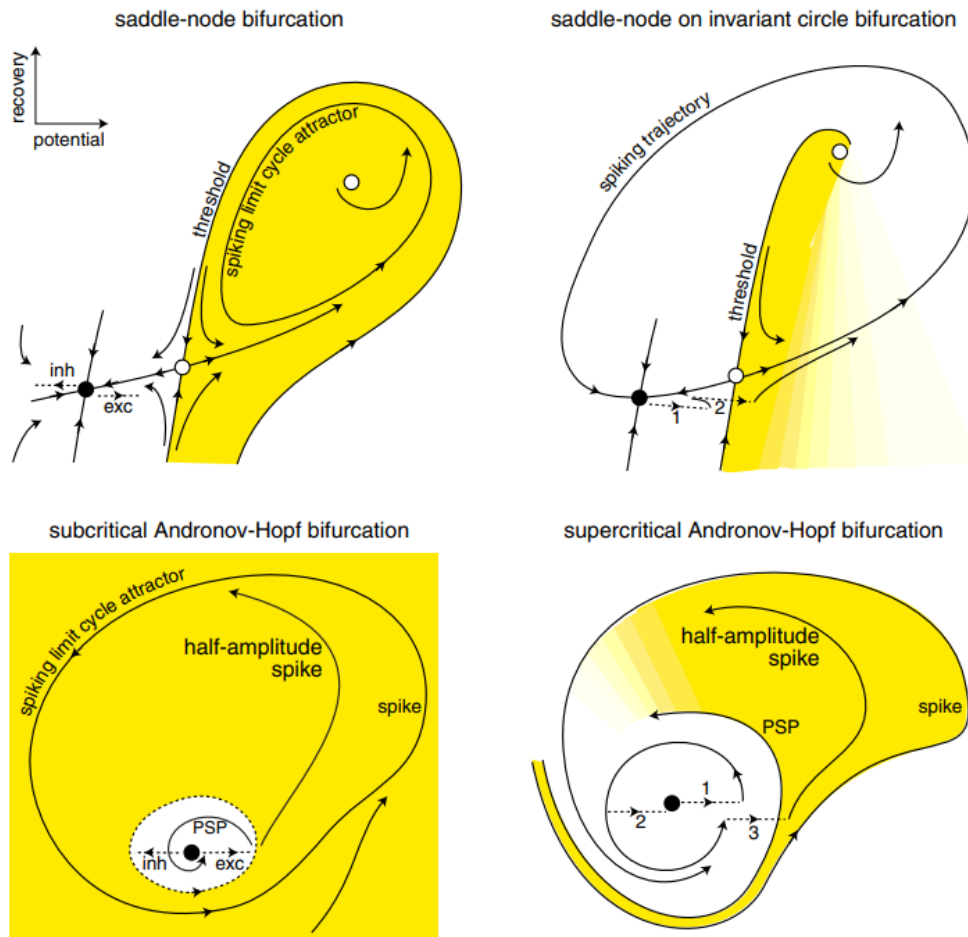


Figure 1.3: Common bifurcations observed in laser systems. Black dots represent stable points and white dots represent unstable points. The top panel shows Type I excitability and the bottom shows Type II. The dashed lines represent perturbations and the solid lines are excitable trajectories and the arrows show the direction of rotation [64].

excitability [64]. Type I excitability is usually associated with a saddle-node infinite period bifurcation (also known as a saddle-node on an invariant cycle (SNIC) bifurcation). As the name suggests there are two fixed points - a stable node and an unstable saddle - created on an infinite period cycle. While phase locked the system will remain in steady state until an external perturbation kicks the system past the unstable point. The only route back to the stable point is via a large trajectory in phase space. When a parameter is changed and the bifurcation point is passed the secondary laser becomes unlocked. The saddle and the node annihilate each other and a limit cycle is born [17].

Type II excitability is usually observed in the vicinity of either a supercritical or subcritical Hopf bifurcation [17]. In the subcritical case, close to the bifurcation point the system is bistable; there is a stable point and a stable limit cycle. There is an unstable boundary (also called a separatrix) separating the two stable behaviours. The separatrix acts similarly to the saddle and if the system can be perturbed from the stable point beyond the separatrix it will jump onto the limit cycle, resulting in pulsing behaviour. A constant pulsing regime can be observed if the system does not return to the stable point. In the case of a supercritical Hopf when a parameter change brings the system past the bifurcation point the stable point is replaced by a stable limit cycle. The amplitude of the cycle increases the further the system is from the bifurcation point. A Canard Explosion is a unique form of supercritical Hopf bifurcation, where a large increase in amplitude occurs after a small change in a parameter value after passing the bifurcation point.

## 1.5 Brief history of optically injected QD lasers

In optical injection experiments, QD lasers are significantly more stable than conventional semiconductor lasers, allowing for phase locked operation over a much larger area of control parameters and with a marked reduction in areas displaying chaotic operation [19, 65–69]. The RO stability means that they are also extremely stable when mutually coupled, even for long delays between devices [70]. There have been many experiments and simulations investigating the behaviour of various lasers systems involving QD lasers but here will focus on optically injected single mode [19, 69, 71] and multi-mode QD lasers [72] biased to emit from the GS only. To make the discussion throughout this thesis simpler we will distinguish between high and low injection strengths. High injection strengths will describe scenarios where the

intensity of light reaching the facet of the secondary laser is greater than or equal to 0.5 times the light emitted from the facet of the secondary laser. Low injection strength is anything less than this, unless otherwise stated.

### 1.5.1 Single mode

Beginning at a very arbitrary point, where injection strength is less than 0.01, and where the detuning is large enough so that the primary and secondary lasers simply produce a beating tone resembling a sine wave. By decreasing the absolute detuning, at either the positive or negative detuning boundary, the sine wave becomes distorted until it resembles a periodic train of pulses [19, 69]. By continuing to decrease the absolute detuning, the period of the train becomes larger and larger. Figure 1.4 shows a stability diagram from [71] and indeed a SNIC bifurcation is predicted at both locking boundaries. A further decrease in absolute detuning leads to random pulses, where an exponential distribution of the interpulse times concludes that these are noise induced excitable pulses [19]. Because the excitable pulses are in the vicinity of a SNIC bifurcation they are classified as Type I. At the negative unlocking boundary the intensity of the pulse initially decreases and then shoots up above the steady state value before returning to the steady state intensity. An experimental reconstruction of the phase of the secondary laser with respect to the primary shows that each optical pulse is accompanied by a  $2\pi$  phase rotation in phase space [19]. Single pulse Type I excitability is also observed at the positive detuning boundary, but of a different shape. The intensity first increases and then quickly goes below the steady state value, there is a ringing oscillation before the system returns to the steady state. These pulses are accompanied by Adler like  $-2\pi$  phase slips.

For injection strengths greater than 0.01 at the positive detuning boundary the SNIC is replaced by a Hopf [71]. An increase in optical injection strength to approximately 0.02 on the negatively detuned boundary leads to a region where there is switching between a stable state and a period one limit cycle of higher average power. By continuing to increase injection strength a switching regime between a stable state and period two limit cycle is observed and an even further increase brings about switching from a stable solution to a chaotic regime.

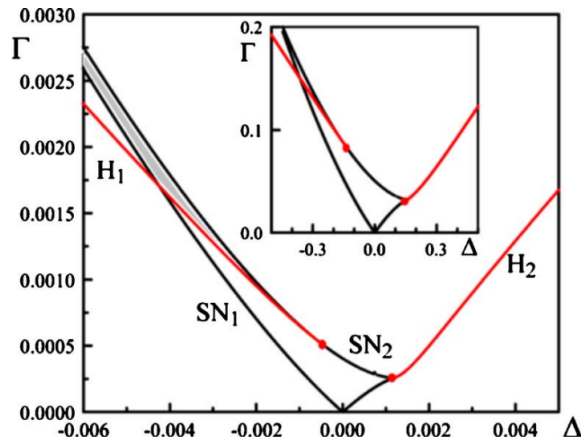


Figure 1.4: Analytic stability diagram for an optically injected QD laser using QD rate equations.  $\Gamma$  is the normalised injection strength and  $\Delta$  is detuning. The saddle-node and Hopf bifurcation points are denoted by SN and H, respectively. The shaded region corresponds to region of steady-state bistability. The dots indicate where where Hopf and SN bifurcation lines merge to create are fold-Hopf points. The inset shows a stability diagram for an injected Class A laser [71].

### 1.5.2 Multi-mode

The first experimental observation of excitability in any optically injected laser involved a multi-mode quantum dot laser [72]. Similar to the single mode case three behaviours are identified near the negatively detuned boundary when detuning is varied: beating, pulsing dynamics and phase locking. The positively detuned boundary was reported to have the characteristics of a Hopf bifurcation and no pulsing was observed. The negatively detuned boundary is then categorised into four regions depending on injection strength. For the lowest injection strength discussed, evidence of a SNIC bifurcation is reported and excitable single pulses similar to those in [19] are observed. Trains of double pulses are found for higher injection strengths. With an increase in injection strength, the QD laser switches between a limit cycle and a steady state, again resembling the single mode case. At even higher injection strengths the authors describe the final observed dynamic as a random switching between two locked states.

## 1.6 Outline of the Thesis

This thesis is organised as follows. Chapter 2 investigates the dynamics observed when a single mode QD laser emitting from the GS only is optically

injected with high injection strengths. Instead of a predicted bistability [71], different pulsing regimes observed are presented for a range of detuning values. Statistical analysis is performed on the inter-pulse times to verify that the pulses are of an excitable nature. An optothermal effect is included in a Class A and QD model to account for the breaking of the bistability and a bifurcation analysis is performed on the updated rate equations. This optothermal effect is then experimentally verified and the pulses are deterministically triggered. Chapter 3 is a review chapter, where we look at the recent experimental and theoretical research carried out on optically injected dual state quantum dot lasers. More specifically when the QD lasers are biased to emit from the ES only and are then injected near the GS. Chapter 4 expands on the work reviewed in Chapter 3, experimental and theoretical locking maps are shown and much of the dynamics are recovered. A second optothermal effect is presented to account for slow oscillations observed near the positive detuning boundary. Chapter 5 looks at a specific region of the locking map, where noise induced excitable GS dropouts are accompanied by ES pulses. Bifurcation analysis and experimental phase diagrams shed light on the phenomenon. These pulses are deterministically triggering with clockwise and anticlockwise phase perturbations in Chapter 6. The presence of different thresholds for each direction is investigated through experimental efficiency curves and phasor plots, and theoretical modelling. Chapter 7 then investigates the neuromorphic capabilities of these pulses. The refractory periods are found for small and large phase perturbations in both directions. Inhibitory perturbations are investigated along with an integrate and fire mechanism which is then applied in a basic image edge detection technique. Finally, Chapter 8 concludes this thesis. The work put forward is summarised and future potential work is discussed.

## Chapter 2

# Square wave excitability

While high injection strengths have been investigated for multimode QD lasers experimentally, as discussed in Section 1.5, there has not been such an investigation using single mode QD lasers. A great deal of agreement has been seen between experiment and theory thus far [69, 71, 72]. The single mode QD laser model predict a bistability [71] at high injection strengths, similar to the one observed in [72]. The presence of a bistability is experimentally investigated along with the mechanism driving a switching behaviour between the two stable states, which up until now is believed to be random [72]. Simulations from the simple Class A model are shown with and without an optothermal effect included. We then move onto the QD model and apply a similar coupling term. Bifurcation analysis reveals that depending on the ratio of the photon lifetime to the carrier lifetime, a supercritical or a subcritical Hopf bifurcation can replace the bistability.

I was responsible for the entirety of the experimental work and partially responsible for the modelling results. This chapter is based on the following publications:

M Dillane, B Tykalewicz, D Goulding, B Garbin, S Barland and B Kelleher, “Square wave excitability in quantum dot lasers under optical injection”, *Optics letters* **44** (2), 347-350 (2019).

M Dillane, J Robertson, M Peters, A Hurtado and B Kelleher, “Neuromorphic dynamics with optically injected quantum dot lasers”, *The European Physical Journal B* **92** (9), 197 (2019).

## 2.1 Introduction

Excitability has been shown to be a pervasive phenomenon in systems of semiconductor optical devices [18–37]. It has been shown in several previous works that Type I excitability is generic in optically injected edge emitting semiconductor lasers. In particular, it arises with injected Quantum Dot (QD) lasers and because of the high relaxation oscillation damping of these devices it arises in many unique forms. QD lasers behave just like idealised Adler phase oscillators at injection levels where the intensity of light entering the laser cavity is less than 1% of light being emitted from the cavity, if it were free running [60]. As the injection level is increased the details of the excitable dynamics evolves.  $2\pi$  phase rotations are obtained for both positive and negative detuning at injection levels near 1% [19] and these phase slips can be deterministically triggered as shown in [73]. For higher injection levels QD lasers display bursting with groups of pulses rather than isolated pulses emitted [69]. Type II excitability is less well known in the optically injected laser system. It typically manifests in fast-slow systems and the Van der Pol Fitzhugh Nagumo model is the prototypical model used to describe it.

In this chapter we demonstrate a new excitable phenomenon in the injected QD laser. The device was operated to emit from the GS only. For injection strengths where the intensity of the injected light is greater than 0.5 times the free-running SL, we find a regime of periodic square waves. Theoretical models have predicted a bistability in such a region [71] and experimental results involving a multimode QD laser describes observations of random switching between two phase locked states [72].

Square wave outputs have been observed in several different feedback configurations [74–76], but they arise from very different underlying physical phenomena to the squares in our work. In our case we find an optothermal dynamic similar to the dynamics observed with semiconductor etalons [77], QD lasers [78–80], photonic crystal structures [81] and optically injected semiconductor optical amplifiers [37, 82]. Our periodic square wave regime is bounded by regions where individual, square pulses or dropouts are observed. We interpret these individual pulses and dropouts as Type II excitable events akin to those observed in the Van der Pol Fitzhugh Nagumo model [58, 83]. They display fast-slow dynamics with two timescales: the timescale of carriers in the nanosecond range and a thermal timescale in the microsecond range. In each case, a bistability is broken by thermally induced dynamics. In this

chapter we show that the predicted bistability is broken by an optothermal coupling, yielding a deterministic square wave cycle.

## 2.2 Experimental setup

A 600  $\mu\text{m}$  QD laser composed of InAs quantum dots on a GaAs substrate was the device under investigation. It could lase from the ground state (GS) or the first excited state (ES), but for this experiment it was operated to emit from the GS only. Slots had been etched into the waveguide and were carefully spaced so as to promote just one longitudinal mode and suppress all other modes within the gain spectrum. It was pumped at 40 mA, 1.25 times threshold. A schematic of the experimental setup is shown in Figure 2.1. The device was mounted and placed on an xyz stage. Light from the QD laser was coupled into a single mode lensed fiber with a coupling efficiency of approximately 70%. A unidirectional optical injection configuration was set up. The primary laser (PL) was a commercial tunable laser source (TLS) with minimum step size of 0.1 pm (0.0178 GHz). Light from the PL was injected into the secondary laser (SL) via a circulator. A polarisation controller was used to set the polarisation of the injected light. Maximum coupling was achieved when the polarisation of the TLS matched the polarisation supported by the waveguide of the QD laser. For this experiment injection strength ( $K$ ) was defined as the ratio of light emitted from the lensed fiber (from the PL) to the light coupled into the lensed fiber from the free-running SL. The injection strength was kept constant for this experiment. First the power of light emitted from the PL to the lensed fiber was recorded. Then the light emitting from the

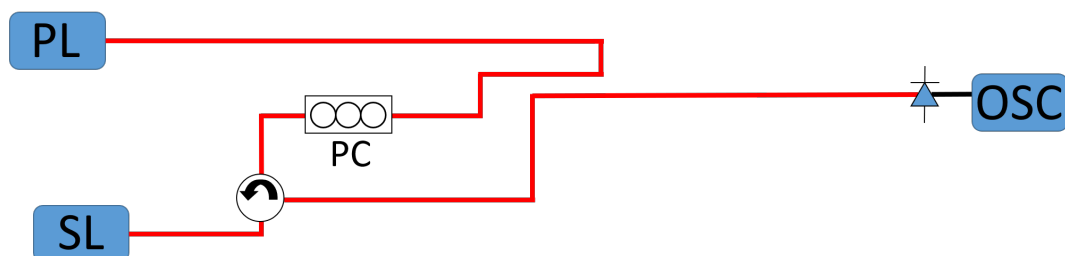


Figure 2.1: Basic setup of an optically injection experiment. A QD laser is acting as the secondary laser (SL). The primary laser (PL) is a tunable laser source. A polarisation controller (PC) is used to maximise coupling. A circulator shines light from the PL into the SL, the light that is emitted from the SL into the circulator is sent to a 12 GHz detector connected to an oscilloscope (OSC).

free running SL was coupled into the lensed fiber and the power was recorded. The injection strength is the ratio of these two values. The output was detected with 12 GHz detectors connected to a real-time digital oscilloscope.

## 2.3 Noise induced excitable square wave trains

### 2.3.1 Square wave onset

For injection strengths where  $K < 0.5$ , the observations were similar to those reported in previous work [19, 60, 65, 69]. For injection strengths where  $K > 0.5$  and for a significant range of negative detuning, a square wave phenomenon was observed.

To describe the dynamics observed in the region,  $K$  will remain fixed and the detuning will be continuously increased (the absolute detuning is decreased). Beginning at a detuning far outside the locking cone where the frequency of the PL was much less than that of the SL, the output of the SL was a limit cycle. The amplitude of the limit cycle decreased as the frequency of the PL was increased until the SL became phase locked to the PL. Here the output became constant (modulo noise). Increasing the PL frequency to a detuning of approximately -6.6 GHz the first square pulses appear. Initially, the occurrence of these square pulses was rare with a large delay between successive pulses. As the detuning was further increased to approximately -6.4 GHz the pulses appeared more frequently as shown in Figure 2.2(a). As the frequency of the PL was brought closer to that of the SL the pulses were replaced by a periodic pulse train, with the lower intensity sections being longer lived than the upper intensity sections. Eventually the train had a 50-50 duty cycle at approximately -4.8 GHz detuning (Figure 2.2(b)). Continuing to increase the PL frequency, rather than a pulse train, the train resembled more a periodic train of square dropouts. (That is, the duration in the upper level became longer than that in the lower level.)

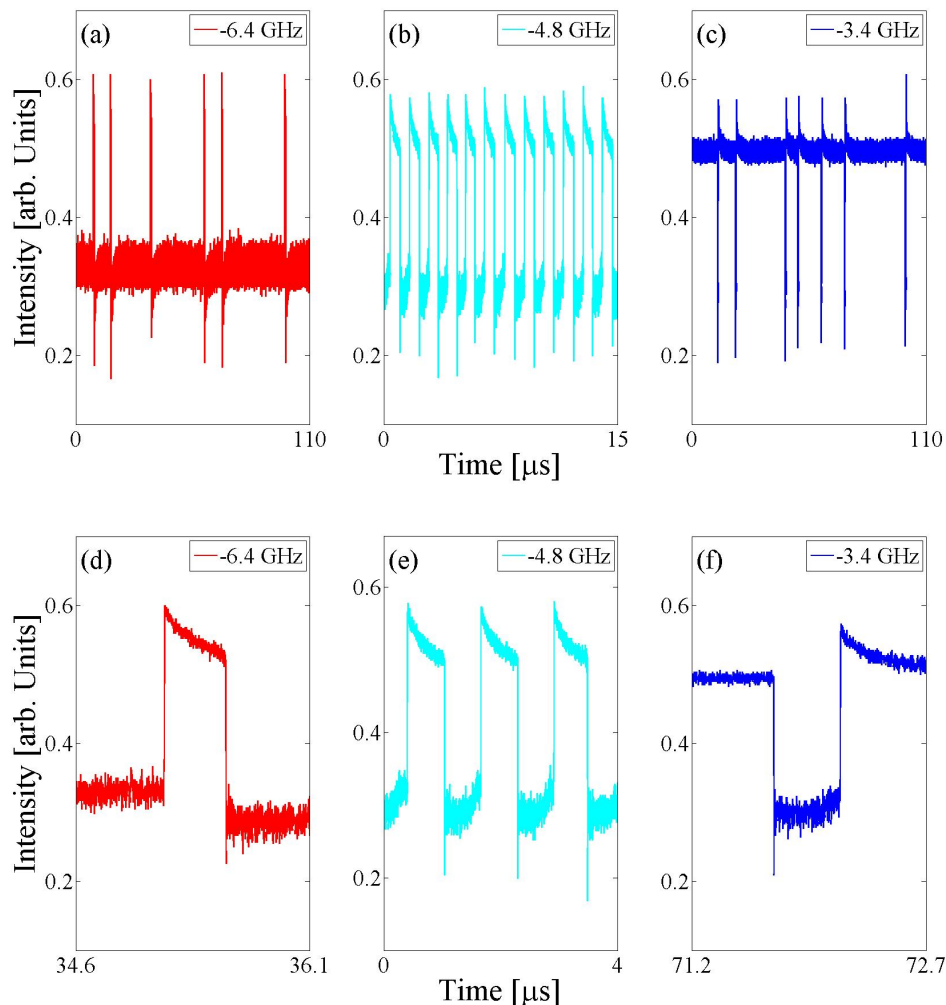


Figure 2.2: Extracts taken from 20 ms timetraces. (a) shows randomly separated pulses at -6.4 GHz detuning. (b) shows periodic squares at -4.8 GHz detuning and (c) shows square dropouts appearing randomly at -3.4 GHz detuning. The bottom row zooms in on a square event from the top row.

### 2.3.2 Statistical Analysis

Bistabilities are common in optically injected lasers, but it is rare to see a bistability between two phase locked states, such bistabilities have been predicted to exist in Class A lasers. In the absence of noise a hysteresis loop would be observed. With sufficient noise the system would be kicked from one state to another and back again. The lifetime in each state should be random. Firstly, looking at an individual pulse or dropout the duration looks very consistent. By looking at the periodic square train with a 50:50 duty cycle it is clear that this is not a random process. To see if the pulses and dropouts are deterministic they are plotted in a heat map shown in Figure 2.3. The

pulses/dropouts are from the 20 ms timetraces as the ones shown in Figure 2.2(a) and (c). The pulse-width was extremely regular, approximately  $0.4 \mu\text{s}$  at  $-6.4 \text{ GHz}$  and  $-3.4 \text{ GHz}$ , meaning there is some deterministic excitable trajectory undertaken for each pulse.

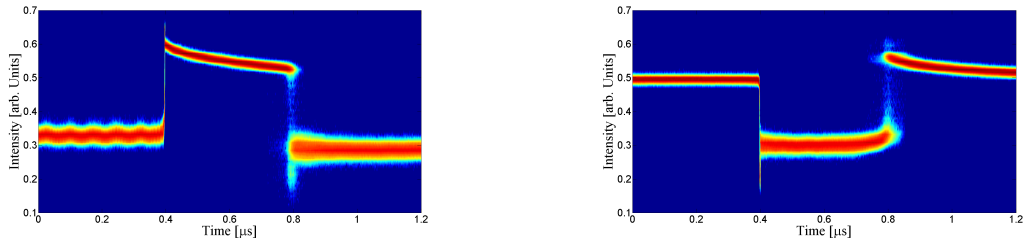


Figure 2.3: Heat map of (a) 2016 pulses and (b) 1818 dropouts plotted on top of each other. The pulses/dropouts are taken from same 20 ms timetraces as the squares shown in Figure 2.2 (a) and (c) at  $-6.4 \text{ GHz}$  and  $-3.4 \text{ GHz}$  detuning, respectively. The pulse widths are extremely regular and approximately  $0.4 \mu\text{s}$  long. A deterministic trajectory appears to be responsible for these square events.

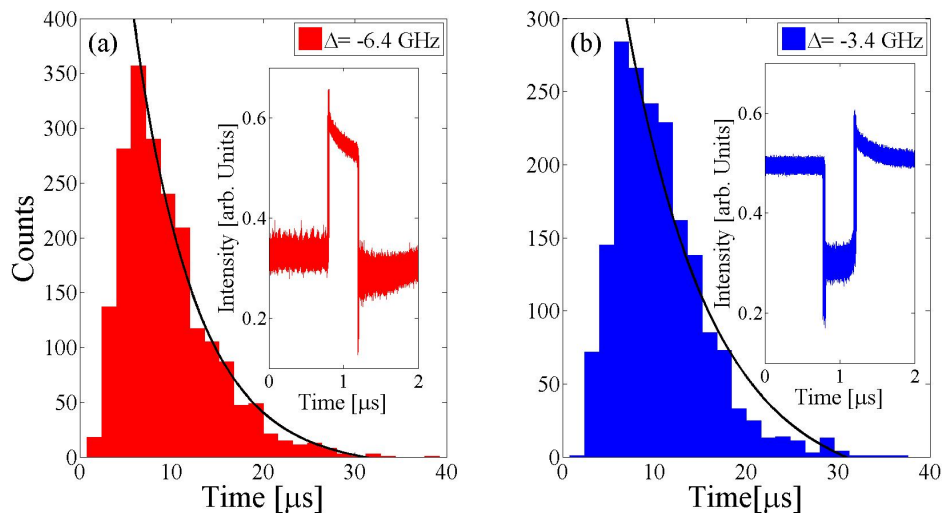


Figure 2.4: Histograms of the interpulse/dropout times taken over 20 ms with detuning values of  $-6.4 \text{ GHz}$  and  $-3.4 \text{ GHz}$ . (a) shows the interpulse time distribution of 2016 pulses shown in Figure 2.2. The exponential shape indicates that these pulses are randomly separated and induced by noise. (b) shows the distribution for 1818 dropouts. Again, the exponential shape is evidence that the dropouts are noise-induced random events. The Kramer's escape times were approximately  $6.9 \mu\text{s}$  and  $6.6 \mu\text{s}$  respectively. The insets are the persistence plots of 100 pulses/dropouts.

The average interpulse time varies as detuning is changed. This is a typical

attribute of noise induced Type I excitability as the excitable threshold can be increased or decreased by altering the detuning. With sufficient noise the threshold can be exceeded and pulses will fire at random times. The interpulse statistics in Figure 2.4 show the interpulse times have a Kramers-like exponentially decaying distribution. This confirms that the pulses and dropouts observed at -6.4 GHz and -3.4 GHz were in fact induced by noise. Exponential curves were fitted to the data and the Kramer's escape times were approximately  $6.9 \mu\text{s}$  and  $6.6 \mu\text{s}$  respectively.

The dynamics resemble those of a Van der Pol/Fitzhugh-Nagumo oscillator and we interpret the pulses and dropouts in the random trains as Type II excitable events. Each escape is noise-induced and is followed by a large deterministic trajectory back to the steady state. The transition between the upper and lower levels of each square is approximately 1 ns and the lifetime in each plateau is on the order of a microsecond. We associate this slow-fast, two timescale phenomenon with an optothermal coupling: the fast time corresponds to carrier dynamics and the slow time with thermal effects.

## 2.4 Periodic square wave trains

In between the regions of excitable pulses and dropouts, periodic square wave trains are found. The duty cycle of these periodic trains changes from having longer lived lower sections, to having a 50:50 duty cycle and then to having longer lived upper sections as the detuning is increased. Figure 2.2(b) shows an example of a 50:50 duty cycle at approximately -4.8 GHz detuning. The histograms in Figure 2.5 show the lifetime in the higher and lower intensity sections to be approximately  $0.6 \mu\text{s}$ . The narrow distribution extends over  $0.25 \mu\text{s}$ , this is in sharp contrast to interpulse time distribution for the noise induced square pulses in Figure 2.4, where the range can extend out as far as  $40 \mu\text{s}$ . Figure 2.6 shows a heatmap where all the upper intensity sections were plotted on top of each other, with the middle of each square being the reference point. Again the regular shape shows that there is a deterministic trajectory and furthermore the periodicity shows there is a deterministic limit cycle and noise is not randomly forcing the system to switch randomly between two states. In the periodic case there is no threshold that is exceeded by noise, it is simply a limit cycle.

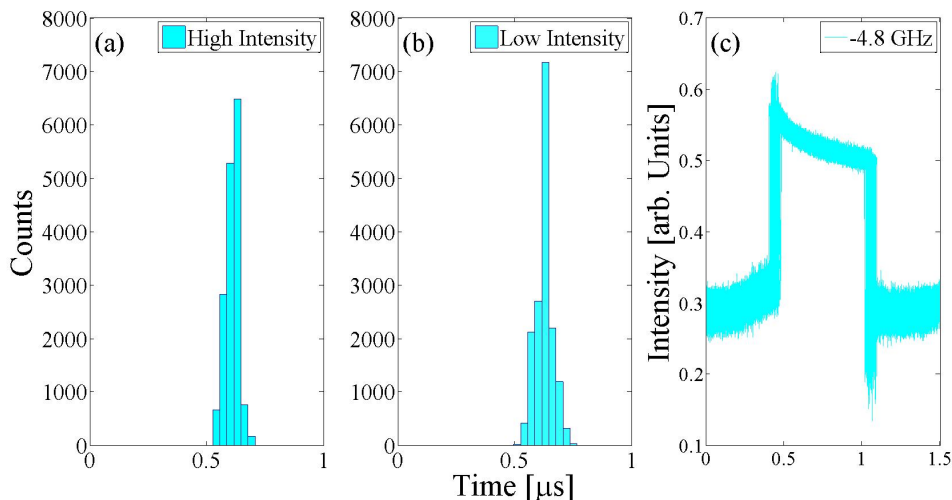


Figure 2.5: Histograms showing (a) the distribution of upper intensity state lifetimes, (b) the distribution of lower intensity state lifetimes and (c) a persistence plot of 100 pulses. The histograms correspond to the time traces in Figure 2.2 (b) at detuning of -4.8 GHz. The narrow distribution shown in (a) and (b) emphasises a deterministic cycle is in fact being undertaken.

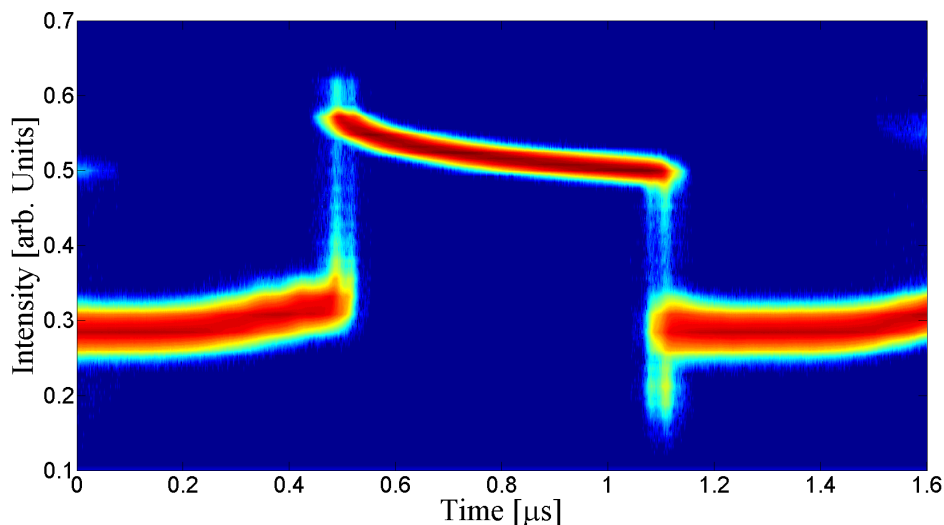


Figure 2.6: Heat map of periodic square wave train at detuning of -4.8 GHz, corresponding to the extracts taken from 20 ms timetraces shown in Figure 2.2 (b). The pulse widths are approximately  $0.6 \mu\text{s}$  long, with a tight distribution. This is a limit cycle and are not noise induced square pulses.

## 2.5 Optothermal measurement

As mentioned above, in [69, 71] a phase locked bistability was predicted theoretically for the system at high injection strengths in the region where the

square waves are found. We interpret the squares as arising from a breaking of this bistability due to the optothermal coupling. The top and bottom of each square then correspond physically to the two phase-locked solutions. Each intensity state has its own carrier density and the number of non radiative recombinations increases with an increase in carrier density. Thus there will be a change in temperature in the device depending on what phase locked state the system is in. A change in temperature leads to a change in refractive index which in turn changes natural frequency the SL would lase at if free running, thus the effective detuning is altered.

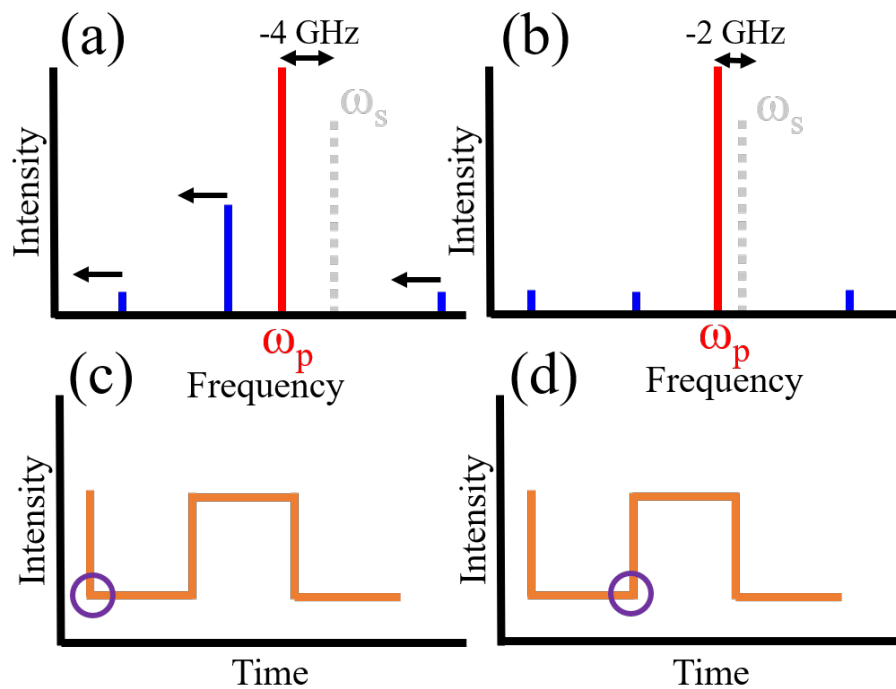


Figure 2.7: Cartoon describing the optothermal effect. (a) and (b) show the optical spectrum of the QD laser. The blue lines represent the subthreshold modes. The red line represents the lasing frequency of the QD laser, which remains fixed as the QD laser is phase locked to the constant TLS  $\omega_p$ . The grey dashed line,  $\omega_s$ , is the longitudinal mode that would lase in this single mode laser, in the absence of optical injection. Detuning is defined as  $\omega_p - \omega_s$ . The bottom panels show timestraces of the square wave train. The circles indicate what part of the cycle the top panel is describing. As shown in (c) the system has just began emitting from the lower intensity section. This increases the temperature, decreasing the frequency of the longitudinal modes and  $\omega_s$ , as indicated by the arrows. Over the duration of the lower intensity section the detuning has increased from -4 GHz to -2 GHz.

It is difficult to observe the optothermal effect because one cannot measure the

frequency of the light that would be supported by the device if it were free running because the SL is always phase locked and frequency locked to the PL. However, to measure the thermally induced change of detuning, the sub-threshold longitudinal modes can be investigated. In the cartoon shown in Figure 2.7(a) and (b) the PL frequency remains constant, so it is a natural reference point when discussing the evolution of the SL and the optothermal effect. At the beginning of the lower intensity section, Figure 2.7 (c), the frequency of the SL is much larger than that of the PL and the detuning is -4 GHz. But during the lower intensity section there is a higher carrier density and the device's temperature increases, decreasing the what would be the free running frequency of the SL and thus changing the detuning. This process continues to heat up the device until the only remaining solution is that of the higher intensity resulting in a fast state switch.

Conversely, Figure 2.8 shows the evolution of the detuning during the upper intensity section of the square. The device cools and the frequency of the SL increases, resulting in a detuning sweep from -2 GHz to -4 GHz, where the only stable solution for this detuning value is the lower intensity state and the cycle begins again.

Depending on the details of the solution, the effective detuning between the primary and secondary lasers can be different for the same experimental control parameters (the wavelength and the power of the primary laser). After a state switch, the associated thermal change moves the system deterministically back in the direction of the original state leading to another state switch after which the process begins again. The hysteresis cycle associated with the bistability is thereby transformed into a deterministic cycle.

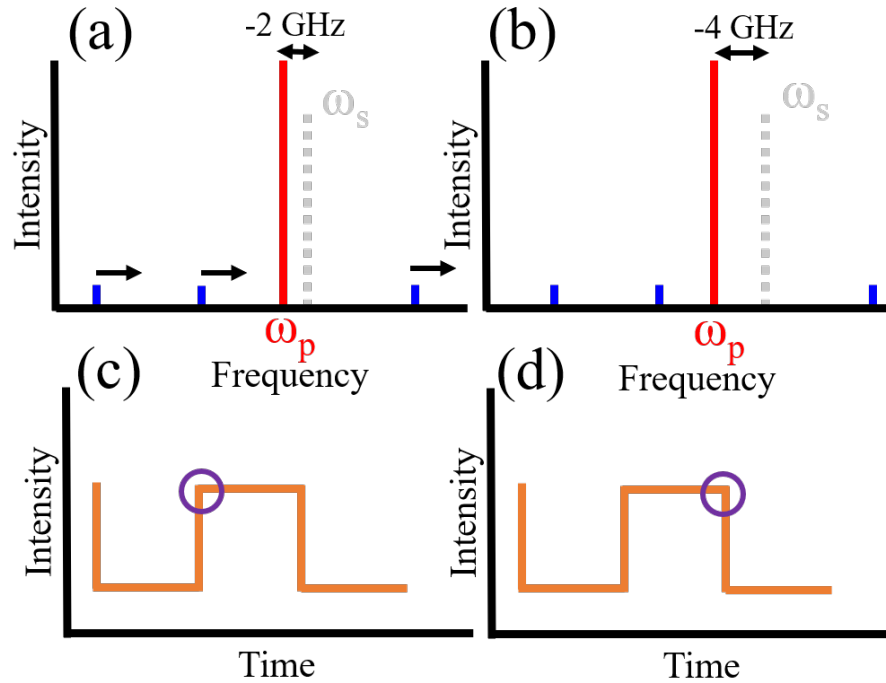


Figure 2.8: Cartoon describing the optothermal effect. (a) and (b) show the optical spectrum of the QD laser. The blue lines represent the subthreshold modes. The red line represents the lasing frequency of the QD laser, which remains fixed as the QD laser is phase locked to the constant TLS  $\omega_p$ . The grey dashed line,  $\omega_s$ , is the longitudinal mode that would lase in this single mode laser, in the absence of optical injection. Detuning is defined as  $\omega_p - \omega_s$ . The bottom panels show timestraces of the square wave train. The circles indicate what part of the cycle the top panel is describing. As shown in (c) the system has just begun emitting from the upper intensity section. This allows the temperature of the device to decrease. As indicated by the arrows, this increases the frequency of the longitudinal modes and  $\omega_s$ . Over the duration of the upper intensity section the detuning has decreased from -2 GHz to -4 GHz.

### 2.5.1 Intrinsic detuning sweep measurement

When free running at 1.25 times threshold, the nearest longitudinal mode of lower frequency happened to be suppressed by only 29 dBm for this device, while all other modes were suppressed by at least 41 dBm. The laser was still considered to operate as a single mode device. A second TLS was added to the experimental setup as a sort of probe laser. It emitted light slightly negatively detuned from this mode and was mixed with the output from the SL, Figure 2.9.

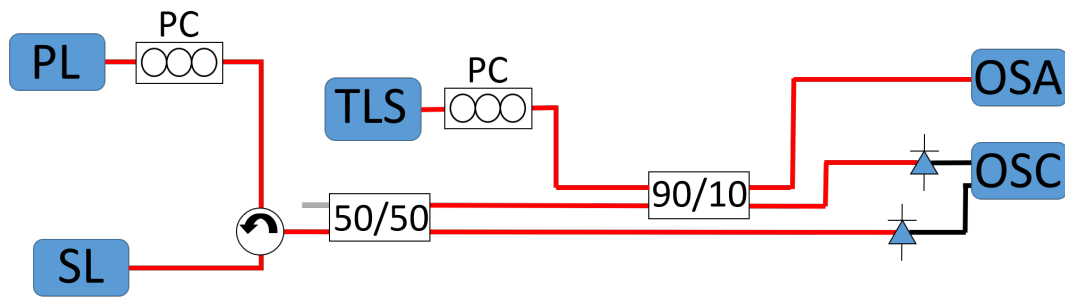


Figure 2.9: Experimental setup of an optically injected laser, where the secondary laser (SL) is a QD laser. The primary laser (PL) is a tunable laser source (TLS). A polarisation controller (PC) is used to maximise coupling. A circulator shines light from the PL into the SL, the light that is emitted from the SL into the circulator is then sent into a 50/50 splitter. 50% of light is sent directly to a 12 GHz detector connected to an oscilloscope (OSC). The other 50% is sent to a 90/10 coupler, where it is mixed with light from a second TLS. A polarisation controlled is used to maximise the amplitude of the beat signal. 90% of the beat signal is sent to a 12 GHz detector connected to an oscilloscope and the remaining 10% is sent to an optical spectrum analyser (OSA).

Figure 2.10 shows the frequency of the probe with respect to the rest of the system. During the upper part of the cycle there was insufficient intensity in the side mode to measure the beat signal. However, during the low intensity part of the square sufficient power existed in the resulting beating cycle to be measured on the oscilloscope, Figure 2.11. The evolution of the frequency of this beating cycle was found by calculating the Fast Fourier Transform (FFT) of many ten nanosecond intervals. Figure 2.11(b) shows that there was a slow deterministic change in the frequency of the SL of approximately 2 GHz over the duration of each square. This confirms that the effective detuning is indeed changing during each square wave.

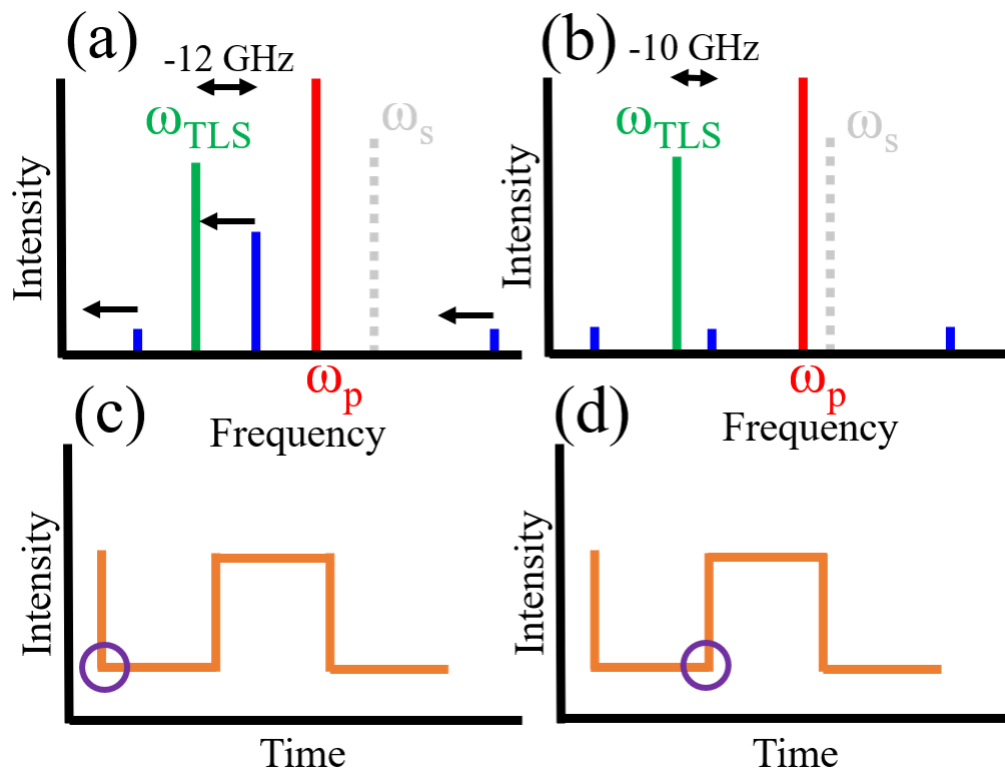


Figure 2.10: Cartoon describing the measurement of the optothermal effect, similar to Figure 2.7. (a) and (b) show the optical spectrum of the QD laser. The blue lines represent the subthreshold modes. The red line represents the lasing frequency of the QD laser, which remains fixed at  $\omega_p$  as the QD laser is phase locked to the constant TLS. The grey dashed line,  $\omega_s$ , is the longitudinal mode that would lase in this single mode laser, in the absence of optical injection. The green line labelled  $\omega_{TLS}$  is a second TLS and is used as a probe laser. When a subthreshold longitudinal mode happened to receive more gain during the low intensity section of the square wave train, as shown in (a), a beating tone is observed showing the frequency difference between the sweeping longitudinal mode and  $\omega_{TLS}$ . It changes from -12 GHz to -10 GHz over the duration of the lower intensity section as indicated by the timestraces in (c) and (d). The circles indicate what part of the cycle the top panel is describing.

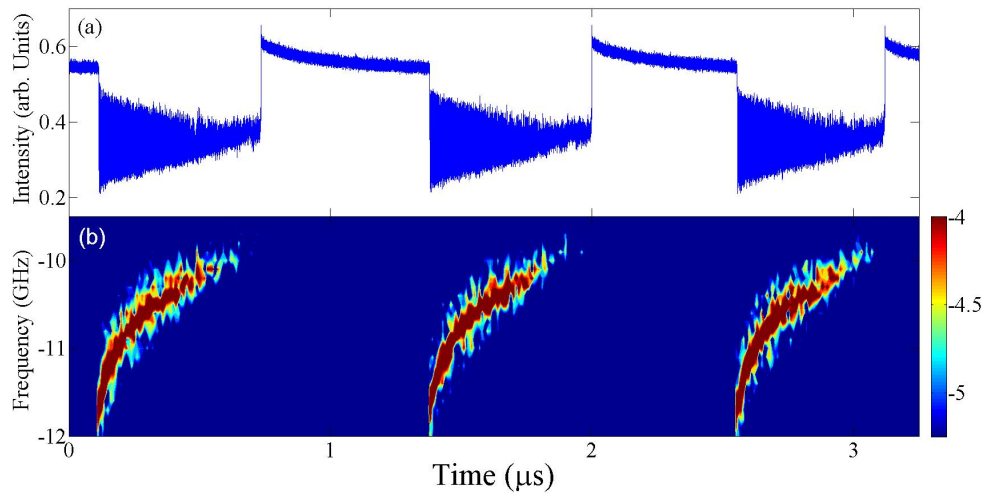


Figure 2.11: (a) The resulting intensity after a square wave train is mixed with and a second TLS (with frequency of approximately 12 GHz from the side mode). The longitudinal mode did not have sufficient power in the upper intensity section to create a beat signal. In the lower intensity section there was enough power from the longitudinal mode to create a beat tone that could be detected. The power of the longitudinal mode decreased over the duration of the lower intensity section and thus the amplitude of the beat tone can also be seen to decrease. (b) 10 ns widows were taken and the FFT was calculated for each window. The resulting frequencies are plotted in a heat map. The frequency recorded is the frequency of the second TLS minus that of the sub-threshold longitudinal mode under investigation. These values are arbitrarily set but it's important to note that the QD laser undergoes a 2 GHz sweep due to an optothermal effect.

## 2.5.2 Phase measurement

We investigate the phase dynamics of the square pulses using the phase resolving technique developed in [84]. This technique involves a  $3 \times 3$  coupler and allows us to reconstruct the phase of the secondary laser with respect to the primary in realtime. One input arm receives all of the light from the secondary laser, another receives 10% from the primary laser (TLS) and the third is left empty. All three outputs are detected using 12 GHz detectors connected to a real time oscilloscope, see Figure 2.12. In this experiment the TLS can be considered as a reference wave.

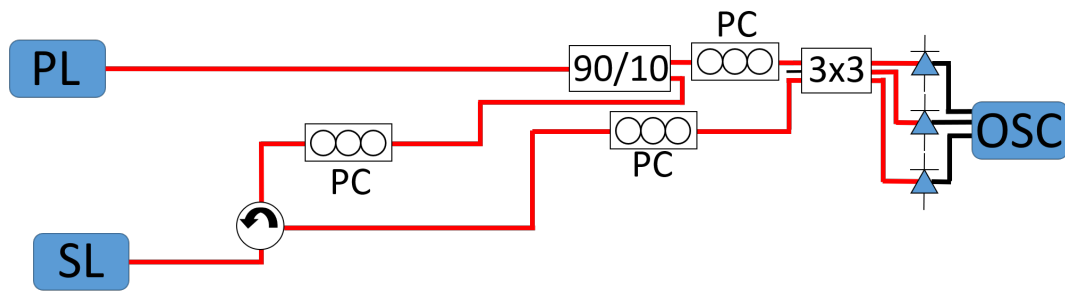


Figure 2.12: The basic setup shown in Figure 2.1 is repeated but more components are added before detection. Experimental setup of an optically injected QD laser acting as the secondary laser (SL). Light from the primary laser (PL) which is a tunable laser source (TLS) is split. 10% is sent into one arm of a  $3 \times 3$  coupler for an interferometric phase measurement technique. 90% is sent to a circulator and is then injected into a QD laser. A polarisation controller (PC) is used to maximise coupling. The light emitted from the SL into the circulator is sent to another arm of the  $3 \times 3$  coupler. The third arm is left empty. Polarisation controllers are used to maximise the interference of the  $3 \times 3$  coupler input signals. All 3 outputs of the  $3 \times 3$  coupler are connected to 12 GHz detectors connected to an oscilloscope (OSC).

If the phase difference between the primary and secondary lasers remains constant, the secondary laser is said to be phase locked to the primary. Figure 2.13 shows a noise induced excitable square pulse and its phase. Before the square pulse is fired the phase remains constant, modulo noise, so the QD laser is indeed phase locked. When the pulse is fired there is an abrupt change in phase of approximately 2.4 rad. Over the duration of the upper section of the square the phase undergoes a slow change of approximately 1 rad. This corresponds to the long narrow section of the phase diagram in Figure 2.14. When the pulse is over there is another fast jump in phase, this time by 1.4 rad. There is then a small drift in phase for about  $0.4 \mu\text{s}$  and then the system returns to its original phase locked state. In the periodic square wave trace in Figure 2.15 this drift in phase during the low intensity section is seen again.

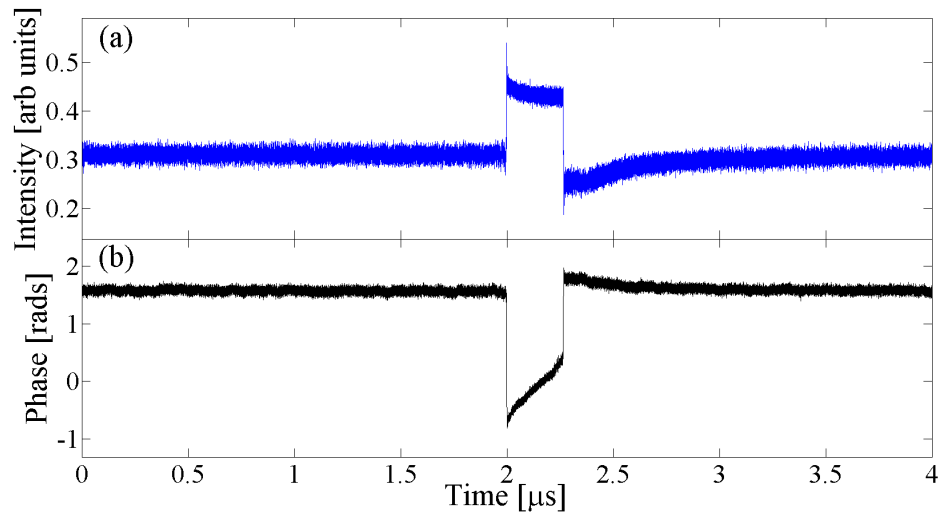


Figure 2.13: (a) Timetrace of a noise induced excitable pulse at approximately  $-6.6$  GHz detuning. (b) The phase associated with the timetrace from (a). The phase undergoes a change of  $2.4$  rad at the onset of a square pulse and over the duration of the pulse the phase undergoes a slow change of approximately  $1.4$  rad before jumping back to the lower intensity section.

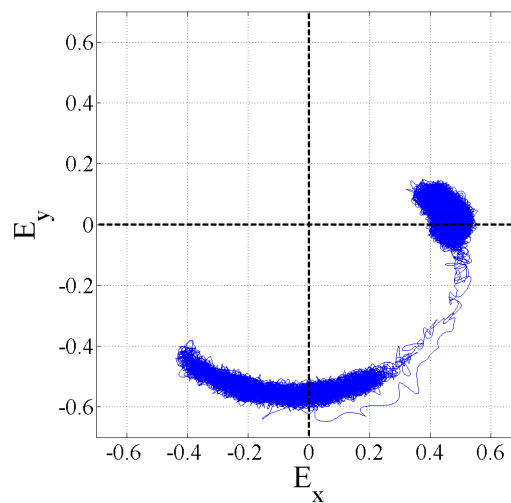


Figure 2.14: Phasor diagram for the secondary laser field, corresponding to the pulse seen in Figure 2.13. The long stretched out part corresponds to the square pulse and the more concentrated section in the lower intensity section.

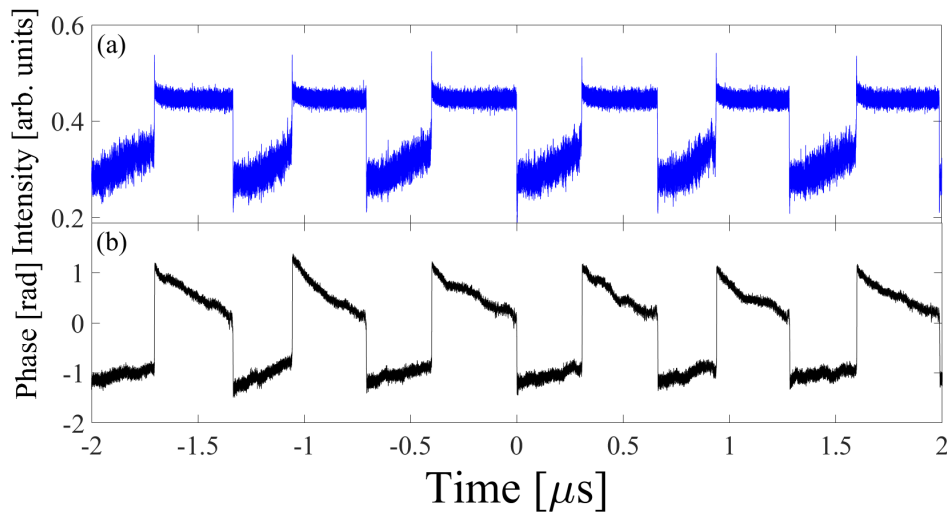


Figure 2.15: (a) Intensity trace of periodic square wave train. (b) The phase corresponding to (a). During the upper intensity section the phase undergoes a slow 1 rad change. During the lower intensity section there is a slow 0.4 rad change of phase.

This is not an intuitive result. We have established that the upper and lower intensity section of the square pulse are the intensities associated with two phase locked states and that an optothermal effect breaks the bistability between the states and produces a square wave cycle. So although each section was once associated with a phase locked state, this is no longer the case and the secondary laser does not appear to be phase locked to the primary and exhibits a bounded phase rotation. However, rather interestingly, it could be argued that the QD laser always remains phase locked. Over the duration of a square, the phase locked solution associated with each state is continuously changing due to the effective detuning sweep, brought about by the optothermal effect. Thus the stable phase solution is evolving and the phase change we observe is the secondary laser simply moving to the new phase locked solution. But because of the finite response time of the QD laser, it is not truly phase locked. While we have established the QD laser is not phase locked during a square event to the primary laser it is always frequency locked and emits light at the same same frequency of the primary laser.

## 2.6 Deterministic triggering

While the presence of stochastic pulses allow us to conclude on the excitable nature of the system, for applications one would typically need to

deterministically trigger pulses [73, 85]. To investigate this we use a  $\text{LiNbO}_3$  phase modulator to perturb the injected light, see Figure 2.16. The modulator is connected to a pulse generator that can generate pulses with a full width half maximum of approximately 1 ns. By varying the perturbation amplitude the presence or otherwise of a threshold can be investigated.

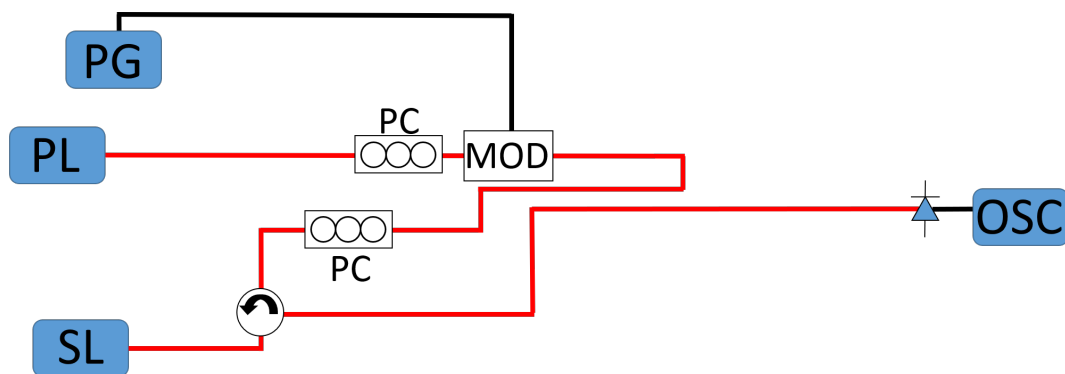


Figure 2.16: The basic setup shown in Figure 2.1 is repeated but a  $\text{LiNbO}_3$  phase modulator (MOD) is introduced after the primary laser (PL). The PL is a tunable laser source (TLS). The modulator is driven by a pulse generator. This modulates the light being injected into the QD secondary laser (SL). A polarisation controller (PC) is used to maximise coupling. A circulator shines light from the PL into the SL, the light that is emitted from the SL into the circulator is sent to a 12 GHz detector connected to an oscilloscope (OSC).

Figure 2.17 shows two perturbations and the resulting laser responses for the device biased at 36.5 mA (1.14 times threshold). In Figure 2.17 (c) a large amplitude voltage spike is applied and a square pulse (Figure 2.17 (a)) is excited in the secondary laser. In Figure 2.17 (d) a low amplitude voltage pulse is applied and a square is not excited in the laser. Instead, the intensity returns to the steady state via a short phase space trajectory (Figure 2.17 (b)). The probability of excitation of a pulse for a particular perturbation strength is calculated by finding the number of successful pulses triggered after making 391 consecutive perturbations. An efficiency curve can then be generated as shown in Figure 2.18. There is a clear threshold (defined at 50% efficiency), at 2.31 V showing that the square pulses can be deterministically triggered with a sufficiently strong voltage pulse applied to the modulator, clearly demonstrating the excitable nature of the square pulses.

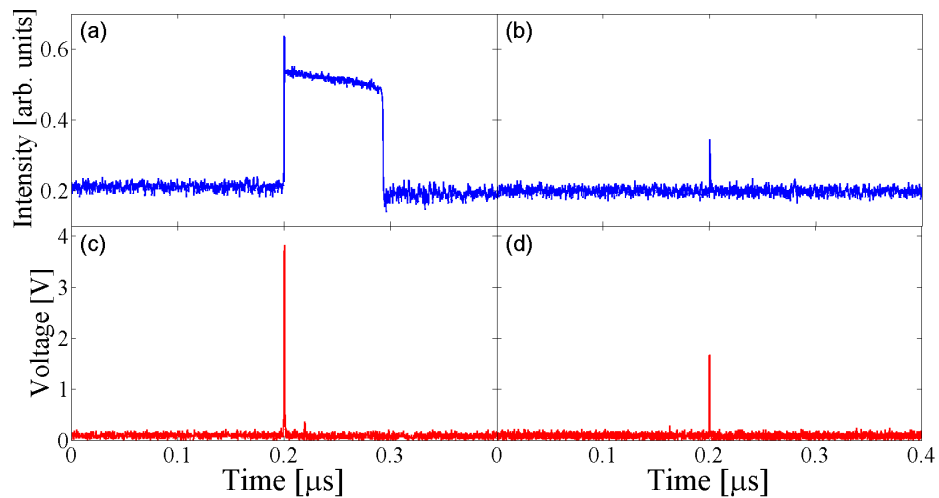


Figure 2.17: (a) and (b) show the output from the secondary laser. (c) and (d) show the electric pulses of different amplitudes that were sent to the phase modulator in order to perturb the injected light. (a) is a successfully triggered optical square pulse and was triggered by the electrical pulse (c) with an amplitude of 3.82 V. The smaller perturbation (d) with an amplitude of 1.67 V, fails to excite a square pulse as shown in (b).

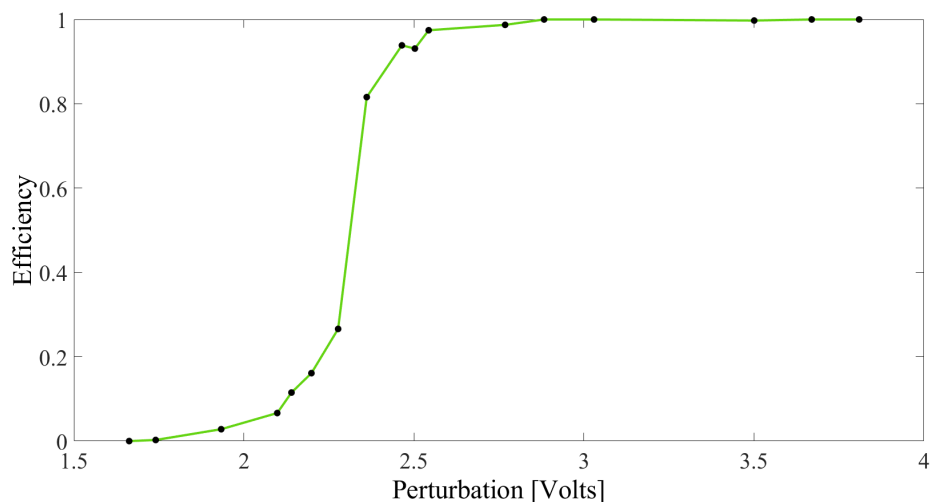


Figure 2.18: Efficiency curve for deterministically triggered square pulses. There is a threshold at approximately 2.3 V. If the strength of the perturbation is greater than this then there is a 50 % probability that a pulse would be fired.

## 2.7 Class A theoretical model

Rate equation models of the optically injected system have proven to be excellent predictors of the experimentally observed dynamics for semiconductor lasers [86]. While specifically tailored QD models do exist, they are necessarily more complicated than their conventional counterparts [71, 87]. It has been shown that qualitatively, one can recover many of the phenomena observed with optically injected QD lasers using the conventional semiconductor rate equations but with very high damping of the relaxation oscillations (ROs) imposed, as found experimentally for QD lasers [66]. In fact, one can even recover virtually all of the phenomena by moving to the Class A, infinite RO damping limit, where the dependence on the carriers is adiabatically eliminated and the behaviour is described using only the electric field [66, 69, 71]. The equations are then,

$$\dot{R} = \frac{P - R^2}{1 + 2R^2}R + K \cos\phi \quad (2.1)$$

$$\dot{\phi} = \alpha \frac{P - R^2}{1 + 2R^2} - (\Delta - \omega) - \frac{K}{R} \sin\phi + D\xi(t), \quad (2.2)$$

where  $R$  is the secondary field amplitude,  $K$  measures the injection strength,  $\phi$  is the phase of the secondary minus that of the primary,  $\Delta$  is the nominal angular detuning,  $\alpha$  is the phase amplitude coupling factor and  $P$  is the pumping current above threshold. We include stochastic effects via  $D\xi(t)$ , where  $\xi(t)$  is a Wiener process and  $D$  is the magnitude. Time is expressed in units of the photon lifetime.

Most importantly here, such lasers display a phase-locked bistability precisely of the form predicted for optically injected QD lasers [66, 69, 71, 88]. Thus, in order to highlight the physics of the phenomenon, we work with this model while recognising that QD lasers are not genuine Class A lasers. Nonetheless, we manage to capture the basic physics and find excellent qualitative agreement.

### 2.7.1 Inclusion of the optothermal effect and the evolution of the region of excitability

The model is modified so as to include thermal effects. Carrier heating effects have previously been incorporated in a very detailed microscopic model for QD lasers in [89] and their importance in large signal modulation highlighted. In our case, we want to focus on the underlying physics of the system and so we modify our model to include thermal effects by adding one equation that couples the effective detuning to the intensity.

$$\dot{\omega} = -\gamma(\omega - cR^2), \quad (2.3)$$

$\omega$  is the thermal change in the detuning,  $\gamma$  gives the slow characteristic time scale for the thermal effects, and  $c$  is the coupling between the thermal dynamics and the intensity. We note that we must couple the optothermal effect to the electric field because the carriers have been adiabatically eliminated. But despite this simplicity, we find that the model is sufficient to understand the essentials of the mechanism.

The bare ( $c = 0$ ) system, shown in [66], has a region of phase-locked bistability and an associated hysteresis loop (with  $K$  in the interval  $[0.5, 0.8]$ , for  $\alpha = 2$  and  $P = 0.5$  for example) due to the interaction of a saddle-node bifurcation and a Hopf bifurcation at negative detuning. No square wave regime is obtained. Consider now the coupled system with finite  $c$ . Some things remain virtually unchanged. For injection strengths around 0.01 the Adler equation can be recovered for the phase equation. Thus, Type I excitability is still obtained as experimentally observed. When we move to higher injection strengths and to the previous region of bistability however, things have changed dramatically.

In the absence of noise, a prominent region of periodic square wave pulses is obtained. The results are robust to changes in  $\alpha$  and  $\gamma$ . (For example,  $\gamma$  can be changed by several orders of magnitude while retaining the qualitative features analysed here). Close to the onset of this regime, the system is excitable.

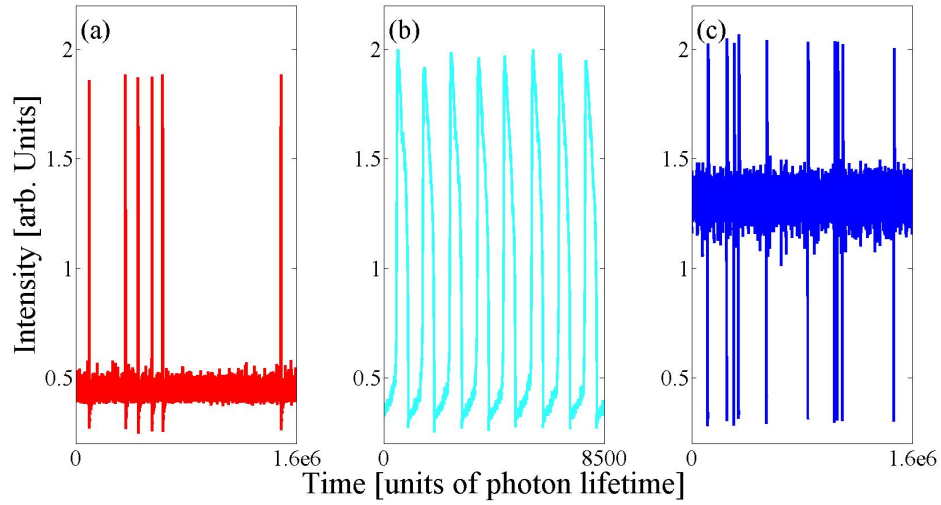


Figure 2.19: Numerical pulse/dropout trains. (a) shows the intensity at a detuning of  $-0.955$ ; (b) shows the intensity at a detuning of  $-0.9225$ ; and (c) shows the intensity at a detuning of  $-0.89$ ,  $K$  is  $0.7056$ .

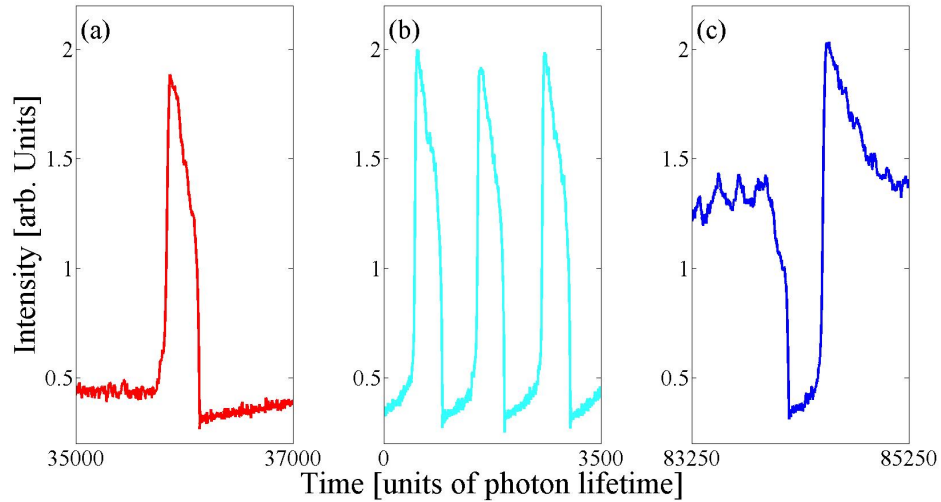


Figure 2.20: Zoomed in traces of the pulse/dropout trains shown in Figure 2.19. (a) shows the intensity at a detuning of  $-0.955$ ; (b) shows the intensity at a detuning of  $-0.9225$ ; and (c) shows the intensity at a detuning of  $-0.89$ ,  $K$  is  $0.7056$ .

To analyse the evolution of the intensity, noise is included with the parameters set as follows:  $\alpha = 2$ ,  $P = 0.5$ ,  $c = 0.1$ ,  $\gamma = 0.001$  and  $D = 0.1$  and the detuning is varied. Excitable square wave trains are obtained as shown in Figure 2.19(a) and Figure 2.19(c) for detuning values of  $-0.955$  and  $-0.89$ . Figure 2.19(b) shows an example of the periodic square regime, with noise included, at  $-0.9225$  detuning. Figure 2.20 zooms in on square events in Figure 2.19.

The associated interpulse/interdropout histograms are shown in Figure 2.21 and the exponential shape of the noise induced excitable pulses match the experimental case extremely well. So too do the narrow distributions of upper and lower intensity durations in the periodic case in Figure 2.22.

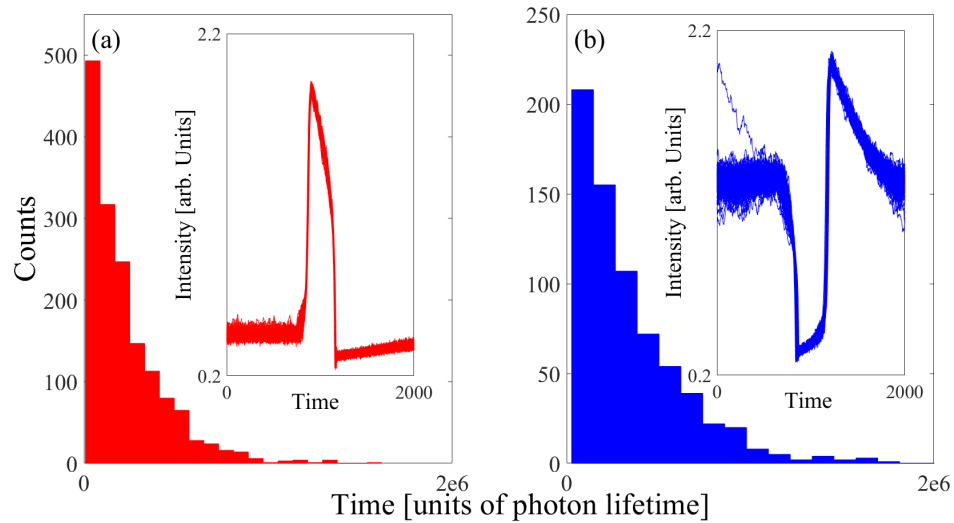


Figure 2.21: The distribution of the interpulse times is shown in (a) and the inset is a persistence plot of 100 consecutive pulses plotted on top of each other illustrating the regular pulse width. (b) shows the distribution for the square dropouts with a persistence plot inset. The control parameters match those in Figure 2.19.

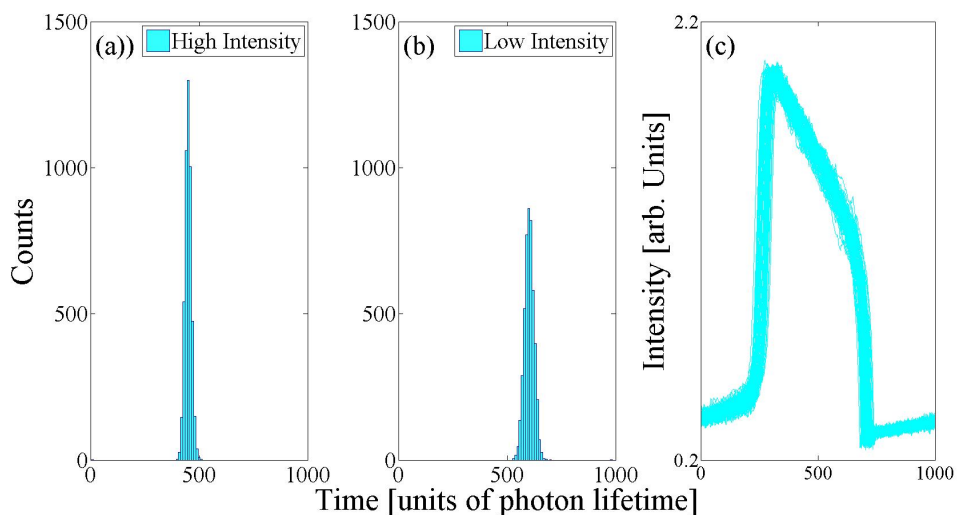


Figure 2.22: (a) shows the distributions of the duration of the high intensity plateaus. Similarly (b) shows the distributions of the low intensity lifetimes. The narrow distributions indicate a consistent and reproducible square wave train. (c) is a persistence plot of 100 consecutive pulses plotted on top of each other illustrating the regular pulse width.

### 2.7.2 Bifurcation analysis

A natural question is what bifurcation leads to this square wave regime. To examine this, we fix the parameters as follows:  $\alpha = 2$ ,  $K = 0.7104$ ,  $P = 0.5$ ,  $\gamma = 5 \times 10^{-6}$ . (We note that the results are robust to changes in  $\alpha$  and  $\gamma$ . For example,  $\gamma$  can be changed by several orders of magnitude while retaining the qualitative features analysed here). We then plot the bifurcation diagram for  $c = 0$  in the bistable region, the blue curve in Figure 2.23 (found using the continuation package AUTO). The stable steady states arise from saddle-node bifurcations and overlap forming the bistable region. We then include the optothermal coupling,  $c = 0.1$ , and plot the intensity of the square wave over the bifurcation curve (red). The squares result from the slow deterministic evolution of the detuning. The intensity of the square corresponds to the steady state intensity of the bare system. The bistability (blue) is destroyed by an optothermal coupling and is replaced by a deterministic cycle represented by the red curve.

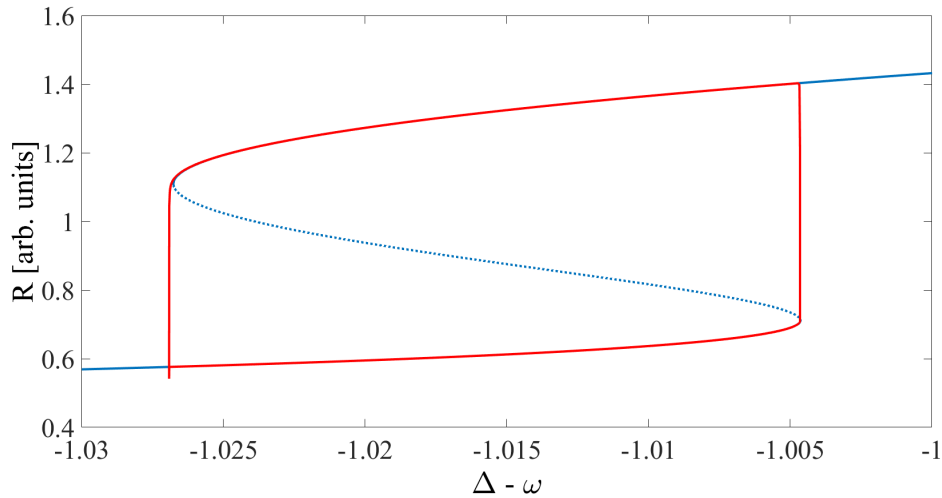


Figure 2.23: Bifurcation diagram using the Class A model. The blue curve shows the saddle node structure of the bare system (no optothermal coupling,  $c = 0$ ). The solid lines represent stable solutions and the dotted lines represent unstable solutions. There is a clear bistability. The red curve shows the trajectory of Figure 2.24 (b) obtained at  $\Delta = -0.9540124775$  with a finite optothermal coupling,  $c = 0.1$  and  $\gamma = 5 \times 10^{-6}$ . For both cases  $K = 0.7104$ .

Via a combination of direct simulation and the numerical continuation software package AUTO we find a new Hopf bifurcation in the system. Figure 2.24 is a bifurcation diagram showing the location of this bifurcation  $\Delta_H$ , and the amplitude of the resulting cycles. Directly after the bifurcation there is a small amplitude cycle as shown in Figure 2.24 (a). However, after a very short

range of detuning, large amplitude cycles appear, Figure 2.24 (b). This occurs via a canard explosion.

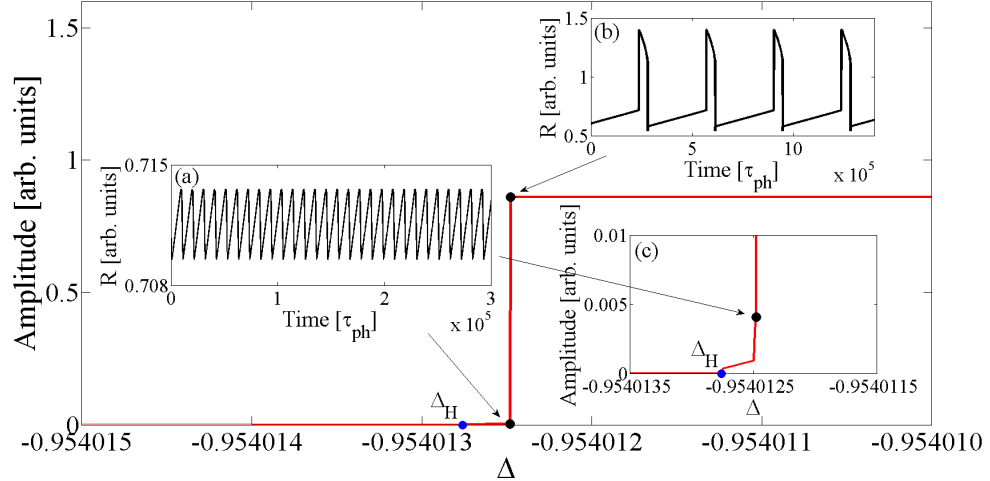


Figure 2.24: Bifurcation diagram showing the new Hopf bifurcation created by the optothermal coupling. The Hopf point  $\Delta_H = -0.95401276$  is shown with a blue dot. Examples of small and large amplitude cycles at  $\Delta = -0.95401248$  and  $\Delta = -0.9540124775$  are shown in insets (a) and (b), where their amplitudes are approximately 0.004 and 0.86 respectively. Zero corresponds to constant output. Inset (c) zooms in on the canard explosion and the associated region of small amplitude oscillations.  $K = 0.7104$  throughout.

So as to gain some physical perspective let us assume a value of 10 ps for the photon lifetime (while acknowledging that this is merely an estimate but of the right order). As is typical with canard explosions, the parameter range for the small amplitude oscillations is extremely small. In the dimensionless units it has a range in detuning of only  $\sim 0.00006$ . The explosion itself occurs over a tiny range and the amplitude of the oscillations increases by a factor of 20 over a very small control parameter range of approximately 1 MHz. The minimum step size of the TLS is approximately 18 MHz and so a detailed investigation of the region is difficult. Further, the inherent experimental noise alone may be enough to mask the small amplitude oscillations.

### 2.7.3 Deterministic triggering

Close to the bifurcation the system is excitable. By including noise in the simulations one can obtain noise induced excitable events as demonstrated in Section 2.7.1. We complement this analysis here by taking a noise free system but investigate excitability by applying discrete perturbations which can lead

to trajectories around the large amplitude cycle for a sufficiently large perturbation. One can obtain such an excitable trajectory at both sides of the bifurcation point  $\Delta_H$ , i.e. when the system is either in the regime of constant intensity output or in the small amplitude oscillation regime, shown in Figure 2.24. The response of the system depends on the amplitude of the perturbation. Figure 2.25 shows two responses to slightly different phase perturbations, when operating in the constant intensity regime, where  $\Delta < \Delta_H$ . One response simply yields a short phase space trajectory back to the stable state (black), while the bigger perturbation is just above the excitable threshold and yields an excitable pulse (red).

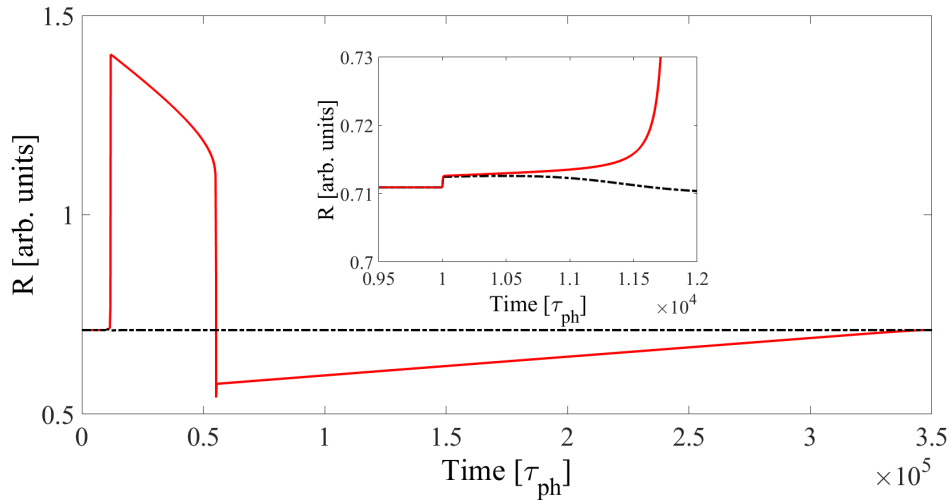


Figure 2.25: Two examples of perturbed trajectories. In the black dashed trace a perturbation of  $\delta\phi = 0.0011$  was applied at  $t = 1000$  yielding a short trajectory back to the steady state behaviour. In the red trace a perturbation of  $\delta\phi = 0.0012$  was applied yielding an excitable trajectory.  $K = 0.7104$ ,  $\Delta = -0.9541$ . The inset zooms in on the perturbation.

We recognise that the model is overly simple and that it would be preferable - and indeed, crucial - to reproduce the results using a model explicitly designed for QD lasers and so we turn to this below.

## 2.8 Quantum dot laser model

In order to best compare with existing work we use the rate equation model of [69, 71]. This consists of equations for the electric field amplitude  $R$  of the laser, the phase  $\phi$  in the frame of the primary and the carrier density in the wetting layer  $n$ . (The occupation probability of the dots has been adiabatically

eliminated as in [69]. The adiabatic elimination arises from the small parameter  $\varepsilon$  which gives the deviation of the dimensionless differential gain from 1. See [51] and references therein for further details). Again, we supplement the model with an extra equation describing the optothermal coupling, just as in the Class A model. The equations are as follows.

$$\begin{aligned}\dot{R} &= 1 - \frac{2(1+R^2)}{2B\varepsilon n}R + \frac{K}{\varepsilon}\cos(\phi) \\ \dot{\phi} &= -\frac{\Delta-\omega}{\varepsilon} + 1 - \frac{2(1+R^2)}{2B\varepsilon n}\alpha - \frac{K}{\varepsilon R}\sin(\phi) + D\xi(T) \\ \dot{n} &= \frac{1}{\varepsilon}\eta\left(J - n - 2(1+R^2)\right) \\ \dot{\omega} &= -\frac{\gamma}{\varepsilon}(\omega - cR^2)\end{aligned}$$

As with the Class A case, time is normalised with the photon lifetime  $\tau_{ph}$ . The dot means differentiation with respect to  $T = \frac{\varepsilon t}{\tau_{ph}}$ .  $J$  is the pump current per dot and  $\alpha$  is the linewidth enhancement factor.  $B \equiv \tau\tau_{cap}^{-1}$  and  $\eta \equiv \tau_{ph}\tau^{-1}$  where  $\tau$  and  $\tau_{cap}$  denote the carrier recombination and capture times, respectively.  $D\xi(t)$  is a white noise term, where  $\xi(t)$  is a Wiener process and  $D$  is the magnitude. To allow direct comparison with Figure 1.14 in [69] we use the same parameter values and keep them fixed:  $\alpha = 1.2$ ,  $J = 5.14$  (1.5 times threshold),  $B = 70$ ,  $\varepsilon = 0.02$  and  $\eta = 2 \times 10^{-3}$ . The optothermal effect is introduced in a similar way to how it was included in the Class A model,  $\gamma$  again provides the slow thermal relaxation time and  $c$  is the optothermal coupling constant. We fix  $\gamma = 5 \times 10^{-6}$  and  $c = 0.03$ . Our control parameters are the injection rate  $K$  and the detuning  $\Delta$  defined as the frequency of the primary laser minus that of the secondary laser.

The bare system with no optothermal coupling yields a region of phase-locked bistability as shown in [69]. Including the optothermal coupling we find as before that a square wave regime is obtained. Figure 2.26(a) shows a noise induced pulses in the excitable region. Again, direct simulation demonstrates that the system is excitable close to this region with pulses arising from discrete perturbations and via noise,  $D = 0.01$ . Figure 2.26 (b) shows the associated phasor trajectory. The agreement with the experiment is excellent. Admittedly, the overall phase rotation is smaller than that found experimentally but we ascribe this to the relatively low value of  $\alpha$  used (deliberately to allow comparison with the existing results in [69, 71]).

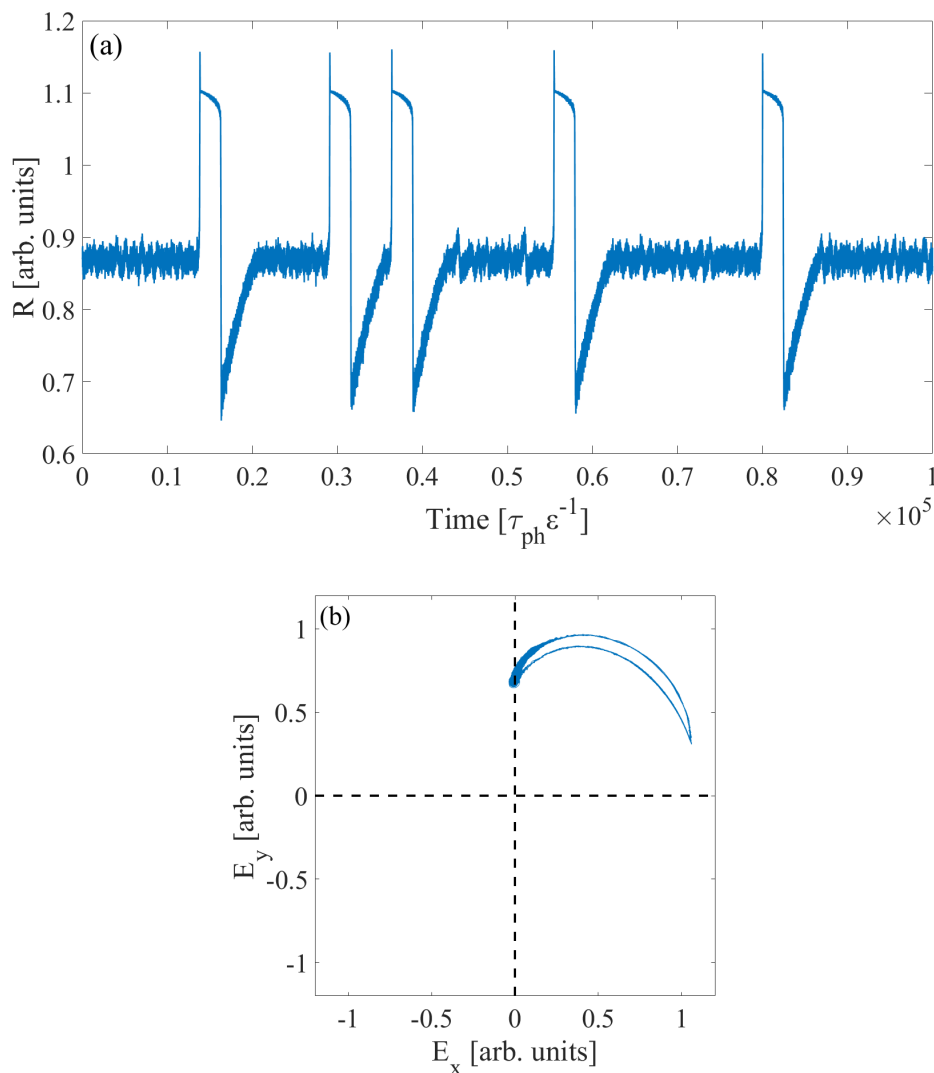


Figure 2.26: (a) Noise induced excitable squares pulses found for  $K = 0.04$ ,  $\Delta = -0.029525$ ,  $D = 0.01$ ,  $\gamma = 5 \times 10^{-6}$  and  $\eta = 2 \times 10^{-3}$ . (b) shows the associated phasor trajectory.

## 2.8.1 Bifurcation analysis

### 2.8.1.1 Subcritical Hopf

Unlike the Class A case, we find a subcritical Hopf bifurcation. The system is in fact bistable between the phase-locked solution and a square wave train just before the Hopf is reached. Figure 2.27 shows the two stable states for the same control parameters but for a noise free system,  $D = 0$ . Only the initial conditions differ. Thus, the excitability arises via the conventional, subcritical Type II dynamic for the QD model with these parameters. However, as we show now, we can regain the canard explosion feature by changing just one parameter.

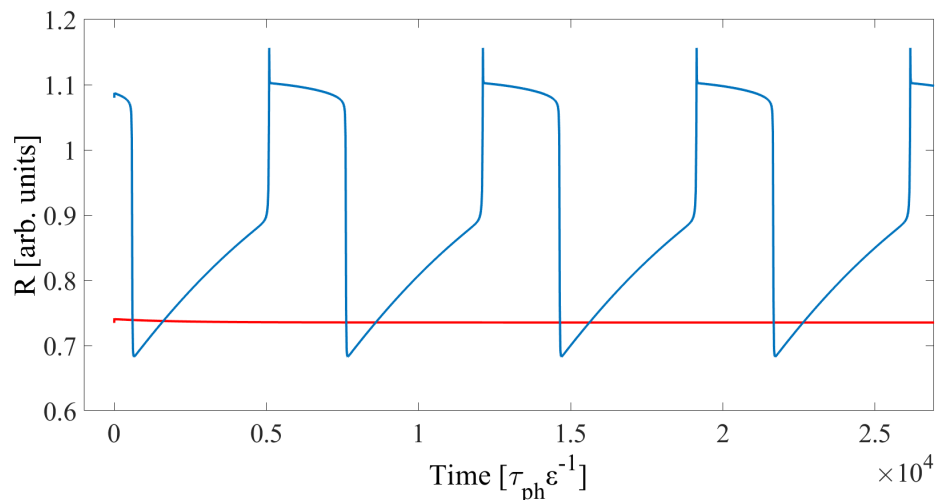


Figure 2.27: Near the subcritical Hopf bifurcation point a bistability is creating and the two solutions are shown above. The solution the system evolves into depends on the initial conditions. Initial conditions for the constant trace are  $R = 0.735$ ,  $\phi = 1.560$ ,  $n = 2.06$  and  $\omega = 0.016$ . For the square trace the initial conditions are  $R = 1.08$ ,  $\phi = 0.667$ ,  $n = 0.795$  and  $\omega = 0.028$ . The operating parameters are the same for both.  $K = 0.04$ ,  $\Delta = -0.02929$ ,  $\eta = 2 \times 10^{-3}$ ,  $\gamma = 5 \times 10^{-6}$  and  $D = 0$ .

### 2.8.1.2 Reduction to Canard Explosion

The Class A model is the limit of the more conventional Class B model as the ratio of the photon lifetime to the carrier lifetime tends to infinity ( $\eta$  in our QD model). However, as shown in [66] many features of the Class A system arise also in the standard Class B system for finite ratio. We find that for a modest  $\eta = 0.03$ , the results are similar to the Class A case. In Figure 2.28 we plot a bifurcation diagram for the bare system,  $c = 0$ , of the bistable region and then include the optothermal coupling and plot the intensity of the square wave regime over the bifurcation figure. The square wave trajectory follows the bistable steady states of the underlying bare system. The Hopf bifurcation becomes supercritical and we recover the canard explosion, see Figure 2.29. Noise induced square pulses that arise from this supercritical Hopf are shown in Figure 2.30.

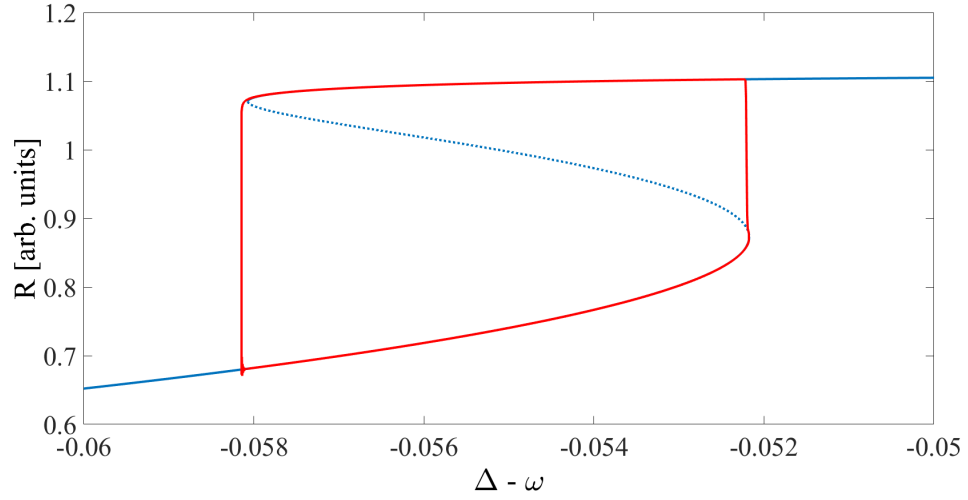


Figure 2.28: Bifurcation diagram using the QD model. The blue curve shows the saddle node structure of the bare system (no optothermal coupling,  $c = 0$ ). The solid lines represent stable solutions and the dotted lines represent unstable solutions. There is a clear bistability. The red curve shows the trajectory shown in Figure 2.29 (b) for  $\Delta = -0.02931155$  with finite optothermal coupling,  $c = 0.03$  and  $\gamma = 5 \times 10^{-6}$ . For both cases  $K = 0.04$ ,  $D = 0$  and  $\eta = 2 \times 10^{-3}$ .

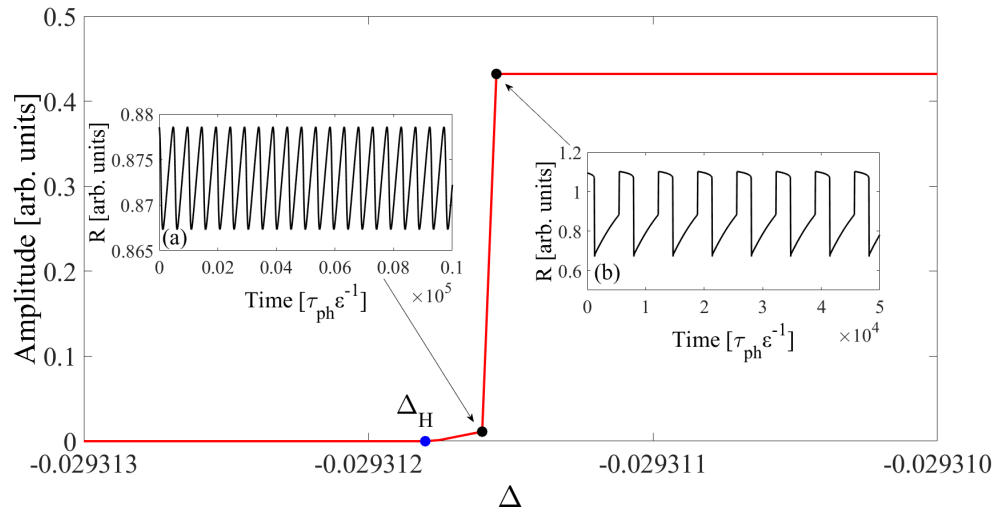


Figure 2.29: Bifurcation diagram for the supercritical Hopf case showing the amplitude of the cycle versus the detuning. (Thus, zero corresponds to constant output.) Small amplitude oscillations are obtained just after the Hopf point (blue dot)  $\Delta_H = -0.0293118$ . A canard explosion then leads to the creation of a large amplitude cycle. The insets show two characteristic examples of the output.  $K = 0.04$ ,  $D = 0$ ,  $\eta = 0.03$ ,  $c = 0.03$  and  $\gamma = 5 \times 10^{-6}$  throughout. The insets show  $\Delta = -0.0293116$  and  $\Delta = -0.02931155$  for the small amplitude and large amplitude cycles with amplitudes of 0.01 and 0.43 respectively.

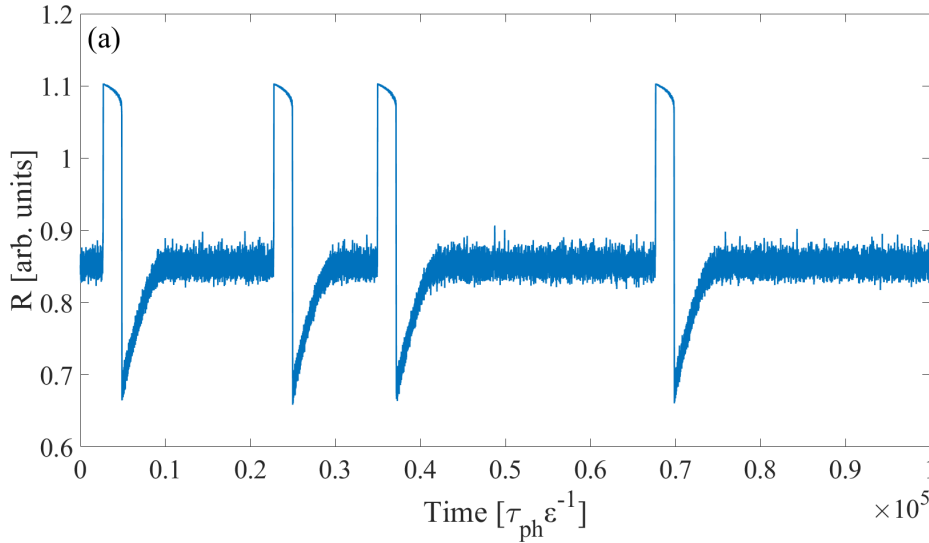


Figure 2.30: Noise induced square pulses for the supercritical Hopf case.  $K = 0.04$ ,  $\Delta = -0.0304$ ,  $\gamma = 5 \times 10^{-6}$ ,  $\eta = 0.03$ ,  $D = 0.01$ .

The question now arises as to which version is observed in the experiment. The traces for the noise induced pulses are extremely similar both for the subcritical (Figure 2.26(a)) and supercritical Hopf (Figure 2.30) cases and both match the experiment well. One feature does stand out: The overshoot at the beginning of each square in the experimental traces. This is reproduced by the QD model with the subcritical Hopf parameters but not with the Class A and not with the supercritical Hopf QD case. We ascribe this overshoot to the lower relaxation oscillation damping of the subcritical case compared with both other cases. It is thus tempting to identify the subcritical case as the underlying scenario. Further, the material parameters for the subcritical case agree with those in the literature while the supercritical case requires a much higher photon lifetime/carrier lifetime ratio. Of course, a more thorough bifurcation analysis is warranted both experimentally and numerically.

To conclude, we have shown the first demonstration of Type II excitability in the optically injected laser system. At high injection strengths, optothermal effects break a phase-locked bistability and endow the system with a periodic square wave regime and associated regions of Type II excitability. The relative detuning undergoes a deterministic sweep over the duration of a square. Interestingly, this is the first laser system displaying both Type I and Type II excitability. This suggests that QD lasers could be of immense interest in neuromorphic systems where artificial neuronal systems are desired, providing prototypical excitable behaviour for both types. Further, we would expect the

phenomenon to be robust to changes in device type with the main requirement being high RO damping.

## Chapter 3

# History of dual state optical Injection

We review results on the optical injection of dual state InAs quantum dot-based semiconductor lasers. The two states in question are the so-called ground state and first excited state of the laser. This ability to lase from two different energy states is unique amongst semiconductor lasers and in combination with the high relaxation oscillation damping of the material and the novel, inherent cascade like carrier relaxation process, this endows optically injected dual state quantum dot lasers with many unique dynamical properties. We compare and contrast some of the physical properties of the system with other optically injected two state systems such as ring lasers and VCSELs. Particular attention is paid to fast state switching, antiphase excitability, novel information processing techniques and optothermally induced neuronal phenomena.

This chapter is based on the following invited review article:

B Kelleher, M Dillane, E.A. Viktorov, “Optical information processing using dual state quantum dot lasers: Complexity through simplicity”, *Light: Science Applications* **10** (1), 1-15 (2021).

### 3.1 A brief history in dual state dynamics

Bistabilities and switching mechanisms in semiconductor lasers are topics of great interest both fundamentally and for applications including signal processing, optical flip-flops, optical memory elements and optical logic gates [90–95]. A particularly successful technique for obtaining bistable operation is via the optical injection of devices that admit two lasing states such as Vertical Cavity Surface Emitting Lasers (VCSELs) [2, 36, 96–100], semiconductor microring lasers [101, 102] and two-colour Fabry-Pérot lasers [103, 104]. The two states in VCSELs arise from two polarisation states, naturally arising due to the broad area of the emitting surface in such devices. Similarly, the two states in ring lasers also arise due to the geometry. The ring configuration means light can propagate either in the clockwise direction or in the anticlockwise direction. On the other hand, the two-colour Fabry-Pérot devices are explicitly designed to emit from two distinct longitudinal modes via careful design of a pattern of slots etched into the active material. When undergoing optical injection, all of such devices can be used as optical switches and all-optical memory elements. The dual state possibilities of QD lasers means they are also of interest for such applications. However, the carrier dynamics in QD devices are very different from all of these other cases. There is a cascade like relaxation pathway for carriers in QD material, from the carrier reservoir, through the ES and into the ground state [49, 50, 54]. Superficially, there are similarities with the other dual emission devices but the physical underpinnings are quite different and allow for phenomena that cannot be obtained with conventional semiconductor lasers as described below. What's more, the QD lasers rely on relatively simple fabrication and their geometry is ideally-suited to in-plane integration.

Apart from injection [105, 106], researchers have considered dual state optical feedback configurations [107–116] where competition between states and their different RO characteristics are often central to results; dual state mode-locking [117–125] where resistor self electro-optic effect device configurations and neuronal applications have been considered among others; and modulation characteristics when emitting from the ES [126–131], where it is shown that emission from the ES can significantly improve the modulation properties of QD lasers. We do not delve into these results here but instead restrict ourselves to optical injection.

## 3.2 Bistability and state switching

For most of the work described here, we consider a dual state QD laser biased so as to emit from the ES only, optically injected at the GS frequency. Figure 3.1 shows the basic concept of an optical injection experiment on a dual state laser. All experiments discussed below will be based on this core setup. Light is coupled from the tunable laser (PL) through port 1 and out of port 2 of an optical circulator providing  $\sim 40$  dB optical isolation, to polarisation controllers (PC) and into the QD laser (SL). The light from SL then passes into port 2 of the circulator and out of port 3 where a filter splits the GS and ES light for independent detection.

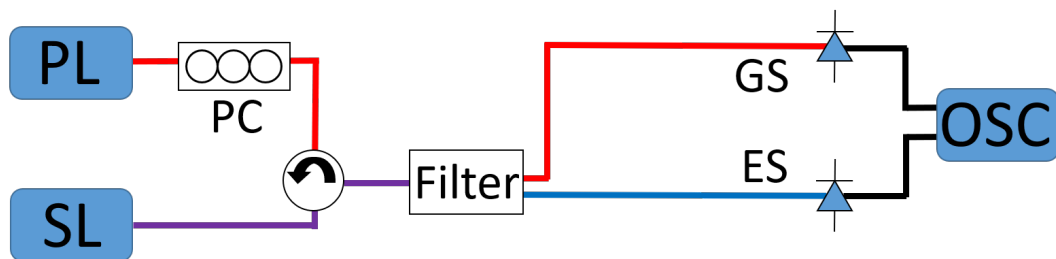


Figure 3.1: Basic optical injection set up. Light from a primary laser (PL), typically a tunable laser source, is injected into a circulator and then into the cavity of the secondary laser (SL), the QD laser. A polarisation controller (PC) maximises coupling. A filter is used to separate the ground state (GS) and excited state (ES), so each state can be monitored independently by detectors connected to an oscilloscope.

In [132] a QD device fabricated to lase from a single longitudinal mode in the GS while remaining multimode when operating from the ES was experimentally analysed. In the free-running configuration the first threshold was for GS only lasing, after which simultaneous GS and ES lasing was obtained and finally, ES only lasing, Figure 3.2. In [132] it was electrically pumped so as to emit from the ES only. Light from a primary laser, in this case a tunable laser source (TLS) emitting near the frequency of the GS, was injected into the QD secondary laser. For sufficiently low detuning (the frequency of the primary laser minus that of the secondary laser), the ES is completely suppressed and light is emitted from the GS only, see Figure 3.3. As pointed out in [46], when the QD laser emits from only the ES, all GS modes are subthreshold. This makes defining the value of the detuning difficult. Thus, the frequency of the primary laser is instead pragmatically set to where a desired qualitative behaviour is achieved.

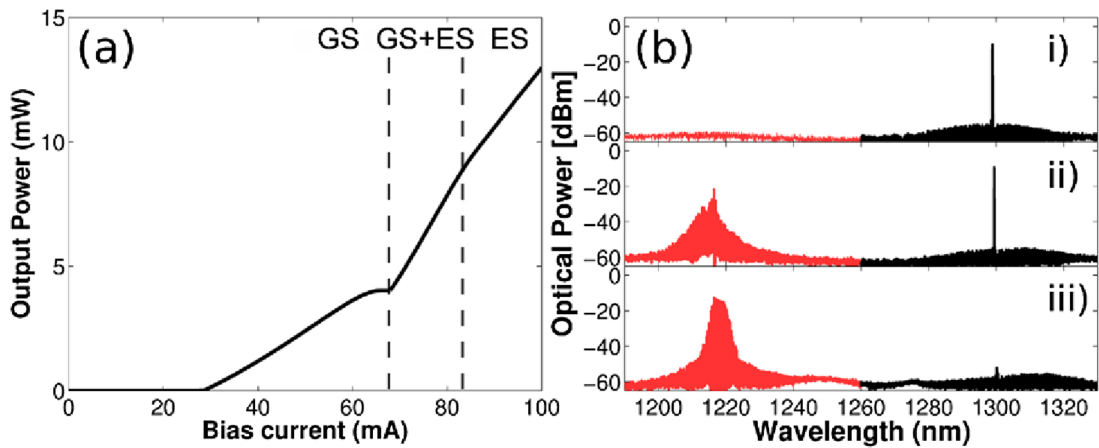


Figure 3.2: (a) the LI curve of a two colour device used in [132] that demonstrates the typical features observed in most devices discussed here. (b) shows the emission spectra of the device and correspond to 3 distinctive lasing regions: (i) There is the GS threshold beyond which only GS light is emitted. (ii) At the ES threshold, both the ES and GS last simultaneously. (iii) At higher pump currents the GS is quenched and only the ES lases. Reprinted with permission from [132] © The Optical Society.

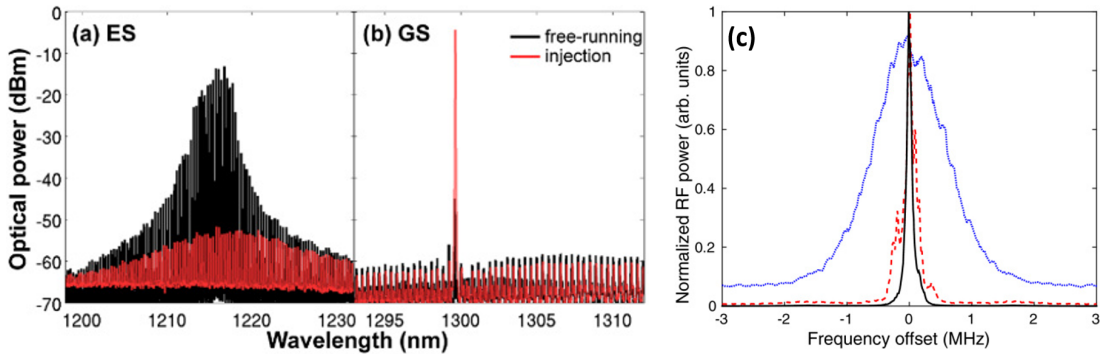


Figure 3.3: (a) the ES and (b) GS spectra before and after optical injection into the GS. Initially the device is pumped so as to emit from the ES only and all the GS modes are subthreshold (black). Injecting close to a GS mode the ES turns off and the GS turns on (red). Figures reprinted with permission from [132] © The Optical Society. (c) shows three line width measurements. The blue shows the line width of the GS when the laser is pumped to emit from GS only. The black shows the very narrow linewidth of the primary laser, the TLS. The red shows the linewidth of the QD laser after injection. Phase locking is verified as the QD laser has adopted a similar line width to the primary laser. Reprinted with permission from [46] © The Optical Society.

To confirm that the emission is phase locked to the injected light, the linewidth was investigated using a delayed self-heterodyne experiment, as shown in Figure 3.3 from [46]. Before any injection the linewidths of the primary and secondary lasers were found separately. When free-running and emitting from

the GS only, the linewidth of the QD laser was  $\sim 1$  MHz. The linewidth of the tunable laser was resolution limited, but less than 100 kHz. The current applied to the QD laser was increased until it lased from the ES only. With optical injection the ES was quenched and GS emission was recovered. The linewidth of the QD laser was then found to be less than 100 kHz, confirming the phase-locking of the QD laser to the tunable laser. The extent of the locking region was then investigated. The detuning was set to where the highest GS output of the QD laser was achieved. The injection strength was then swept up and down. While there were instances of oscillations noted, dynamics were not investigated in [46]. Instead, only the average output powers of the GS and ES were recorded. A hysteresis loop was found indicating a bistability. Both states in this bistability displayed simultaneous ES and GS lasing; the bistability was between a state where the GS dominated the emission and one where the ES dominated.

The findings were investigated using a rate equation model designed for the dual state QD system. This model consists of rate equations for the GS field, the ES intensity, the occupation probabilities for holes and electrons in the ES and in the GS and the carrier population in the carrier reservoir.

$$\dot{E}_g = \frac{1}{2}[(1 + i\alpha)(2g_0^g(n_e^g + n_h^g - 1) - 1) + i4\beta g_0^e(n_e^e + n_h^e - 1)]E_g - iE_g\Delta + \varepsilon, \quad (3.1)$$

$$\dot{I}_e = [4g_0^e(n_e^e + n_h^e - 1) - 1]I_e, \quad (3.2)$$

$$\dot{n}_{e,h}^g = \eta[2B_{e,h}n_{e,h}^e(1 - n_{e,h}^g) - 2C_{e,h}n_{e,h}^g(1 - n_{e,h}^e) - n_e^g n_h^g - g_0^g(n_e^g + n_h^g - 1)|E_g|^2], \quad (3.3)$$

$$\dot{n}_{e,h}^e = \eta[-B_{e,h}n_{e,h}^e(1 - n_{e,h}^g) + C_{e,h}n_{e,h}^g(1 - n_{e,h}^e) + B_{e,h}^w n_{e,h}^w(1 - n_{e,h}^e) - C_{e,h}^w n_{e,h}^e - n_e^e n_h^e - g_0^e(n_e^e + n_h^e - 1)I_e], \quad (3.4)$$

$$\dot{n}_{e,h}^w = \eta[J - n_e^w n_h^w - 4B_{e,h}^w n_{e,h}^w(1 - n_{e,h}^e) + 4C_{e,h}^w n_{e,h}^e]. \quad (3.5)$$

A dot denotes differentiation with respect to  $t = \tilde{t}/\tau_{ph}$ , where  $\tilde{t}$  is time and  $\tau_{ph}$  is the photon lifetime.  $\eta = \tau_{ph}/\tau$ , where  $\tau$  denotes the carrier recombination time. The subscripts  $e$  and  $h$  represent electron and hole respectively.  $\alpha$  is the usual GS phase-amplitude coupling. For simplicity here we take this to be a

constant although other models undertake a more rigorous approach [87]. Despite this simplification, this assumption is sufficient to reproduce the experimental findings.  $g_0^g$  and  $g_0^e$  are gain coefficients. Parameters that are controlled are  $\varepsilon$  the injection strength and  $\Delta \equiv \omega_i - \omega_g$  the detuning between the frequency of the injected light and that of the GS. The pump current is  $J$ . The  $B$  terms  $B_{e,h}$  and  $B_{e,h}^w$  are the capture rates to the GS and ES, respectively while the  $C$  terms are the escape rates and are linked to the capture rates via Kramers type relations, as described in [46]. The different spin degeneracies in the QD energy levels, Pauli blocking, and interstate captures and escapes are all included.

To obtain hysteresis, it was necessary to include phase-amplitude coupling between the ES carriers and the GS field, modelled by  $\beta$  in the above, see Figure 3.4. This is similar to the well-known GS only phase-amplitude coupling term  $\alpha$  arising from the dependence of semiconductor refractive index on carrier density, but it instead couples the GS field to the ES carriers. Such a phase-amplitude coupling arises fundamentally via the semiconductor

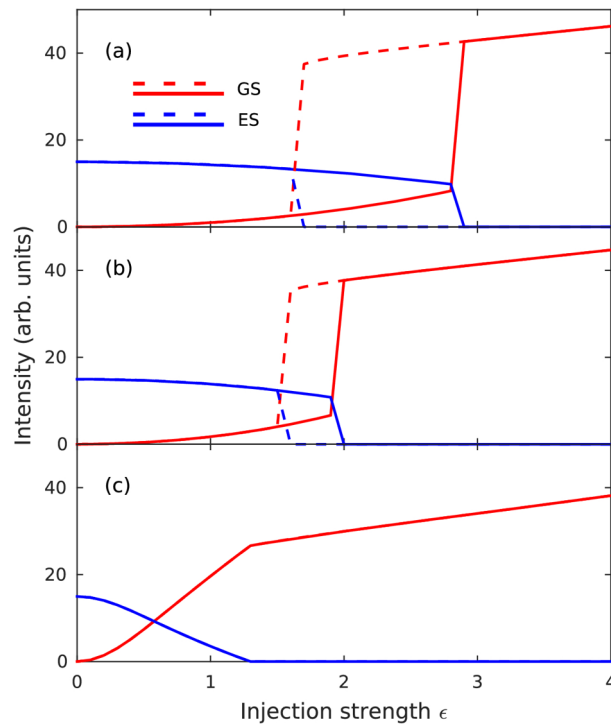


Figure 3.4: Hysteresis cycle analyses using Equations 6.1-3.5. The QD laser is biased to emit from the ES when free-running. The panels show the effect of changing  $\beta$ . (a)  $\beta = 3$ , (b)  $\beta = 2.5$ , and (c)  $\beta = 1$ . For  $\beta > 2$  the experimentally observed bistability is reproduced. Reprinted with permission from [132] © The Optical Society.

Bloch equations just as the usual  $\alpha$ . Thus, even when the ES is not lasing, the changing carrier density still has an impact on the refractive index and on the GS emission. (In this way, it also phenomenologically models some aspects of inhomogeneous broadening [46, 133]). In the absence of  $\beta$ , no hysteresis was obtained. For sufficiently high  $\beta (> 2)$  the hysteresis was found, matching the experiment very well.

In [134] Lüdge and co-authors considered a microscopic model for the system. All of their results are numerical but they consider carefully the experimental results of [46]. They have performed successful analyses for the GS only situation previously using such a model [67, 87, 135]. Rather than having an explicit  $\alpha$ , they extract the frequency shift of the GS field brought about by changes in the full carrier distribution, thereby going beyond the conventional approach where only the active carrier population is considered (and linear scaling assumed). Because they consider phase amplitude coupling of the GS and all the carriers, there are effective  $\alpha$  and  $\beta$  terms in this model, even when inhomogeneous broadening is omitted.

The experimental hysteresis results described above are reproduced successfully for control parameters where the free-running behaviour of the QD laser is emission from the ES only. As with the simpler model, the phase-amplitude coupling needs to be sufficiently strong to allow the hysteresis to arise and does not arise for very low values. By changing device and control parameters, they also examine if the bistability can arise for the other free-running operating possibilities: GS only and simultaneous GS and ES lasing. They show that the bistability can in fact also arise in these situations with sufficient parameter tuning. Further, it turns out that the largest bistable regions are found with the GS only parameters. This might seem counter intuitive at first, but is explained as follows. As is well-known for optical injection, the injected light can cause the intensity of the emitted light to exceed that of the free-running emission but can also cause it to drop below the free-running value. When it drops below the free-running emission, it frees up carriers. For conventional single mode lasers, there are typically no other states to utilise these excess carriers. In the QD case, this can allow the ES threshold to be reached and so emission from the ES can arise.

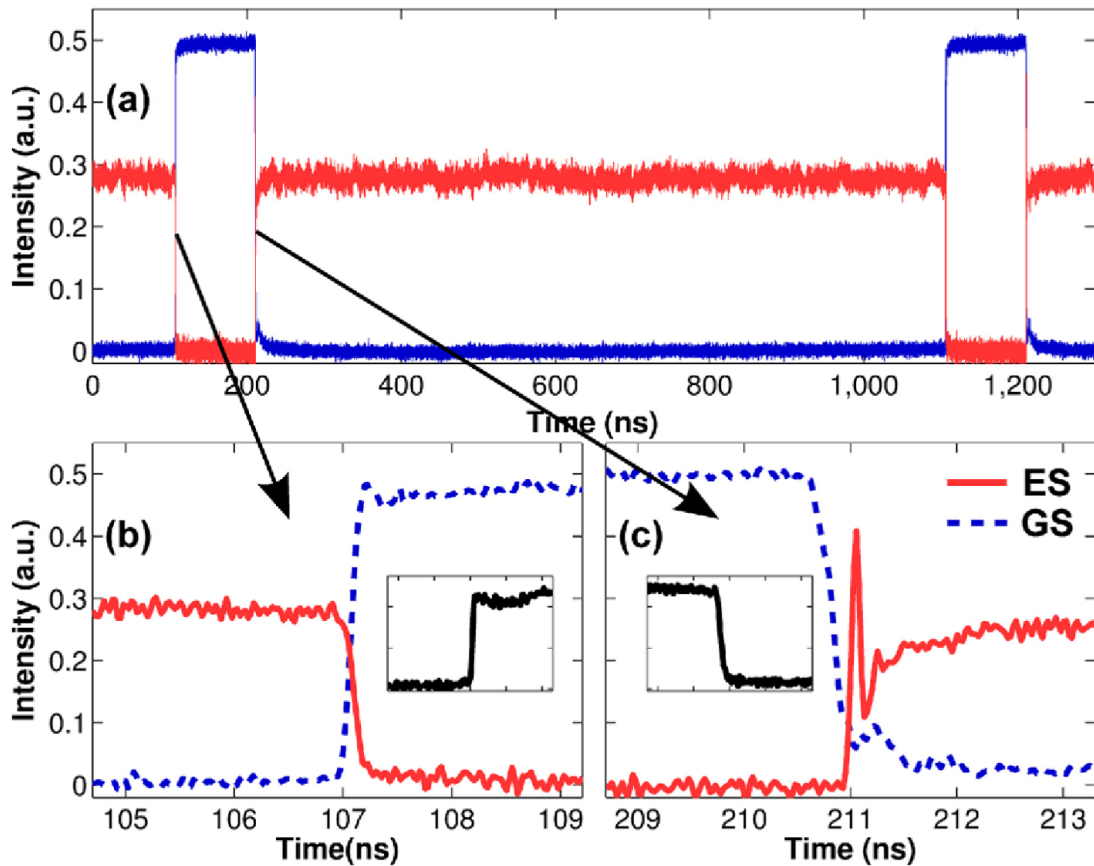


Figure 3.5: Experimental optical switching between a bistability. A Mach Zehnder Modulator is connected to a pulse generator that produces square pulses, the insets in (b) and (c) show the electrical signals. During a short square pulse GS light injects into the QD laser that is free running in the ES. The ES quickly turns off and the GS quickly turns on until the Mach Zehnder Modulator switches off the injected light again. Reprinted with permission from [132] © The Optical Society.

So far we have discussed only the steady state behaviour of the injection configuration. Dynamics are also of course important. One of the first experiments considering dynamics examined the details of the switching between the CW GS on solution induced by injection and the free-running ES on solution. This work thus bridges the gap between the steady state analyses above and the dynamics presented below. In [132], a similar device to that in [46] was studied experimentally. Again, it was electrically pumped so as to emit from the ES only when free running. Under continuous wave injection, the ES is fully suppressed and the device lases from the GS only. In order to go beyond steady state results, a Mach Zehnder modulator modulates the injected light to induce switching between the two lasing states. The rise time of the injected GS pulse is  $\sim 100$  ps. The switching time - the time it takes for the QD

laser to switch from ES to GS lasing - is less than 300 ps, Figure 3.5. There is a notable absence of RO oscillations, as is typical for QD devices due to their extremely high RO damping in the GS. The injected pulse has a fall time of approximately 300 ps. The time to switch back from GS to ES only lasing was less than 700 ps. In contrast to the GS case, the switching on of the ES was accompanied with a pronounced ring in the intensity suggesting that the RO damping in the ES is high, but not as high as in the GS case. These switches are extremely fast but likely significantly affected by somewhat slow switching pulses. With faster pulses, the state switching times would also be faster.

The optical switching technique was also investigated numerically using the microscopic model in [134]. The QD laser is operated so as to emit from the ES and a square GS pulse is injected, with rise and fall times of 100 ps. As the GS square is injected the ES turns off and the GS turns on as in the experiment. The timescales for the GS switch-on of about 300 ps and the GS switch-off of about 900 ps, again, similar to those reported in [132]. Short pulses can be used to dislodge the system from its current state. Beginning with a constant GS injection where the QD laser is phase locked and the ES emission is suppressed, a short negative pulse can induce a state switch, turning on the ES and significantly reducing the GS intensity. A short positive pulse can induce a switch back to ES off.

### 3.3 Boundary dynamics

In conventional optical injection configurations, dynamics are typically found and studied near locking/unlocking boundaries and the dynamical regimes obtained depend on the bifurcations leading to phase locking. The same is found in the dual state injection case for the most part.

#### 3.3.1 Intrinsic Q-switching

In [136], a pulsing regime close to the locking boundary for negative detuning was studied. A fixed injection strength was chosen and the frequency of the injected light was varied. Just outside the unlocking boundary, a periodic train of GS dropouts (with ringing minima) and corresponding sharp antiphase ES pulses of around 80 ps duration were observed, Figure 3.6.

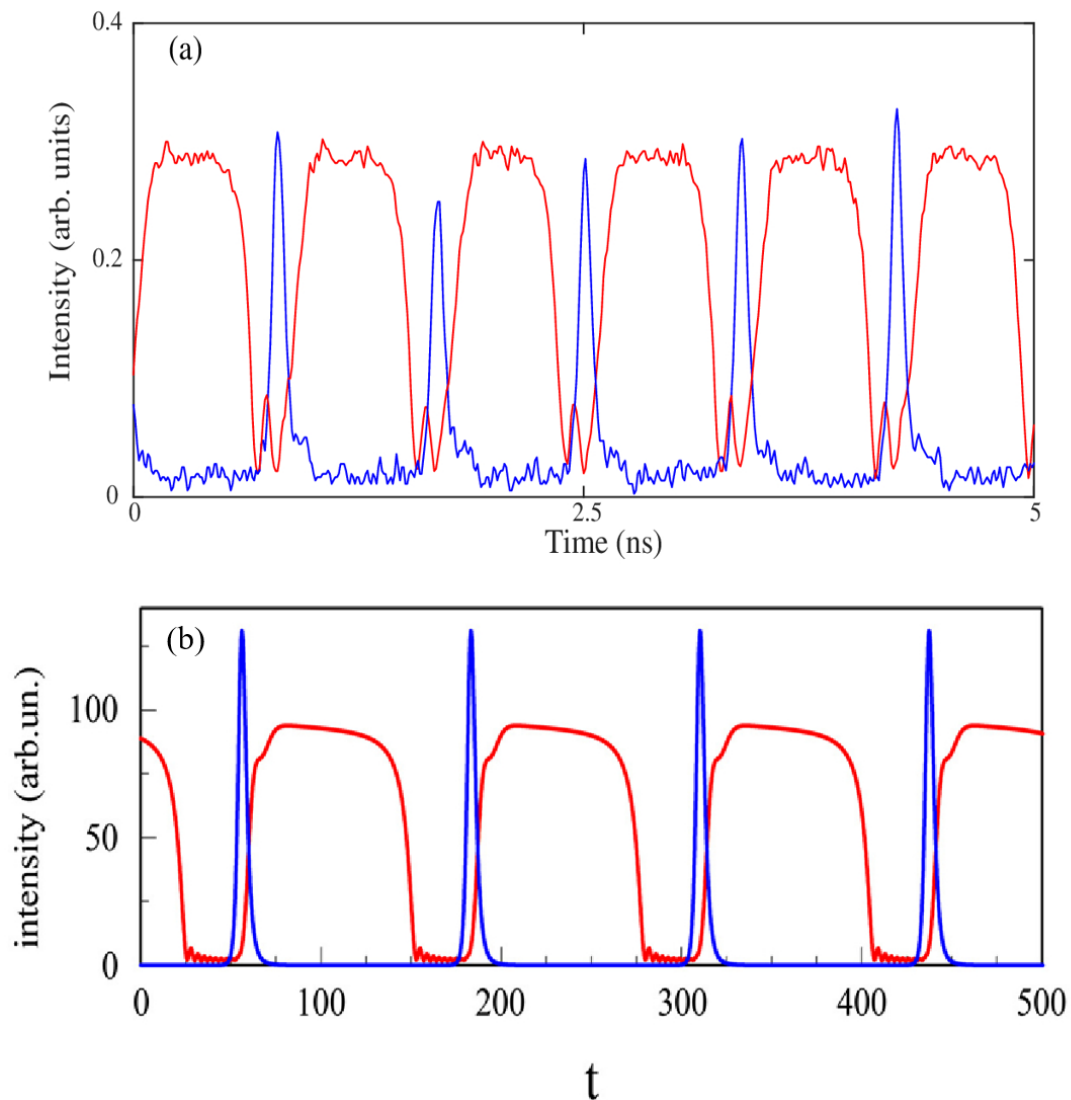


Figure 3.6: (a) Experimental and (b) numerical periodic pulse trains of GS dropouts accompanied by sharpened ES pulses. The small ringing oscillations at the minima of each GS dropout correspond to oscillations around a saddle focus. By experimentally varying the detuning the frequency of the train can be tuned between 0.3 and 1.3 GHz. In the bottom panel time is in units of photon lifetime. Figures reprinted with permission from [136] © The Optical Society.

The period of the trains can be tuned as shown in [136] and a tuning range of approximately 1 GHz (0.3 - 1.3 GHz) was demonstrated for the injection strength considered. This is much larger than the tuning ranges of passively Q switched semiconductor lasers.

Using the model (Equations 6.1-3.5), a bifurcation analysis of the stable solutions was undertaken. Figure 3.7 shows a mapping of the ES and GS intensities versus the detuning and the corresponding map for the phase of the

GS (originally shown in [136]). As suspected from the experiment, the boundary is defined by a saddle node infinite period (homoclinic) bifurcation (a SNIPER, also known as a saddle node on an invariant cycle - SNIC - bifurcation)  $LP$ , just as in the conventional injection case. Then, for injection strengths just below the position of  $LP$ , direct numerical integration yields periodic GS dropouts and ES pulses just as in the experiment, Figure 3.6. Similar to the experiment, the GS dropouts have multiple ringing oscillations.

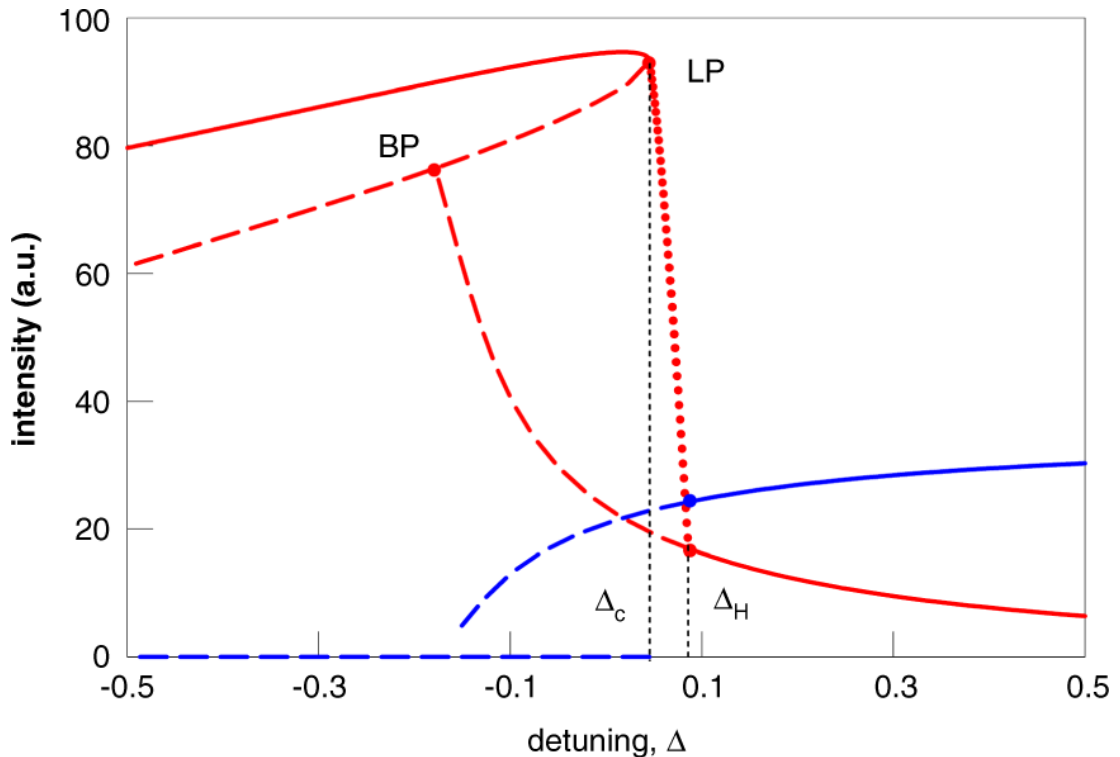


Figure 3.7: Bifurcation diagram of the GS (red) and ES (blue) intensities vs detuning using the rate equations from [136]. Continuous (dashed) lines correspond to stable (unstable) branches.  $LP$  denotes a homoclinic bifurcation point. Other models [134, 137] also produce a homoclinic bifurcation point at the negative detuning boundary. Reprinted with permission from [136] © The Optical Society. Note that the sign of the detuning in this figure is the opposite of that used in the rate equations presented in this Chapter .

The physical explanation of the phenomenon is somewhat analogous to the phenomenon of Q switching in lasers with saturable absorbers. After unlocking, the GS intensity drops, and its gain saturates due to Pauli blocking. This saturation of the GS allows carriers to build up in the ES. It acts as a gate allowing the ES carrier population to increase until it eventually overcomes the device losses and yields another sharp ES pulse. The tuning ranges in the injection experiment however, go well beyond those achieved with Q switching

since in that case, the pulse rate is set by the pump and absorber time scales. This intrinsic Q switching phenomenon is unique to QD lasers, arising directly from the carrier cascade pathway described above without any requirement for multisection fabrication.

In [137] Mesaritakis and co-workers considered a numerical analysis of a single section QD laser, with a view to integrate and fire functionality. They utilise a multi-population model, with electron-hole dynamics describing waveband transitions from both the ground and excited energy state. The electric fields of both the GS and ES are found and the carriers in the bulk semiconductor layer are included. They focus on the behaviour near the SNIPER (SNIC) bifurcation as also previously reported in [134, 136]. The resulting pulse/dropout trains are very reminiscent of those described above, first reported in [136]. The authors perform a numerical analysis of the effect of periodic perturbations of the injection strength on ES pulse and GS dropout generation and map the effect of perturbation strength and period. The underlying physics is very reminiscent of the work of Hurtado and Javaloyes in [36] where temporary reductions in the injection strength produced periodic pulse trains. Good control of the repetition rate is suggested by the numerics. That this should be so is also strongly suggested by our demonstration of repetition rate tuning in [136] where rather than varying the strength of the primary laser, we change its frequency.

In [125], the same group has also analysed a two section mode locked QD laser injected by an identical device. Both excitatory and inhibitory pulses can be excited depending on the injected signal and the control parameters of the neuron device (the injected laser). They show that they can achieve either excitation or inhibition simply by changing the reverse bias of the absorber section.

### 3.3.2 Two-colour bursting

In the GS only system, at high injection strengths, an optothermal coupling induced square wave excitability was reported in Chapter 2 and the controlled triggering of these pulses was also demonstrated. The phenomenon arises from the optothermal destruction of a phase-locked bistability. As shown in Chapter 2 there are two potential routes to the square waves, both via a new Hopf bifurcation; one leads to a canard explosion and the other to a subcritical Hopf induced bistability. There is a similar dynamic regime in the dual state

configuration when the injection strength is increased. As shown in [78], an optothermally induced periodic square wave switching on microsecond time scales, appears between two states, associated with the two states from the dual state bistability described earlier. The periodic trace switches between a quiescent upper level, where the GS emits a constant intensity and the ES is off and a lower level distinguished by complex oscillations, Figure 3.8. In fact, there are multiple distinct regions within the lower level. The initial GS dropout and ES turn on is characterised by a few damped oscillations in both states followed by a prolonged almost flat region of low GS intensity and higher ES intensity. After a certain critical time, ever growing oscillations appear in both outputs. These oscillations last for a significant duration (in [78] a bursting duration of  $1.5 \mu\text{s}$  was shown). Following the oscillations the GS returns to its initial quiescent state. The fast-slow time scales and the alternation between large and small amplitude oscillations suggest these are mixed mode oscillations (MMOs) [138]. In [78] the rate equation model is supplemented with an optothermal coupling that allows the detuning to vary with the total intensity. This reproduces the dynamics perfectly and also explains the bursting cycle. The entire cycle is manifested from a series of slow passages through bifurcation points. The initial dropout from the quiescent phase arises from a slow passage through a limit point. The transit from

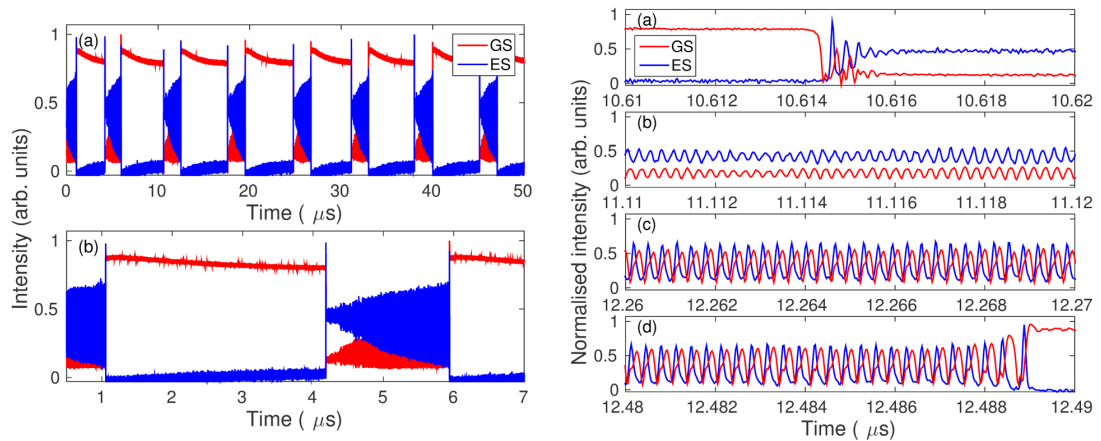


Figure 3.8: Left panel: Periodic switching between a quiet state and a bursting state. During the quiet state the GS is the dominant frequency and during the bursting state the ES is dominant. Right Panel: A zoom of an individual bursting state. The intensity of both states oscillate in antiphase, the amplitude and the frequency of the oscillations continuously grow until there is a state switch back to the quiet state. An optothermal effect is responsible for an intrinsic detuning sweep and slow passage through bifurcation points. Figures reprinted from [78].

constant intensities to the evolving oscillations arises via a slow passage through a Hopf bifurcation. Finally, the return to the quiescent phase arises via a slow passage through a limit point of limit cycles.

Over the course of a cycle, effects such as changing carrier recombination rates result in temperature changes in the device, in turn changing the frequency of the device and a resulting deterministic sweep of the detuning. This is similar to the Type II excitability reported in Chapter 2. The period and intensity of the oscillations match perfectly those of the first branch of the snaking branch of periodic solutions, as seen in the right hand panel of Figure 3.9. The duration of the bursting phase can be from times of approximately  $1 \mu\text{s}$  to as long as several 10s of microseconds, via adjustments of the injection strength and the detuning. This could provide useful applications in both artificial neural networks and in optical communications since bursts can contain more information than single pulses.

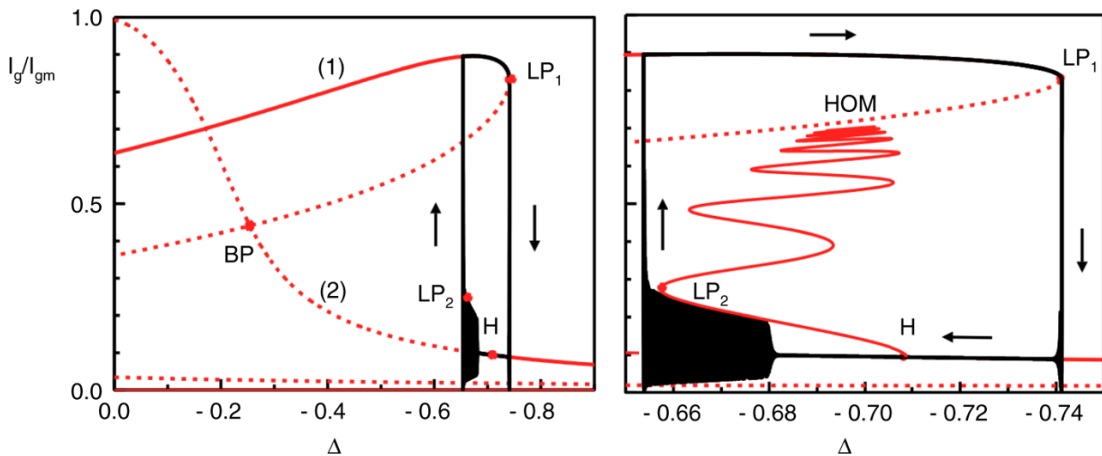


Figure 3.9: Bifurcation diagrams showing the intensity of the GS vs detuning. Stable and unstable branches are shown by full and dotted lines, respectively. An optothermal effect is included and the black bursting cycle is reproduced. The points LP1 and H mark a limit point of steady states and a Hopf bifurcation point, respectively. Right: A branch of periodic solutions represented by the maximum intensity is emerging from H and snakes with various stability changes until it reaches the unstable steady state branch at a homoclinic bifurcation point (HOM). The figure shows that the bursting oscillations follow a stable branch of periodic solutions until it reaches a limit-point of limit-cycles (LP2). Reprinted figure from [78]. Note that the sign of the detuning in this figure is the opposite to that used in the rate equations presented in this Chapter.

As with many of the phenomena described here, this is again a result that has its basis the existence of an inherent bistability. In this case, the bistability is broken by the thermal coupling yielding the fast-slow MMO regime. MMOs are

of course a generalised canard phenomenon [138] and so this is yet another instance of the dual state behaviour mimicking the single state behaviour but with added richness in the structure.

### 3.4 Where is the chaos?

With all of the dynamic scenarios described above, one feature is conspicuous by its absence: chaos. Chaotic operation is typically one of the standout features of optically injected semiconductor lasers. A conventional semiconductor laser can be well described using just two equations. The inclusion of optical injection increases the dimensionality of the system and allows the generation of chaos [140]. With conventional semiconductor material, prominent areas of chaos are found, in large part due to the weak damping of the ROs. However, even with highly damped QD lasers, chaos is found under injection albeit with a smaller footprint in the mapping [69, 134]. When the laser is biased so that the free-running operation is from the ES only, chaos does not seem to appear in the injection map at all, Figure 3.10, or if it does, it does so in extremely small regions. The system has a high dimensionality, higher than the GS only system where chaos does arise.

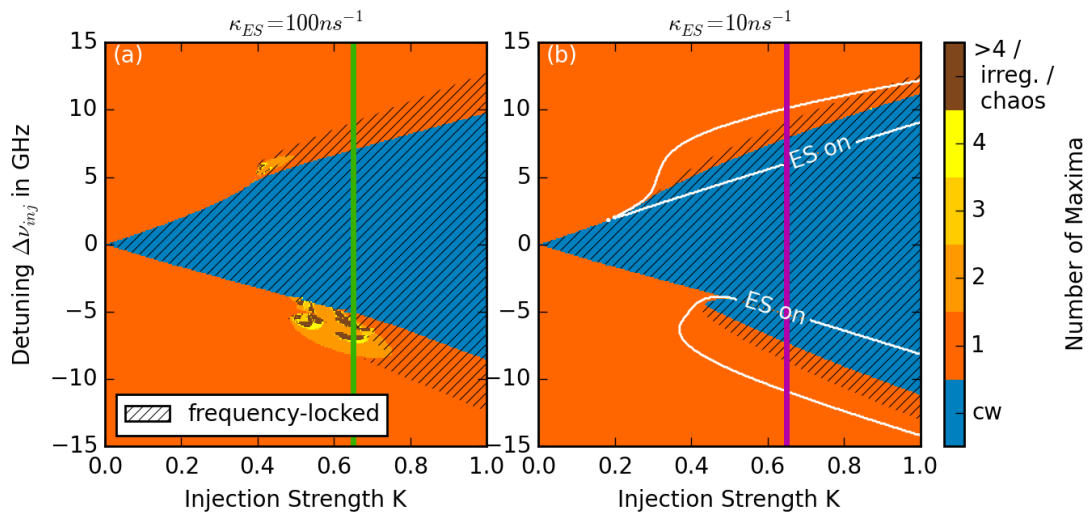


Figure 3.10: Maps comparing a single-colour laser (a) and a two-state laser (b) under optical injection using the microscopic model. There are regions of chaos near the unlocking boundaries of the single-colour laser map. However there is no chaos or even multi-frequency dynamics observed in the map for the two-state laser. Reprinted with permission from [139], S. Meinecke, B. Lingnau and K. Lüdge, in *Physics and Simulation of Optoelectronic Devices XXV*, Vol. 10098, International Society for Optics and Photonics (SPIE, 2017).

However, as shown in [134], and in agreement with the predictions of the rate equation model (Equations 6.1-3.5), chaos is simply not a feature of the dual state injection system. Rather, regions where chaos would appear in the single state system become dual emission states. This is borne out by experiment.

Of course, the absence of chaos does not equate to an absence of complexity. There is ample complexity in the interplay between the states, even in the free-running case where even the quenching of the GS due to ES lasing is a very involved phenomenon and the optothermal bursting cycle described above is incredibly rich in structure with MMOs, homoclinic snaking and slow passage phenomena. The stability and wide range of dynamics of optically injected dual state lasers make them the ideal testbed for excitability and artificial photonic neurons.

# Chapter 4

## Locking Maps

An important figure for understanding the optically injected laser system is the two parameter stability mapping of the dynamics found by examining the output of the injected laser under different combinations of the injection strength and the detuning (the frequency of the primary laser minus that of the secondary). We experimentally and theoretically generate this map for an optically injected QD laser biased to emit from the ES and injected near the GS.

Regions of different dynamical behaviours, including phase-locking, excitability and periodic regimes are identified. At the negatively detuned locking boundary, GS dropouts and ES pulses are observed near a hysteresis cycle for low injection strengths. Higher injection strengths reveal square wave trains where the intensities of the GS and ES squares operate in antiphase. A narrow region of slow oscillations is observed at the positively detuned boundary. An optothermal effect similar to the one implemented in Chapter 2 is included in the simulations to recreate the square wave train on the negatively detuned locking boundary. However, this then creates a new bistability at the positively detuned boundary. A second optothermal effect associated with the intensity of light is also included resulting in slow oscillations matching the experiment very well.

I was responsible for the entirety of the experimental work and took part in discussions regarding the numerical work, which was primarily carried out by Dr. Benjamin Lingnau. This chapter is based on the following publication:

M Dillane, B Lingnau, EA Viktorov and B Kelleher, "Mapping the Stability and Dynamics of Optically Injected Dual State Quantum Dot Lasers", *Photonics* **9** (2), 101 (2021).

## 4.1 Introduction

Stability maps are an effective tool used to show regions of excitability, bistability, oscillatory behaviour, chaos and phase locking. In [141] an automated, efficient and quick technique for creating an experimental map was presented, in that case for a two frequency quantum well (QW) based device but applicable to any device type. The injection power is swept up and down at fixed values of the detuning. The output power is measured at regular intervals and then analysed by measuring the mean and the standard deviation allowing for easy discrimination of different regions in the parameter space and also allowing for identification of hysteretic regions. On the theory side, rate equation modelling of the system has proved to be extremely accurate with quantitative agreement between the maps produced experimentally and those arising from the model. A particularly striking example of this agreement is shown in [62] for a single frequency QW based laser. In this example the map took the form of a two parameter bifurcation diagram showing where qualitative changes in the laser's behaviour occur and identifying the associated bifurcations via the continuation software *AUTO*. Analytic studies can also be performed such as those in [69, 71, 88, 142] and in particular, analytic expressions for the two most important bifurcations for the generation of phase locking, namely, the saddle node bifurcation, and the Hopf bifurcation. In [65, 143, 144] numerical analyses of the Lyapunov exponents were used to produce the stability maps. One can also perform numerical studies analogous to the experimental technique to produce the mapping as also shown in [141].

As mentioned in Chapter 1, InAs/GaAs based quantum dot (QD) lasers have several characteristics not found with conventional QW based semiconductor lasers. One such feature is their very high damping of the relaxation oscillations (ROs), endowing them with very high levels of stability when undergoing external optical feedback [67, 145, 146]. This also leads to unique features when optically injected. In [69, 71] the stability map for a single mode QD laser biased to emit from the GS only was analysed both experimentally and analytically with excellent qualitative agreement between the experimental and analytical figures. The striking similarity to the Class A stability diagram was also discussed [88]. Microscopic rate equation analysis has also been performed, again agreeing well with experiment [87]. This model allows for more accurate analyses of phase-amplitude coupling going

beyond the simplified constant  $\alpha$  factor typically assumed. In [147] excellent agreement between experimentally and numerically generated maps for multimode optically injected QD lasers was demonstrated with the importance of including spatial hole-burning emphasised. Bidirectionally coupled QD lasers also display a greatly increased stability relative to their QW counterparts, again due to the high damping of the ROs [70, 148]. The increased stability of QD lasers due to the high relaxation oscillation damping leads to a particularly notable feature in the modelling of optically injected QD lasers, namely a region of phase-locked bistability [71]. However, in Chapter 2 it was shown that this region is not found experimentally and instead an optothermal coupling in the system breaks the bistability and induces a periodic square wave phenomenon. Physically this can be understood as a thermally induced slow sweep of the refractive index of the cavity and thus the sweep of the frequency of light the cavity supports. This sweep transforms the hysteresis cycle of the bistability to a deterministic periodic cycle. The rate equation model for the system was easily extended to take this coupling into account and then returns excellent agreement between experiment and theory. Such a coupling has also been discussed and observed in free running semiconductor lasers [77, 79, 80, 82], in optically injected semiconductor optical amplifiers [37] and optically injected photonic crystal lasers [81].

Another characteristic feature of InAs/GaAs QD lasers is their ability to lase from multiple different energy levels [40, 48]. In particular they typically display ground state (GS) emission close to 1300 nm and first excited state (ES) emission at approximately 1215 nm. Each of these states has its own threshold and which state lases depends on many factors including the optical losses and the pump current. A typical evolution as the pump current is described as follows. First the GS threshold is reached at which GS only light is emitted. This is followed by the ES threshold where the GS and ES emit simultaneously. Further increasing the pump current typically results in quenching of the GS emission after which only the ES lases. However, in other cases - such as with short device lengths - there may not be sufficient gain available in the GS to overcome the losses. Thus higher pump current is required, but this also populates the ES. If the ES becomes sufficiently populated before the GS can overcome the losses it can lase and there may never be emission from the GS at any pump current. This is the case for the device investigated in this chapter.

This multi-state structure allows for unique dual state injection scenarios. In

Chapter 3, particular attention was paid to devices (secondary laser) biased to emit from the ES only and injected into the GS. It has been shown that, the ES can be made to turn off and the GS turn on, with the output phase locked to the injecting laser (primary laser)[46]. The experiments discussed in Chapter 3 inject light into QD lasers that have the ability to emit from the GS while free-running. Here we show that while the short QD laser cannot ever lase from the GS while free running, it can be forced to emit from the GS under optical injection and similar dynamics are observed near the unlocking boundary.

One very interesting feature discussed in Chapter 3 from [134] is the absence of chaos in the dual state system, a feature confirmed experimentally in the sense that chaos has not been reported for the system. This is further confirmed in the work presented here. Instead, dual state interactions arise in regions where chaos arises in the single state system. We present a comprehensive combined experimental and theoretical analysis of the stability map for an optically injected dual state QD device. As well as previously discovered dynamical regions, we uncover new features such as slow oscillations with a period of 10s of milliseconds near the positive unlocking boundary. It also turns out that optothermal effects play an important role in the dynamics observed.

## 4.2 Experiment

The device under investigation is a 300  $\mu\text{m}$  QD laser composed of InAs quantum dots on a GaAs substrate. It had the same epitaxial structure as the device used in Chapter 2, but this device is shorter. Slots have also been etched into the waveguide in order to promote one GS longitudinal mode and suppress all other modes within the gain spectrum. However, it never lases from the GS and could only lase from the ES. It is pumped at 75 mA (1.3 times threshold at 20.5 °C). A schematic of the experimental setup is shown in Figure 4.1. The device is mounted and placed on an xyz stage. Light from the laser is coupled into a single mode lensed fiber. A unidirectional optical injection configuration is set up. The primary laser (PL) is a commercial tunable laser source (TLS) with minimum step size of 0.1 pm (0.0178 GHz). Light from the PL is injected into the secondary laser (SL) via a circulator. A polarisation controller is used to set the polarisation of the injected light and maximise coupling. The light from the SL goes through a circulator and is directed to a

filter, where the ES light is separated from the GS light. ES emission is sent straight to a 12 GHz detector while the GS emission goes to a 90/10 splitter. 10% is sent to a power meter to monitor alignment and the remaining goes into another 12 GHz detector. All detectors are connected to an oscilloscope.

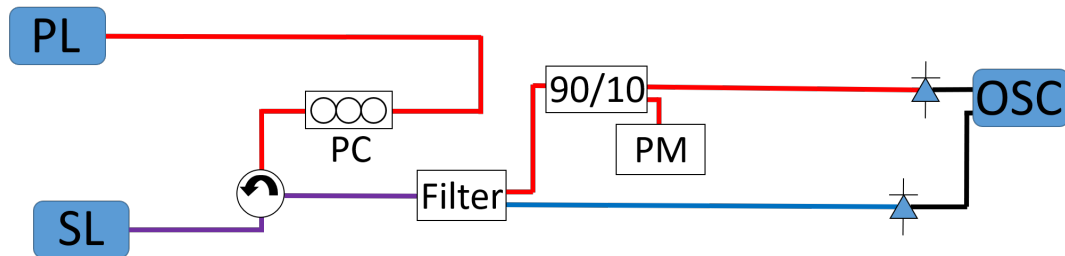


Figure 4.1: Schematic representing the experimental set up. A unidirectional injection experiment similar to the one shown in Figure 2.12 is setup, where the secondary laser (SL) is a QD laser and the primary laser (PL) is a tunable laser source (TLS). The main difference is that a filter is added to separate the GS emission from the ES emission. Light from the (PL) is sent to a circulator and is then injected into a QD laser. A polarisation controller (PC) is used to maximise coupling. The light emitted from the SL is sent into the circulator and then to a filter where the ES and GS light are separated. The ES light is sent directly to a 12 GHz detector. The GS light goes into a 90/10 splitter, 10% is sent to a power meter (PM) and the remain goes to a detector connected to an oscilloscope. The red lines represent light at approximately 1300 nm close to the GS emission, the blue is ES only and the purple is both GS and ES. The black are high speed electrical cables.

Typically injection strength is given as the ratio of the magnitude of the electric field of injected light to the magnitude of the electric field of the free running laser, where the electric field is the square root of the intensity. But here the GS is never lasing. So instead, the injecting strength, is defined as the square root of the power reaching the facet of the laser normalised to the maximum power reaching the facet,  $K = \sqrt{\frac{P}{P_{max}}}$ . Since the GS mode being injected is always subthreshold the detuning is then also difficult to define. We thus pragmatically define zero detuning to be where the ES is at a minimum power after injection.

The experimental technique to build the stability maps is similar to that of [141] but the injection strength is constant when a measurement is taken. We record and analyse 20  $\mu\text{s}$  long time series of both the GS and ES intensities at regular intervals. Initially the wavelength of the TLS is set and the power of injected light reaching the facet of the secondary laser from the TLS is swept

from 0.25 mW to 2.47 mW in 120 equal steps of  $K$ . Then a down sweep is performed where the power reaching the facet is swept from 2.47 mW to 0.25 mW with the same 120 steps. The wavelength is then decreased in steps of 0.2 pm (0.0356 GHz) and the power sweeps are repeated.

### 4.2.1 Stability maps

The average power from each state is plotted in Figure 4.2. The variance of the ES output is also calculated and plotted. The variance plots, (c) and (f), are particularly useful for immediate identification of the constant output regions (dark blue) and areas where the ES intensity is oscillating (green/yellow). The upper panels in all stability map figures in this section show the results generated when the injection sweep is upwards (from low strengths to high strengths) and the lower panels show the corresponding maps for the downward sweep (from high strengths to low strengths).

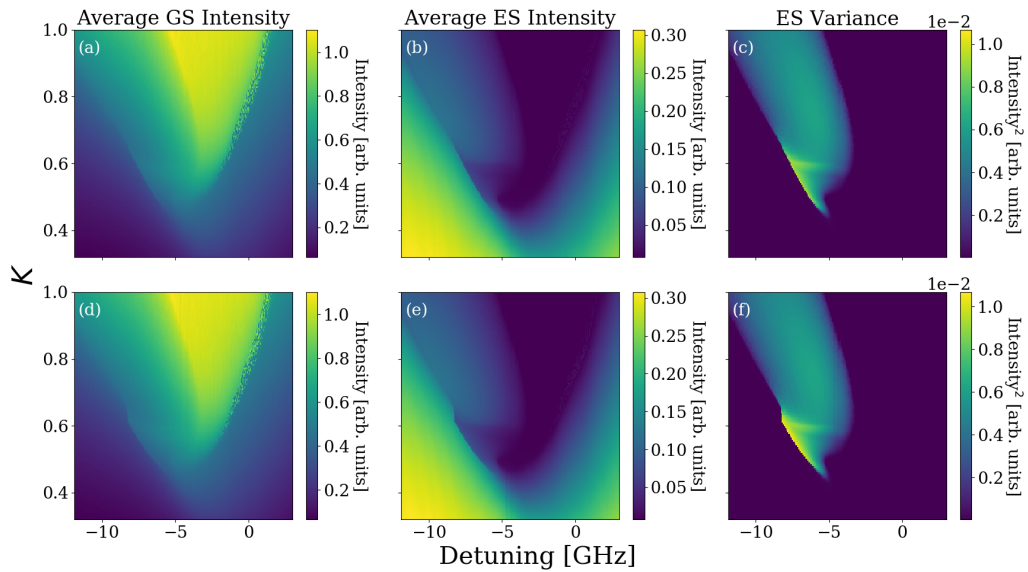


Figure 4.2: Experimental stability map. The top panels show results when the injection strength,  $K$ , is swept from low to high. The bottom panels show the results when injection strength is swept from high to low. The average ES and GS intensities are calculated for 20  $\mu$ s long measurements. The phase locked region is identified as the bright yellow/cyan area in (a) and (c), where the GS has high output intensity. This corresponds to a quenched ES, shown as dark blue in (b) and (e). The ES variance is shown in (c) and (f), green is where oscillatory behaviour is observed and dark blue corresponds to constant output. The speckled area on the positively detuned boundary of (a) and (c) is related to very slow oscillations. A more detailed stability map of this boundary is shown in Figure 4.7.

In Figure 4.2 (a) the bright yellow region in the centre is the phase-locked region. Here only the GS is lasing and the ES is completely quenched as indicated by the corresponding dark blue region in Figure 4.2 (b) and the zero variance in Figure 4.2 (c). To the negative detuning side of the phase locked region there is a broad area of dynamics as indicated by the green and yellow region in the variance in Figure 4.2 (c). On the positive boundary of the phase locked region there is a region of very slowly varying GS power, indicated by the non-smooth colouring/speckled pixels in Figure 4.2 (a). We defer discussion of this for now and return to it below. To the positive side of this slowly varying speckled region, the device behaves as a dual state emitter, with both states emitting constant intensities. As the detuning is increased there is a smooth, continuous evolution of both, with the GS power decreasing and the ES power increasing. The same dual state behaviour is mirrored on the negative detuning region to the left of the dynamic, oscillatory regime. We interpret this as follows; in the GS only system (or indeed any conventional optical injection system) there are unlocking boundaries after which there are only oscillating unlocked solutions. In the limit of large detuning the oscillations can be physically interpreted as a beating between the injected light and the emission of the secondary laser. However, in our dual state system there is no free-running GS. Thus, this beating cannot arise. The output of the QD laser can then be thought of as a mixture of regenerated injected light and ES emission from the secondary laser. We distinguish between the phase-locked output (dark blue) in Figure 4.2 (b), where the ES is completely off, and the regenerated injected light output of somewhat large detunings where there is dual state emission. For the purposes of identification we refer to these as the phase locked region and the regenerated injected light region for the remainder of this chapter.

Figure 4.3 shows just some of the traces taken during a single up-sweep of the injection strength  $K$  for a fixed detuning, -6.9 GHz. The coloured labels correspond to the coloured dots in Figure 4.4, which mark their location on the maps. The maps in Figure 4.4 are the same as in Figure 4.2 with some additional markings to make our discussion clearer. Figure 4.3 (a) shows a periodic train of GS dropouts and the corresponding ES pulses as reported in [136]. As the injection strength is increased these periodic trains disappear and various bursting regions are observed in (b), (c) and (d). In Figure 4.3 (b) there is a switching between a quiescent output where the GS is on and the ES is off, and an active output with oscillations in both states (similar to the

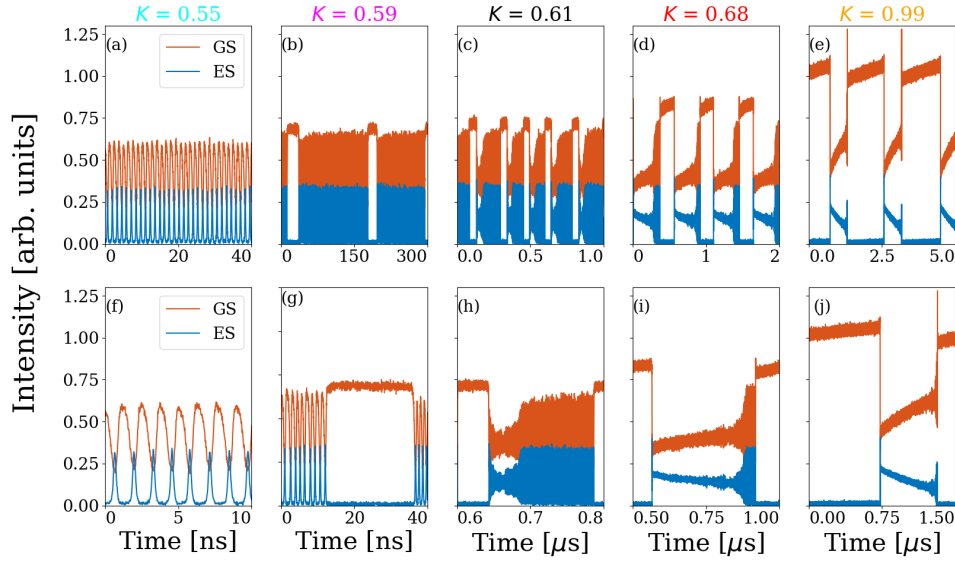


Figure 4.3: Qualitative behaviours observed for various injection strengths during an upswep, the detuning remains fixed at  $-6.9$  GHz. The lower panels zoom into the dynamics shown in the corresponding upper panels. The title on top of the subplots show the injection strength value. The colour of the font corresponds to the colour of dots in Figure 4.4. The dots mark the location on the map where the timetraces were recorded. (a) shows a periodic cycle where the GS and ES intensities oscillate in antiphase, with a period in the order of a nanosecond. (b) there is a quiet state between long periods of oscillations. (c) a periodic square wave emerges with large amplitude oscillations at the start and end of bursting state. (d) oscillations at the beginning of the bursting state become damped, but growing amplitude oscillations still appear before there is a switch back to the quiet state. (e) all fast oscillations are strongly damped and a square wave train is observed.

dropouts and pulses of (a)). A further increase where  $K = 0.61$  leads to a different bursting dynamic as shown in Figure 4.3 (c). In this region the switching is between a quiescent phase with the GS on and the ES off, and an evolving bursting phase. The switch to the bursting phase is via an initial period of decreasing amplitude oscillations, followed by a long series of growing oscillations before a switch back to the quiescent phase. In Figure 4.3 (d)  $K = 0.68$  and qualitatively the trace is similar to that in (c) but here the oscillations following the quiescent phase are quickly damped out. Such evolving bursts were previously reported in [78] and shown to arise via an optothermal coupling. The evolution of the bursting state arises via a deterministic thermal sweep of the detuning leading to slow passages through several bifurcations. Finally when  $K$  is increased to 0.99, a periodic square

wave train is observed. Again we interpret this as resulting from the aforementioned optothermal coupling and such a feature has previously been observed in the GS only system seen in Chapter 2.

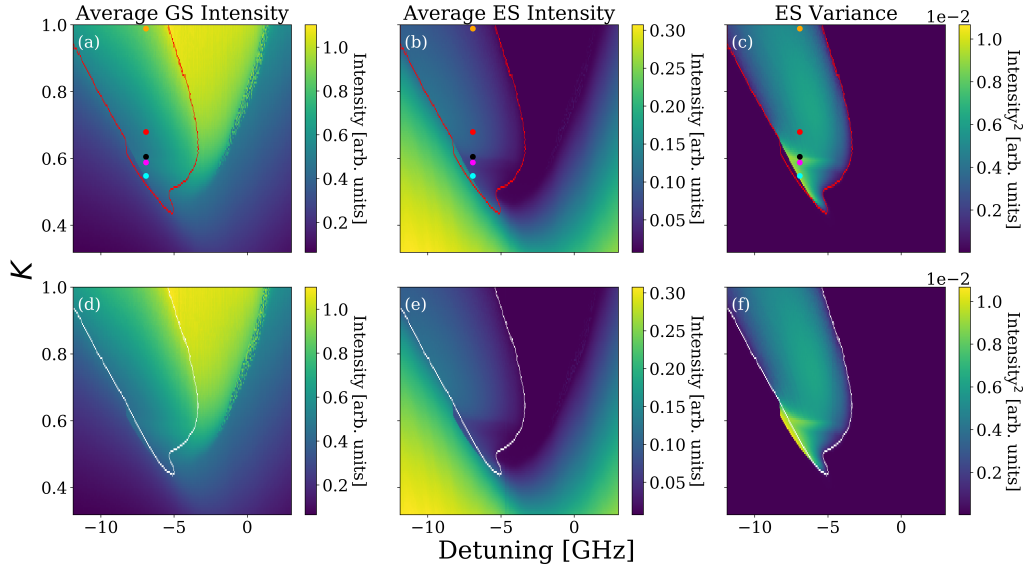


Figure 4.4: The same experimental stability maps of average GS and ES intensities, and ES variance, previously shown in Figure 4.2. Here markings have been added to make our discussion easier. The injection strength is swept up in (a)-(c) and down in (d)-(f). The coloured dots correspond to the timetraces in Figure 4.3. For a more obvious identification of a hysteresis the boundary of oscillating dynamics observed in the downsweep is plotted on top of the upsweep data as a red line. Similarly the boundary of oscillating dynamics seen in the upsweep is plotted as a white line on top of the down sweep map. Hysteresis is evident in (f) where the region of oscillating dynamics extends beyond the white line, which marks the boundary observed (c).

### 4.2.2 Bistability

In order to identify regions of bistability in the maps, we can compare the upsweep and downsweep figures in Figure 4.4. The upper panel shows the upsweep with a red line superimposed marking the boundaries from the downsweep. The lower panel shows the downsweep with a white line superimposed, corresponding to the boundaries of oscillatory behaviour from the upsweep. The boundaries are largely the same, but reveal bistabilities where they differ. The left hand side of the phase-locked region (the red/white line in the centre of each figure) is the same in both cases. At negative detunings and for  $K > 0.6$ , the two directions match at the boundary between

the dynamical region and the regeneration region. However, at injection strengths from approximately  $K = 0.5$  to  $K = 0.65$  and between detunings of approximately  $-8.5$  GHz and  $-6$  GHz, there is a clear region of hysteresis. This stands out clearly in all three plots, but most obviously in Figure 4.4 (f).

Figure 4.5 and Figure 4.6 compare the timetraces from an upswing and a downswing respectively. The sweeps move across the widest part of hysteresis region at  $-8.2$  GHz, just to the right of the almost vertical part of the red line shown in the upper panels of Figure 4.4. The subplots in Figure 4.5 show the output of the QD laser for different injection strengths during an upswing. Subplot (a) was recorded first, then (b) and so on in alphabetical order to (l). Figure 4.6 shows subplots during a downswing. Here, subplot (l) was recorded first, then (k), then (j) and so on in reverse alphabetical order to the final subplot, (a). It is important to note that the injection strengths are plotted in the same grid position of both figures for easy comparison. So in both cases subplot (b) shows  $K=0.611$ , but it is easy to identify that the dynamics are different.

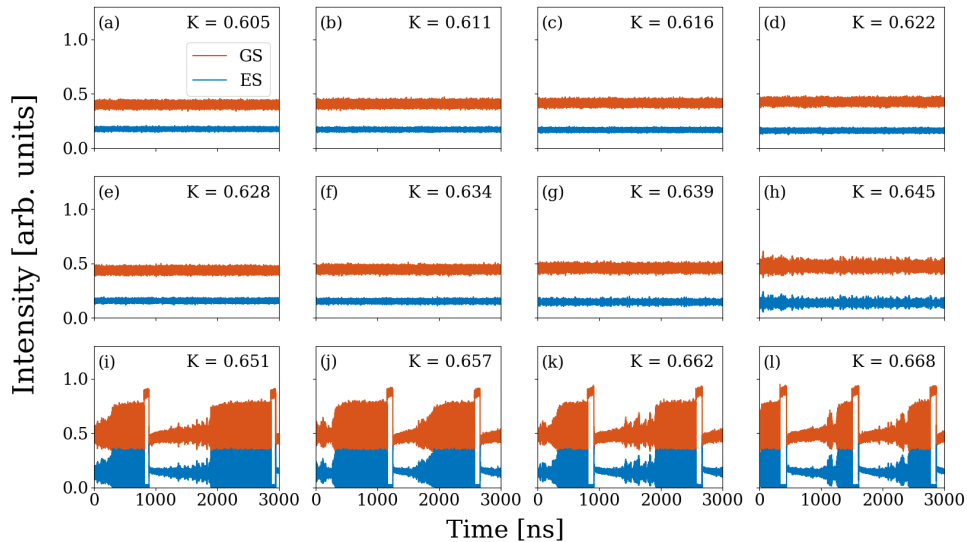


Figure 4.5: Timetraces from an upswing in the region of hysteresis at  $-8.2$  GHz detuning. The corresponding downswing timetraces are shown in Figure 4.6. Initially the QD laser is unlocked and as injection strength is increased the intensity of the regenerated GS slowly increases and the ES intensity decreases. Small oscillations are visible in the GS intensity at  $K=0.645$  before a sudden change in behaviour. When  $K > 0.651$  short quiet regions appear between long bursting states. As  $K$  is increased the length of time spent in the bursting state decreases.

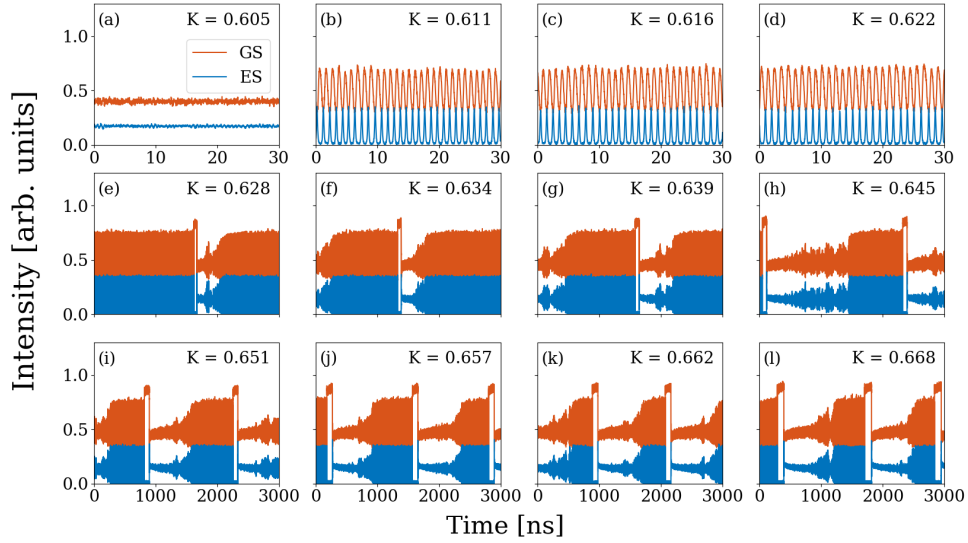


Figure 4.6: Timetraces from a downsweep in the region of hysteresis at -8.2 GHz detuning. These subfigures correspond to the same  $K$  levels in Figure 4.5 but the direction of the injection strength sweep starts at (l) and then moves in reverse. In the bottom row the duration of the quiet and bursting states is very similar to that of Figure 4.5. But as  $K$  is decreased below 0.645 the QD laser continues to operate in an oscillatory regime, whereas in Figure 4.5 continuous dual state emission is observed. The time between quiet states becomes larger as  $K$  is decreased. The top line then zooms in on the traces to show the fast oscillations that become the dominant behaviour. When  $K = 0.611$  no quiet state is detected over the course of a 20  $\mu\text{s}$  time window on the oscilloscope. When injection strength is decreased below 0.605 the QD laser suddenly moves to a dual state continuous emission regime.

In the case of the upsweep in Figure 4.5 ((a)-(g)), the SL is unlocked where dual state emission is observed with the GS light being regenerated. As  $K$  is increased to 0.645, Figure 4.5(h), the GS appears to oscillate with a very small amplitude before the onset of mixed mode oscillations (MMOs) at  $K = 0.651$ , Figure 4.5(i). The lifetime of the bursting state decreases as the injection strength is increased.

Similar MMOs are seen for injection strengths during the downsweep from  $K=1$  until  $K=0.645$ , then the presence of hysteresis can be seen. As  $K$  is further decreased below 0.645 the laser doesn't move to a continuous wave dual state emission output. Instead the lifetime of the bursting state continues to increase and switches to the quiet state become more rare. Eventually a train of GS dropouts with ES pulses is observed, Figure 4.6(b). We are not able to confirm that the quiet states do not occur for  $K = 0.611$  because our

measurement was limited to a 20  $\mu\text{s}$  timetrace recorded on the oscilloscope. Since there are fewer quiet states, the overall variance is large and is therefore represented as bright yellow in the variance map, Figure 4.2(f). Clearly the yellow region extends beyond the white line marking the upswing dynamical boundary, highlighting the hysteresis cycle. In Figure 4.6 (a) for  $K=0.605$ , the oscillations disappear, where the same continuous wave dual state emission as from the upswing in Figure 4.5 ((a)-(g)) is observed. Thus, in this region there is a bistability between the constant dual state emission (constant ES and regenerated injected light) and dynamic, pulsing behaviour with MMOs.

### 4.2.3 Slow Oscillations

As mentioned above, on the positive detuning side close to the transition between the phase-locked and regeneration regions, there is a region of dynamics indicated by a speckled, non-uniform colour along the diagonal boundary in Figure 4.2 (a) and (d). In fact, there are essentially two colours, indicating that there are two distinct average GS intensities. The binomial nature of the colouring suggests a slow dynamic of which we only sample a short, nearly constant part within the 20  $\mu\text{s}$  measurement interval. The sampling window is increased to 1 second and new maps are created, Figure 4.7. We note that there is also a very narrow regions of hysteresis on both the left and right of this region.

Figure 4.8 shows timetraces from an upswing at -0.6 GHz marked by a white line in Figure 4.7. The period of the oscillations is slow, approximately 40 ms, the average period of the oscillations of the entire region can be seen in Figure 4.9 (a). The output is strongly dominated by the GS, but very small corresponding oscillations are also observed in the ES, see Figure 4.8. High GS power corresponds to that of a phase-locked output and the other to the dual state output. On the higher injection strength boundary, where  $K=0.737$ , the higher GS intensity section is longer lived than the lower GS intensity section, see Figure 4.8 (k) and Figure 4.9 (b) and (e). Moving further away from the locking region by decreasing  $K$ , the duty cycle changes, eventually reaching 0.5, as seen in Figure 4.8 (h). Decreasing the injection strength even further, the lower intensity section becomes longer lived than the upper, see Figure 4.8 (b) and Figure 4.9 (c) and (f). The variance of the high and low lifetimes is shown in Figure 4.10, it's highest near the edges suggesting that the oscillations are not periodic at their onset. Qualitatively, this behaviour is

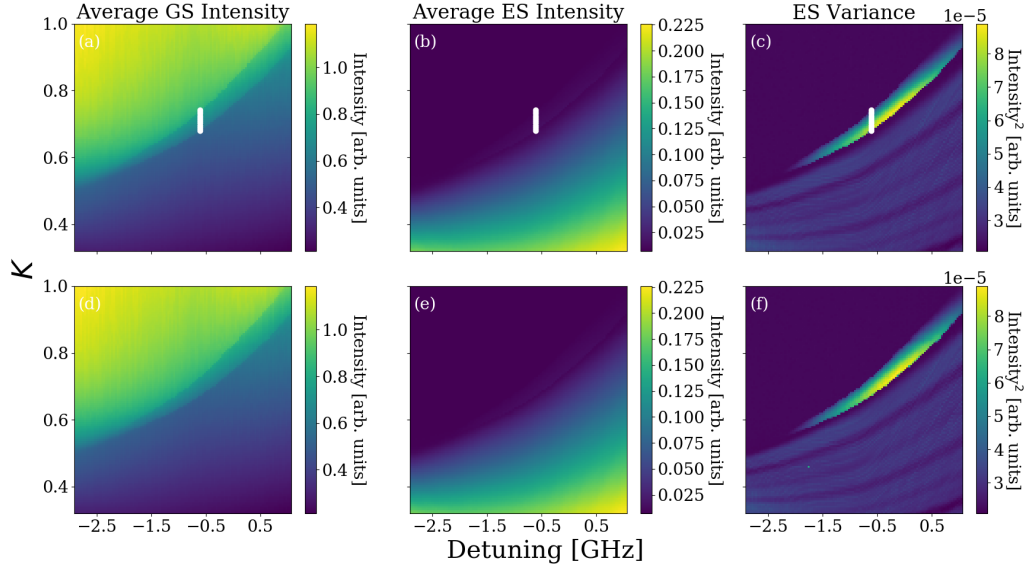


Figure 4.7: Experimental maps of the positively detuned side of the unlocking boundary. The top row shows an upswEEP and the bottom shows a downswEEP. The timetraces used to build this map were 1 second long. Three regions are visible in (a) and (b). The large yellow region with high GS intensity extending all the way from the negatively detuned unlocking boundary is a phase locked region. The blue region extending from the right is the unlocked region with low GS intensity and dual state emission. The narrow green region in the middle is where there are slow oscillations between the high and low GS intensity solutions and thus the average intensity lies somewhere in the middle. (b) and (e) show a completely quenched ES with dark blue when the laser is phase locked. The region of slow oscillations is represented by the slightly lighter shade of dark blue. For positive detuning values dual state emission is clear. The variance shows the region where slow oscillations occur more clearly, (c) and (f). There is a small hysteresis cycle of one to two pixels at both sides. The white line marks corresponds to the timetraces shown in Figure 4.8.

extremely similar to the optothermal square waves on the negative detuning side, both in this dual state system and in the GS only system Chapter 2, where the effect breaks a phase-locked bistability. We interpret this region as another broken bistability between a low power GS output such as that shown in Figure 4.8 (a) and a high power GS output such as that shown in Figure 4.8 (l). However, the oscillations here are  $\sim 100,000$  times slower.

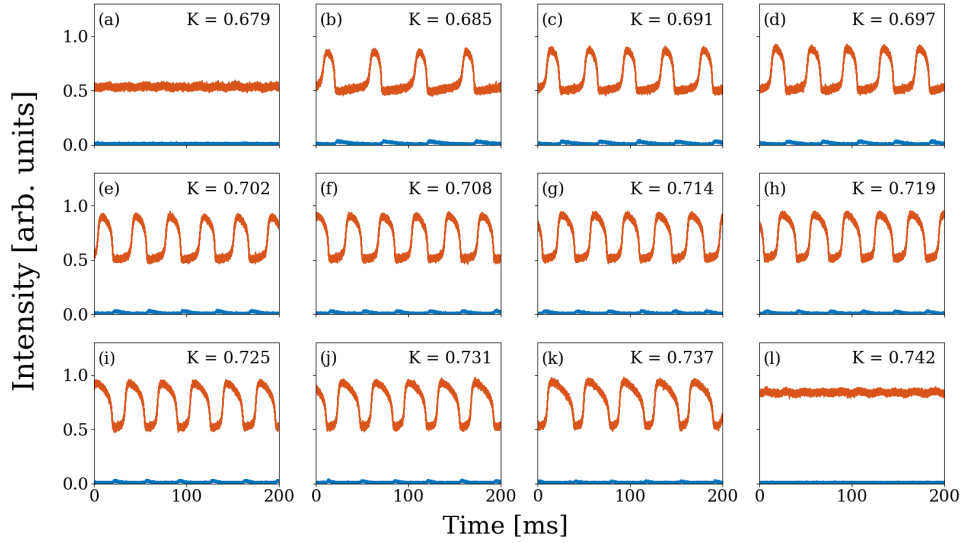


Figure 4.8: Slow oscillations observed during an upswEEP at -0.6 GHz, near the positively detuned side of the unlocking boundary. The sweep is marked by a white line in Figure 4.7. Comparing (a) and (l), there are two very different GS amplitudes at either side of the region of oscillations. The slow oscillations are between these two underlying intensities, suggesting there is a bistability.

The qualitative similarity of the oscillations with the previously investigated optothermal effect is very suggestive. However, there is a significant difference that prevents the explanation of the oscillations via the original coupling. For the bistability near the negative detuning boundary, the low power solution is on the negatively detuned side and the high power solution on the positive side. The physical optothermal coupling arises due to non-radiative carrier recombination. Thus, the low-power solution results in high carrier density and an ensuing higher temperature via increased non-radiative recombination. In the high power solution the carrier density is lower and so the temperature is lower. Thus, higher power leads to lower temperature and vice versa and the deterministic cycle is driven by the low power solution being pushed towards positive detuning and the high power solution pushed towards negative detuning (yielding an anticlockwise phasor cycle as shown in Figure 2.28). However, in the new region identified in this chapter, the *high* power solution is the more negatively detuned of the two and so heating due to non-radiative recombinations cannot account for the phenomenon. Instead, a coupling with the opposite sign is required. Such a coupling does exist. There are several important ways in which heating can arise in the device. The first is the non-radiative recombination coupling already investigated. The second is

via reabsorption of light in the device. In [77] the importance of the absorption at the mirrors (formed by cleaved facets in our case) was emphasised. Furthermore, it is also known that self-absorption arises in QD lasers in particular, due to the wide distribution of states and dot sizes [149]. For the absorption case, a higher optical power leads to an increased temperature and so the effect results in an effective detuning sweep in the opposite direction to that of the first optothermal effect. What's more, the timescale for the second effect should be significantly longer as the time over which the absorption heating is distributed through the device can be of the order of tens of milliseconds (or even longer) [77, 150]. This matches the observed timescale extremely well. We see below that including such an effect in the model allows for excellent agreement with the experiment.

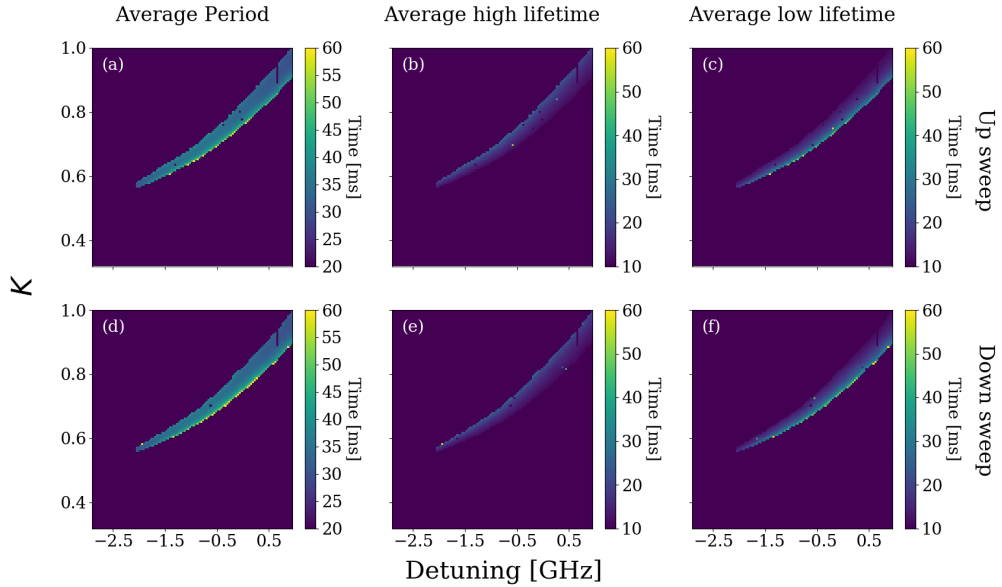


Figure 4.9: Experimental maps of the positively detuned side of the unlocking boundary. The top row shows an up-sweep and the bottom shows a down-sweep. (a) and (d) show the average period of the GS oscillations, and are always approximately 40 ms. (b) and (e) show the average lifetime of the higher intensity GS state which is longer lived closer close to the centre locking region. (c) and (f) show the average lifetime in the lower intensity GS section and it is longer lived at the more positively detuned boundary.

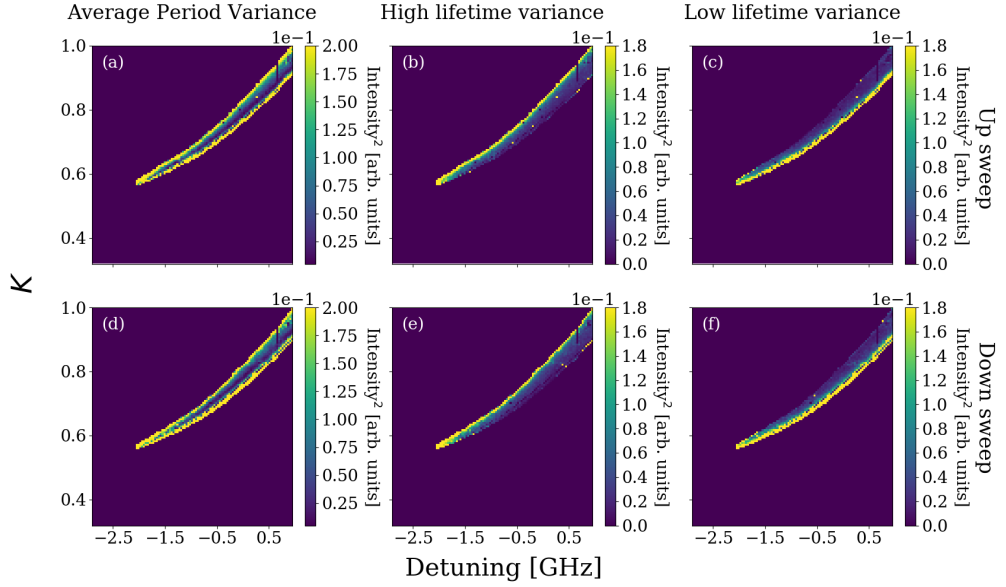


Figure 4.10: Experimental maps of the positively detuned side of the unlocking boundary. The top row displays the results from an up-sweep and the bottom displays results from a down-sweep. These maps show the variance of the data used to calculate the averages in Figure 4.9. (a) and (d) show the variance of the period of the GS oscillations, the variance is greatest at the boundary suggesting noise may have more of an influence there. (b) and (e) show the variance of the time spent in the higher intensity GS state. It is largest at the negative side of the slow oscillation region. This corresponds to a low variance for time spent in the lower GS intensity region, (c) and (f). The opposite is true at the positively detuned side of the slow oscillation region. Here there is a large variance in the time spent in the low intensity section but low variance in the time spent in the higher intensity section.

### 4.3 Theory

For simulations we use an extension of the rate equation model previously used in [134, 139] to model the dual state system under optical injection. The basic model has rate equations for  $E_{GS}$ , the electric field of the GS;  $I_{ES}$ , the power of the ES;  $\rho_{GS}$  and  $\rho_{ES}$ , the occupation probabilities; and  $N$  is the normalised charge carrier number in the quantum well reservoir. We supplement these with two further equations to include the optothermal couplings. The model is

$$\begin{aligned}\dot{E}_{\text{GS}} &= g(1 + i\alpha_{\text{GS}}) [(2\rho_{\text{GS}} - 1) - \kappa] E_{\text{GS}} \\ &\quad + 2ig\alpha_{\text{ES}} [(2\rho_{\text{ES}} - 1) - \kappa] E_{\text{GS}} \\ &\quad - 2\pi i(\Delta_0 + \Delta_1 + \Delta_2) E_{\text{GS}} + K\end{aligned}\quad (4.1)$$

$$\dot{I}_{\text{ES}} = [4g(2\rho_{\text{ES}} - 1) - 2\kappa] I_{\text{ES}} + \beta\rho_{\text{ES}}/\tau \quad (4.2)$$

$$\dot{\rho}_{\text{GS}} = \mathcal{S}_{\text{rel}} - g|E_{\text{GS}}|^2(2\rho_{\text{GS}} - 1) - \rho_{\text{GS}}/\tau \quad (4.3)$$

$$\dot{\rho}_{\text{ES}} = -\frac{1}{2}\mathcal{S}_{\text{rel}} + \mathcal{S}_{\text{cap}} - 2gI_{\text{ES}}(2\rho_{\text{ES}} - 1) - \rho_{\text{ES}}/\tau \quad (4.4)$$

$$\dot{N} = J - 4\mathcal{S}_{\text{cap}} - N/\tau \quad (4.5)$$

with the scattering terms

$$\mathcal{S}_{\text{rel}} = S_{\text{rel}} \left[ (1 - \rho_{\text{GS}})\rho_{\text{ES}} - \exp\left(\frac{-\varepsilon_{\text{GSSES}}}{k_{\text{B}}T}\right) \rho_{\text{GS}}(1 - \rho_{\text{ES}}) \right], \quad (4.6)$$

$$\mathcal{S}_{\text{cap}} = S_{\text{cap}}(\rho_{\text{ES}}^{\text{eq}} - \rho_{\text{ES}}), \quad (4.7)$$

$$\rho_{\text{ES}}^{\text{eq}} = \left( 1 + \exp\left(\frac{-\varepsilon_{\text{ES}}}{k_{\text{B}}T}\right) \left[ \exp\left(\frac{N}{D_{2\text{D}}}\right) - 1 \right]^{-1} \right)^{-1}. \quad (4.8)$$

There are three  $\Delta$  terms controlling the detuning in the system.  $\Delta_0$  allows us to choose our reference frame. We define  $\Delta_0 \equiv \delta_0 + \delta$  with  $\delta_0$  chosen so that the GS frequency of the free-running laser is at zero. Thus,  $\delta_0$  compensates the frequency shift due to the phase-amplitude coupling and the optothermal effects in the free-running laser. Then  $\delta = 0$  is at the centre frequency of the free-running quantum dot laser and it is  $\delta$  that defines the x-axis in each of our maps below. The other two terms,  $\Delta_1$  and  $\Delta_2$ , are used to implement the aforementioned optothermal coupling mechanisms.  $\Delta_1$  accounts for heating of the active region due to recombinative heating, while  $\Delta_2$  models overall device heating via re-absorption. We implement these two different effects with individual coupling strengths  $c_{1,2}$ , and characteristic time scales  $\gamma_{1,2}$  in the following two equations.

$$\dot{\Delta}_1 = \gamma_1(c_1[2(\rho_{\text{GS}} - \rho_{\text{GSth}}) + 4(\rho_{\text{ES}} - \rho_{\text{ESth}}) + (N - N_{\text{th}})] - \Delta_1), \quad (4.9)$$

$$\dot{\Delta}_2 = \gamma_2(c_2[|E_{\text{GS}}|^2 + I_{\text{ES}}] - \Delta_2) \quad (4.10)$$

where the subscript “th” denotes the value of the corresponding charge-carrier variable at the laser threshold. We note that in Chapter 2 we coupled the thermal effect to the power even though the physical explanation is via the

carriers. In the Class A case, this is unavoidable since the carriers are adiabatically eliminated. In the QD case here, it is possible to couple to the carriers instead and we do so. The parameters used and their values are given in Table 4.1 below.

Table 4.1: Parameter values

Symbol	Value	Meaning
$J$	$25 \text{ ns}^{-1}$	Normalised pump current
$\alpha_{\text{GS}}$	2	Phase-amplitude coupling from the GS
$\alpha_{\text{ES}}$	0.5	Phase-amplitude coupling from the ES
$g$	$80 \text{ ns}^{-1}$	Optical gain coefficient
$\kappa$	$76 \text{ ns}^{-1}$	Optical loss coefficient
$\beta$	$10^{-5}$	Spontaneous emission factor
$\tau$	1 ns	Charge-carrier recombination time
$S_{\text{cap}}$	$0.2 \text{ ps}^{-1}$	QD capture rate
$S_{\text{rel}}$	$1 \text{ ps}^{-1}$	QD relaxation rate
$\varepsilon_{\text{ES}}$	50 meV	Confinement energy of the ES
$\varepsilon_{\text{GSES}}$	40 meV	Energy separation between GS and ES
$D_{2\text{D}}$	10.9	Normalised 2D density of states
$T$	300 K	Temperature
$\gamma_1$	$40 \mu\text{s}^{-1}$	Characteristic time scale of non-radiative thermal effects
$\gamma_2$	$4 \mu\text{s}^{-1}$	Characteristic time scale of reabsorption thermal effects

It turns out to be quite instructive to first consider the system in the absence of any optothermal effects (Figure 4.11), then with only one effect (Figure 4.12), and finally with both effects included, thereby allowing for a more comprehensive description of how many of the observed features emerge.

There are many features that are common to all. There is a large phase-locked region; there are large dual state, regenerated injected light regions for large magnitude detunings; and at the lower injection strength negatively detuning boundary, an antiphase dropout and pulsing dynamic is found in each case.

On the other hand, in the absence of any optothermal coupling, there are no bursting phenomena and there are no square waves for either negative or positive detuning. Instead, we find multiple bistabilities near the negative detuning boundary, see Figure 4.11. One of these is very clear from Figure 4.11 in the top left corner of each subplot. Consider the leftmost edge of Figures 4.11 (a) and (d). In the up-sweep the regenerated, two state output

persists right up to the top of the figure. Figure 4.11 (c) shows that the regenerated two state output eventually destabilises via a Hopf bifurcation along the bright line in the top left corner. There is only a very narrow region over which the resulting oscillatory solution exists after which the system moves to the phase locked output. In the downsweep case however, the bright yellow phase-locked region extends down to  $K \approx 4.8$  at the extreme left of Figure 4.11 (d). Thus there is a clear bistability (Bistability 1) between the phase-locked output and the regenerated two state output over a large region and indeed, another bistability (Bistability 2) between the phase-locked output and the oscillating two state output over a small region. There is another region of hysteresis (Bistability 3) near  $K \approx 4.8$ . This is not as easy to see as it is over a much smaller area. At this injection strength, the phase-locked solution first destabilises into the oscillating GS dropout/ES pulse regime as the injection strength is decreased. This phase-locked/pulsing regime is bistable with the regenerated two state output and its destabilising Hopf

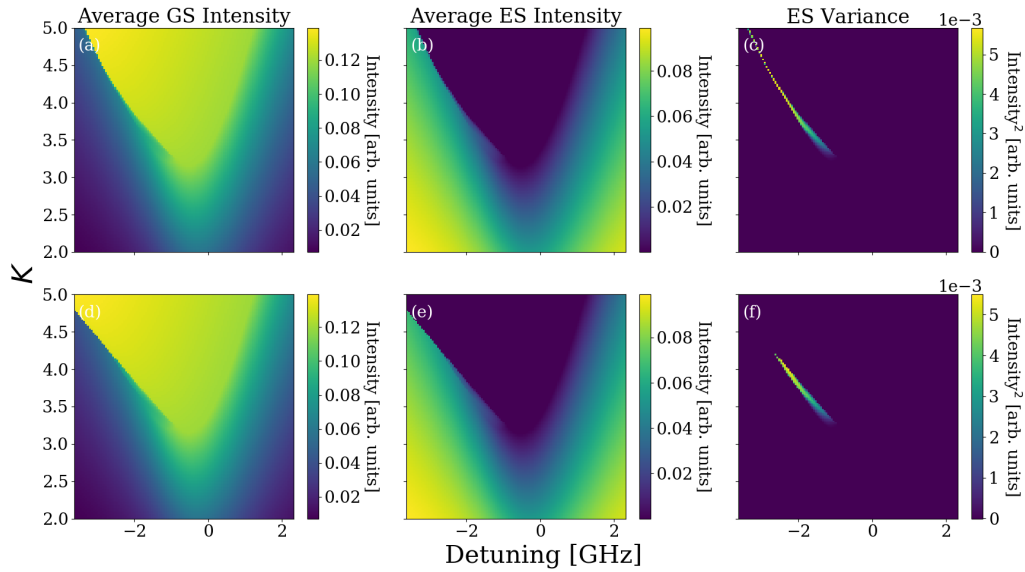


Figure 4.11: Stability maps in the absence of any optothermal effects. The upper panel shows the results for the upswEEP and the lower panel shows the corresponding downswEEP. Bistability 1, the bistability between the phase-locked output and the regenerated two state output can be seen by comparing the top left corners of (a) and (c) at high injection strengths near  $K = 5$ . Bistability 2, the bistability between the phase-locked output and the oscillating two state output is clear when looking at the top left corners of the variance plots, (c) and (f). Bistability 3, the bistability with lowest injection strength between phase-locked/pulsing regime and regenerated two state output can be seen in (c) and (f).

induced cycle discussed above. Notably though, there is not a bistability for positive detuning (where we find the extremely slow dynamic in the experiment). One might reasonably expect the negative detuning bistabilities from previous GS only analyses [71, 87] and some have even already been described in [46, 78, 134]. In [78] it was shown that the introduction of an optothermal coupling leads to the destruction of a bistability and that a periodic bursting dynamic is instead obtained. We repeat this analysis here with our model.

### 4.3.1 First optothermal effect

We now introduce the first optothermal effect, arising from non-radiative recombinations and modify the locking maps as shown in Figure 4.12. As predicted, this breaks Bistability 1, the negative detuning phase-locked bistability and yields the periodic square wave regime just as in the GS only case. In fact most of the most of the dynamic structure observed in the experiment is reproduced with this inclusion of this optothermal effect. It also breaks Bistability 2, the bistability between the phase locked and dual state

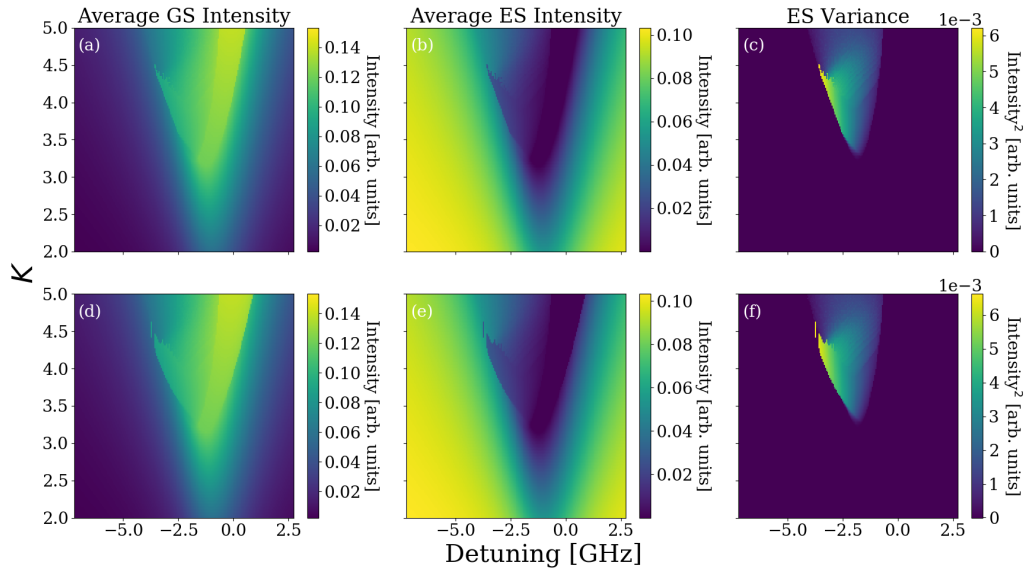


Figure 4.12: Simulated stability map with one optothermal effect. The top panel shows the results from an up-sweep and the lower panel shows the corresponding down-sweep. (a) and (d) are the average GS intensity and (b) and (e) are the average ES intensity. The region of high ES variance, (c) and (f), is much larger than in Figure 4.11 as Bistability 1 is broken and is replaced with a square wave regime.  $\gamma_1 = 40 \mu\text{s}^{-1}$ ,  $c_1 = 3 \text{ ns}^{-1}$ .

solutions to recover the bursting and slow passage effects as in the experiment and as reported in [78]. Bistability 3, the dual state bistability, is maintained although the precise location and shape of the region changes. An important modification of the map arises for the positive detuning region. Now, where before there was no bistability, we find one, between the phase-locked output of high GS intensity and the constant dual state output with lower GS intensity as indicated in Figure 4.13 (a) at detunings near 1 GHz. This arises as the first optothermal effect shears the map so that the two solutions now overlap.

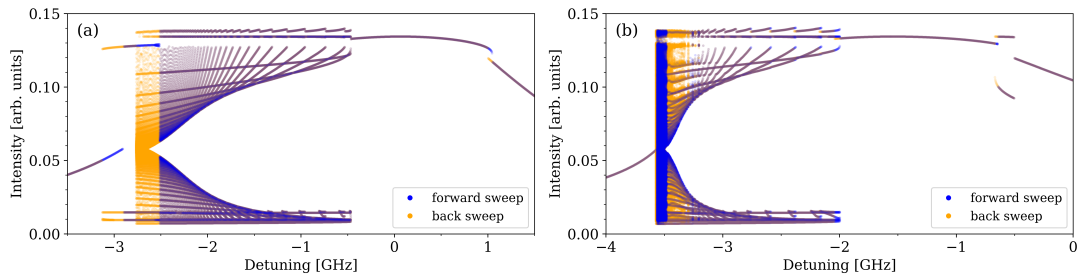


Figure 4.13: 1D bifurcation diagrams showing the bistabilities. The many diagonal lines are brought about by the bursting phenomenon, where the amplitude is growing even though the input parameter for detuning remains fixed. (a) only one optothermal effect is included. A bistability is created on the positive unlocking boundary. At the negative unlocking boundary, there is a large cycle between the remnants of a bistability, with some of the bistability remaining in tact. (b) both optothermal effects are included. Figure 4.15 shows the evolution of the time traces during a sweep. The bistability at the positive boundary is now a limit cycle. In both cases  $K = 4.5$ .

### 4.3.2 Second optothermal effect

We now introduce the second optothermal effect and again revise the locking maps, see Figure 4.14. We use a characteristic timescale of  $\gamma_2 = 4 \mu\text{s}^{-1}$  which is not quite as slow as the experiment but allows for a reasonable computation time while maintaining a large enough timescale separation with the existing dynamic timescales. We have verified that an even longer timescale for  $\gamma_2$  reproduces qualitatively identical dynamics. With the addition of the second optothermal effect, the square wave and bursting solutions, as well as the dual state bistability are preserved, see Figure 4.15. On the positive detuning side the new thermal effect yields a region of very slow oscillations in the region where there had been a bistability. In fact, there is even still a very small region of hysteresis as shown in Figure 4.13. This is in superb agreement with the experiment and all of the features have been recovered.

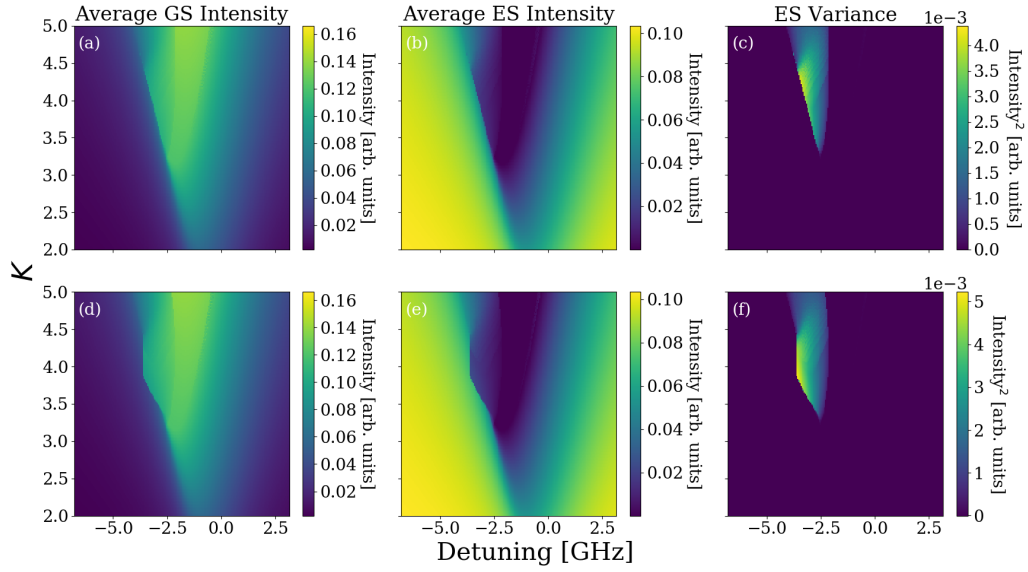


Figure 4.14: Simulated map with two optothermal effects. Top panel shows the results from the upswEEP and the lower panel shows the corresponding the downswEEP.  $c_1$  is different because the second optothermal effect counteracts the first one. In order to get the same overall shape  $c_1$  must change.  $\gamma_1 = 40 \mu\text{s}^{-1}$ ,  $c_1 = 4.5 \text{ ns}^{-1}$ ,  $\gamma_2 = 4 \mu\text{s}^{-1}$ ,  $c_2 = 0.7 \text{ ns}^{-1}$

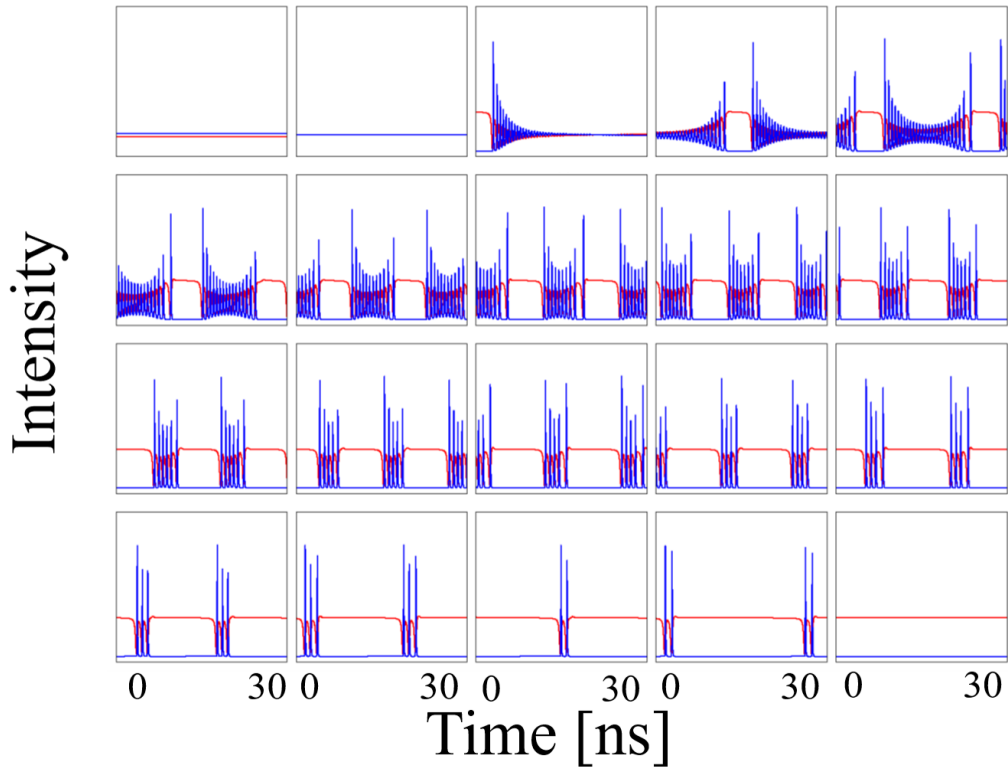


Figure 4.15: Time series progression for Figure 4.13 (b). There is an increased number of bursting oscillations when going from positive to negative detuning.  $\gamma_1 = 40 \mu\text{s}^{-1}$ ,  $c_1 = 4.5 \text{ ns}^{-1}$ ,  $\gamma_2 = 4 \mu\text{s}^{-1}$ ,  $c_2 = 0.7 \text{ ns}^{-1}$

## 4.4 Discussion

As mentioned in the introduction of this chapter and in Chapter 3, there is a marked absence of chaos when a QD laser emitting from the ES is optically injected near the GS. We have not observed any chaotic regimes in the experiment or in the numerical studies, see Figure 4.16. Analysing the system with the parameters adjusted to allow for GS only lasing, we note that chaos does indeed arise. Even though the incidence of chaos in the GS only case is much less pronounced than in the optically injected QW laser system due to the high RO damping, its presence has still been reported several times [134, 135, 141].

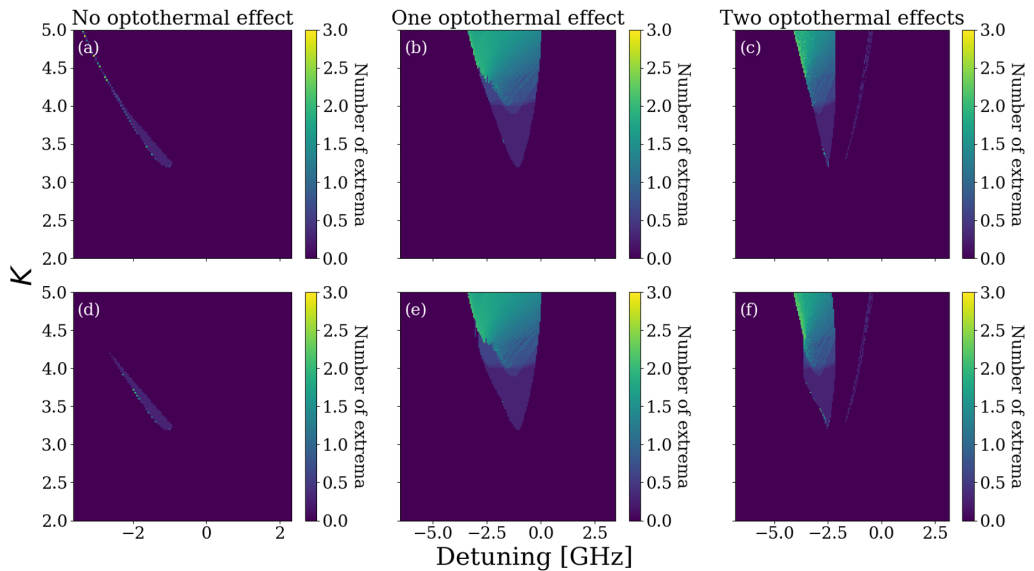


Figure 4.16: Simulated maps showing the number of maxima in log scale when no optothermal effect is included, (a) and (d), when the non-radiative optothermal effect is included, (b) and (e), and when both the non-radiative and light reabsorption optothermal effects are included (c) and (f). The top panel shows the results from the upswing and the lower panel shows the corresponding downswing. Chaos is not present for any case.

We have presented a detailed stability map for the optically injected dual state QD system. This is the first comprehensive experimental map in the literature to the best of our knowledge. We also present the first numerical map taking optothermal effects into account, which have a dramatic effect on the overall system. Our experimental and numerical results are in excellent agreement. Unlike with the injected conventional semiconductor laser, heating plays a somewhat prominent role in the map and there is an array of intact and

broken bistabilities due to competing optothermal effects. The route to the extremely slow squares near the positive detuning boundary is quite fascinating. As with the implementation of optothermal effects in other systems, a bistability is broken yielding a deterministic optothermal cycle. However, the bistability only exists because of a different, competing, optothermal coupling in the first place!

# Chapter 5

## Noise induced dual state excitability

In this chapter, we show how with a dual state quantum dot laser, a new variation of Type I excitability is possible that cannot be described by the Adler model. The laser is operated so that emission is from the ES only. The GS can be activated and phase-locked to the primary laser via optical injection while the ES is completely suppressed. Close to the phase-locking boundary, a region of GS emission dropouts correlated to ES pulses can be observed. We show that the phase of the GS undergoes bounded rotations due to interactions with the ES. We analyse the system both experimentally and numerically and find excellent agreement.

I was responsible for the entirety of the experimental work and took part in discussions regarding the numerical work, which was primarily carried out by Dr. Ilya Dubinkin, Dr. Nikita Fedorov and Dr. Evgeny Viktorov. This chapter is based on the following publication:

M Dillane, I Dubinkin, N Fedorov, T Erneux, D Goulding, B Kelleher and EA Viktorov, “Excitable interplay between lasing quantum dot states”, *Physical Review E* **100** (1), 012202 (2019).

## 5.1 Introduction

Chapter 4 shows the locking maps for a short 300  $\mu\text{m}$  QD laser that can only lase from the ES. In this chapter the device under investigation is the same 600  $\mu\text{m}$  long, InAs/GaAs QD laser used in Chapter 2 and can lase from the GS or ES or simultaneously from both. We experimentally and theoretically analyse this optically injected QD laser when the free-running operation is lasing from the ES only. We optically inject the GS and find a SNIC bifurcation at low injection levels, similar to that observed in [134, 136, 137] and discussed in Section 3.3.1. Noise-induced excitable ES intensity pulsations and corresponding antiphase GS intensity dropouts are obtained close to this phase-locking boundary. These antiphase excitable events display Type I excitability characteristics. We show that the asymmetric cascade-like coupling leads to excitable events built on an itinerary of unstable lasing states. By measuring the phase of the GS during an excitable event, we find that  $2\pi$  phase slips are not obtained and thus, the excitable response cannot be explained by the Adler equation [59]. This is in sharp contrast to all existing reports on excitability at such injection strengths. Bounded phase phenomena are possible for the optical injection system but have typically been associated with Hopf bifurcations [151, 152]. In contrast, here the dual state property of our QD lasers allows bounded phase excitable pulses near the SNIC bifurcation.

## 5.2 Experimental setup

As mentioned the device used is the same 600  $\mu\text{m}$  long, InAs/GaAs QD laser used in Chapter 2. At 20°C, the GS threshold is 32 mA. A dual state lasing regime exists between 57 mA and 72 mA where emission is obtained from both the GS (at  $\sim 1300$  nm) and the ES (at  $\sim 1215$  nm). For pump currents greater than 72 mA, the GS is completely suppressed and only ES light is emitted (the ES emission is more than 30 dB higher than that from the GS). For this experiment the laser is pumped at 73 mA. A schematic of the experimental set up is shown in Figure 5.1. The laser emits on a single longitudinal mode from the GS while the ES emission is from many longitudinal modes. The QD laser is optically injected with light from a primary laser (PL) - an Agilent 81672B tunable laser source (TLS) - with linewidth of approximately 100 kHz and minimum step increment of 0.1 pm. 10% of the PL light is used for a phase measurement (see below). The remaining 90% goes through a circulator and

is injected into the QD secondary laser (SL). A polarization controller maximises the coupling between the PL and the QD laser. The output from the injected secondary is sent to a filter where the ES and GS light is separated. The GS light went to the second arm of the  $3 \times 3$  and the third remained empty. The ES went to a 12 GHz detector. Each arm of the  $3 \times 3$  coupler is connected to a similar detector which is then connected to the oscilloscope. In the conventional injection system the detuning is easily determined. However, for the control parameters used in this system, the GS is subthreshold when the QD laser is free-running, making it difficult to accurately define detuning.

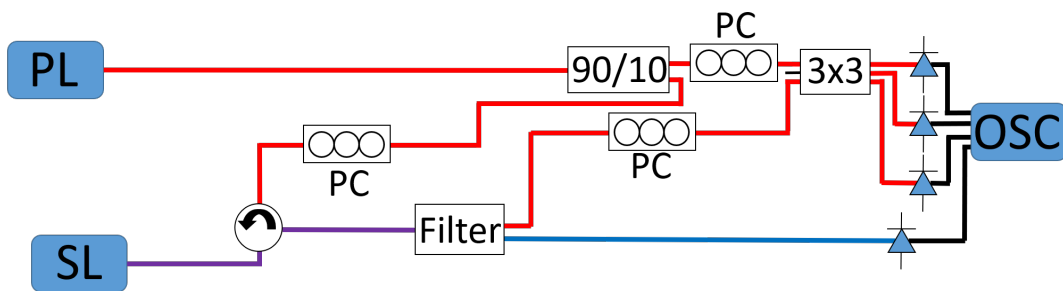


Figure 5.1: Setup for unidirectional optical injection experiment where the secondary laser (SL) is a QD laser and the primary laser (PL) is a tunable laser source (TLS). Light from the (PL) is split; 10% is sent into one arm of a  $3 \times 3$  coupler for an interferometric phase measurement technique. 90% is sent to a circulator and is then injected into a QD laser. A polarisation controller (PC) is used to maximise coupling. The light emitted from the SL is sent into the circulator and then to a filter where the ES and GS are separated. The GS light goes into another arm of the  $3 \times 3$  coupler and the ES light is sent directly to a 12 GHz detector. The third arm of the  $3 \times 3$  coupler is left empty. Polarisation controllers are used to maximise the interference of the  $3 \times 3$  coupler input signals. All 3 outputs of the  $3 \times 3$  coupler are connected to 12 GHz detectors and each detector is connected to the oscilloscope (OSC). The red lines represent light at approximately 1300 nm close to the GS emission, the blue lines represent ES only and the purple is both GS and ES. The black are high speed electrical cables.

The two control parameters are the injection strength controlled by the PL power and the detuning controlled by the PL wavelength. Initially the QD laser is free running and emitting from the ES only. By injecting into the GS with sufficient strength, the GS can be made to lase with the ES suppressed by 39.7 dB relative to its free-running value, phase locked to the primary laser. As the frequency of the primary laser is decreased toward the unlocking boundary, eventually deep GS intensity dropouts are observed, see Figure 5.2.

The GS dropouts have widths of approximately 300 ps and the minimum intensity is close to zero. These dropouts have corresponding large pulsations in the ES achievable due to the gain available during the dropout. The ES pulses are much shorter with a FWHM of approximately 80 ps. We interpret the behaviour as antiphase, dual-state excitability.

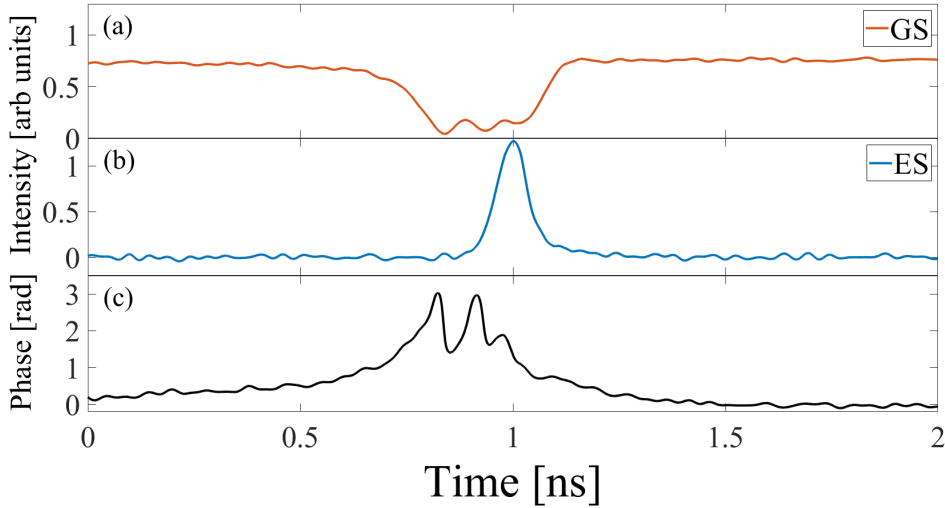


Figure 5.2: Timetrace of dual state excitability. (a) shows the 300 ps GS dropout, (b) shows the 80 ps ES pulse and (c) is the phase of the GS.

### 5.2.1 Phase measurement

Using the phase resolving technique of [84] and previously described in Chapter 2, we can analyse the phase behaviour of the GS. For the conventional one state injection system, with low injection strength and where only the ground state is involved,  $2\pi$  phase rotations (or multiples thereof) are observed for each excitable event [19, 153]. In the dual state system of this work, however, this is not the case and we observe bounded phase trajectories as shown in Figure 5.2 (c). Figure 5.3 shows the phase evolution in a two-dimensional projection onto the electric field plane.

This bounded phase trajectory cannot be explained by the simple Adler equation. Moreover, the presence of spiralling oscillations are also visible. They correspond to the ringing in the lower plateau of the dropout in Figure 5.2 (a) and in the upper part of the phase trajectory in Figure 5.2 (c). This ringing can be identified as a form of relaxation oscillation and is evocative of the turn-off transient for the underlying off-state for the GS in the free-running configuration, itself a focus point. The ringing should not be identified with

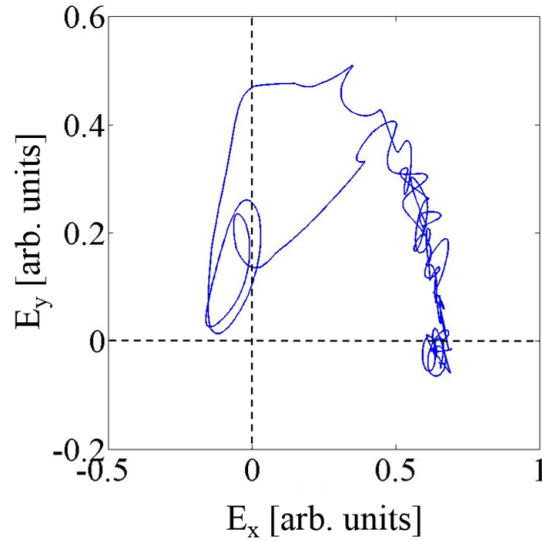


Figure 5.3: Phasor diagram showing the real and imaginary parts of the electric field. The steady state is at approximately (0.6,0). When noise triggers a pulse it results in a bounded trajectory that does not go around the origin. The spiral close to the origin suggests the presence of a saddle focus.

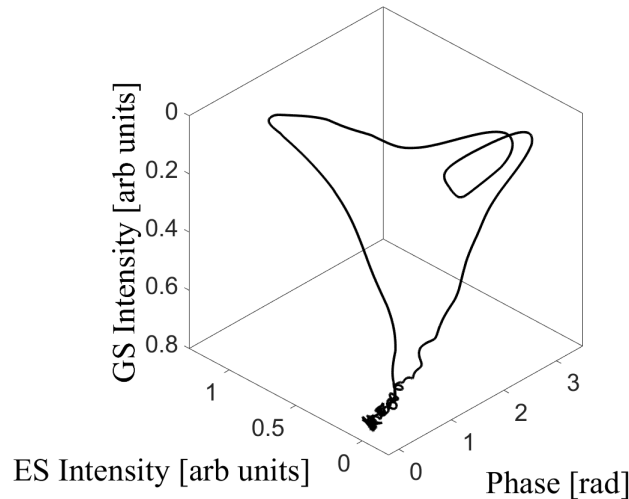


Figure 5.4: A 3 dimensional figure showing the phase and the GS and ES intensities. When the ES turns on it pulls the phase away from the origin, stopping a  $2\pi$  rotation. The saddle focus has 2 oscillations as in Figure 5.3 but it is not visible from this reference angle.

the relaxation oscillations of the free-running laser emitting from the ES only. The ringing is also visible in the three dimensional plot of the phase and the intensities of the GS and ES shown in Figure 5.4.

We ascribe the bounded GS phase to the presence of the ES pulse and the interstate phase amplitude coupling. This phenomenon has been shown to play an important role in the system, leading to hysteresis with control

parameter variation, see Figure 3.4 in Chapter 3.

We note that in [148] pulses could be created without accompanying  $2\pi$  rotations. This is very different from the case presented here. Firstly, [148] considers a mutually coupled system where the presence of delay coupling allows for the generation of pulse trains rather than individual excitable pulses. Further, the pulse generating the train in [148] always arises from a  $2\pi$  slip: It is only subsequent pulses in the train that might not involve a full slip. What's more, the influence of noise is also crucial in determining whether a  $2\pi$  slip arises or not in [148]. Here, the bounded rotation is deterministically induced by the inherent coupling of the ES and GS.

### 5.3 Model

To reveal the central feature of the dual state excitable dynamics, we consider rate equations appropriate for our QD laser system [46]. They consist of equations for the complex electric field of the GS ( $E_g$ ), the intensity of the ES ( $I_e$ ), the occupation probabilities of the GS ( $n^g$ ) and ES ( $n^e$ ) and the carrier density in the wetting layer ( $n^w$ ), see Figure 1.2. We assume a cascade-like (wetting layer (WL)-ES-GS) relaxation pathway for the carriers in the dot as suggested in [154]. Since the equation for electric field of the GS ( $E_g$ ) is complex, the phase space is 9-dimensional.

$$\begin{aligned} \dot{E}_g = & \frac{1}{2}[(1 + i\alpha)(2g_0^g(n_e^g + n_h^g - 1) - 1) \\ & + i4\beta g_0^e(n_e^e + n_h^e - 1)]E_g - i\Delta(t)E_g + \varepsilon, \end{aligned} \quad (5.1)$$

$$\dot{I}_e = [4g_0^e(n_e^e + n_h^e - 1) - 1]I_e, \quad (5.2)$$

$$\begin{aligned} \dot{n}_{e,h}^g = & \eta[2B_{e,h}n_{e,h}^e(1 - n_{e,h}^g) - 2C_{e,h}n_{e,h}^g(1 - n_{e,h}^e) \\ & - n_e^g n_h^g - g_0^g(n_e^g + n_h^g - 1)|E_g|^2], \end{aligned} \quad (5.3)$$

$$\begin{aligned} \dot{n}_{e,h}^e = & \eta[-B_{e,h}n_{e,h}^e(1 - n_{e,h}^g) + C_{e,h}n_{e,h}^g(1 - n_{e,h}^e) \\ & + B_{e,h}^w n_{e,h}^w(1 - n_{e,h}^e) - C_{e,h}^w n_{e,h}^e - n_e^e n_h^e \\ & - g_0^e(n_e^e + n_h^e - 1)I_e], \end{aligned} \quad (5.4)$$

$$\begin{aligned} \dot{n}_{e,h}^w = & \eta[J - n_e^w n_h^w - 4B_{e,h}^w n_{e,h}^w(1 - n_{e,h}^e) \\ & + 4C_{e,h}^w n_{e,h}^e]. \end{aligned} \quad (5.5)$$

The subscripts  $e$  and  $h$  stand for electron and hole respectively. The dots indicate differentiation with respect to  $t = \tilde{t}/\tau_{ph}$ , where  $\tilde{t}$  is time and  $\tau_{ph}$  is the photon lifetime.  $\eta = \tau_{ph}/\tau$ , where  $\tau$  denotes the carrier recombination time.  $J$  is the pump current, and the terms  $B_{e,h}$  and  $B_{e,h}^w$  are the capture rates to the GS and ES, respectively. The escape rates are given by the C terms and are linked to the capture rates B via the Kramers relation, as described in [46].  $\alpha$  is the usual GS phase-amplitude coupling/linewidth enhancement factor. It is well known that a full treatment of this quantity in QD systems involves subtle details [87]. However, for simplicity, we treat it as a constant here and find that this is sufficient to analyse the physics of the system.  $g_0^g$  and  $g_0^e$  are gain coefficients,  $\beta$  models the effect of inhomogeneous broadening [46, 87],  $\varepsilon$  is the injection strength and  $\Delta = \omega_i - \omega_g$  is the detuning between the frequency of the injected light and that of the GS. The model takes into account the differing spin degeneracies in the QD energy levels, Pauli blocking, and interstate captures and escapes. Our two primary control parameters are the injection strength  $\varepsilon$  and the detuning  $\Delta$ . To induce the excitable dynamics stochastically, a Gaussian white noise term,  $D\xi(t)$ , where  $D$  is the amplitude, was added to Eq. (6.1).

The bifurcation diagrams of the steady state solutions are shown in Figure 5.5. The point at which phase-locking of the GS is achieved is at a SNIC point labelled LP1 at  $\varepsilon = 4.4373$ . By injecting from the PL into the GS with  $\varepsilon > 4.4373$ , we find steady lasing from the GS with the ES suppressed. By progressively decreasing  $\varepsilon$ , there is a gradual decrease of the GS intensity while the ES remains off. As  $\varepsilon$  is further decreased below 4.4373, the system exhibits a cycle that emerges from a homoclinic loop at the limit point of the GS branches. This cycle manifests via GS dropouts and corresponding ES pulses and it disappears at the Hopf bifurcation, H. The presence of the homoclinic bifurcation at the limit point means that at the onset of the pulsing, the repetition rate is arbitrarily low, confirming the Type I characteristics of the phenomenon.

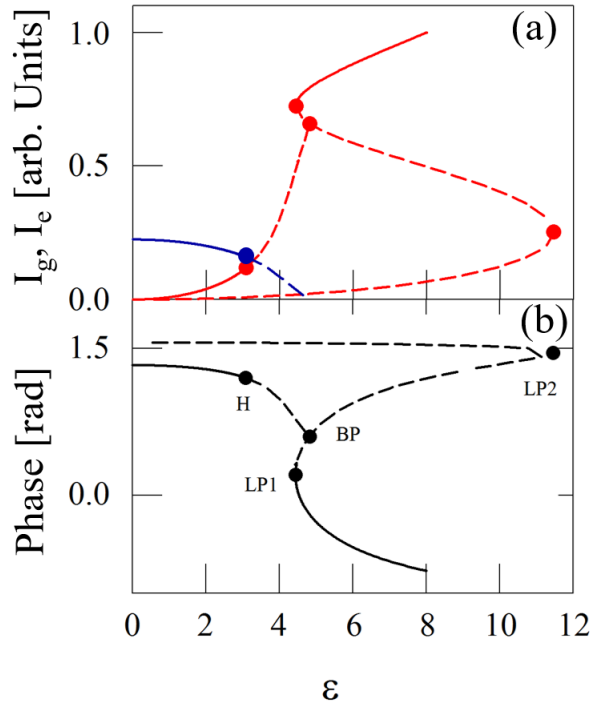


Figure 5.5: Numerical bifurcation diagram. (a) shows the GS (red) and ES (blue) intensities vs  $\varepsilon$ . (b) shows the phase of the GS vs  $\varepsilon$ , the injection strength. Continuous (dashed) lines correspond to stable (unstable) branches. *LP* and *H* denote limit points and Hopf bifurcation points, respectively. *BP* denotes an unstable bifurcation point. *LP1* denotes a SNIC bifurcation and arises at  $\varepsilon = 4.4373$ . The fixed parameters are:  $\eta = 0.01$ ,  $\Delta = 0$ ,  $\alpha = 3$ ,  $\beta = 2.4$ ,  $g_0^g = g_0^e = 0.55$ ,  $J = 56$ ,  $B_{e,h} = B_{e,h}^w = 100$ ,  $C_e^w = 0$ ,  $C_h^w = 10^2$ ,  $C_e = B_e \exp(-2)$ ,  $C_h = B_h$ .  $I_g$  is normalised by its value ( $I_g = 223.83$ ) at  $\varepsilon = 8$ .

## 5.4 Discussion

Close to *LP1* but still in the phase-locked region, noise-induced dropout/pulse trains can be obtained. Figure 5.6 shows the evolution of both the GS and ES intensities and the GS phase for  $\varepsilon = 4.4$ . Figure 5.7 shows 3D plots of one noise induced excitation at the same  $\varepsilon$ . All of these plots clearly show a ringing in the GS during the dropout. This is also clear in the experiment. This ringing results from a unique feature in this system: the presence of a saddle-focus on the lower unstable branch in the bifurcation diagram as shown in Figure 5.8 which is a zoom of Figure 5.5 (b). The excitable trajectory of the GS involves an attraction to this saddle-focus with accompanying small amplitude oscillations. In practice, the number of oscillations depends on the noise and can be small if the noise level is large as is clear from Figure 5.6 and the 3D diagrams for different levels of noise shown in Figure 5.7. Eventually the

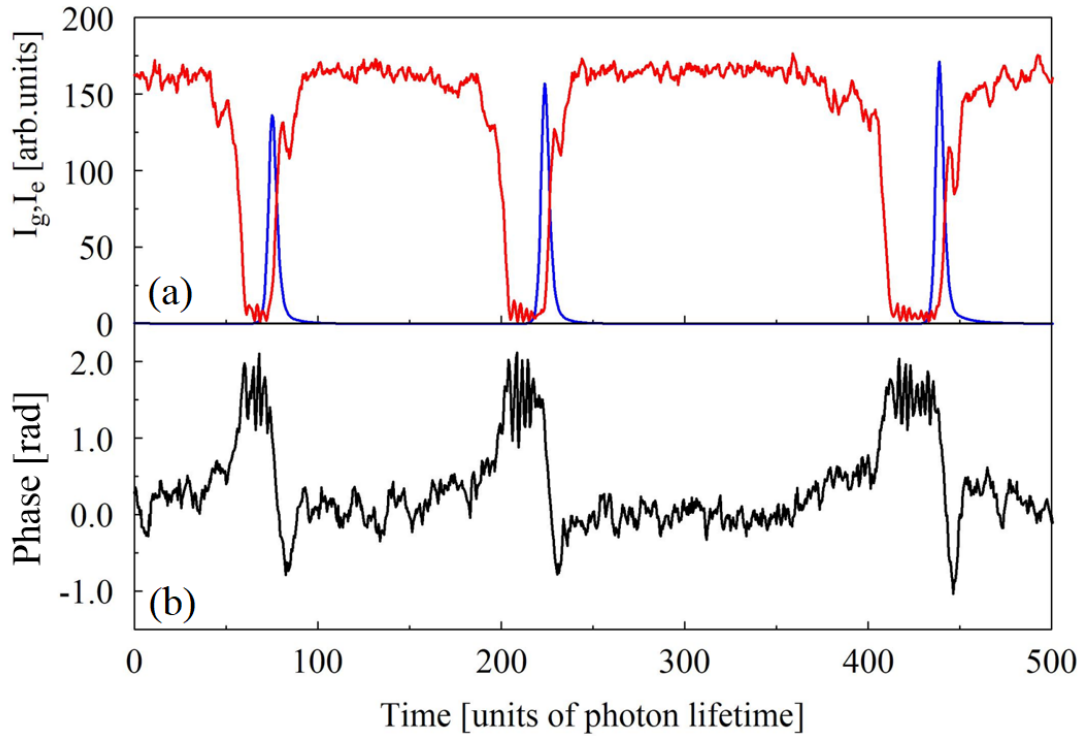


Figure 5.6: Numerically obtained noise induced excitable events ( $D = 0.5$ ). (a) shows the GS (red) and ES (blue) intensities. (b) shows the corresponding phase evolution. The parameters are the same as in Figure 5.8, where the vertical line indicates the point of operation.

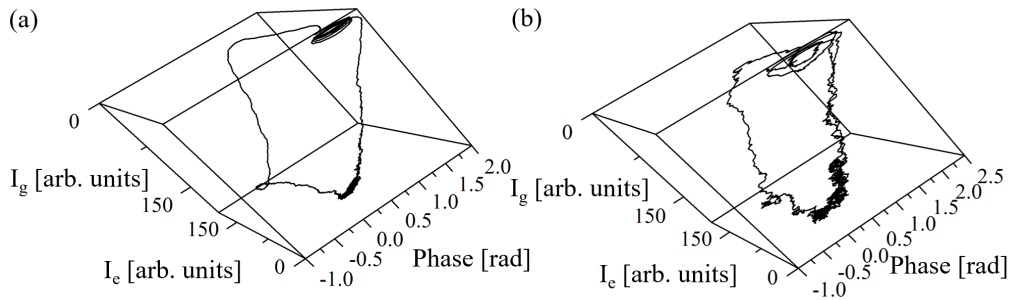


Figure 5.7: Simulated 3D plots. (a) has a low noise level ( $D = 0.5$ ) and consequently displays many rotations in the spiral. (b) has a more realistic noise level ( $D = 1$ ) and is in close agreement with the experimental results in Figure 5.4.

system hits the saddle-focus and is kicked along the repulsive trajectory. This corresponds to the observed large amplitude ES pulsation which in turn affects the GS phase dynamics due to the inhomogeneous broadening induced phase amplitude coupling  $\beta$ . As with the experiment, the phase of the GS laser field is bounded in contrast to the unbounded phase of the Adler system. Thus, while the initial excitable trajectory arises as usual with the passing of the

saddle created in the SNIC bifurcation, the ensuing trajectory involves a passage through a saddle-focus yielding both the ES pulse and the bounded phase GS cycle.

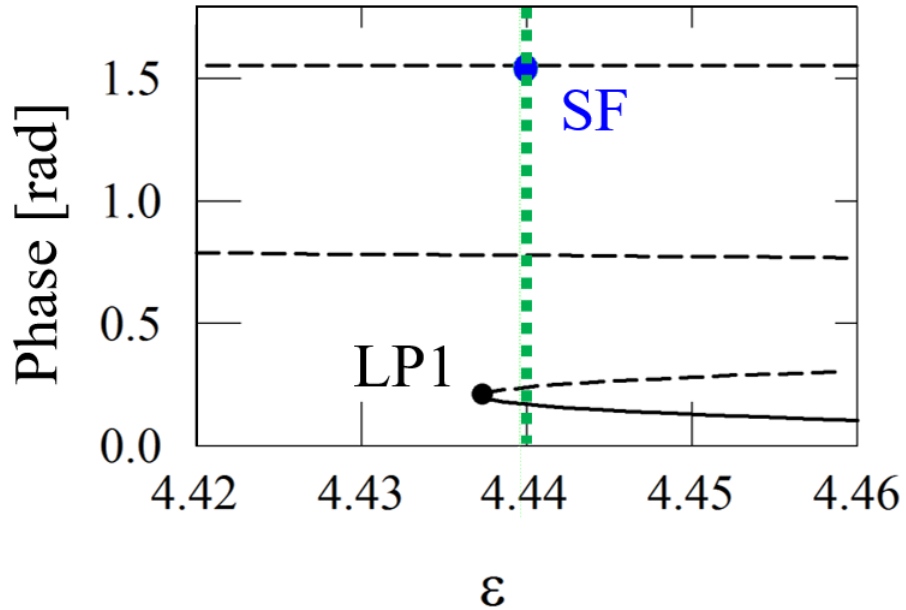


Figure 5.8: Zoom of Figure 5.5 (b). Where LP1 denotes the limit point which is a SNIC bifurcation. The blue dot labelled SF represents the saddle focus. The green dotted line marks the operating injection strength where the noise induced events in Figure 5.6 and Figure 5.7 are found. The dashed lines are unstable branches and the solid lines are stable. The same operating parameters described in Figure 5.6 are used here.

It is instructive to consider the ES excitation itself. Within the phase locked region the steady state behaviour is GS on and ES off. The switching on of the ES during the excitable trajectory is similar to a Q-switched event. (This analogy was previously described in [46] where periodic trains were reported). This excitable dynamic is reminiscent of that found in [155] where a laser with a saturable absorber was considered using the Yamada model. Below threshold in the Yamada model, sufficiently strong perturbations can trigger a high intensity pulse after which the system returns to the off state. The similarity with the behaviour of the ES in our system is natural given the Q-switching like behaviour of our system. We note that while we require a primary laser in our work, our secondary device is somewhat simpler since the need for a saturable absorber is removed: the single section acts both as the amplifier and the gate for the pulses.

In conclusion we show experimentally and theoretically a form of Type I excitability for an optically injected QD laser which differs from the classical mechanism described by the Adler equation for semiconductor lasers. The excitable response depends on the interplay of two lasing states operating in antiphase. While the underlying bifurcation structure of the excitation is of SNIC form, there are several unique features in this system. The GS intensity undergoes a dropout featuring relaxation oscillation like ringing while the ES displays antiphase short pulses. The excitable trajectory of the GS passes through a saddle focus which is responsible for the short ES pulses obtained. The very short ES pulses are excitable and thus could be used for pulse re-shaping by feeding back some of the output into the device. Indeed, tunable pulse trains could be achieved in such a configuration. (Tunability outside the excitable regime was described in [46]). Further, while the SNIC bifurcation is responsible for the generation of the excitable events, the phase trajectories are bounded, in contrast to all other instances of Type I excitability in the optical injection system. It also provides another avenue for the study of neuromorphic systems using semiconductor lasers, which we investigate below.

## Chapter 6

# Dual state excitability with two asymmetric thresholds

One of the defining characteristics of excitability is the existence of an excitable threshold: The minimum perturbation amplitude necessary to produce an excitable response. We optically inject a QD laser which can only emit from the ES when free running, to operate in a region near that of a dual state stochastic excitability dynamic previously discussed in Chapter 5. We show that deterministic triggering of this dynamic can be achieved via optical phase perturbations. Further, we demonstrate that there are in fact two asymmetric excitable thresholds in this system corresponding to the two possible directions of optical phase perturbations. For fast enough perturbations an excitable interval arises and there is a limit to the perturbation amplitude above which excitations no longer arise, a phenomenon heretofore unobserved in studies of excitability.

I was responsible for the entirety of the experimental work and took part in discussions regarding the numerical work, which was primarily carried out by Dr. Ilya Dubinkin, Dr. Nikita Fedorov and Dr. Evgeny Viktorov. This chapter is based on the following publication:

M. Dillane, B. Lingnau, E. A. Viktorov, I. Dubinkin, N. Fedorov, and B. Kelleher, “Asymmetric excitable phase triggering in an optically injected semiconductor laser”, *Optics letters* **46**, 440-443 (2021).

## 6.1 Introduction

In Chapter 5, excitable Ground state (GS) dropouts and the corresponding Excited State (ES) pulses were triggered by noise. Now we go one step further and deterministically trigger these pulses. Excitable optical pulses can be triggered via both coherent [20, 85] and incoherent perturbations [73]. The coherent perturbations consist of rapid rotations of the phase of the secondary laser relative to the primary. The direction of the phase perturbation is crucial in this system even if this is not often explicitly described. This can be seen easily in the for low injection levels (approximately 0.01) where the system can be shown to reduce to the prototype, one dimensional Adler model [60]. Close to the negative detuning boundary, anticlockwise phase perturbations must be applied to achieve an excitable pulse. Close to the positive detuning boundary the converse is true.

The existence of a perturbation threshold that must be exceeded in order to excite a pulse is well-known. Increasing the amplitude of the perturbation ever further beyond the threshold results in a continuous evolution of the response with the return to the phase-locked regime consisting of ever shorter trajectories, following the perturbation. This arises since all perturbations in the 1D Adler case merely move the system along the (trivially in 1D) invariant cycle. This finding carries over to the conventional optical injection system for both quantum well and single state quantum dot (QD) devices, despite the higher dimensionality. As the perturbation is increased beyond the threshold, the intensity pulse changes continuously, becoming ever smaller as the perturbation amplitude grows, and vanishing as the perturbation approaches  $2\pi$ . In the limit of discrete, instantaneous perturbations, the  $2\pi$  periodicity means that anticlockwise perturbations of amplitude  $\delta\phi$  are equivalent to clockwise perturbations of amplitude  $|2\pi - \delta\phi|$ . This raises the question can the threshold be observed with perturbations from both directions? By increasing the clockwise perturbations from zero in the 1D Adler case an all or none response will not be observed. Instead there will be a continuous increase in the amplitude of a pulse as the perturbation simply kicks the system further along the invariant circle. Thus we investigate what effect perturbation direction has on the dual state system and compared it to the naive 1D Adler picture.

## 6.2 Experiment

The primary laser is an Agilent 81672B tunable laser source (TLS). It injects the secondary laser, a 300  $\mu\text{m}$  InAs/GaAs Fabry-Perot QD device via a lensed optical fiber. The QD device has the same structure as the 600  $\mu\text{m}$  device discussed in Chapter 5 but here it is only 300  $\mu\text{m}$  long and is the same device used in Chapter 4. As a result, this device never lases from the GS when free-running, instead moving directly from the off state to multimode ES lasing as the pump current is increased. It is pumped at 75 mA (1.3 times threshold at 20.5  $^{\circ}\text{C}$ ), with the strongest ES mode 42.5 dB greater than the GS amplified spontaneous emission, see Figure 6.1(a).

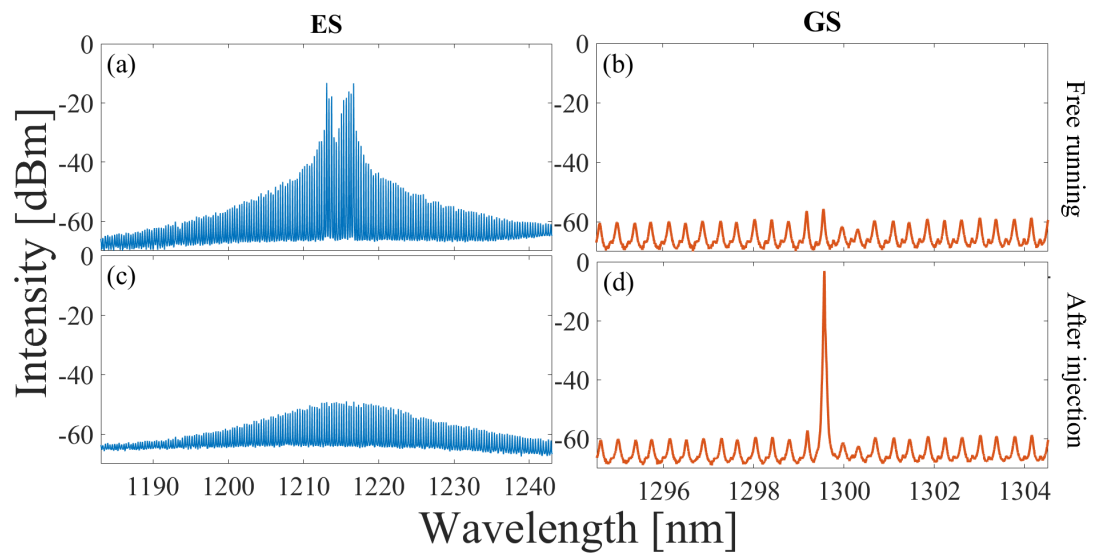


Figure 6.1: Spectra of the ES (a) and (c) and the GS (b) and (d) before and after optical injection. While Free running at 75 mA the strongest ES mode is 42.5 dB greater than the strongest GS mode which is visible due to amplified spontaneous emission. After optically injecting into a GS mode the ES is quenched and the GS mode increased by 52.6 dB.

By optically injecting close to the frequency of one of the GS modes (all of which are below lasing threshold), all the ES modes can be suppressed (maximum mode reduced by 36 dB, Figure 6.1(c)) and the device made to emit from one mode in the GS instead (increased by 52.6 dB), see Figure 6.1(d). The SL is now phase locked to the primary laser.

Outside this phase locked region and close to the negatively detuned unlocking boundary, a stochastic antiphase intensity dynamic is obtained where the GS undergoes deep intensity dropouts accompanied by sharp ES

pulsations, similar to the ones shown in Chapter 5. For the experiment, we choose the wavelength of the primary laser by first moving to the dynamical, pulsing regime and then progressively reducing the wavelength of the primary laser until no stochastic pulses are obtained, as indicated by the dark blue region in Figure 4.2 in Chapter 4. This is an important consideration both for potential applications and indeed for statistical measures in this work. As the free-running GS is always below the lasing threshold it is not possible to obtain an accurate detuning value. The phase of the secondary laser is monitored with respect to that of the primary laser using a phase resolving technique described below. A constant phase difference is observed, verifying that the secondary laser is indeed phase locked. Further, linewidth measurements such as that shown for a similar system in [46] also confirm the phase locking.

The experimental setup is similar to the one discussed in Chapter 5, but here light from the primary laser is first sent through a LiNbO<sub>3</sub> phase modulator and is then split, see Figure 6.2. 90% is injected into the secondary laser via an optical circulator and a polarisation controller is used to maximise the coupling. The remaining 10% is sent into one arm of a 3×3 optical coupler used for an interferometric phase resolving technique which allows us to measure the amplitude of the phase perturbations directly and verify phase locking [84]. The output of the secondary laser is filtered, the ES emission is sent to a 12 GHz detector and the GS emission is sent into the second arm of the 3×3 coupler while the third input arm remains unconnected. All three output arms of the 3×3 coupler are connected to a real-time digital oscilloscope via 12 GHz detectors. The phase modulator is controlled by a pulse generator producing 5 ns square pulses. The perturbing elements of the square pulse are the rising and falling edges that quickly change the optical path length and thus the phase difference between the primary and secondary lasers. The rise and fall times of approximately 200 ps and 470 ps respectively are the duration of the perturbations. The different times are a result of the pulse generator's limitations. A clockwise perturbation is generated by the rise of the pulse and an anticlockwise perturbation via the fall of the pulse.

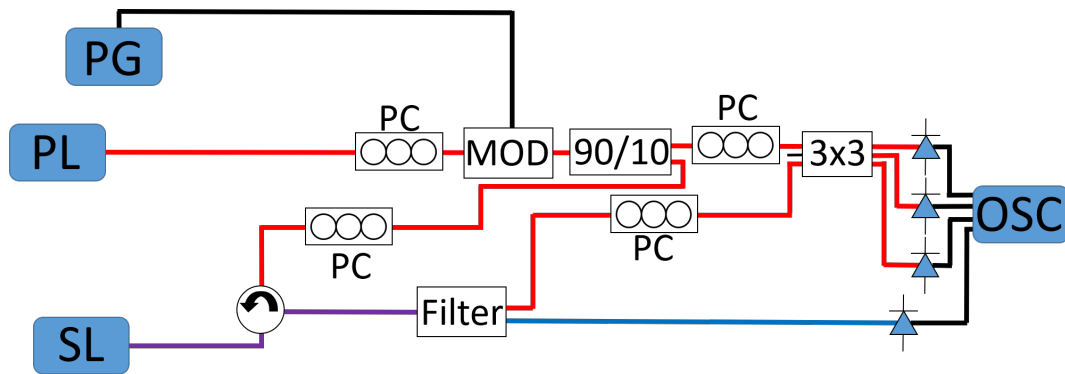


Figure 6.2: A unidirectional optical injection experiment similar to the one shown in Figure 5.1 is set up, where the secondary laser (SL) is a QD laser and the primary laser (PL) is a tunable laser source (TLS). The main difference is a  $\text{LiNbO}_3$  phase modulator (MOD) driven by a pulse generator (PG) is introduced between the PL and SL, which perturbs the injected light. After modulation, light from the (PL) is split; 10% is sent into one arm of a  $3 \times 3$  coupler for an interferometric phase measurement technique. 90% is sent to a circulator and is then injected into a QD laser. A polarisation controller (PC) is used to maximise coupling. The light emitted from the SL is sent into the circulator and is then to a filter where the ES and GS are separated. The GS light goes into another arm of the  $3 \times 3$  coupler and the ES light is sent directly to a 12 GHz detector. The third arm of the  $3 \times 3$  coupler is left empty. Polarisation controllers are used to maximise the interference of the  $3 \times 3$  coupler input signals. All 3 outputs of the  $3 \times 3$  coupler are connected to 12 GHz detectors and each detector is connected to the oscilloscope (OSC). The red lines represent light at approximately 1300 nm close to the GS emission, the blue is ES only and the purple is both GS and ES. The black are high speed electrical cables.

### 6.2.1 Dual threshold

One thousand perturbations were applied for each amplitude value in both directions in order to create excitation efficiency curves, Figure 6.3 (a). For conventional anticlockwise phase rotations, the threshold, which is defined at 50% efficiency, is located at approximately 2 radians. The unconventional clockwise perturbations also produce an efficiency curve with a clear threshold at -3.5 rad. Figure 6.4 (a) and (c) show the response of the secondary laser to a 1 rad anticlockwise and a -3 rad clockwise phase perturbation respectively. Both amplitudes always fail to trigger a pulse, and correspond to 0% efficiencies in Figure 6.3 (a). From  $\sim 2.7$  rad up to our highest amplitude of approximately 4.2 rad we find 100% efficiency for anticlockwise perturbations. To obtain 100% efficiency using clockwise perturbations the absolute amplitude must be greater than -4.1 rad. Figure 6.4 (b) and (d) show

examples of successfully triggered pulses using 4.2 rad and -4.2 rad anticlockwise and clockwise perturbations. In a noise free system the threshold would be a step function, but noise can bring the system further or closer to threshold introducing a probabilistic element.

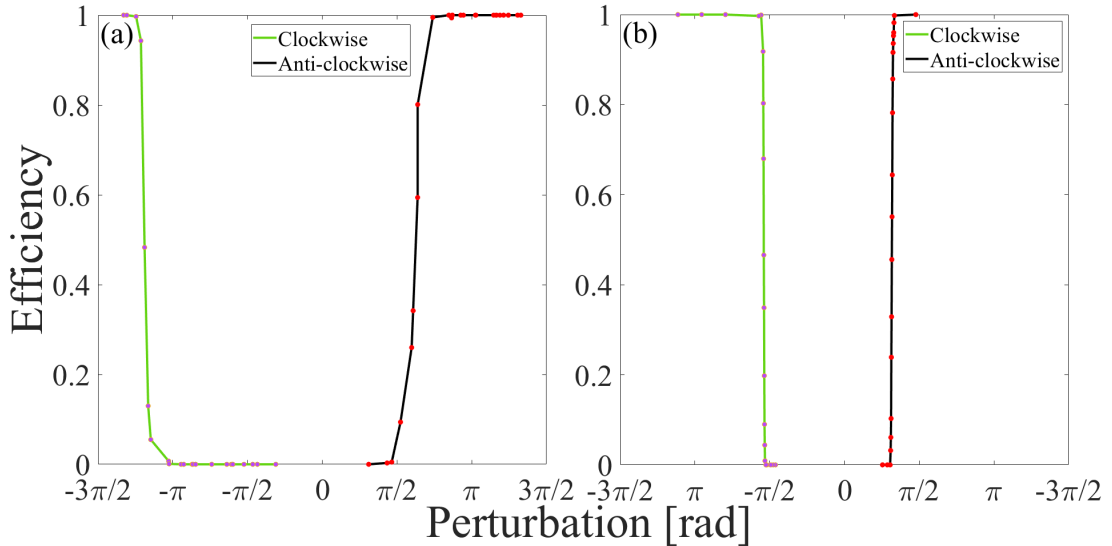


Figure 6.3: (a) Experimental efficiency curves for anticlockwise and clockwise perturbations. The thresholds, defined at 50% efficiency, are at approximately 2 rad and -3.5 rad respectively. (b) The corresponding theoretical efficiency curves with thresholds at 0.975 rad for anticlockwise perturbations and at -1.7 rad for clockwise, where  $\sigma = 1$ .

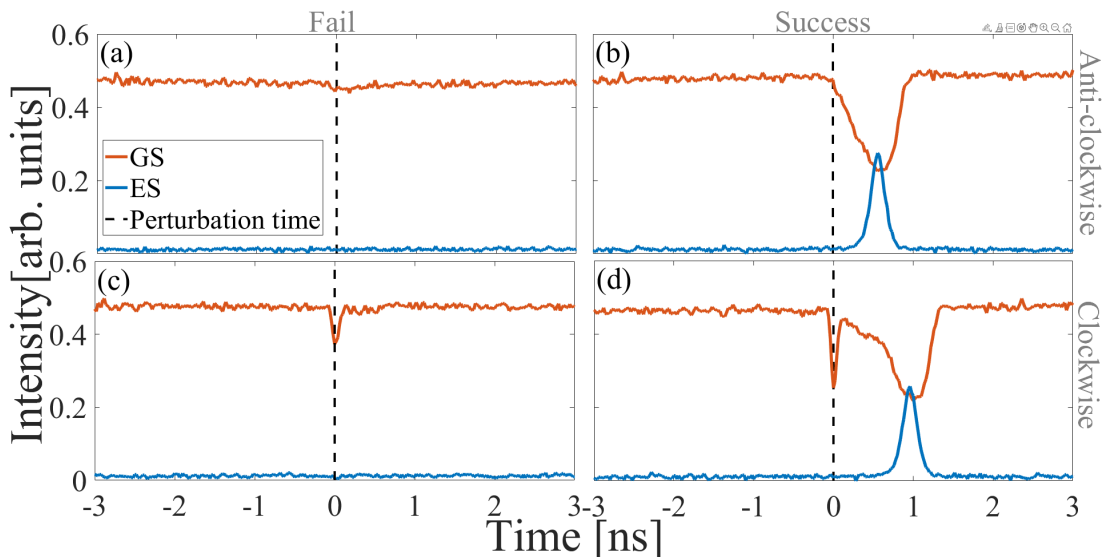


Figure 6.4: The response of the secondary laser to phase perturbations. (a) and (b) are for anticlockwise perturbations of 1 and 4.2 rad. (c) and (d) are for clockwise perturbations of -3 and -4.2 rad. The left panels show unsuccessful perturbations and the right show successfully triggered excitations.

The dual state nature of our system leads to another interesting detail. While sub threshold perturbations do not yield excitable events, their presence is nonetheless visible in the output of the GS albeit much less pronounced than the excitable dropout. Since the ES pulse only arises close to the end of the full GS excitable dropout, sub-threshold effects are completely invisible in the ES intensity, as is clear in Figure 6.4 (a) and Figure 6.4 (c) yielding a striking example of a true all-or-none response.

### 6.2.2 Delay time

Both the primary and secondary lasers have some spontaneous emission, so while the secondary laser remains phase locked to the primary there are some small fluctuations and the system is continuously changing to remain phase locked. As mentioned, the noise can bring the system closer or further from separatrix, making it easier or more difficult to trigger a pulse. We have seen in the section above that this led to a stretched out efficiency curve rather than the ideal step like function. The closer the perturbation brings the system to the separatrix the slower the escape time. An escape here corresponds to the triggering of a pulse. In fact, in the absence of noise, if conditions place the system right on a separatrix, it will remain there indefinitely. When the amplitude of a perturbation is close to the value of the threshold, noise heavily influences the delay time of a pulse.

The delay time or response time is the time it takes the system to fire a single pulse after a single supra-threshold perturbation has been applied. In a Leaky Integrate and Fire (LIF) photonic neural network each neuron fires a train of pulses. The information is encoded in the specific timing of each pulse in the train, therefore it is vital that the time at which a neuron fires is predictable and reproducible. Thus the first step in creating a LIF network is finding the perturbation amplitude that will produce pulses with a consistent delay time. The delay times for the clockwise and anticlockwise perturbations are shown in Figure 6.5. For anticlockwise perturbations with amplitudes of  $\pi/2$  rad the resulting pulse could be triggered anywhere between 1 and 4 ns after the perturbation arrives. An amplitude greater than  $\pi$  rad will produce a reliable delay time as the distribution in time is narrow. The delay for clockwise perturbations also has a wide distribution when efficiency is small. When clockwise perturbations are greater than 4.1 rad, there is minimal variation in the delay time. The perturbation amplitudes with consistent response times

will be used below when discussing the refractory periods.

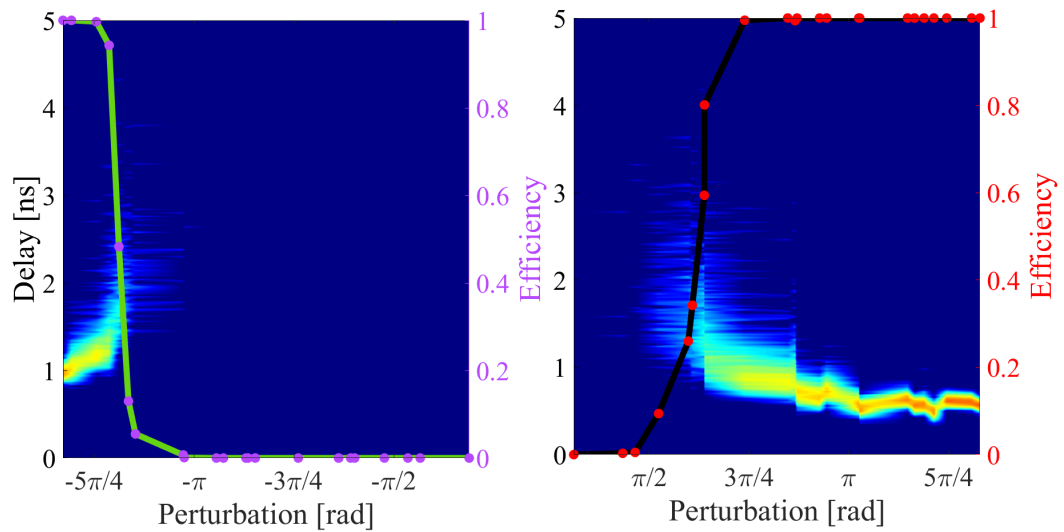


Figure 6.5: Heatmap showing delay times; the time a pulse is fired after the system has been perturbed. The left panel is for clockwise and the right is for anticlockwise. The efficiency curves are also plotted. The delay time is largest when the efficiency is below 100%.

## 6.3 Model

We now show that the phenomenon is reproduced by direct numerical simulations. The model is the same nine dimensional set of ordinary differential equations described in Chapter 5 and is included again for completeness.

$$\begin{aligned} \dot{E}_g = & \frac{1}{2}[(1 + i\alpha)(2g_0^g(n_e^g + n_h^g - 1) - 1) \\ & + i4\beta g_0^e(n_e^e + n_h^e - 1)]E_g - iE_g\Delta + \varepsilon, \end{aligned} \quad (6.1)$$

$$\dot{I}_e = [4g_0^e(n_e^e + n_h^e - 1) - 1]I_e, \quad (6.2)$$

$$\begin{aligned} \dot{n}_{e,h}^g = & \eta[2B_{e,h}n_{e,h}^e(1 - n_{e,h}^g) - 2C_{e,h}n_{e,h}^g(1 - n_{e,h}^e) \\ & - n_e^g n_h^g - g_0^g(n_e^g + n_h^g - 1)|E_g|^2], \end{aligned} \quad (6.3)$$

$$\begin{aligned} \dot{n}_{e,h}^e = & \eta[-B_{e,h}n_{e,h}^e(1 - n_{e,h}^g) + C_{e,h}n_{e,h}^g(1 - n_{e,h}^e) \\ & + B_{e,h}^w n_{e,h}^w(1 - n_{e,h}^e) - C_{e,h}^w n_{e,h}^e - n_e^e n_h^e \\ & - g_0^e(n_e^e + n_h^e - 1)I_e], \end{aligned} \quad (6.4)$$

$$\begin{aligned} \dot{n}_{e,h}^w = & \eta[J - n_e^w n_h^w - 4B_{e,h}^w n_{e,h}^w(1 - n_{e,h}^e) \\ & + 4C_{e,h}^w n_{e,h}^e]. \end{aligned} \quad (6.5)$$

A dot denotes differentiation with respect to  $t = \tilde{t}/\tau_{ph}$ , where  $\tilde{t}$  is time and  $\tau_{ph}$  is the photon lifetime.  $\eta = \tau_{ph}/\tau$ , where  $\tau$  denotes the carrier recombination time. The subscripts  $e$  and  $h$  stand for electron and hole respectively.  $\alpha$  is the usual GS phase-amplitude coupling. For simplicity here we take this to be a constant although the true situation is more complex [87]. Despite this simplification, this assumption is sufficient to reproduce the experimental findings.  $g_0^g$  and  $g_0^e$  are gain coefficients and  $\beta$  couples the phase of the GS to ES carriers and also models the effect of inhomogeneous broadening [46]. The primary laser control parameters are  $\varepsilon$  and  $\Delta \equiv \omega_i - \omega_g$ , respectively the injection strength and the detuning between the frequency of the injected light and that of the GS. The pump current is  $J$ . The  $B$  terms  $B_{e,h}$  and  $B_{e,h}^w$  are the capture rates to the GS and ES respectively, while the escape rates are given by the  $C$  terms and are linked to the capture rates via Kramers type relations, as described in [46]. The different spin degeneracies in the QD energy levels, Pauli blocking, and interstate captures and escapes are all included.

As shown in Chapter 5 this model reproduces the phase-locking phenomenon

and the stochastic generation of excitable GS dropouts/ES pulses when noise is included. The dropouts in Chapter 5 were shown to terminate in a saddle focus with oscillations at each dropout minimum. However, as seen in the experimental traces, Figure 6.4, these oscillations do not appear in the dropouts with our shorter device and so we use a different set of parameters to better match the reduced photon lifetime. The dropouts then terminate in a saddle rather than a saddle-focus and there are no oscillations at the bottom of the dropout (see Figure 6.6) as in the experiment. Once the saddle is reached, the system moves along the repulsive trajectory, the ES emits a sharp pulse and the GS returns to CW operation.

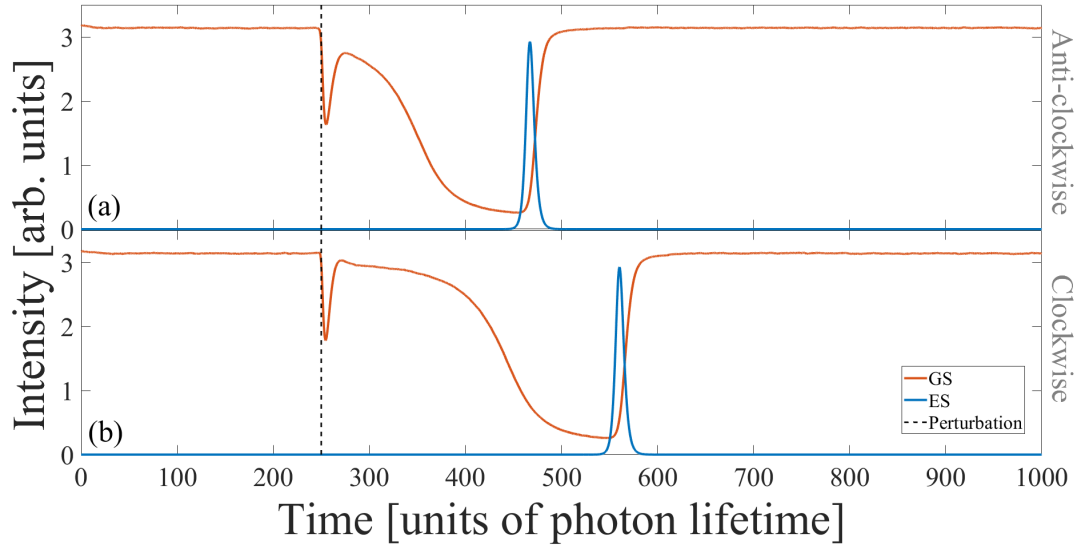


Figure 6.6: Numerically generated sample responses to an above threshold (a) anticlockwise perturbation where  $d = 1.7$  and (b) clockwise perturbation where  $d = -2$ . The longer response time for clockwise perturbations is partially due to the positive and non-zero  $\alpha$ . The fixed parameters are  $\eta = 0.01$ ,  $\Delta = 0$ ,  $\alpha = 3$ ,  $\beta = 1.5$ ,  $g_0^g = g_0^e = 0.55$ ,  $J = 5$ ,  $B_{e,h} = B_{e,h}^w = 100$ ,  $C_e^w = 0$ ,  $C_h^w = 100$ ,  $C_e = B_e e^{-2}$ ,  $C_h = B_h$ ,  $\varepsilon = 0.327$ .

For instantaneous perturbations the system displays asymmetric directional thresholds as found in the experiment. In fact, using instantaneous perturbations one can find an excitable interval. By increasing the amplitude of the perturbations from 0 rad to  $2\pi$  rad in one direction the  $2\pi$  periodicity means that there is a closed interval over which excitations are possible. However, instantaneous perturbations are unphysical and so we also investigate the more realistic case of finite time perturbations, specifically using sigmoid perturbations of the phase, to induce our excitations. These perturbations take the form  $d/(1 + e^{(-\sigma(t-t_0))})$  where  $d$  is the amplitude of the

perturbation,  $t_0$  is the centre of the perturbation and  $1/\sigma$  sets the rise time of the perturbation. To compare directly with the experiment, we analyse the effect of perturbations in both the anticlockwise and clockwise directions. Figure 6.3(b) shows the efficiency curves generated for the two perturbation directions for  $\sigma = 1$ . The existence of a threshold in each direction is clear. The anticlockwise threshold is approximately 0.975 rad while the clockwise threshold is approximately -1.7 rad for the chosen parameters, reproducing the experimentally observed asymmetry.

## 6.4 Discussion

There are some subtle details in using finite rise time perturbations, where the behaviour is necessarily more complicated than in the instantaneous perturbation case. During the perturbation the system can also evolve due to the intrinsic dynamics and the fast intrinsic timescales. As a result, the thresholds vary significantly depending on the duration of the perturbation. For sufficiently fast rise times of the perturbations, an interval can be obtained as with the instantaneous case. For example, with  $\sigma = 5$  we find an anticlockwise interval of excitation from 0.9 rad to 5.4 rad. That is, for anticlockwise perturbations above 5.4 rad, excitations are not obtained. The evolution of the system depends on the direction of the perturbation and so the interval also changes depending on the direction of the perturbation. Further, for slow rise times, an interval is not obtained. In fact, for sufficiently slow perturbations, pulses are never excited; instead the system simply adiabatically follows the slowly changing phase. Of course, this is also found in the case of optical injection of conventional devices.

### 6.4.1 Phase measurement

The phase measurement technique has already been described in Chapter 2 and Chapter 5. These were relatively straightforward experiments but when performing phase measurements for deterministic triggerings there are some subtleties that cannot be overlooked. As mentioned there are two inputs into a  $3 \times 3$  coupler. One arm receives light from the TLS after it has gone through the phase modulator and the other receives light from the QD laser and the third is left empty. The path lengths to each arm are set so that when the 10% of perturbed light from the TLS enters the  $3 \times 3$  coupler it is mixed with CW light

from the QD laser. Consequently the light from the response of the QD laser is mixed with CW light from the TLS.

To reconstruct the phase of the QD laser, two measurements must be taken. First, the phase of the perturbed TLS and then the response of the QD laser. These are later subtracted from each other in a post processing step. To measure the perturbation encoded by the modulator on the light coming from the TLS, the QD laser is operated in CW and acts as a reference. The blue line in Figure 6.7(c) shows the phase of the perturbed light with respect to a CW reference. This is an effective way to measure the amplitude of the perturbation applied. In Figure 6.7 (c) the square pulse has amplitude 5.7 rad. The orange line in figure 6.7(c) shows the optically injected QD with respect to a CW TLS signal.

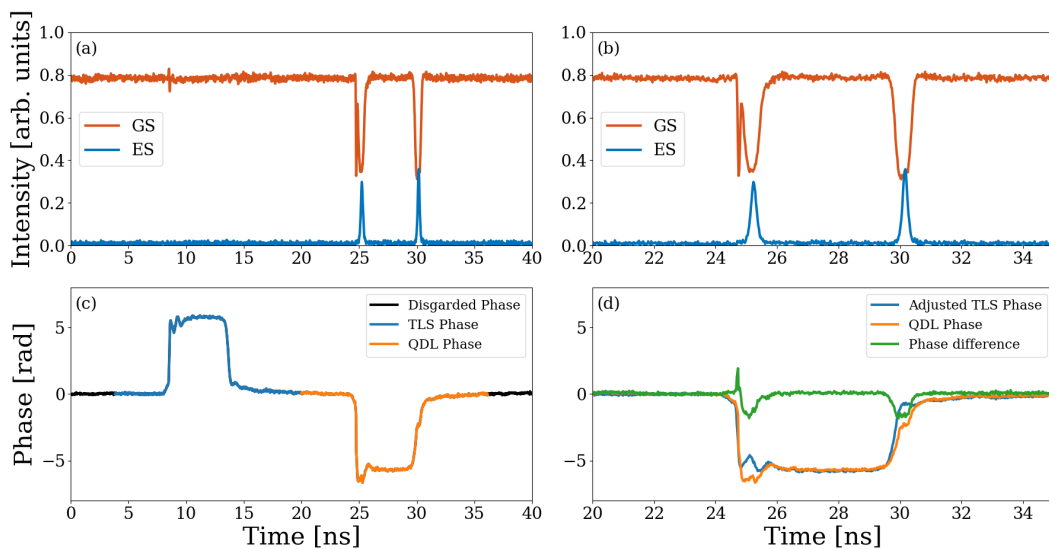


Figure 6.7: (a) Intensity traces from a QD laser. (b) A zoom in on the intensities where the QD laser is emitting pulses after clockwise and anticlockwise perturbations were applied. (c) The phase of the TLS with respect to CW QD laser and the phase of the QD laser light with respect to CW TLS light. The phase perturbation amplitude can be measured, 5.7 rad. (d) To see what the QD laser is doing with respect to the TLS while it is perturbed, the two must be aligned and subtracted.

The end goal of this technique is to measure how the phase of the secondary laser evolves with respect to the primary laser. At the moment the electric field of the secondary laser is only shown with respect to a CW field, the orange line in Figure 6.7(c). Because of phase locking the primary laser's phase will simply be mirrored by the secondary laser and appear inverted when the CW field of

the TLS is used as the reference. Here, in Figure 6.7(c) there are two similar square shapes, one shows the phase change of the TLS (blue) and the other shows the secondary laser (orange) trying to follow the primary, but importantly there are some differences (apart from the fact they are inverted). These differences are where the secondary laser momentarily loses phase locking and pulses are triggered, due to sufficiently fast perturbations. It is difficult to interpret the result because when observing the phase of the secondary laser (orange) with respect to a CW reference there is information about both the perturbations and the response of the secondary laser. To decouple the information and see how the secondary laser is acting with respect to the perturbing primary, the primary laser's phase (blue) is inverted and aligned with the phase of the QD laser (orange) and the difference between them is calculated. The green line in Figure 6.7(d) shows the response of the secondary laser with respect to the perturbed primary. Initially the QD laser tries to follow the clockwise perturbation as there is a sharp increase in phase. Then the phase begins to decrease and appears to go on an excitable trajectory as a pulse is triggered, Figure 6.7(b) and 6.7(d). The phase returns to steady state before the anticlockwise perturbation triggers a second pulse and a similar phase trajectory is observed.

The GS and ES intensities are shown in Figure 6.7 (a). There is a small fluctuation around 8 ns where the rise time of the perturbation is measured. This is a result of the light from the TLS and the CW QD laser mixing in the  $3 \times 3$  coupler, a quick change in phase alters the amount of constructive/deconstructive interference. The intensity fluctuation therefore is a result of the measurement and is not related to the light being injected into the QD laser.

Figure 6.8 (d) and Figure 6.9 (d) show rainbow plots that illustrate that it is in fact the same excitable trajectory being undertaken regardless of the perturbation direction. The different colours show different sections of the timetrace. The dark purple section in Figure 6.8 (e) show the clockwise phase perturbation. 5.7 rad is very close to  $2\pi$  so the perturbation almost completes a full circle. The pink line shows the anticlockwise perturbation and it returns to the same point. There are much fewer points on the clockwise perturbation than in the anticlockwise due the faster rise time. Figure 6.8 (d) shows the phase of the QD laser after the perturbations were applied. The dark purple corresponds to the response of the QD laser when the clockwise perturbation was applied. Initially the QD laser tries to follow the TLS and moves in the

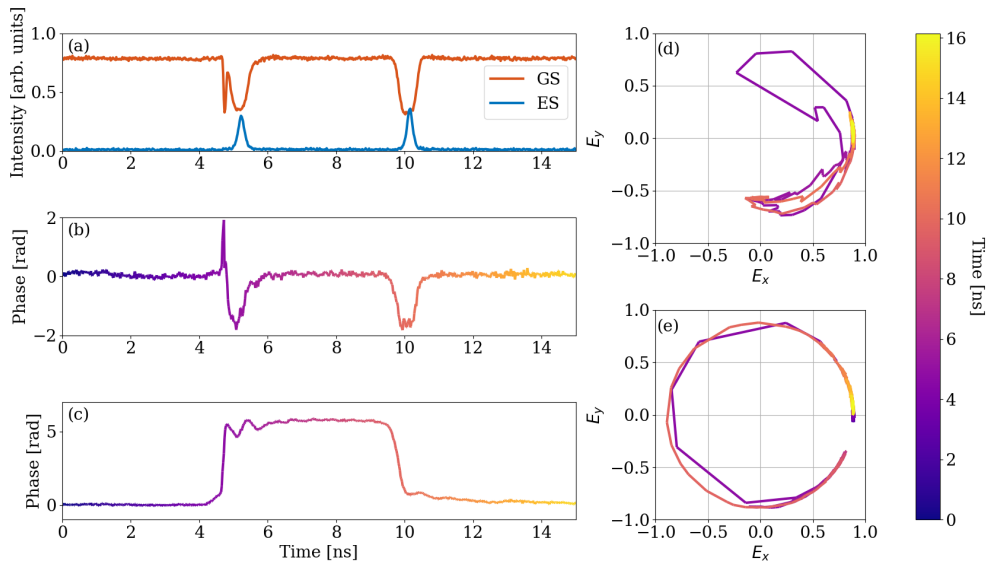


Figure 6.8: (a) intensity timetraces of the GS and ES after successful clockwise and anticlockwise perturbation. (b) the phase measurement is shown in a rainbow plot. The colour of the line changes in time for easy comparison to the phasor plot (d). (c) shows the phase of the TLS, the perturbation is 5.7 rad. (d) the phasor diagram showing the phase of the QD laser. Initially there is a large kick brought about by the clockwise perturbation. The trajectory turns around and completes a bounded rotation. After the anticlockwise perturbation the initial trajectory is not present, but the bounded trajectory is the same. (e) shows the phasor diagram corresponding to the TLS perturbation in (c).<sup>1</sup>

same direction and then changes course and completes an excitable bounded trajectory. When the excitable trajectory brought about by the anticlockwise perturbation is plotted on top (pink) it's clear that the traces are very similar. It is likely that these pulse are from the same trajectory in phase space. Two different routes can each achieve an excitable response which leads to two thresholds. When a smaller amplitude perturbation is applied in Figure 6.9 a similar result is observed. The initial kick in the clockwise direction doesn't produce as large an initial excursion but inevitably the excitable trajectory is the same.

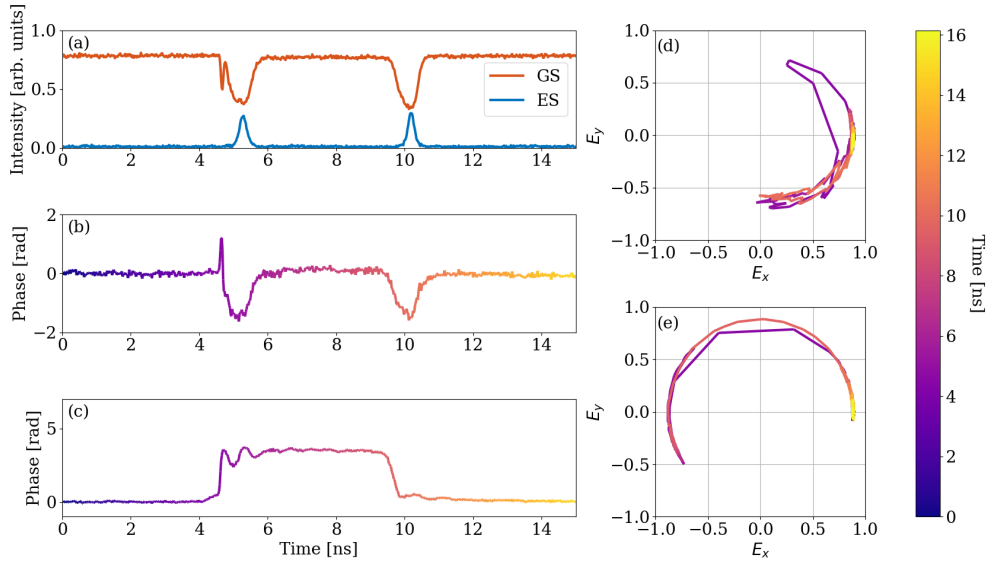


Figure 6.9: (a) intensity timetraces of the GS and ES after successful clockwise and anticlockwise perturbation. (b) the phase measurement is shown in a rainbow plot. The colour of the line changes in time for comparison to the phasor plot (d). (c) shows the phase of the TLS, the perturbation is 3.5 rad. (d) the phasor diagram showing the phase of the QD laser. The clockwise perturbation is not as large as it was in Figure 6.8 so the initial trajectory is not as far. The trajectory still turns around and completes a bounded rotation. After the anticlockwise perturbation the initial trajectory is not present, but the bounded trajectory is the same. (e) shows the phasor diagram corresponding to the TLS perturbation in (c).<sup>1</sup>

With all conventional single state only Type I excitable scenarios in the optical injection configuration, the phase evolution is the dominant characteristic of the excitable trajectory and much of the underlying physics can be understood via the Adler model. In particular, this results in the appearance of one threshold only. However, in our dual state system, the phase is not the dominant parameter since the underlying physics is akin to that of Q-switching [136] rather than phase rotations and so a one dimensional reduction of the dynamic is not possible. This is reflected in the excitable trajectory which can now be reached via either direction.

<sup>1</sup>We have chosen to discuss phase in the reference frame of the primary laser. As mentioned earlier, the rising edge of the square electrical pulse corresponds to a clockwise perturbation, where the phase of the secondary laser is moving in a clockwise direction with respect to the primary. However, when measuring the perturbation directly using the  $3 \times 3$  technique, we can only observe the phase of the primary laser in the reference frame of the secondary laser. This is why the phase appears to rotate in the opposite direction in (e).

In summary, we have shown that the novel Type I excitable behaviour first reported in Chapter 5 can be deterministically triggered - a crucial property for any potential applications. What's more, in contrast to all existing reports of Type I excitability in the optical injection configuration, there are two asymmetric excitable phase perturbation thresholds in this system. The insensitivity of the ES response to sub threshold perturbations may also be valuable for error avoidance. Other excitable regimes where phase is not the dominant characteristic may also have similar two threshold properties, such as the Type II excitability [37].

# Chapter 7

## Dual state excitability neuromorphic capabilities

### 7.1 Refractory Periods

Obviously the faster a network can process data the better, but there is a limit. After a pulse is fired the system takes some time to recover as it returns to a steady state. After this time has passed another pulse can be triggered. This period of time is known as the refractory period. The end of the refractory period is called the refractory time. More specifically there are two; during the absolute refractory period it is impossible to trigger a second pulse; during the relative refractory period it is possible to trigger a second pulse but it is somewhat inhibited and the delay times can be difficult to predict. Therefore the fastest a reliable LIF neuron can fire a subsequent pulse is after the relative refractory period has passed.

Previous studies have found the absolute and relative refractory periods for a semiconductor laser with a saturable absorber [30]. During the relative refractory period the second pulse was inhibited because the gain did not have sufficient time to fully recover. The absolute refractory period was also investigated in an optically injected VCSEL laser, where phase perturbations were used to excite pulses [20]. The theoretical simulations indicate that the relaxation oscillations (ROs) are responsible for a small number of pulses being triggered before the absolute refractory period had passed.

Similar to Chapter 6 the detuning was set so the secondary laser remained phase locked to the primary and noise was not sufficient to trigger any pulses.

To measure the refractory period we need to perturb the QD laser with two perturbations and vary the time between them, then measure the response of the system. The perturbations are of the same form as those discussed in Chapter 6. A second phase modulator was placed in series with the original, see Figure 7.1. The signal from the pulse generator was split with a 50/50 power splitter. A variable electrical delay line was used to finely adjust the time at which a perturbation arrived at one modulator, relative to the other modulator. Different length high speed RF cables were used for coarse adjustments. There are some limitations to the setup. Because the cable length and number of connections are different the signals reaching each phase modulator are not identical. Although the modulators are the same model they have slightly different responses.

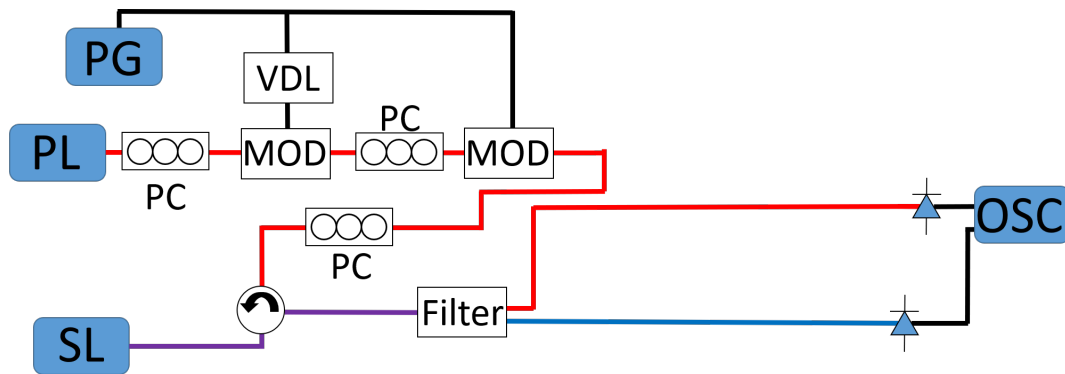


Figure 7.1: A second  $\text{LiNbO}_3$  phase modulator is added in series to the setup shown in Figure 6.2. Again the secondary laser (SL) is a QD laser and the primary laser (PL) is a tunable laser source (TLS). The  $\text{LiNbO}_3$  phase modulators are driven by a pulse generator (PG). A 50:50 power splitter sends a similar signal to each modulator (MOD). A variable electrical delay line (VDL) is added to adjust the time between two perturbations. A polarisation controller (PC) is used to maximise coupling. The light emitted from the SL is sent into the circulator and then to a filter where the ES and GS light are separated and are sent directly to 12 GHz detectors connected to an oscilloscope (OSC). The red lines represent light at approximately 1300 nm close to the GS emission, the blue is ES only and the purple is both GS and ES. The black are high speed electrical cables.

### 7.1.1 Small amplitude anticlockwise perturbations and refractory periods

Remembering that the signal from the pulse generator is a square pulse, clockwise and anticlockwise perturbations always perturb the system 5 ns

apart. The perturbation strength was initially set to approximately  $\pi$  rad, where there was little variation in delay time for a single anticlockwise perturbation, see Figure 6.5. This amplitude provides the simplest case where only anticlockwise perturbations excite a pulse. The clockwise perturbations were still sub-threshold but the time at which they perturbed the system corresponded to sharp negative spikes in the GS intensity. This allowed for a convenient measurement of the time between perturbations, see Figure 7.2 at approximately 2 ns.

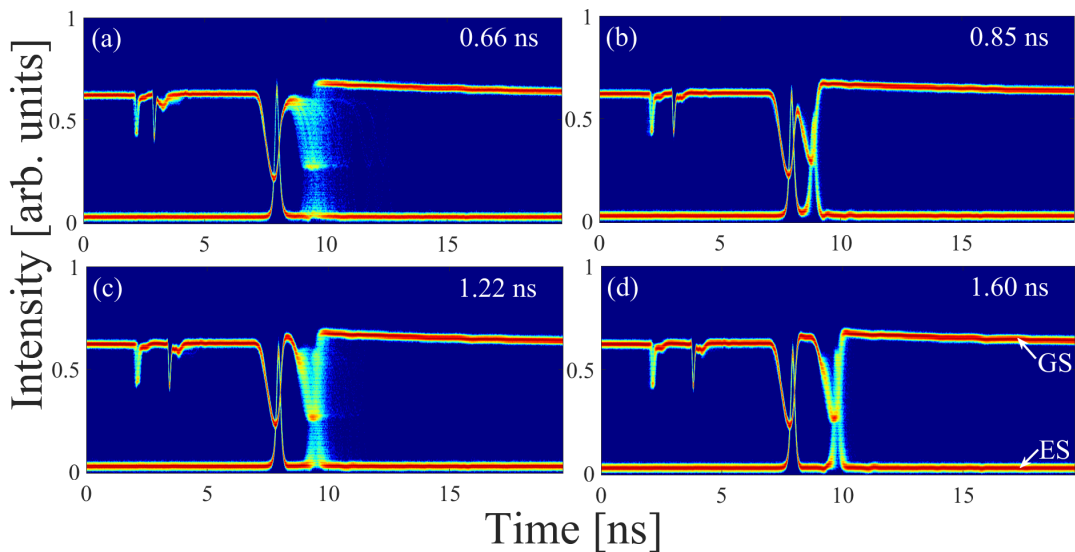


Figure 7.2: (a) Timetraces close to the absolute refractory period, the second pulse can have long escape times. (b) Perturbations separated by 0.85 ns. There is a narrow distribution as the first dropout is interrupted. (c) Perturbations are separated by 1.22 ns, there is a large distribution of delay times because a relaxation oscillation increases the threshold. (d) The system has returned to steady state when the second perturbation is applied and the relative refractory period has passed. The two small GS negative spikes at approximately 2 ns are the location of the subthreshold clockwise perturbations.

The first perturbation always triggered a pulse, see Figure 7.2. Figure 7.3 (a) shows the average times between two ES pulses vs the time between two perturbations, in the cases where two perturbations triggered two pulses. If the second perturbation arrived before 0.62 ns a second pulse is never fired, 0% efficiency shown by the red dotted line in Figure 7.3(a). This marks the boundary of the absolute refractory period. Close to the absolute refractory time the escape time for the second pulse refractory time can be as large as 2 ns for perturbations 0.62 ns apart, see Figure 7.3 (a). To get a better idea of how the system reacts with respect to the perturbations, the responses are

normalised to the time between perturbations in Figure 7.3 (b). A value of 1 represents the case where the time between two pulses is equal to the time between perturbations. Figure 7.3 (b) shows a large standard deviation of times between ES pulses close to the absolute refractory time, highlighting how the escape time of the second pulse is influenced by noise. In Figure 7.4 a heatmap shows the distribution of response times of the second pulse and it is clearly much wider for perturbations that arrive closely in time.

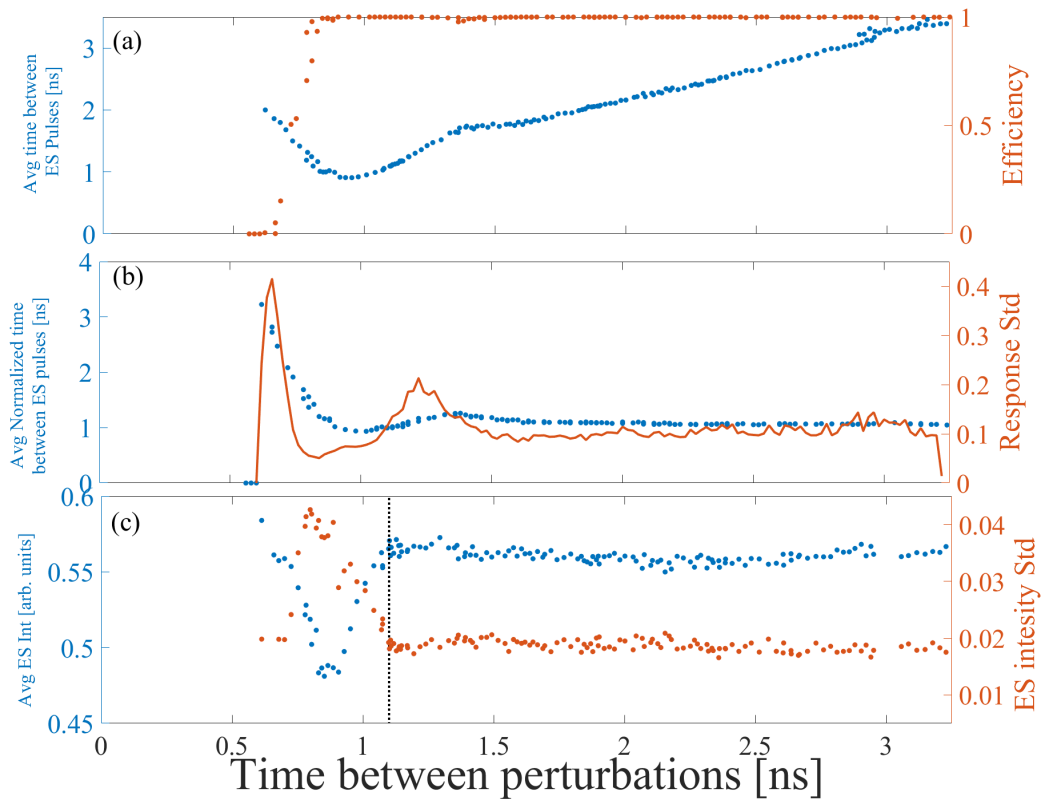


Figure 7.3: (a) (Blue) Average time between two ES pulses after two perturbations were applied vs the time between two perturbations. Each data point is the average of 1000 sets of perturbations. The first perturbation was always successful. The absolute refractory period was 0.62 ns. (Red) Efficiency of the second perturbation. The first perturbation was always 100 % successful. (b) (Blue) the normalised average times between two ES pulses after two perturbations were applied vs the time between perturbations. The average is of 1000 sets of perturbations. (Red) standard deviation of the times between two ES pulses. (b) The average peak intensity of the second ES pulse vs the time between perturbations. (Red) The standard deviation of the peak intensities vs the time between perturbations.

Now we look at the characteristics slightly after the absolute refractory time has passed in Figure 7.2 (a). A heatmap shows many pulses being fired, where

the time between perturbations is 0.66 ns. This value is chosen as multiple second pulses are fired, making it possible to visualise the large distribution of the second pulse's delay times even though the time between perturbations remains constant.

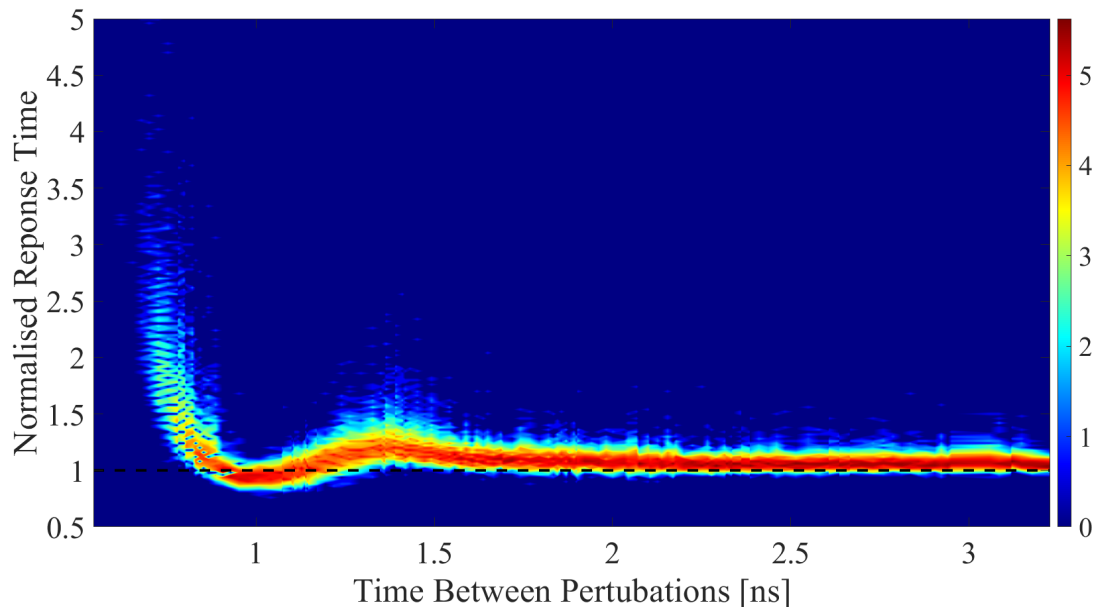


Figure 7.4: The normalised times between two ES pulses after two perturbations were applied, shown in Figure 7.3 (a), have been normalised to the time between perturbations. The first perturbation was always successful.

Between 0.8 ns and 1.2 ns the normalised time between two ES pulses goes below 1, see Figure 7.3 (b). This means that the time between pulses is less than the time between perturbations. Although this appears like the system is preempting a pulse, this is not the case. The second pulse is indeed triggered after the second perturbation. After the first pulse is fired the system has not had adequate time to return to a steady state when the second perturbation arrives. The system appears to be very close to the excitability threshold, hence it doesn't take as much of the perturbation's rise time to kick the system past the threshold again. Figure 7.2 (b) shows the GS intensity does not return to its steady state value before the second dropout is triggered. So the time between the second perturbation and second pulse is shorter than the time between the first perturbation and first pulse. Figure 7.3 (b) shows the standard deviation of times between ES pulses and it is smallest between 0.8 ns and 1.2 ns. We have seen that the distribution of response times for a single perturbation gets smaller with larger perturbation amplitudes in Figure

6.5. Here, when the second perturbation is applied, the system is closer to the threshold so it has a similar effect to a very large perturbation.

Between 1.2 and 1.5 ns the normalised time between two ES pulses increases beyond 1 and the standard deviation of times between two ES pulses increases again, see Figure 7.3 (b). This also corresponds to a small decrease in efficiency shown in Figure 7.3 (a) to 98% at 1.36 ns. This is due to GS relaxation oscillations. Figure 6.9(d) shows the phase diagram of a pulse after one perturbation. The yellow section is the steady state phase value, but above it there is a small overshoot represented by light pink. This overshoot occurs when the system is returning to steady state. The system finds itself further away from the separatrix, which will make it more difficult to trigger a subsequent pulse. The amplitude of the second perturbation is not large enough to perturb the system far enough beyond the separatrix to negate the effects of noise. So the system finds itself close to the separatrix and thus there is a large distribution of escape times and an increase in the probability of failure. This failure can be avoided by using a slightly larger perturbation amplitude, as discussed below. When the time between perturbations goes beyond 1.5 ns in Figure 7.3 (b) the normalised time between two ES pulses remains constant at 1, and the standard deviation remains fixed at 1.5 shown in Figure 7.3 (b), thus we define 1.5 ns as the relative refractory time.

Figure 7.3 (c) shows the average peak intensities of the second ES pulses and their standard deviation for different times between perturbations. Initially the average peak intensity is large, then it decreases to a small plateau before increasing again as the time between perturbations increases. The high intensities for short times between perturbations are because the pulses have long delay times and are actually triggered hundreds of picoseconds after the perturbation arrives, as shown in Figure 7.3 (a). The decrease in the average ES pulse peak intensity around 0.85 ns is due to the first dropout being interrupted by the second perturbation and the subsequent trajectory of the second GS dropout not being not as deep, Figure 7.2 (b). Therefore there is less gain available for the ES pulse. This is not to be misunderstood with a lack of ES gain due to slow carrier scattering into the dot, where the scattering rate into the dots is of the order of 10s of picoseconds. Figure 7.5 shows the relationship between the GS and ES intensities and the time between triggered pulses. For close triggerings the GS trough depth intensity can vary between 0.25 and 0.31, whereas the ES pulse varies from 0.4 to 0.6. The width of a GS dropout is much larger than the ES pulse width so a small change in GS

dropout depth has a bigger impact on ES pulse peak intensity. Surprisingly, Figure 7.3 (c) shows that the ES pulse peak intensity varies most in the region where the response time is most predictable, shown in Figure 7.3 (b). As mentioned the system hasn't reached steady state if the second perturbation is applied between 0.8 ns and 1.2 ns after the first one. So the path to the trough of the dropout (corresponding to the saddle/saddle focus in phase space discussed in Chapter 5) is no longer the natural trajectory. The forced trajectory is sensitive to noise leading to different dropout depths. The variation in the ES intensity is less than industry standard 3 dB tolerance, therefore, the optimal rate to pass information through the device is actually inside the relative refractory period at 0.85 ns.

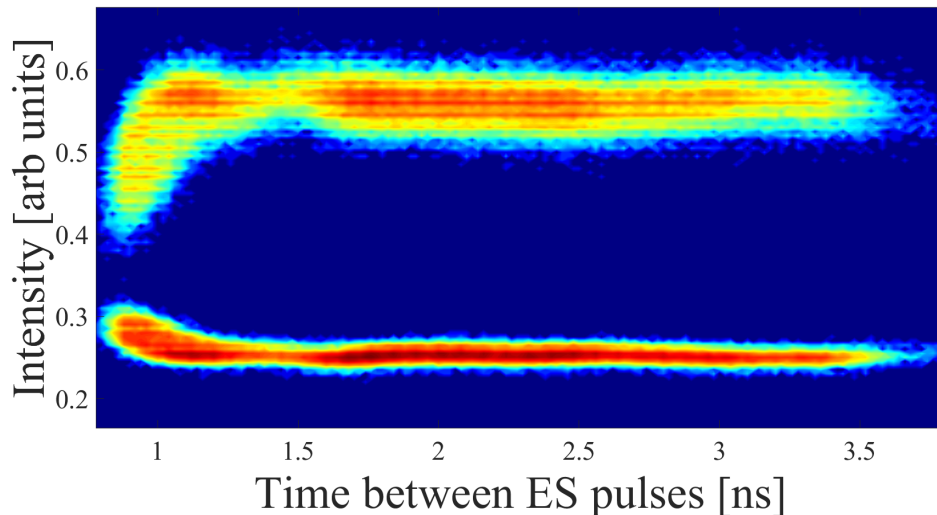


Figure 7.5: Heat map showing the ES peak intensity (top) and the intensity of GS dropout troughs (bottom) vs the time between ES pulses.

### 7.1.2 Large amplitude perturbations and refractory periods

In order to investigate the refractory periods using clockwise perturbations the amplitude of the perturbations was increased to approximately 5.5 rad, where a single clockwise perturbation was 100% successful in triggering a pulse with short delay times. Due to the nature of the square electrical pulse, the refractory periods using large anticlockwise perturbations were simultaneously investigated. Because clockwise perturbations are now triggering pulses the GS intensity cannot be used to measure the time between perturbations. To obtain the time between two perturbations the derivative of the phase is found, Figure 7.6, and the time a perturbation occurs is defined to be the point where

its slope is steepest. This is necessary because it can be difficult to resolve two perturbations when the time between them is much less than their rise times.

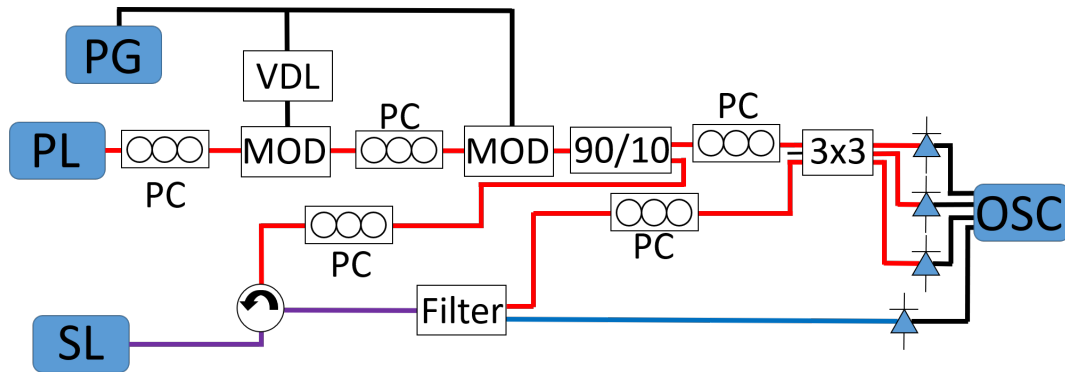


Figure 7.6: A unidirectional optical injection experiment similar to the one shown in Figure 7.1 is set up, where the secondary laser (SL) is a QD laser and the primary laser (PL) is a tunable laser source (TLS). Two  $\text{LiNbO}_3$  phase modulators, driven by a pulse generator (PG), are placed between the PL and SL, which perturbs the injected light. A variable delay line (VDL) is used to adjust the time between perturbations. After modulation, light from the (PL) is split; 10% is sent into one arm of a  $3 \times 3$  coupler for an interferometric phase measurement technique. 90% is sent to a circulator and is then injected into a QD laser. A polarisation controller (PC) is used to maximise coupling. The light emitted from the SL is sent into the circulator and then to a filter where the ES and GS light are separated. The GS light goes into another arm of the  $3 \times 3$  coupler and the ES light is sent directly to a 12 GHz detector. The third arm of the  $3 \times 3$  coupler is left empty. Polarisation controllers are used to maximise the interference of the  $3 \times 3$  coupler input signals. All 3 outputs of the  $3 \times 3$  coupler are connected to a 12 GHz detectors which are connected to an oscilloscope (OSC). The red lines represent light at approximately 1300 nm close to the GS emission, the blue is ES only and the purple is both GS and ES. The black are high speed electrical cables.

### 7.1.2.1 Anticlockwise perturbations

Large anticlockwise perturbations produced similar results to those seen in Section 7.1. The first perturbation always excites a pulse as shown in Figure 7.7 but the absolute refractory period is shorter with a pulse recorded where the time between perturbations was 0.42 ns, the timetrace is shown in Figure 7.8. After 0.63 ns the second perturbation is 100% successful in triggering a pulse, Figure 7.7. However, just before this efficiency is achieved a new dynamic arises as a result of the anticlockwise perturbations being so large. If the second perturbation arrives between 0.56 ns and 0.90 ns after the first, then three pulses appear to be triggered. As usual the first perturbation always

triggers a pulse, but when the second perturbation interrupts the first dropout it can force the GS into a much more shallow dropout with a corresponding small increase in ES intensity. A third dropout and full ES pulse can then fire after some delay, see Figure 7.9(b). The efficiency curve for three ES maxima has a peak probability of 95% at perturbations separated by 0.72 ns, although it never reaches 100 % this high probability still suggests that there may be some deterministic trajectory being undertaken. After the first perturbation the system hasn't returned to steady state and a large kick moves the system even further from its natural trajectory in phase space, the most likely route back to the steady state appears to be through an extra oscillation. When three pulses do not fire, the two perturbations operate as expected and produce two dropouts with two ES pulses. Figure 7.9(a) shows a timetrace for the same perturbation spacing as Figure 7.9(b) but only two pulses fire. The minimum peak intensity of a second ES pulse, when only two pulses fire, is defined to be the minimum amplitude required to claim a full ES pulse has indeed been fired, which will be used in the next section.

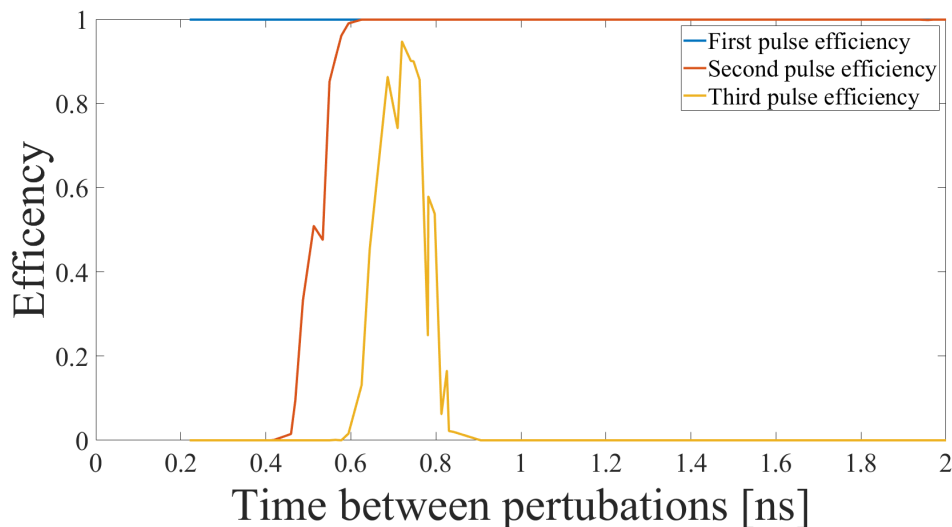


Figure 7.7: Blue line shows the efficiency of the first perturbation. It always excites a pulse. The red line shows the efficiency of the second perturbation. 0.42 ns marks the end of the absolute refractory period, if the second perturbation arrives 0.42 ns after the first, a second pulse can be observed, timetrace shown in Figure 7.8. After 0.63 ns the second perturbation always triggers a pulse. Between 0.56 ns and 0.90 ns two perturbations can produce three pulses, timetrace shown in Figure 7.9.

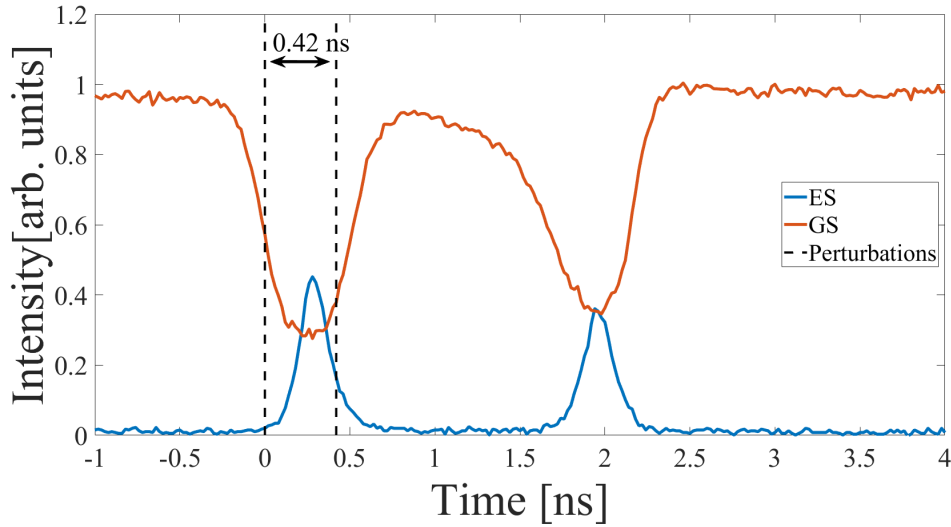


Figure 7.8: Timetrace showing two anticlockwise perturbations applied 0.42 ns apart and both trigger a pulse. This marks the absolute refractory time.

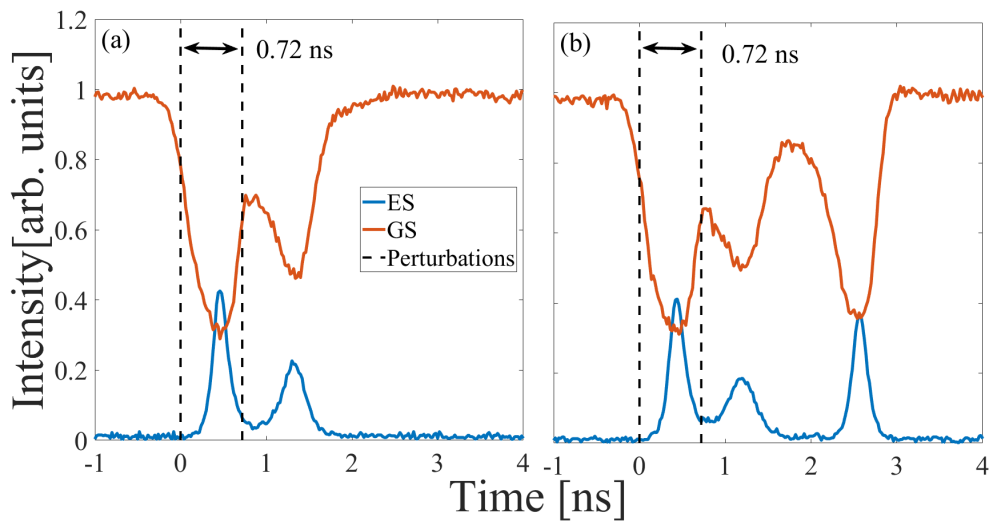


Figure 7.9: (a) Timetrace showing two pulses arising from two perturbations, the time between the two perturbations is 0.72 ns. (b) Timetrace showing three pulses arising from two perturbations with the same time between them as in (a). There is a 95% probability of three pulses occurring for this perturbation separation.

Figure 7.10 shows the average normalised time between ES pulses after two large anticlockwise perturbations were applied. The average normalised time goes below 1 at 0.9 ns, similar to the case where two smaller anticlockwise perturbations were used in Figure 7.3 (b). The first dropout is interrupted and system is close to the threshold when the second perturbation arrives. Less of

the perturbation's amplitude is required to trigger a pulse, so the threshold is exceeded earlier in the perturbation's rise time. What is absent in the case for large perturbations is the increase in average response time at 1.3 ns, where the GS relaxation oscillations previously brought the system further from threshold. This is however a slight increase in the standard deviation. With the larger perturbation amplitude we can help to compensate for the GS relaxation oscillation which temporarily makes the threshold larger. The relative refractory period ends at 1.4 ns.

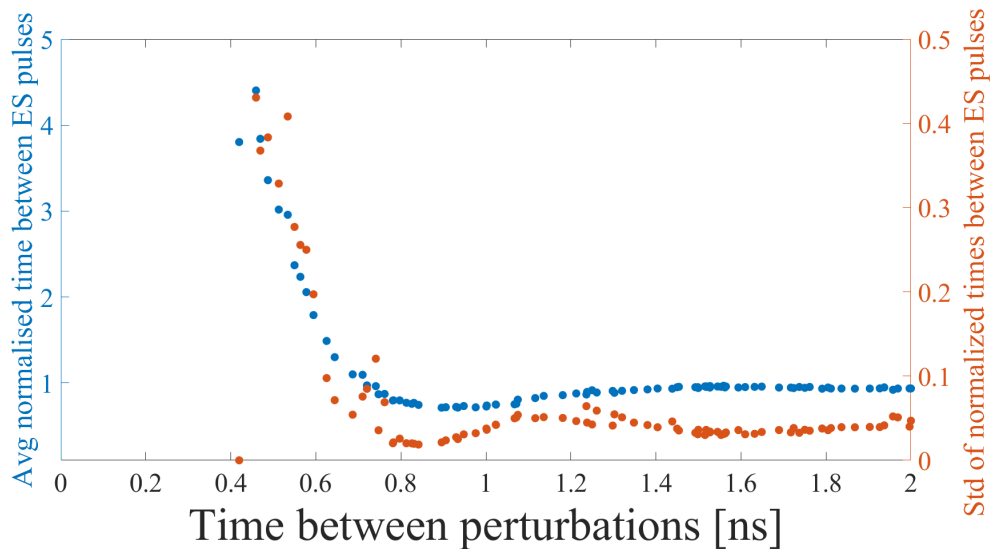


Figure 7.10: (Blue) the average time between two ES pulses after two anti-clockwise perturbations are applied. (Red) the standard deviation of the times between two ES pulses.

### 7.1.2.2 Clockwise perturbations

#### Inhibitory perturbations

The presence of an excitable interval was proposed in Section 6.3 for instantaneous perturbations. This interval was not observed using one phase modulator with its finite rise time. However, a slow rise time can be compensated for by applying a large enough perturbation. Alternatively, two perturbations arriving closely in time can sum together to produce this large perturbation. The closest time recorded between two clockwise perturbations was 0.22 ns. If the time between two clockwise perturbations is between 0.22 and 0.47 ns the second perturbation stops the first perturbation from triggering a pulse, a timetrace is shown in Figure 7.11. This inhibitory behaviour is not observed for anticlockwise perturbations. This is likely due to

the clockwise perturbation resembling more of an instantaneous perturbation as the rise time is faster than the anticlockwise fall time given by the electrical pulse from the pulse generator. The ability to inhibit a pulse is a useful tool in the toolbox for optical computation and photonic neural networks.

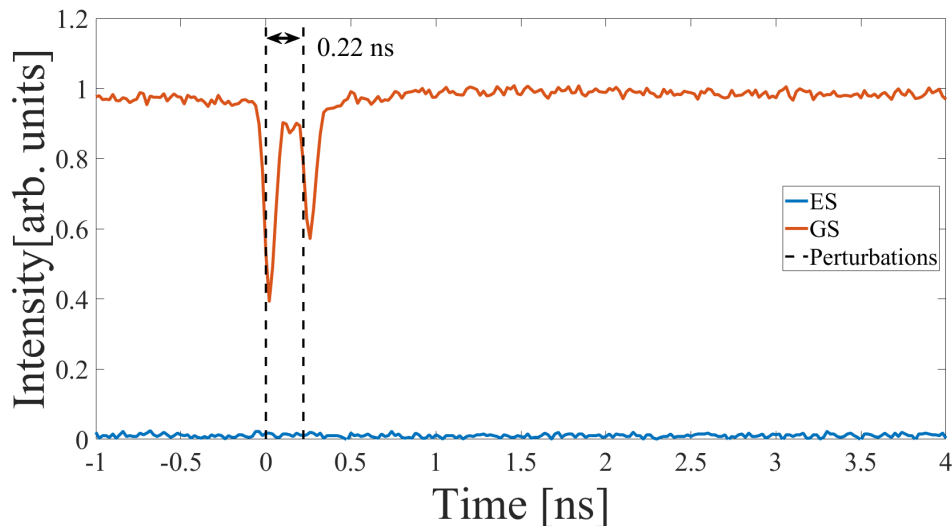


Figure 7.11: Timetrace showing that a second clockwise perturbation can inhibit the first perturbation if it arrives close enough in time. In this case the perturbations are separated by 0.22 ns.

### Perturbations arriving during first GS dropout

As the time between clockwise perturbations is increased the system has more time to undergo the first dropout before the second perturbation arrives. The second perturbation does not always completely inhibit the pulse triggered by the first perturbation. In fact we classify the laser's responses into four different categories when the perturbations are separated by between 0.47 and 0.93 ns. Figure 7.12 shows all four behaviours which were observed when the time between between perturbations remained constant at 0.84 ns. Figure 7.12 (a) is the inhibitory case discussed in Section 7.1.2.2. In Figure 7.12 (b) the ES intensity increases slightly but not enough to be deemed a pulse, which has previously been defined in Section 7.1.2.1. Figure 7.12 (c) shows the conventional case when the second perturbation arrives before the absolute refractory time has passed. The first perturbation excites an ES pulse which has sufficient amplitude to be considered a full pulse and the second arrives too early and does not. In Figure 7.12 (d) a small increase of ES intensity is observed when the first perturbation is applied but similar to the case shown in Figure 7.12 (c) it is not large enough to deem it a pulse. The second

perturbation can trigger a pulse with a significant delay time.

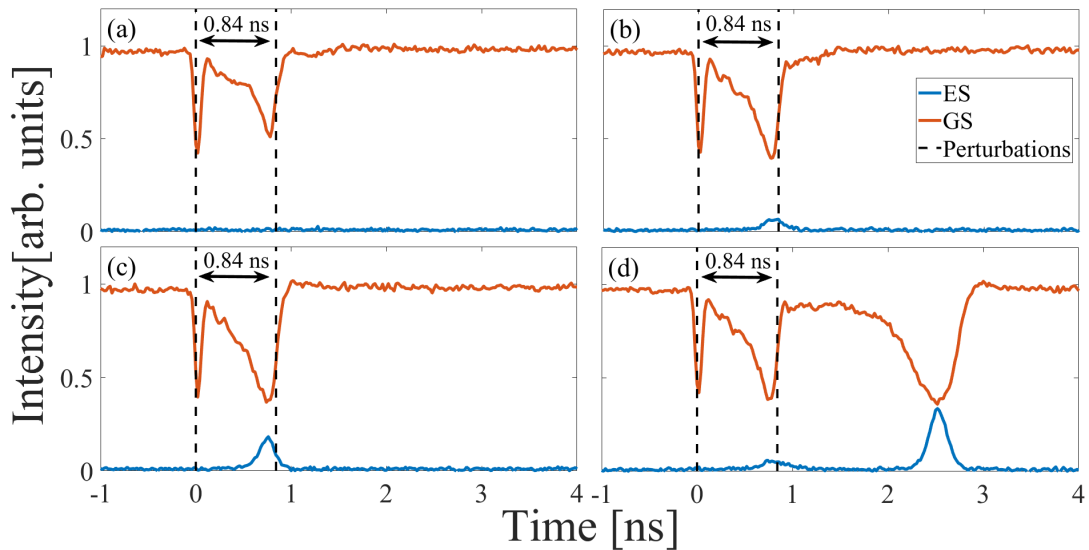


Figure 7.12: Four different behaviours are observed when the time between two clockwise perturbations is between 0.47 and 0.93 ns. This figure shows examples of each behaviour when the perturbations are separated by 0.84 ns. (a) the second perturbation inhibits an ES pulse that would have been triggered by the first perturbation. (b) there is a small increase in ES intensity but not enough to deem it a pulse. (c) the peak ES intensity is large enough and is considered a pulse. (d) the first perturbation does not trigger a pulse as the second perturbation acted as an inhibitory signal. But a pulse is triggered after the second perturbation.

If two perturbations can sum together and do not produce a pulse and if the time between them is increased so as the same two perturbations can trigger two separate pulses, it is no surprise that there is a region between these distinct behaviours where both of these dynamics are observed for the same experimental parameters. As mentioned the region spans from 0.47 to 0.93 ns, which has similar values to the region where three pulses are observed for two anticlockwise perturbations shown in Section 7.1.2.1, which spans from 0.56 ns to 0.90 ns. Although both cases show small increases in ES intensity, these are very different behaviours. In the anticlockwise case the first pulse always fired and the second perturbation caused a shallow dropout freeing up some gain for the ES. Here the first dropout is shallow because it was partly inhibited but some gain was still available for an increase in ES intensity. When the perturbations are this large the all or none response of the system, previously observed for smaller anticlockwise perturbations in Section 7.1, can be destroyed. However, this is obviously necessary in order to achieve an

integrate and inhibit mechanism.

### Conventional refractory times

To investigate refractory times the first perturbation must always excite a pulse, so the behaviour in Figure 7.12 (c) must first be achieved. An efficiency curve for this case is plotted in Figure 7.13. If perturbations arrive at least 1 ns apart there is 100% probability that the first perturbation will trigger a pulse. The absolute refractory period ends when two perturbations are separated by 1.02 ns, where there is a 0.003% probability that the second perturbation will trigger a pulse given that the first perturbation already has excited a pulse. When the time between perturbations is increased to 1.18 ns the second perturbation is 100% successful in triggering a pulse.

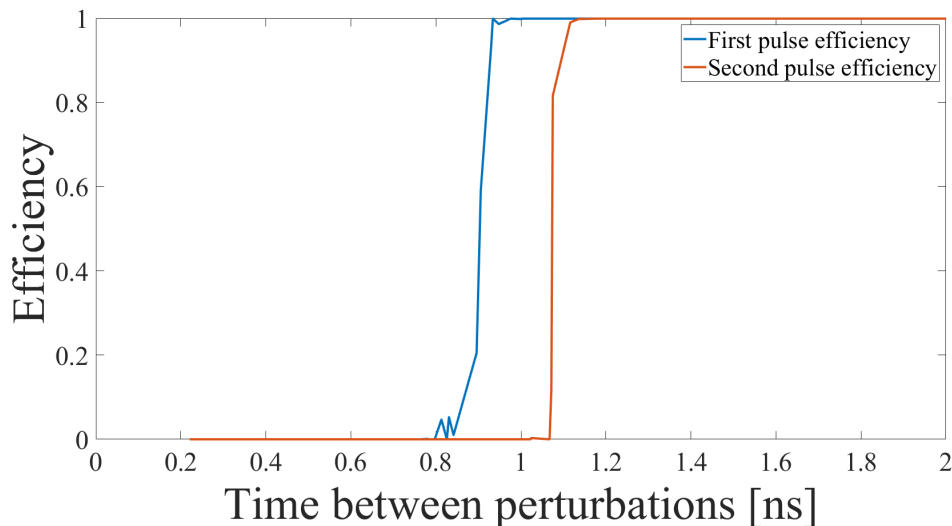


Figure 7.13: Efficiency curves for the first clockwise perturbation (blue) and the second clockwise perturbation (red) given that the first perturbation has already triggered a pulse.

The shape of the normalised time between two ES pulses curve in Figure 7.14 is similar to the anticlockwise case in Figure 7.10. Here the average time between ES pulses is large close to the absolute refractory period (1.02 ns) and then it levels off to a constant value at 1.25 ns marking the end of the relative refractory period. A feature missing from the clockwise curve is that the average time between ES pulses never goes below 1. For this to happen the system must be perturbed when it is close to its threshold. But as mentioned in Chapter 6 there are two separate thresholds for each perturbation direction. In the clockwise case the threshold is not as close to the excitable trajectory, see

Figure 6.8. This is further evidence that the two thresholds are indeed separate. There is also not an increase in average response time like there was in Figure 7.3 (b) because the perturbation amplitude was large enough to exceed the threshold even if a relaxation oscillation increases it marginally.

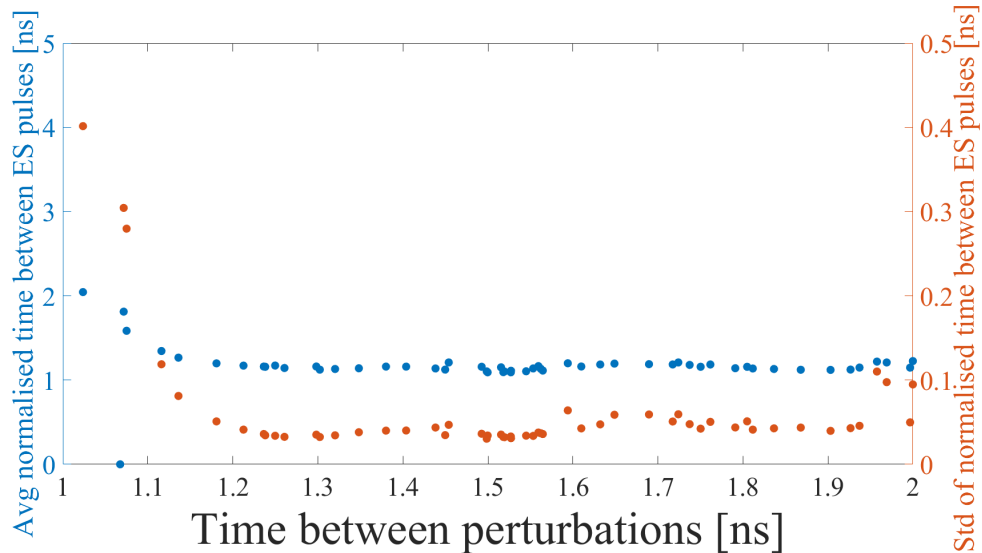


Figure 7.14: (Blue) the average time between two ES pulses after two clockwise perturbations are applied. (Red) the standard deviation of the times between two ES pulses.

To conclude the discussion on the effects of two above threshold perturbations we now summarise the results:

- For small anticlockwise perturbations the first perturbation always triggered a pulse. The absolute refractory period ended at 0.62 ns and the relative refractory period ended at 1.5 ns. There is an optimal time where subsequent pulses can be reliably triggered in time with a small fluctuation in the ES pulse amplitude at 0.85 ns.
- For large anticlockwise perturbations the first perturbation was always 100% successful in triggering a pulse. The absolute refractory period was recorded at 0.42 ns. The relative refractory period ended at 1.4 ns.
- Large clockwise perturbations can integrate an inhibit. If perturbations are separated by 1 ns the first perturbation always triggers a pulse. The absolute refractory period ends at 1.02 ns and the relative refractory period ends at 1.25 ns.

While the absolute refractory times vary depending on the amplitude and direction the relative refractory times are all within 0.25 ns of each other

showing that the system is robust to changes in perturbation amplitude and direction.

## 7.2 Subthreshold perturbation integration

In an integrate and fire network two or more sub threshold perturbations can be integrated together to yield a supra-threshold perturbation. The time between the perturbations must be short, so that the second subthreshold perturbation arrives before the system has adiabatically returned to a steady state.

### 7.2.1 Setting new thresholds

To investigate an integrate and fire mechanism the same setup described in Section 7.1 is used, but the amplitude of the phase perturbations are decreased so that individually they are subthreshold. It is important to remember that the clockwise and anticlockwise perturbations come from the rise and fall times of the same square pulse so their amplitudes are inherently tied to each other. Thus selecting a sub-threshold perturbation amplitude to suit both perturbation directions is not straight forward. In Figure 6.3 the perturbation amplitude must be at least 4.1 rad to obtain 100% efficiency for clockwise perturbations. Then, in a crude integrate and fire calculation using just two perturbations, to get reliable firing, each individual perturbation must be at least 2.05 rad to achieve threshold when integrated. However, moving now to the anticlockwise case, each perturbation must be at most 1.5 rad so that each individual perturbation is subthreshold. Clearly the conditions necessary to obtain an integrate and fire mechanism for both perturbation directions for the same experimental parameters are not met. To overcome this the frequency of the TLS is increased (magnitude of the detuning is decreased), changing the threshold values for each perturbation direction. This is simply an equipment enforced limitation not a system limitation. It could easily be resolved with an arbitrary waveform generator.

### 7.2.2 Measurement of large thresholds

To find the new thresholds the electrical delay line is varied so as two phase perturbations occur at the same time, effectively acting as one large perturbation. The amplitude of the square pulses from the pulse generator are

varied. Two efficiency curves are shown in Figure 7.15, one showing two clockwise perturbations summed together and the other two anticlockwise perturbations summed together. The magnitude of both the clockwise and anticlockwise thresholds have increased from  $-3.5$  rad and  $2$  rad in Figure 6.3 to  $-5.6$  rad and  $5.2$  rad in Figure 7.15. For Figure 6.3 the maximum peak voltage that could be applied to a single phase modulator was  $4.5$  V producing the largest possible phase shift of approximately  $4.2$  rad. Therefore, it is not possible to measure the new threshold in Figure 7.15 with one phase modulator alone. Care must be taken when comparing the thresholds in Figure 7.15 directly with those in Figure 6.3. The delay between the two perturbations is set to be a minimum. But this is limited by the resolution of the oscilloscope ( $20$  ps). Therefore the rise time or fall time of the integrated perturbation could be  $20$  ps longer than what it would be if it was a single phase modulator. This is relatively small compared to the rise and fall times of the perturbations themselves but it must be pointed out for completeness as the rise and fall times play a large roll when trying to exceed a threshold, see Chapter 5.

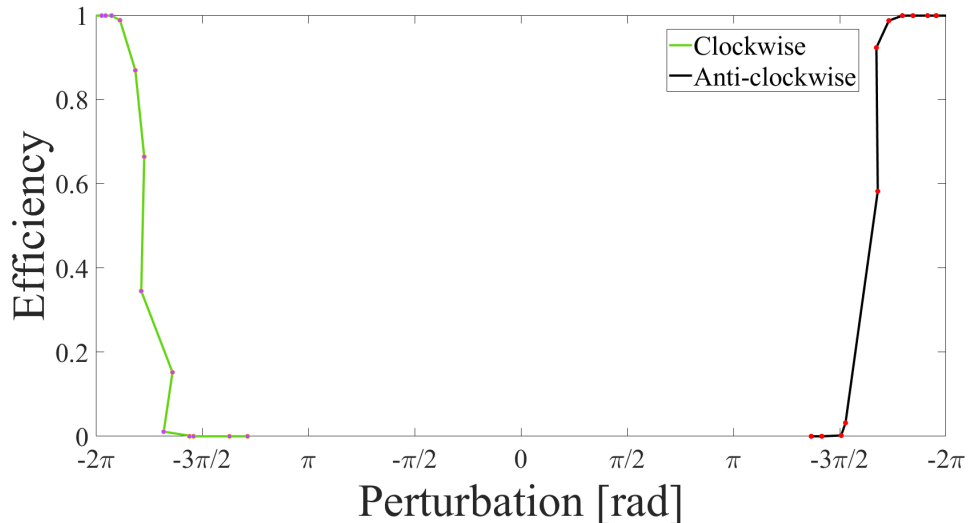


Figure 7.15: Two clockwise perturbations with similar amplitudes are summed together (green line). The amplitude of the perturbations are coupled to each other as the signal from the pulse generator is split 50/50. Thus the amplitude of both are varied simultaneously. The green line shows the efficiency curve for their total effective amplitude. The clockwise threshold is at  $-5.6$  rad. The same experiment was done using two anticlockwise perturbations and the efficiency curve is represented by the black line. The anticlockwise threshold is  $5.2$  rad.

### 7.2.3 Integrate and fire mechanism

From this point on the perturbation amplitude from the pulse generator will be fixed so that each modulator will produce sub-threshold perturbations only. Similar to the figures discussed in Chapter 5, the first half of Figure 7.16 (b) shows the perturbations encoded on the light being injected into the QD laser. The time between two subsequent clockwise perturbations is set beyond the width of a square electrical pulse. This allows us to observe the perturbations applied from each modulator independently. The response of the QD laser (the last 20 ns of the timetrace) can also be monitored. 1000 sets of square signals never triggered a pulse, confirming all perturbations are sub-threshold. In Figure 7.16 (a) an example is shown where no pulses fire and the ES is acting in an all or none fashion.

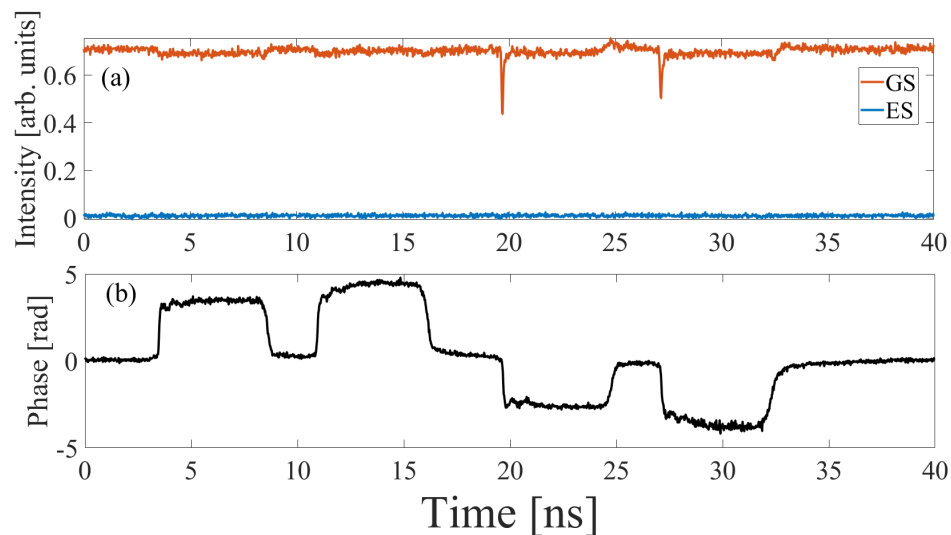


Figure 7.16: Timetraces that show two sets of perturbations from two electrical square signals, four perturbations in total. The perturbations are shown in the first 19 ns of (b). The subsequent 20 ns shows the laser's response, similar to the figures shown in Chapter 5. (a) shows the intensity traces of the GS and ES. No ES pulses are triggered, confirming that these perturbations are indeed sub-threshold.

Next, the time between the perturbations will be varied. To begin the perturbations are brought together and the time between two anticlockwise perturbations is approximately zero and consequently the time between clockwise perturbations is the same. The two perturbations appear as one large phase perturbation as shown in Figure 7.17 (c). The time between two anticlockwise perturbations is increased and an efficiency curve is plotted in

Figure 7.18<sup>1</sup>. There is 100% efficiency as long as the time between the perturbations is less than 320 ps, then the efficiency begins to decrease. Figure 7.17 (a) shows a successfully fired pulse when two anticlockwise perturbations with approximately zero delay are integrated together. Figure 7.17 (b) shows an example when two perturbations integrated together fail to trigger a pulse. They are separated by 320 ps and are 99% successful. The phase of the perturbation is shown in Figure 7.17 (d), the amplitude is very similar to the successful phase amplitude shown Figure 7.17 (c). Increasing the time between perturbations has a similar effect to increasing the rise time of a single perturbation.

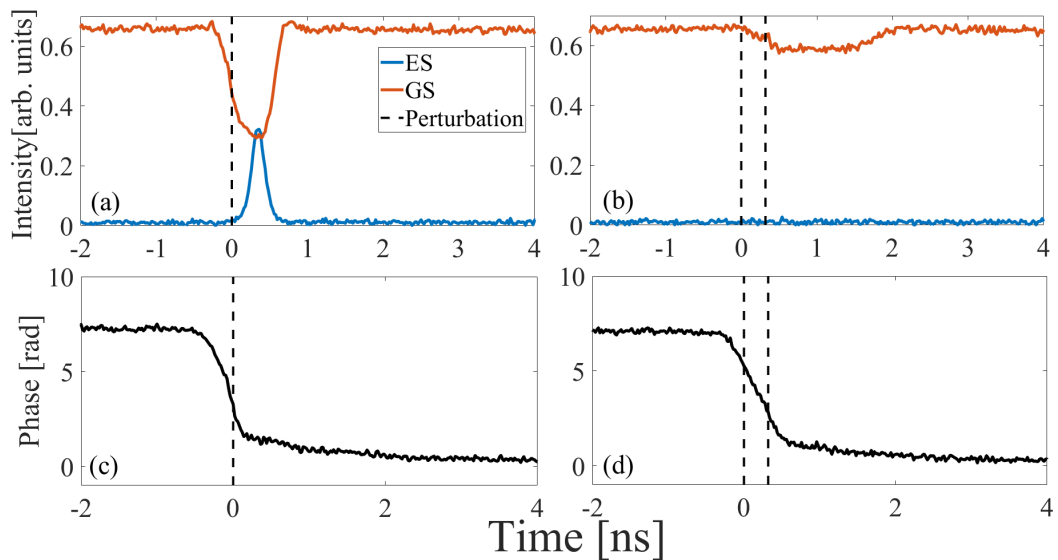


Figure 7.17: (a) ES and GS intensities when a pulse has been successfully triggered. The time between two anticlockwise perturbations is 0 ns. (c) shows the effective perturbation amplitude from two anticlockwise perturbations summed together. When the time between perturbations is increased to 320 ps the efficiency of a pulse being triggered decreases to 0.991. (b) is an example of the intensities after two perturbations summed together are unsuccessful and (d) shows the phase has longer rise time when the time between perturbations is 320 ps.

<sup>1</sup>To obtain data where the times between perturbations was greater than 420 ps an extra RF cable and connector had to be included in the experimental setup. As this measurement is so sensitive to rise time it would be misleading to compare these measurements directly with those shown in Figure 7.18.

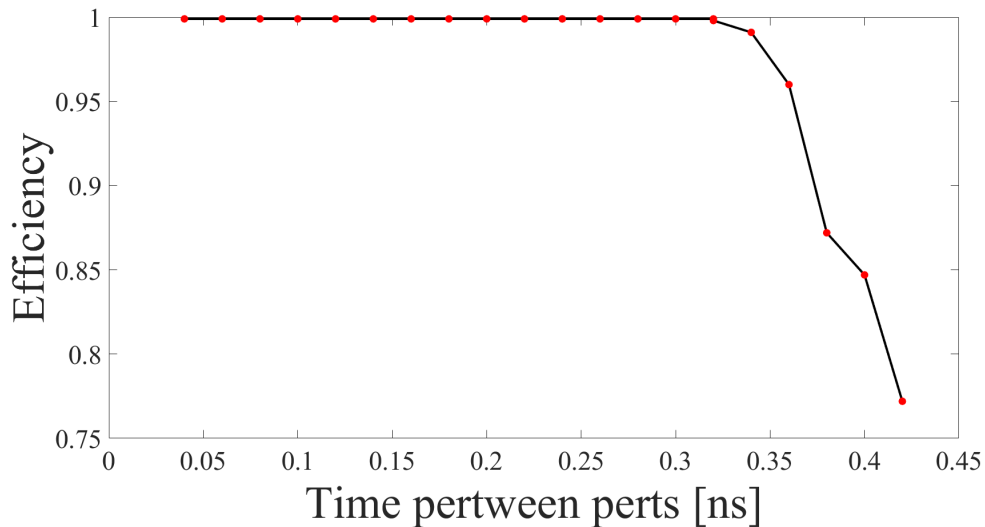


Figure 7.18: The time between two anticlockwise perturbations is varied and an efficiency curve is plotted.

Clockwise perturbations are also integrated together and fire with 100% efficiency when the time between them is zero, Figure 7.19 (a). When the time between the perturbations is increased to 120 ps the efficiency drops to 0%. The story is similar to that of the anticlockwise perturbations, where the

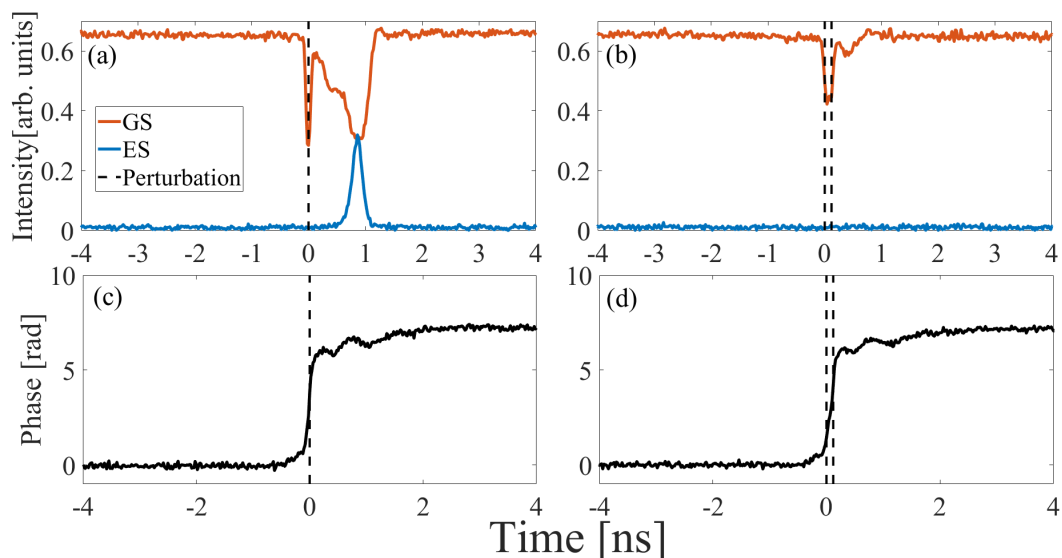


Figure 7.19: (a) ES and GS intensities when a pulse has been successfully triggered. The time between two clockwise perturbations is 0 ns. (c) shows the effective perturbation amplitude from two clockwise perturbations summed together. When the time between perturbations is increased to 120 ps the efficiency of a pulse being triggered decreases to 0. (d) is an example of the intensities after two clockwise perturbations summed together are unsuccessful and shows the effective phase perturbation.

amplitude of the phase perturbation is similar between Figure 7.19(c) and Figure 7.19(d) but the rise time of the perturbation has increased.

Next perturbations of different directions are integrated together.

Unsurprisingly these sub-threshold perturbations become even less likely to trigger a pulse. They simply cancel each other out as they rotate the phase in opposite directions and have similar amplitudes. Figure 7.20 (a) shows an example of an anticlockwise perturbation followed by a clockwise perturbation, where the time between perturbations is 200 ps, no pulse is triggered. The phase initially decreases and then increases, see Figure 7.20 (c). Figure 7.20 (b) shows an example of a clockwise perturbation followed by an anticlockwise perturbation 40 ps later. Now the phase in Figure 7.20 (d) begins to increase but then the clockwise perturbation arrives and effectively cancels out the first perturbation.

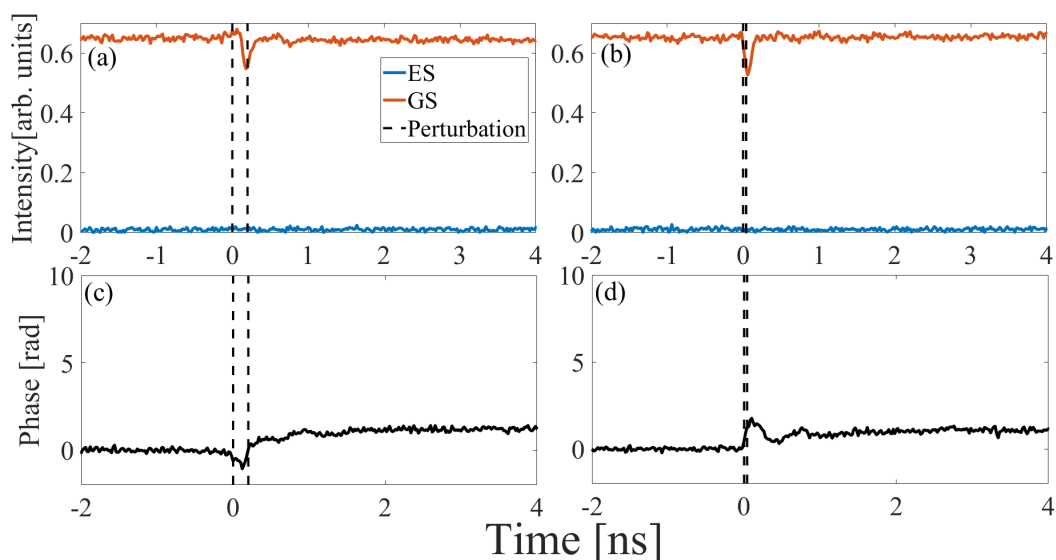


Figure 7.20: (a) ES and GS intensities when a clockwise perturbation is applied 200 ps after an anticlockwise perturbation, a pulse is not triggered. (c) shows the effective perturbation amplitude, there is a small dip related to the anticlockwise perturbation, but when the clockwise perturbation is applied they effectively cancel each other out. (b) shows the ES and GS intensities when a clockwise perturbation is applied and then an anticlockwise one is applied 40 ps later. (d) shows the effective perturbation applied and similar to (c), the two opposing perturbations essentially cancel out.

## 7.3 Image edge detection

The integrate and fire mechanism described above is the basis of a leaky integrate and fire neuron, the core building block of a spiking neural network.

But because we are limited to just one device we will take a closer look at the function of one neuron in convolution neural networks for image edge detection.

Convolution neural networks have been central to computer vision and image processing over the past few decades. These networks have multiple layers of neurons each performing their own operation. The first layer usually performs some kind of an edge detection, using the Sobal, Prewitt or Canny method [156]. In these techniques an image can first be converted to greyscale, where each pixel is given an integer value between 0 and 255, the result contains only information about the pixel's intensity. Then a kernel (matrix/filter) is applied to the image. Figure 7.21 shows how the kernel is applied; sections of the image are taken and the intensity values of a section are multiplied by the kernel in a matrix multiplication. The results are placed in an output matrix. The output matrix is essentially a measurement of the intensity gradient, similar to a derivative. The kernel continuously slides one pixel over and other multiplications are calculated. In the case of the Roberts kernel shown in Figure 7.21, this is done horizontally to produce the output matrix  $G_x$  (horizontal gradient) and then the kernel is rotated by  $90^\circ$  and applied to the image to produce  $G_y$  (vertical gradient). After the kernel is applied to all horizontal components in that line it is moved down a pixel and repeated. Both output matrices are combined when calculating the magnitude  $G = \sqrt{G_x^2 + G_y^2}$ . After this a threshold is applied and if the magnitude of the intensity gradient is greater than the threshold, an edge is detected. The parallel nature of a neural network means that instead of sliding the kernel across sequentially, many neurons can perform convolutions simultaneously.

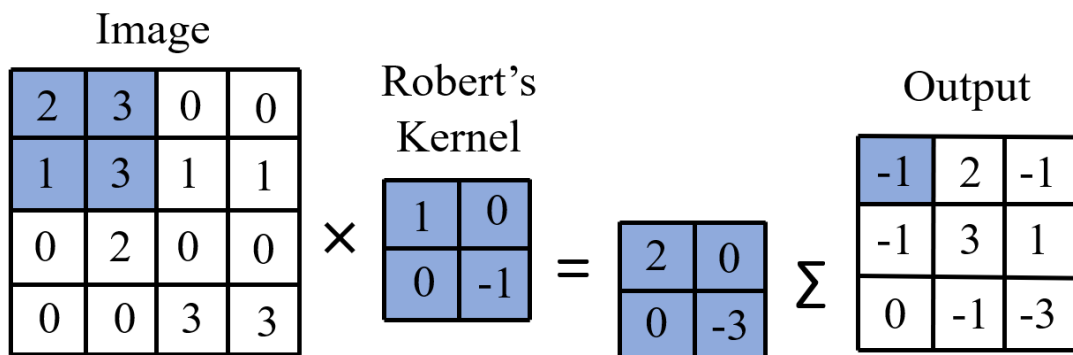


Figure 7.21: An example of a matrix multiplication when applying the Roberts Kernel to an image.

### 7.3.1 Binary

We would like to detect the edge of the image shown in Figure 7.22, similar to the work in [157]. To begin we simplify the greyscale image, Figure 7.22 (a), once more and convert the greyscale image into a binary image, Figure 7.22 (c). A threshold is chosen in a preprocessing step, in this case 166, and if a pixel is brighter than this threshold it is assigned to be to a white pixel (1). If the intensity of the pixel is below the threshold it is assigned as a black pixel (0).

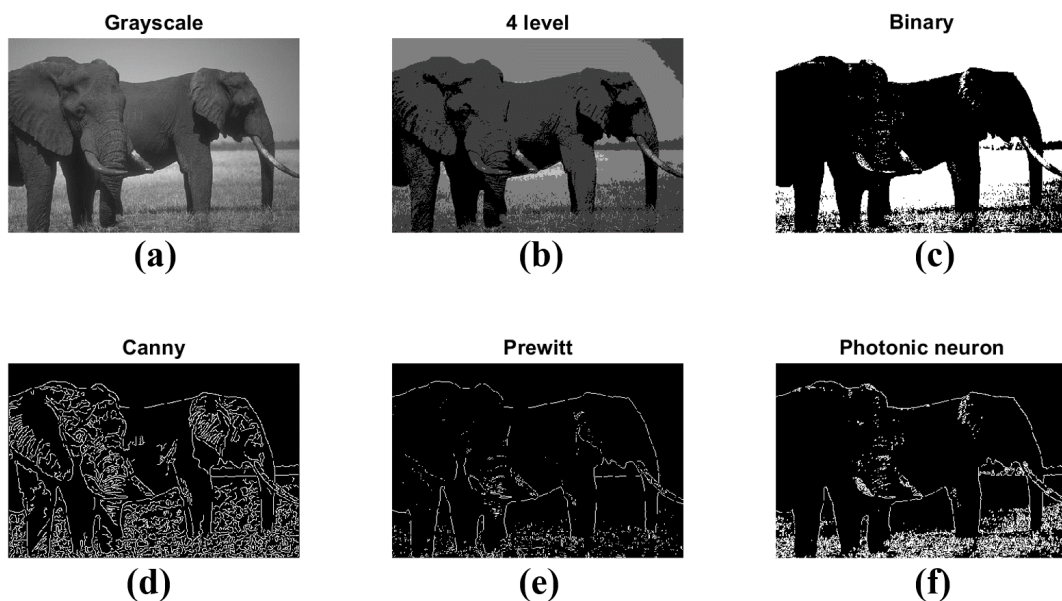


Figure 7.22: A 256 level greyscale image of two elephants. The image is converted into a 4 level image and a binary image. Prewitt and Canny edge detection techniques are applied on the greyscale image and are compared to the  $2 \times 1$  kernel photonic neural network.

#### 7.3.1.1 $2 \times 1$ kernel

These binary values can then be converted into a form that a photonic neuron can compute. Sub-threshold clockwise perturbations are chosen to represent white pixels (1) and sub-threshold anticlockwise perturbations are chosen to represent black pixels (0). A very rudimentary  $2 \times 1$  kernel,  $[1 \ 1]$ , is applied to the binary image. Because this kernel contains unitary values it is more intuitive to consider this matrix multiplication in following way: The same integrate and fire scheme described in Section 7.2.3 is set up, where each perturbation is sub-threshold and the time between them is zero. The end goal

is to detect when two neighbouring pixels are different, this is the definition of an edge. Pairs of perturbations, containing information about neighbouring pixels, are passed into the photonic neuron (QD laser). If neighbouring pixels are the same, be they both clockwise or both anticlockwise, the perturbations integrate together and exceed a threshold, triggering a pulse. However, if neighbouring pixels are different then a clockwise and anticlockwise perturbation sum together and fail to trigger a pulse, indicating an edge has been detected. Figure 7.22 (f) shows the results of applying the technique to an image of two elephants. First the pixels which neighbour each other horizontally are compared, and to create a matrix  $G_x$ . The kernel is rotated  $90^\circ$  and the same is done for vertically neighbouring pixels to obtain  $G_y$ . The magnitude is calculated in a post processing step using  $G = \sqrt{G_x^2 + G_y^2}$ . The edges detected by the binary photonic neuron are shown in Figure 7.22 and are compared to Canny and Prewitt methods which are well-known edge detection techniques on full greyscale images.

The magnitude post processing calculation can actually be approximated in the photonic neuron. With a dual threshold system, large positive and large negative perturbations each have an intrinsic threshold so there is no need to square anything to make them positive in  $G = \sqrt{G_x^2 + G_y^2}$  before applying a threshold.  $G_x$  and  $G_y$  can be taken separately. This approximation actually produces the exact same result with this binary image and  $2 \times 1$  kernel but can also be implemented in more advanced techniques. The advantage of the dual threshold system is that the calculation can be done optically rather than adding another post-processing step.

### 7.3.1.2 $2 \times 2$ kernel

As mentioned the Roberts filter is one of the simplest kernels used to detect the edge of an image. Again in the binary image black pixels are given the value 0 and white pixels are 1. In a preprocessing step the intensity of each pixel is multiplied by the weight. When we used the  $2 \times 1$  kernel the weights were always unitary, but here the weights are assigned to be perturbation directions; 1 is a clockwise perturbation, 0 is no action and -1 is an anticlockwise perturbation. What the matrix multiplication means in terms of our system is if any weight is applied to a black pixel (0), no perturbation will be sent to the neuron, because trivially anything multiplied by zero is zero. If a weight is applied to a white pixel (1) a signal can be sent to the neuron. To

make this convolution even easier, only the two diagonal components of the Roberts filter are non-zero, so only two elements need to be summed in the last step of the matrix multiplication. A similar integrate and fire set up in Section 7.2.3 can be set up where these are the two values that will be passed to the photonic neuron at the same time. But here we set the perturbation amplitudes of both directions representing  $\pm 1$  to be above threshold. In the case where a  $\pm 1$  is summed with 0, the integrator of the photonic neuron will simply produce the non-zero value, and since  $\pm 1$  has been set to be above threshold, a pulse will be fired. As we have seen in Section 7.2.3 if a clockwise (1) and anticlockwise (-1) perturbation integrate together, no pulse is produced, the mathematical result is 0 and this has the net effect of taking no action/ sending no perturbation to the photonic neuron.

Figure 7.23 (a) and (d) show the output matrices  $G_x$  and  $G_y$ , the convolutions after the filter was applied, what the mathematically output would look like. 0 are represented by grey pixels, +1 are white and -1 are black. Our photonic neuron will not produce these images. Instead it goes directly to edge

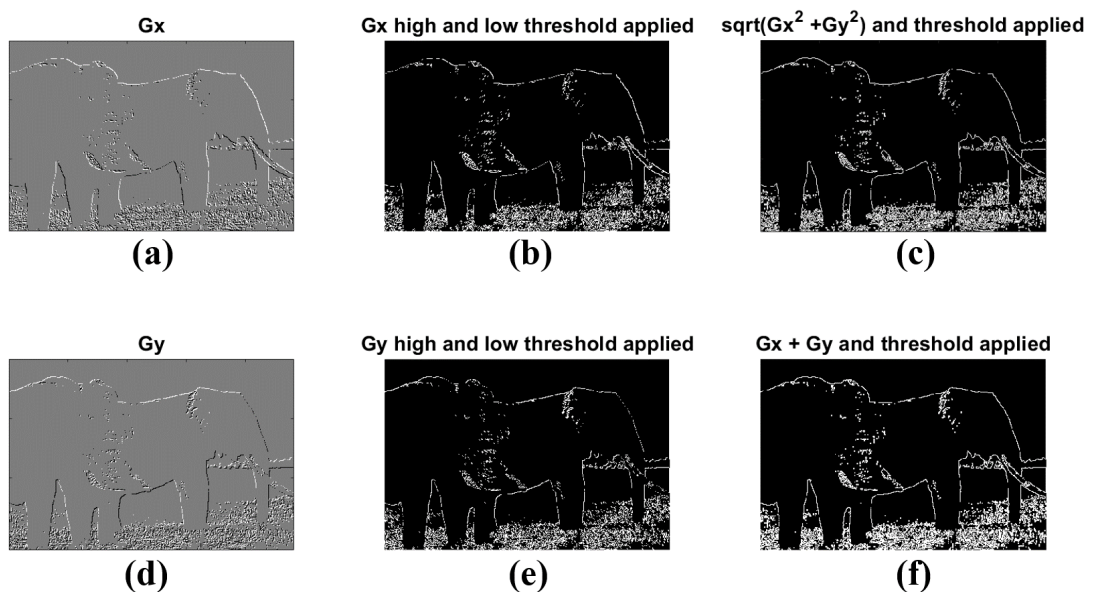


Figure 7.23:  $G_x$  and  $G_y$  show the output matrix after the Roberts filter was applied to a binary image. 0 is represented by grey pixels, +1 are white and -1 are black. High (+1) and low (-1) thresholds are applied to both  $G_x$  and  $G_y$ , where +1 and -1 perturbations that are sent to the photonic neuron trigger a pulse. The conventional magnitude is compared to the approximated  $G_x + G_y$ , that is built into the dual threshold system.

detection. The black and white pixels in Figure 7.23 (a) and (d) are large positive and negative gradients. When an integration in the photonic neuron has the net effect of +1 or -1 both would be above threshold and will fire a pulse marking an edge, Figure 7.23 (b) and (e). So both the black and white edges seen in Figure 7.23 (a) and (d) have a threshold immediately applied due to the dual threshold of this system, Figure 7.23 (f). This approach is just as good as that shown in Figure 7.23 (c) where extra steps to calculate the magnitude and then apply a threshold were added.

### 7.3.2 4 level system

We would like to apply a more advanced filter such as the Prewitt filter to a 256 level greyscale image. The maximum value in an output matrix is then  $(256 \times 1) + (256 \times 1) + (256 \times 1) = 768$  and the minimum is  $-768$ . The range of phase perturbations applied to the system in Figure 7.15 was from  $2\pi$  to  $-2\pi$ , so 1,536 ( $2 \times 768$ ) values must exist in this range, meaning each element of a matrix multiplication would need to be separated by 0.004 rad. The main challenge of this method is the slow rise time of the pulse generator stretching out the efficiency curve. If the efficiency curve was an ideal step function then there would be no problem. A perturbation amplitude that is not either 100% successful or 100% unsuccessful introduces a probability, which leads to the failure of an edge being detected or the detection of an erroneous edge respectively. Therefore the minimum amplitude difference between the results of the convolution is limited by the width of the efficiency curve. In this case 1.9 rad, see Figure 7.15. This is sufficient to apply the Roberts filter to a 4 level system shown in Figure 7.22, where the intensity values go from 0 to 3.

In Section 7.2.3 we have demonstrated that the phase perturbations can be added and subtracted. This was using similar sized perturbations, but we propose that the following is realistic and achievable with an arbitrary waveform generator. Again the weights of the kernel are assigned to be perturbation directions; 1 is a clockwise perturbation, 0 is no action and -1 is an anticlockwise perturbation. The intensity of the pixel could define the amplitude of the perturbation in preprocessing step, where 0, 1, 2 and 3 can be assigned 0, 2, 4 and 6 rad respectively. The thresholds shown in Figure 7.15 are -5.6 and 5.2 rad. When computing the edge from the convolution, Figure 7.24 (a) and (d), mathematically the required threshold is 1 as shown, the results are shown in Figure 7.24 (b) and (e). This would be the equivalent to

$\pm 2$  rad for our system and practically, this means any non-zero result in the output matrix should indicate an edge. Clearly 2 rad is less than 5.2 rad so another preprocessing step is added.  $2\pi$  is subtracted from positive perturbations and is summed to the negative. This essentially moves any 0 value of  $G_x$  or  $G_y$  above threshold and everything else below, now the absence of a pulse indicates an edge. The results of this theoretical and achievable example are quite impressive as some features around the ear of the elephant are now detected in Figure 7.24.

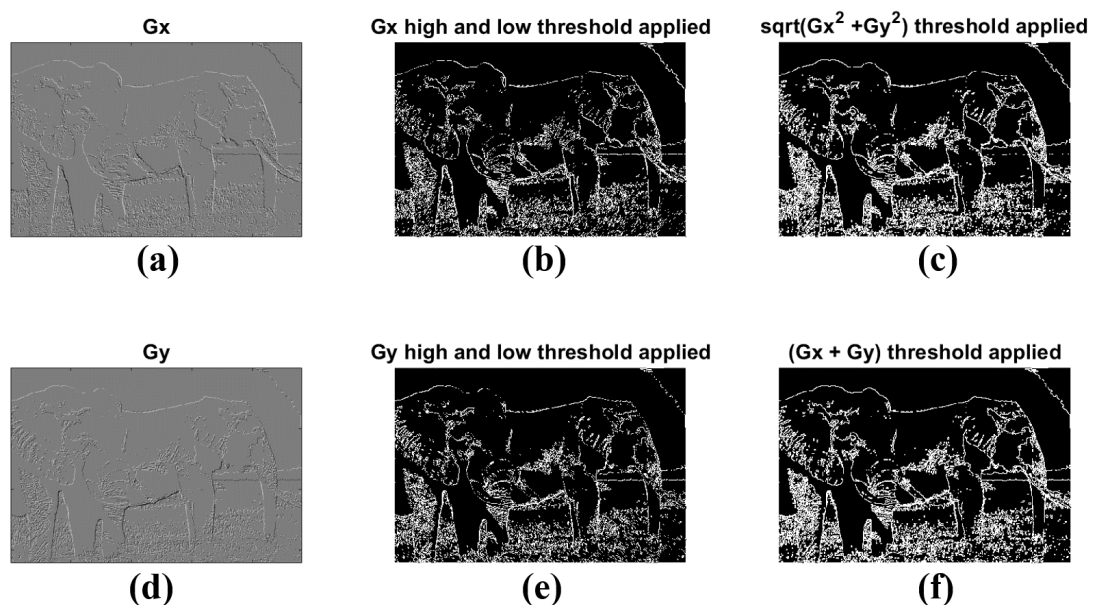


Figure 7.24:  $G_x$  and  $G_y$  show the output matrix after the Roberts filter was applied to a binary image. The values range from +3 to -3. +3 are white and -3 are black and integers in between are represented by different shades of grey. A high and low thresholds of (1) are applied to both  $G_x$  and  $G_y$ . The conventional magnitude is compared to the approximated  $G_x + G_y$ , that is built into the dual threshold system.

To conclude we have shown a working example of a leaky integrate and fire neuron. Two subthreshold anticlockwise perturbations can be integrated together to trigger a pulse, similarly two clockwise perturbations integrated together will also excite a pulse. If a clockwise and anticlockwise perturbation are summed they simply cancel each other out. The ability to have positive and negative weights is useful in neural networks and a very basic image edge detection technique was demonstrated using these weights. Although rudimentary it performed well against other well known methods. The

asymmetric dual threshold allowed us to combine the convolution and thresholding steps involved in edge detection into a single step, allowing for faster processing. Using optical devices for image edge detection is logical. Live images could be kept in the optical domain without ever needing to be converted to the electrical domain, again increasing the speed of detection.

# Chapter 8

## Conclusion

The objective of this work was to investigate different excitable regimes of optically injected quantum dot lasers with a view to implement them in photonic neural networks. Because of their highly damped ROs they are stable in optical injection configurations and their ability to lase from two states opens up the possibilities for multiple ways of performing a computation.

### 8.1 Overview of the results presented

Chapter 1 was an introduction where the fundamental concepts of a laser are introduced. It goes on to introduce the motivation for photonic neurons, inspired by biological neurons. Excitability previously observed in injected laser systems and the bifurcations used to describe the phenomenon are discussed.

Chapter 2 looks at an optically injected QD laser biased so as to emit from the GS. A theoretically predicted bistability is destroyed by an optothermal effect. A new cycle is born where the intensity operates in a square wave train where the upper and lower plateaus are related to the two states of the bistability. As the magnitude of the detuning (at the negative side) is varied from large to small values, different dynamics are observed, from noise induced square pulses, to periodic square wave trains to noise induced square dropouts. The square pulses are deterministically triggered and a bounded phase is observed. Bifurcation analysis begins with a Class A model where a Canard Explosion is found. A quantum dot model shows that depending on the ratio of the photon lifetime to the carrier lifetime, either a subcritical Hopf bifurcation is observed

or the Class A case is recovered and a supercritical Hopf with associated Canard Explosion is found.

Chapter 3 is a review of dual state optical injection experiments and simulations. QD lasers are biased to emit from the ES and optically injected into the GS. This quenches the ES and the laser emits from the GS, the laser is then experimentally shown to be phased locked to the primary laser. Fast switching is observed and is simulated using a semi-classical rate equation model and a microscopic model. A tunable Q-switching regime is found where GS dropouts had corresponding ES pulses. A hysteresis cycle which was observed experimentally was recovered in simulations by the introduction of a term to couple the phase of the GS to the carriers of the ES. Higher injection strengths show square wave trains similar to the ones discussed in Chapter 2, where an optothermal effect breaks a bistability. The intensity of the ES and GS squares operate in anti-phase. One plateau is CW while the other undergoes a slow passage through a Hopf bifurcation, leading to oscillations with continuously varying frequency and amplitude in the bursting section of the square wave. Simulations show no sign of chaos at the unlocking boundaries, highlighting the stability of this configuration, an ideal candidate for neuromorphic applications.

In Chapter 4 locking maps are created. Again a QD laser biased to emit from the ES is optically injected near the GS. The injection strength and frequency of the TLS are varied and the intensities recorded. A wide phase locking region is observed. The negatively detuned boundary shows individual excitable pulses, periodic pulses, a switching regime where the system moves from periodic pulses to a phase locked state, and square wave trains similar to those discussed in Chapter 3. The positively detuned boundary shows slow oscillations with period of tens of milliseconds. Simulations incorporate two optothermal effects; the first is couples the detuning to the carriers and the second couples the detuning to the intensity of the light. The changes in temperature changes the refractive index and thus the detuning.

Chapter 5 looks at the noise induced GS dropouts and ES pulses in detail. The phase of the GS is experimentally obtained and it's clear that it is bounded, thus very different to the Adler mechanism often used to describe optically injected QD lasers. Simulations reveal that these pulses are born from a SNIC bifurcation and a saddle focus corresponds to end of the GS dropout. These pulses are deterministically triggered by phase perturbations in Chapter 6.

Two asymmetric thresholds are found, one for each perturbation direction, a unique characteristic that doesn't exist in the Adler mechanism. The delay times are found and the phase is investigated. Although the thresholds are different the excitable trajectory remains the same. Chapter 7 investigates the refractory periods of clockwise and anticlockwise perturbations. When two supra-threshold clockwise perturbations arrive closely in time the second perturbation can inhibit the pulse triggered by the first perturbation. The amplitude of the perturbations can be set so each of them is sub-threshold. When two sub-threshold perturbations of the same direction are summed together they can exceed the threshold and excite a pulse. Perturbations of opposite direction have the net effect of cancelling each other out. The integrate and fire mechanism is investigated and is used in a basic application to find the edges of an image.

The novelty of obtaining both Type I and Type II excitability is also noteworthy. To the best of our knowledge, this has not been described for any other single optical system in literature. Thus, the optically injected QD system remains a treasure trove of excitability and related phenomenon and given the intensive ongoing research in neuromorphic dynamics, is of great potential interest to researchers in a range of fields.

## 8.2 Future work

### 8.2.1 Optothermal

Future work includes further investigation of the optothermal effect responsible for producing square waves trains. It would be very interesting to experimentally analyse a device identical in all respects apart from the photon lifetime (via reflective coatings for example) to see if the supercritical case and the associated Canard Explosion could be identified. Perhaps by pumping the device just above threshold it would be possible to achieve a Class A like behaviour [66] and recover a Canard Explosion. We also believe that depending on device details (such as fabrication methods), the optothermal coupling may vary from device to device and that for sufficiently low values of  $c$ , a true phase-locked bistability may be possible.

The optothermal effects could also be further investigated using CCD-thermoreflectance imaging [158]. It would be particularly interesting to

experimentally verify that the second optothermal effect does indeed originate from facet heating, discussed in Chapter 4. The period of the optothermally induced oscillations are of the order of tens of milliseconds. With such slow oscillations it may even be possible to even capture multiple images during a single heating and cooling cycle to produce a live measurement.

### 8.2.2 Neuromorphic

The maturation of integration technology presents great opportunities for applications based on coupled semiconductor lasers. Several aspects of QD lasers make these extremely attractive for implementation on photonic integrated circuits. The high RO damping means that they may be coupled on chip without the requirement for isolators, they display superb thermal insensitivity, and they offer a multitude of controllable dynamic responses from coherent outputs to deterministic dual state bursting. Further, the carrier confinement in QD material results in a much higher tolerance to crystalline defects compared to quantum well based material [159]. What's more, since the ES lasing regime is utilised, it should be possible to integrate very short lasers, as can be done with conventional quantum well based devices. Thus, the integration of QD lasers is extremely promising.

Recently in [160] on-chip coupled quantum well based devices were analysed and their potential as building blocks for excitable neuromorphic networks highlighted. Utilising QD material in place of the quantum well material would greatly enhance the capabilities in this direction, and bring a multitude of controllable, excitable regimes and in particular both the dual state excitability and dual state bursting MMOs described above. The stability of phase-locked QD lasers means conventional information processing applications could also benefit. In particular, the intrinsic bistabilities and consequent memory and optical flip flop functionalities of dual state QD lasers are extremely promising for optical signal processing, including optical logic gates and interconnects.

Throughout this thesis phase perturbations were used as the input signals to a dual state QD laser acting as an artificial photonic neuron. The advantages of using this form of perturbation with this type of laser is that a true all or none responses can be achieved, two asymmetric thresholds can be accessed and importantly for neural networks, inhibitory signals can be implemented as negative weights and can stop pulses from firing. But the output of a neuron should be a signal that can be interpreted by another neuron. At the moment

the output of the QD laser is not of the same form as the step-like function of a phase modulator. One possible solution is to use the dual state QD laser as the leaky integrator and place another QD device in series to convert the ES pulse and GS dropout into a phase perturbation. The dual state integrator would then act a primary laser and optically inject a QD laser biased to emit from the GS only with low injection strength.  $2\pi$  clockwise and anticlockwise phase slips have been observed at the positive and negative unlocking boundaries [19] for optically injected GS only QD lasers and have been deterministically triggered with incoherent light sources [73]. We have shown that the rise and fall time of phase perturbations determines whether or not the threshold is surpassed. The rise and fall time of the  $2\pi$  slips can be controlled be varied the detuning of the GS QD laser, which has the same effect of varying the amplitude of the perturbation. This would be relatively straightforward to implement on a photonic integrated chip and is a promising building block of a neural network for the future.

# Bibliography

- [1] P. Minzioni, C. Lacava, T. Tanabe, J. Dong, X. Hu, G. Csaba, W. Porod, G. Singh, A. E. Willner, A. Almainan, V. Torres-Company, J. Schröder, A. C. Peacock, M. J. Strain, F. Parmigiani, G. Contestabile, D. Marpaung, Z. Liu, J. E. Bowers, L. Chang, S. Fabbri, M. R. Vázquez, V. Bharadwaj, S. M. Eaton, P. Lodahl, X. Zhang, B. J. Eggleton, W. J. Munro, K. Nemoto, O. Morin, J. Laurat, and J. Nunn, “Roadmap on all-optical processing”, *Journal of Optics* **21**, 063001 (2019).
- [2] H. Kawaguchi, “Recent progress in polarization-bistable vcsels and their applications to all-optical signal processing”, in *Advanced lasers: laser physics and technology for applied and fundamental science*, edited by O. Shulika and I. Sukhoivanov (Springer Netherlands, Dordrecht, 2015), pages 1–17.
- [3] P. R. Prucnal, B. J. Shastri, T. F. de Lima, M. A. Nahmias, and A. N. Tait, “Recent progress in semiconductor excitable lasers for photonic spike processing”, *Advances in Optics and Photonics* **8**, 228–299 (2016).
- [4] B. J. Shastri, A. N. Tait, T. F. de Lima, W. H. Pernice, H. Bhaskaran, C. D. Wright, and P. R. Prucnal, “Photonics for artificial intelligence and neuromorphic computing”, *Nature Photonics* **15**, 102–114 (2021).
- [5] Y. LeCun, Y. Bengio, and G. Hinton, “Deep learning”, *nature* **521**, 436–444 (2015).
- [6] A. L. Hodgkin and A. F. Huxley, “A quantitative description of membrane current and its application to conduction and excitation in nerve”, *The Journal of physiology* **117**, 500–544 (1952).
- [7] W. Maass, “Networks of spiking neurons: the third generation of neural network models”, *Neural Networks* **10**, 1659–1671 (1997).
- [8] J. Schemmel, D. Brüderle, A. Grübl, M. Hock, K. Meier, and S. Millner, “A wafer-scale neuromorphic hardware system for large-scale neural

- modeling”, in 2010 IEEE International Symposium on Circuits and Systems (ISCAS) (IEEE, 2010), pages 1947–1950.
- [9] S. B. Furber, F. Galluppi, S. Temple, and L. A. Plana, “The spinnaker project”, *Proceedings of the IEEE* **102**, 652–665 (2014).
- [10] P. A. Merolla, J. V. Arthur, R. Alvarez-Icaza, A. S. Cassidy, J. Sawada, F. Akopyan, B. L. Jackson, N. Imam, C. Guo, Y. Nakamura, et al., “A million spiking-neuron integrated circuit with a scalable communication network and interface”, *Science* **345**, 668–673 (2014).
- [11] B. V. Benjamin, P. Gao, E. McQuinn, S. Choudhary, A. R. Chandrasekaran, J.-M. Bussat, R. Alvarez-Icaza, J. V. Arthur, P. A. Merolla, and K. Boahen, “Neurogrid: a mixed-analog-digital multichip system for large-scale neural simulations”, *Proceedings of the IEEE* **102**, 699–716 (2014).
- [12] J. Feldmann, N. Youngblood, C. D. Wright, H. Bhaskaran, and W. H. Pernice, “All-optical spiking neurosynaptic networks with self-learning capabilities”, *Nature* **569**, 208–214 (2019).
- [13] A. N. Tait, M. A. Nahmias, B. J. Shastri, and P. R. Prucnal, “Broadcast and weight: an integrated network for scalable photonic spike processing”, *Journal of Lightwave Technology* **32**, 4029–4041 (2014).
- [14] Y. Shen, N. C. Harris, S. Skirlo, M. Prabhu, T. Baehr-Jones, M. Hochberg, X. Sun, S. Zhao, H. Larochelle, D. Englund, et al., “Deep learning with coherent nanophotonic circuits”, *Nature Photonics* **11**, 441–446 (2017).
- [15] B. Krauskopf, K. Schneider, J. Sieber, S. Wiczorek, and M. Wolfrum, “Excitability and self-pulsations near homoclinic bifurcations in semiconductor laser systems”, *Optics Communications* **215**, 367–379 (2003).
- [16] W. Maass and C. Bishop, editors, *Pulsed neural networks*, English (MIT Press, 1999).
- [17] E. M. Izhikevich, *Dynamical systems in neuroscience* (MIT press, 2007).
- [18] A. M. Yacomotti, M. C. Eguia, J. Aliaga, O. E. Martinez, G. B. Mindlin, and A. Lipsich, “Interspike time distribution in noise driven excitable systems”, *Phys. Rev. Lett.* **83**, 292–295 (1999).
- [19] B. Kelleher, D. Goulding, S. P. Hegarty, G. Huyet, D.-Y. Cong, A. Martinez, A. Lemaître, A. Ramdane, M. Fischer, F. Gerschütz, and

- J. Koeth, “Excitable phase slips in an injection-locked single-mode quantum-dot laser”, *Opt. Lett.* **34**, 440–442 (2009).
- [20] B. Garbin, A. Dolcemascolo, F. Prati, J. Javaloyes, G. Tissoni, and S. Barland, “Refractory period of an excitable semiconductor laser with optical injection”, *Physical Review E* **95**, 012214 (2017).
- [21] M. Giudici, C. Green, G. Giacomelli, U. Nespolo, and J. R. Tredicce, “Andronov bifurcation and excitability in semiconductor lasers with optical feedback”, *Phys. Rev. E* **55**, 6414–6418 (1997).
- [22] F. Plaza, M. Velarde, F. Arecchi, S. Boccaletti, M. Ciofini, and R. Meucci, “Excitability following an avalanche-collapse process”, *EPL (Europhysics Letters)* **38**, 85 (1997).
- [23] S. Beri, L. Mashall, L. Gelens, G. Van der Sande, G. Mezosi, M. Sorel, J. Danckaert, and G. Verschaffelt, “Excitability in optical systems close to z2-symmetry”, *Physics Letters A* **374**, 739–743 (2010).
- [24] H. J. Wünsche, O. Brox, M. Radziunas, and F. Henneberger, “Excitability of a semiconductor laser by a two-mode homoclinic bifurcation”, *Phys. Rev. Lett.* **88**, 023901 (2001).
- [25] L. Gelens, L. Mashal, S. Beri, W. Coomans, G. Van der Sande, J. Danckaert, and G. Verschaffelt, “Excitability in semiconductor microring lasers: experimental and theoretical pulse characterization”, *Physical Review A* **82**, 063841 (2010).
- [26] T. Sorrentino, C. Quintero-Quiroz, A. Aragoneses, M. Torrent, and C. Masoller, “Effects of periodic forcing on the temporally correlated spikes of a semiconductor laser with feedback”, *Optics Express* **23**, 5571–5581 (2015).
- [27] G. Giacomelli, M. Giudici, S. Balle, and J. R. Tredicce, “Experimental evidence of coherence resonance in an optical system”, *Phys. Rev. Lett.* **84**, 3298 (2000).
- [28] G. Spühler, R. Paschotta, R. Fluck, B. Braun, M. Moser, G. Zhang, E. Gini, and U. Keller, “Experimentally confirmed design guidelines for passively q-switched microchip lasers using semiconductor saturable absorbers”, *JOSA B* **16**, 376–388 (1999).
- [29] M. A. Nahmias, B. J. Shastri, A. N. Tait, and P. R. Prucnal, “A leaky integrate-and-fire laser neuron for ultrafast cognitive computing”, *IEEE journal of selected topics in quantum electronics* **19**, 1–12 (2013).

- [30] F. Selmi, R. Braive, G. Beaudoin, I. Sagnes, R. Kuszelewicz, and S. Barbay, “Relative refractory period in an excitable semiconductor laser”, *Phys. Rev. Lett.* **112**, 183902 (2014).
- [31] B. J. Shastri, M. A. Nahmias, A. N. Tait, A. W. Rodriguez, B. Wu, and P. R. Prucnal, “Spike processing with a graphene excitable laser”, *Scientific reports* **6**, 1–12 (2016).
- [32] S. Barbay, R. Kuszelewicz, and A. M. Yacomotti, “Excitability in a semiconductor laser with saturable absorber”, *Optics Letters* **36**, 4476–4478 (2011).
- [33] M. A. Larotonda, A. Hnilo, J. M. Mendez, and A. M. Yacomotti, “Experimental investigation on excitability in a laser with a saturable absorber”, *Physical Review A* **65**, 033812 (2002).
- [34] W. Coomans, L. Gelens, S. Beri, J. Danckaert, and G. Van der Sande, “Solitary and coupled semiconductor ring lasers as optical spiking neurons”, *Physical Review E* **84**, 036209 (2011).
- [35] T. Van Vaerenbergh, M. Fiers, P. Mechet, T. Spuesens, R. Kumar, G. Morthier, B. Schrauwen, J. Dambre, and P. Bienstman, “Cascadable excitability in microrings”, *Optics Express* **20**, 20292–20308 (2012).
- [36] A. Hurtado and J. Javaloyes, “Controllable spiking patterns in long-wavelength vertical cavity surface emitting lasers for neuromorphic photonics systems”, *Applied Physics Letters* **107**, 241103 (2015).
- [37] S. Barland, O. Piro, M. Giudici, J. R. Tredicce, and S. Balle, “Experimental evidence of van der pol–fitzhugh–nagumo dynamics in semiconductor optical amplifiers”, *Phys. Rev. E* **68**, 036209 (2003).
- [38] A. Yariv and J. Gordon, “The laser”, *Proceedings of the IEEE* **51**, 4–29 (1963).
- [39] Y. Arakawa and H. Sakaki, “Multidimensional quantum well laser and temperature dependence of its threshold current”, *Applied physics letters* **40**, 939–941 (1982).
- [40] D. Bimberg, N. Kirstaedter, N. Ledentsov, Z. I. Alferov, P. Kop’Ev, and V. Ustinov, “Ingaas-gaas quantum-dot lasers”, *IEEE Journal of selected topics in quantum electronics* **3**, 196–205 (1997).
- [41] G. Liu, A. Stintz, H. Li, K. Malloy, and L. Lester, “Extremely low room-temperature threshold current density diode lasers using inas dots in in/sub 0.15/ga/sub 0.85/as quantum well”, *Electronics Letters* **35**, 1163–1165 (1999).

- [42] B. Ellis, M. A. Mayer, G. Shambat, T. Sarmiento, J. Harris, E. E. Haller, and J. Vučković, “Ultralow-threshold electrically pumped quantum-dot photonic-crystal nanocavity laser”, *Nature photonics* **5**, 297–300 (2011).
- [43] S. Mikhlin, A. Kovsh, I. Krestnikov, A. Kozhukhov, D. Livshits, N. Ledentsov, Y. M. Shernyakov, I. Novikov, M. Maximov, V. Ustinov, et al., “High power temperature-insensitive 1.3  $\mu\text{m}$  InGaAs/GaAs quantum dot lasers”, *Semiconductor science and technology* **20**, 340 (2005).
- [44] J. C. Norman, Z. Zhang, D. Jung, C. Shang, M. Kennedy, M. Dumont, R. W. Herrick, A. C. Gossard, and J. E. Bowers, “The importance of p-doping for quantum dot laser on silicon performance”, *IEEE Journal of Quantum Electronics* **55**, 1–11 (2019).
- [45] T. Walther, A. G. Cullis, D. J. Norris, and M. Hopkinson, “Nature of the stranski-krastanow transition during epitaxy of InGaAs on GaAs”, *Phys. Rev. Lett.* **86**, 2381–2384 (2001).
- [46] B. Tykalewicz, D. Goulding, S. P. Hegarty, G. Huyet, I. Dubinkin, N. Fedorov, T. Erneux, E. A. Viktorov, and B. Kelleher, “Optically induced hysteresis in a two-state quantum dot laser”, *Opt. Lett.* **41**, 1034–1037 (2016).
- [47] M. Grundmann and D. Bimberg, “Theory of random population for quantum dots”, *Physical Review B - Condensed Matter and Materials Physics* **55**, 10.1103/PhysRevB.55.9740 (1997).
- [48] A. Markus, J. X. Chen, C. Paranthoën, A. Fiore, C. Platz, and O. Gauthier-Lafaye, “Simultaneous two-state lasing in quantum-dot lasers”, *Applied Physics Letters* **82**, 1818–1820 (2003).
- [49] A. Markus, J. X. Chen, O. Gauthier-Lafaye, J. G. Provost, C. Paranthoën, and A. Fiore, “Impact of Intraband Relaxation on the Performance of a Quantum-Dot Laser”, in *Ieee journal on selected topics in quantum electronics*, Vol. 9, 5 (Sept. 2003), pages 1308–1314.
- [50] E. A. Viktorov, P. Mandel, Y. Tanguy, J. Houlihan, and G. Huyet, “Electron-hole asymmetry and two-state lasing in quantum dot lasers”, *Applied Physics Letters* **87**, 10.1063/1.1995947 (2005).
- [51] H. Y. Wang, H. C. Cheng, S. D. Lin, and C. P. Lee, “Wavelength switching transition in quantum dot lasers”, *Applied Physics Letters* **90**, 10.1063/1.2709987 (2007).

- [52] K. Lüdge and E. Schöll, “Temperature dependent two-state lasing in quantum dot lasers”, in 2011 5th rio de la plata workshop on laser dynamics and nonlinear photonics, ldnP 2011 (2011).
- [53] A. E. Zhukov, M. V. Maximov, Y. M. Shernyakov, D. A. Livshits, A. V. Savelyev, F. I. Zubov, and V. V. Klimenko, “Features of simultaneous ground- and excited-state lasing in quantum dot lasers”, *Semiconductors* **46**, 231–235 (2012).
- [54] A. Röhm, B. Lingnau, and K. Lüdge, “Understanding ground-state quenching in quantum-dot lasers”, *IEEE Journal of Quantum Electronics* **51**, 10.1109/JQE.2014.2370793 (2015).
- [55] C. Henry, “Theory of the linewidth of semiconductor lasers”, *IEEE Journal of Quantum Electronics* **18**, 259–264 (1982).
- [56] J. R. Tredicce, F. T. Arecchi, G. L. Lippi, and G. P. Puccioni, “Instabilities in lasers with an injected signal”, *J. Opt. Soc. Am. B* **2**, 173–183 (1985).
- [57] C. Huygens and H. Oscillatorium, “The pendulum clock”, *Trans RJ Blackwell, The Iowa State University Press, Ames* (1986).
- [58] B. Van Der Pol, “Vii. forced oscillations in a circuit with non-linear resistance.(reception with reactive triode)”, *The London, Edinburgh, and Dublin Philosophical Magazine and Journal of Science* **3**, 65–80 (1927).
- [59] R. Adler, “A study of locking phenomena in oscillators”, *Proceedings of the IEEE* **61**, 1380–1385 (1973).
- [60] B. Kelleher, D. Goulding, G. Huyet, E. Viktorov, T. Erneux, and S. Hegarty, “Dimensional signature on noise-induced excitable statistics in an optically injected semiconductor laser”, *Physical Review E* **84**, 026208 (2011).
- [61] T. Erneux and P. Glorieux, *Laser dynamics* (Cambridge University Press, 2010).
- [62] S. Wieczorek, B. Krauskopf, T. Simpson, and D. Lenstra, “The dynamical complexity of optically injected semiconductor lasers”, *Physics Reports* **416**, 1–128 (2005).
- [63] S. Wieczorek, T. Simpson, B. Krauskopf, and D. Lenstra, “Bifurcation transitions in an optically injected diode laser: theory and experiment”, English, *Optics Communications* **215**, Bifurcation transitions in an optically injected diode laser: theory and experiment, 125–134 (2003).
- [64] S. A. Prescott, *Excitability: types i, ii, and iii*. 2014.

- [65] B. Kelleher, C. Bonatto, G. Huyet, and S. P. Hegarty, “Excitability in optically injected semiconductor lasers: contrasting quantum-well- and quantum-dot-based devices”, *Phys. Rev. E* **83**, 026207 (2011).
- [66] B. Kelleher, S. Hegarty, and G. Huyet, “Optically injected lasers: the transition from class b to class a lasers”, *Physical Review E* **86**, 066206 (2012).
- [67] B. Lingnau, W. W. Chow, E. Schöll, and K. Lüdge, “Feedback and injection locking instabilities in quantum-dot lasers: a microscopically based bifurcation analysis”, *New Journal of Physics* **15**, 093031 (2013).
- [68] C. Otto, K. Lüdge, and E. Schöll, “Modeling quantum dot lasers with optical feedback: sensitivity of bifurcation scenarios”, *physica status solidi (b)* **247**, 829–845 (2010).
- [69] B. Kelleher, D. Goulding, S. Hegarty, G. Huyet, E. Viktorov, and T. Erneux, “Optically injected single-mode quantum dot lasers”, in *Quantum dot devices* (Springer, 2012), pages 1–22.
- [70] S. P. Hegarty, D. Goulding, B. Kelleher, G. Huyet, M.-T. Todaro, A. Salhi, A. Passaseo, and M. De Vittorio, “Phase-locked mutually coupled 1.3  $\mu\text{m}$  quantum-dot lasers”, *Optics letters* **32**, 3245–3247 (2007).
- [71] T. Erneux, E. Viktorov, B. Kelleher, D. Goulding, S. Hegarty, and G. Huyet, “Optically injected quantum-dot lasers”, *Optics letters* **35**, 937–939 (2010).
- [72] D. Goulding, S. P. Hegarty, O. Rasskazov, S. Melnik, M. Hartnett, G. Greene, J. G. McInerney, D. Rachinskii, and G. Huyet, “Excitability in a quantum dot semiconductor laser with optical injection”, *Physical review letters* **98**, 153903 (2007).
- [73] B. Garbin, D. Goulding, S. P. Hegarty, G. Huyet, B. Kelleher, and S. Barland, “Incoherent optical triggering of excitable pulses in an injection-locked semiconductor laser”, *Opt. Lett.* **39**, 1254–1257 (2014).
- [74] G. Friart, L. Weicker, J. Danckaert, and T. Erneux, “Relaxation and square-wave oscillations in a semiconductor laser with polarization rotated optical feedback”, *Opt. Express* **22**, 6905–6918 (2014).
- [75] C.-H. Uy, L. Weicker, D. Rontani, and M. Sciamanna, *Beyond the relaxation frequency limit in square-wave dynamics*, International Society for Optics and Photonics, 2018.

- [76] L. Mashal, G. V. der Sande, L. Gelens, J. Danckaert, and G. Verschaffelt, “Square-wave oscillations in semiconductor ring lasers with delayed optical feedback”, *Opt. Express* **20**, 22503–22516 (2012).
- [77] Y. A. Rzhanov, H. Richardson, A. A. Hagberg, and J. V. Moloney, “Spatiotemporal oscillations in a semiconductor étalon”, *Phys. Rev. A* **47**, 1480–1491 (1993).
- [78] B. Kelleher, B. Tykalewicz, D. Goulding, N. Fedorov, I. Dubinkin, T. Erneux, and E. A. Viktorov, “Two-color bursting oscillations”, *Scientific Reports* **7**, 10.1038/s41598-017-08751-y (2017).
- [79] A. Tierno, N. Radwell, and T. Ackemann, “Low-frequency self-pulsing in single-section quantum-dot laser diodes and its relation to optothermal pulsations”, *Phys. Rev. A* **84**, 043828 (2011).
- [80] E. A. Viktorov and T. Erneux, “Self-sustained pulsations in a quantum-dot laser”, *Phys. Rev. E* **90**, 052914 (2014).
- [81] A. M. Yacomotti, P. Monnier, F. Raineri, B. B. Bakir, C. Seassal, R. Raj, and J. A. Levenson, “Fast thermo-optical excitability in a two-dimensional photonic crystal”, *Phys. Rev. Lett.* **97**, 143904 (2006).
- [82] F. Marino, G. Catalán, P. Sánchez, S. Balle, and O. Piro, “Thermo-optical “canard orbits” and excitable limit cycles”, *Phys. Rev. Lett.* **92**, 073901 (2004).
- [83] R. FitzHugh, “Impulses and physiological states in theoretical models of nerve membrane”, *Biophysical journal* **1**, 445–466 (1961).
- [84] B. Kelleher, D. Goulding, B. B. Pascual, S. P. Hegarty, and G. Huyet, “Phasor plots in optical injection experiments”, *The European Physical Journal D* **58**, 175–179 (2010).
- [85] M. Turconi, B. Garbin, M. Feyereisen, M. Giudici, and S. Barland, “Control of excitable pulses in an injection-locked semiconductor laser”, *Phys. Rev. E* **88**, 022923 (2013).
- [86] S. Wiczorek, T. B. Simpson, B. Krauskopf, and D. Lenstra, “Global quantitative predictions of complex laser dynamics”, *Physical Review E* **65**, 045207 (2002).
- [87] B. Lingnau, K. Lüdge, W. W. Chow, and E. Schöll, “Failure of the  $\alpha$  factor in describing dynamical instabilities and chaos in quantum-dot lasers”, *Phys. Rev. E* **86**, 065201 (2012).
- [88] C. Mayol, R. Toral, C. R. Mirasso, and M. A. Natiello, “Class-a lasers with injected signal: bifurcation set and lyapunov–potential function”, *Physical Review A* **66**, 013808 (2002).

- [89] K. Ludge, R. Aust, G. Fiol, M. Stubenrauch, D. Arsenijevic, D. Bimberg, and E. Scholl, “Large-signal response of semiconductor quantum-dot lasers”, *IEEE Journal of Quantum Electronics* **46**, 1755–1762 (2010).
- [90] T. MORI, Y. SATO, and H. KAWAGUCHI, “10-gb/s optical buffer memory using a polarization bistable vcsel”, *IEICE Transactions on Electronics* **E92.C**, 957–963 (2009).
- [91] H. Kawaguchi, *Bistabilities and nonlinearities in laser diodes*, Artech House optoelectronics library (Artech House, 1994).
- [92] S. Ishii and T. Baba, “Bistable lasing in twin microdisk photonic molecules”, *Applied Physics Letters* **87**, 181102 (2005).
- [93] M. Raburn, M. Takenaka, K. Takeda, X. Song, J. S. Barton, and Y. Nakano, “Integrable multimode interference distributed bragg reflector laser all-optical flip-flops”, *IEEE photonics technology letters* **18**, 1421–1423 (2006).
- [94] M. T. Hill, H. J. Dorren, T. De Vries, X. J. Leijtens, J. H. Den Besten, B. Smalbrugge, Y.-S. Oei, H. Binsma, G.-D. Khoe, and M. K. Smit, “A fast low-power optical memory based on coupled micro-ring lasers”, *nature* **432**, 206–209 (2004).
- [95] S. V. Zhukovsky, D. N. Chigrin, A. V. Lavrinenko, and J. Kroha, “Switchable lasing in multimode microcavities”, *Physical review letters* **99**, 073902 (2007).
- [96] Z. G. Pan, S. Jiang, M. Dagenais, R. A. Morgan, K. Kojima, M. T. Asom, R. E. Leibenguth, G. D. Guth, and M. W. Focht, “Optical injection induced polarization bistability in vertical-cavity surface-emitting lasers”, *Applied physics letters* **63**, 2999–3001 (1993).
- [97] I. Gatara, J. Buesa, H. Thienpont, K. Panajotov, and M. Sciamanna, “Polarization switching bistability and dynamics in vertical-cavity surface-emitting laser under orthogonal optical injection”, *Optical and quantum electronics* **38**, 429–443 (2006).
- [98] A. Valle, M. Gomez-Molina, and L. Pesquera, “Polarization bistability in 1550 nm wavelength single-mode vertical-cavity surface-emitting lasers subject to orthogonal optical injection”, *IEEE Journal of Selected Topics in Quantum Electronics* **14**, 895–902 (2008).
- [99] A. Hurtado, I. D. Henning, and M. J. Adams, “Different forms of wavelength polarization switching and bistability in a 1.55  $\mu\text{m}$  vertical-cavity surface-emitting laser under orthogonally polarized optical injection”, *Optics letters* **34**, 365–367 (2009).

- [100] A. Hurtado, M. Nami, I. D. Henning, M. J. Adams, and L. F. Lester, “Two-wavelength switching with a 1310-nm quantum dot distributed feedback laser”, *IEEE Journal on Selected Topics in Quantum Electronics* **19**, 10.1109/JSTQE.2013.2244570 (2013).
- [101] T. Pérez, A. Scirè, G. Van der Sande, P. Colet, and C. R. Mirasso, “Bistability and all-optical switching in semiconductor ring lasers”, *Optics express* **15**, 12941–12948 (2007).
- [102] L. Gelens, G. Van der Sande, S. Beri, and J. Danckaert, “Phase-space approach to directional switching in semiconductor ring lasers”, *Physical Review E* **79**, 016213 (2009).
- [103] S. Osborne, K. Buckley, A. Amann, and S. O’Brien, “All-optical memory based on the injection locking bistability of a two-color laser diode”, *Optics express* **17**, 6293–6300 (2009).
- [104] S. Osborne, S. O’Brien, K. Buckley, R. Fehse, A. Amann, J. Patchell, B. Kelly, D. R. Jones, J. O’Gorman, and E. P. O’Reilly, “Design of single-mode and two-color fabry–pérot lasers with patterned refractive index”, *IEEE Journal of Selected Topics in Quantum Electronics* **13**, 1157–1163 (2007).
- [105] A. Dehghaninejad, M. M. Sheikhey, and H. Baghban, “Dynamic behavior of injection-locked two-state quantum dot lasers”, *Journal of the Optical Society of America B* **36**, 1518 (2019).
- [106] L. Olejniczak, K. Panajotov, S. Wieczorek, H. Thienpont, and M. Sciamanna, “Intrinsic gain switching in optically injected quantum dot laser lasing simultaneously from the ground and excited state”, *Journal of the Optical Society of America B* **27**, 10.1364/josab.27.002416 (2010).
- [107] E. A. Viktorov, P. Mandel, I. O’Driscoll, O. Carroll, G. Huyet, J. Houlihan, and Y. Tanguy, “Low-frequency fluctuations in two-state quantum dot lasers”, *Optics Letters* **31**, 10.1364/ol.31.002302 (2006).
- [108] N. A. Naderi, F. Grillot, K. Yang, J. B. Wright, A. Gin, and L. F. Lester, “Two-color multi-section quantum dot distributed feedback laser”, *Optics Express* **18**, 10.1364/oe.18.027028 (2010).
- [109] F. Grillot, N. A. Naderi, J. B. Wright, R. Raghunathan, M. T. Crowley, and L. F. Lester, “A dual-mode quantum dot laser operating in the excited state”, *Applied Physics Letters* **99**, 10.1063/1.3667193 (2011).

- [110] M. Virte, K. Panajotov, and M. Sciamanna, “Mode competition induced by optical feedback in two-color quantum dot lasers”, *IEEE Journal of Quantum Electronics* **49**, 578–585 (2013).
- [111] M. Virte, S. Breuer, M. Sciamanna, and K. Panajotov, “Switching between ground and excited states by optical feedback in a quantum dot laser diode”, *Applied Physics Letters* **105**, 10.1063/1.4896576 (2014).
- [112] M. Virte, R. Pawlus, M. Sciamanna, K. Panajotov, and S. Breuer, “Energy exchange between modes in a multimode two-color quantum dot laser with optical feedback”, *Optics Letters* **41**, 3205 (2016).
- [113] H. Huang, D. Arsenijević, K. Schires, T. Sadeev, D. Bimberg, and F. Grillot, “Multimode optical feedback dynamics of InAs/GaAs quantum-dot lasers emitting on different lasing states”, *AIP Advances* **6**, 10.1063/1.4973335 (2016).
- [114] R. Pawlus, S. Breuer, and M. Virte, “Relative intensity noise reduction in a dual-state quantum-dot laser by optical feedback”, *Optics Letters* **42**, 4259 (2017).
- [115] L.-C. Lin, C.-Y. Chen, H. Huang, D. Arsenijević, D. Bimberg, F. Grillot, and F.-Y. Lin, “Comparison of optical feedback dynamics of InAs/GaAs quantum-dot lasers emitting solely on ground or excited states”, *Optics Letters* **43**, 210 (2018).
- [116] S. Meinecke, L. Kluge, J. Hausen, B. Lingnau, and K. Lüdge, “Optical feedback induced oscillation bursts in two-state quantum-dot lasers”, *Optics Express* **28**, 3361 (2020).
- [117] J. Kim, M. T. Choi, and P. J. Delfyett, “Pulse generation and compression via ground and excited states from a grating coupled passively mode-locked quantum dot two-section diode laser”, *Applied Physics Letters* **89**, 10.1063/1.2410217 (2006).
- [118] M. A. Cataluna, W. Sibbett, D. A. Livshits, J. Weimert, A. R. Kovsh, and E. U. Rafailov, “Stable mode locking via ground- or excited-state transitions in a two-section quantum-dot laser”, *Applied Physics Letters* **89**, 10.1063/1.2338767 (2006).
- [119] M. A. Cataluna, D. I. Nikitichev, S. Mikroulis, H. Simos, C. Simos, C. Mesaritakis, D. Syvridis, I. Krestnikov, D. Livshits, and E. U. Rafailov, “Dual-wavelength mode-locked quantum-dot laser, via ground and excited state transitions: experimental and theoretical investigation”, *Optics Express* **18**, 10.1364/oe.18.012832 (2010).

- [120] S. Breuer, M. Rossetti, W. Elsässer, L. Drzewietzki, P. Bardella, I. Montrosset, M. Krakowski, and M. Hopkinson, “Reverse-emission-state-transition mode locking of a two-section InAs/InGaAs quantum dot laser”, *Applied Physics Letters* **97**, 10.1063/1.3480405 (2010).
- [121] S. Breuer, W. Elsässer, and M. Hopkinson, “State-switched modelocking of two-segment quantum dot laser via self-electro-optical quantum dot absorber”, *Electronics Letters* **46**, 161–162 (2010).
- [122] S. Breuer, M. Rossetti, L. Drzewietzki, P. Bardella, I. Montrosset, and W. Elsaser, “Joint experimental and theoretical investigations of two-state mode locking in a strongly chirped reverse-biased monolithic quantum dot laser”, *IEEE Journal of Quantum Electronics* **47**, 1320–1329 (2011).
- [123] C. Mesaritakis, C. Simos, H. Simos, A. Kapsalis, E. Roditi, I. Krestnikov, and D. Syvridis, “Effect of the number of quantum dot layers and dual state emission on the performance of InAs/InGaAs passively mode-locked lasers”, *Applied Physics Letters* **101**, 10.1063/1.4772592 (2012).
- [124] T. Xu, M. Rossetti, P. Bardella, and I. Montrosset, “Simulation and analysis of dynamic regimes involving ground and excited state transitions in quantum dot passively mode-locked lasers”, *IEEE Journal of Quantum Electronics* **48**, 1193–1202 (2012).
- [125] C. Mesaritakis, A. Kapsalis, A. Bogris, and D. Syvridis, “Artificial Neuron Based on Integrated Semiconductor Quantum Dot Mode-Locked Lasers”, *Scientific Reports* **6**, 10.1038/srep39317 (2016).
- [126] P. F. Xu, T. Yang, H. M. Ji, Y. L. Cao, Y. X. Gu, Y. Liu, W. Q. Ma, and Z. G. Wang, “Temperature-dependent modulation characteristics for 1.3  $\mu\text{m}$  InAs/GaAs quantum dot lasers”, *Journal of Applied Physics* **107**, 10.1063/1.3277042 (2010).
- [127] P. Bhattacharya, D. Klotzkin, O. Qasaimeh, W. Zhou, S. Krishna, and D. Zhu, *High-Speed Modulation and Switching Characteristics of In(Ga)As-Al(Ga)As Self-Organized Quantum-Dot Lasers*, technical report 3 ().
- [128] A. Röhm, B. Lingnau, and K. Lüdge, “Ground-state modulation-enhancement by two-state lasing in quantum-dot laser devices”, *Applied Physics Letters* **106**, 10.1063/1.4921173 (2015).

- [129] C. Wang, M. Osiński, J. Even, and F. Grillot, “Phase-amplitude coupling characteristics in directly modulated quantum dot lasers”, *Applied Physics Letters* **105**, 10.1063/1.4903493 (2014).
- [130] C. Wang, F. Grillot, and J. Even, “Impacts of wetting layer and excited state on the modulation response of quantum-dot lasers”, *IEEE Journal of Quantum Electronics* **48**, 1144–1150 (2012).
- [131] Z. R. Lv, H. M. Ji, S. Luo, F. Gao, F. Xu, D. H. Xiao, and T. Yang, “Dynamic characteristics of two-state lasing quantum dot lasers under large signal modulation”, *AIP Advances* **5**, 10.1063/1.4933194 (2015).
- [132] B. Tykalewicz, D. Goulding, S. P. Hegarty, G. Huyet, D. Byrne, R. Phelan, and B. Kelleher, “All-optical switching with a dual-state, single-section quantum dot laser via optical injection”, *Opt. Lett.* **39**, 4607–4610 (2014).
- [133] C. Wang, B. Lingnau, K. Lüdge, J. Even, and F. Grillot, “Enhanced dynamic performance of quantum dot semiconductor lasers operating on the excited state”, *IEEE Journal of Quantum Electronics* **50**, 723–731 (2014).
- [134] S. Meinecke, B. Lingnau, A. Röhm, and K. Lüdge, “Stability of Optically Injected Two-State Quantum-Dot Lasers”, *Annalen der Physik* **529**, 10.1002/andp.201600279 (2017).
- [135] J. Pausch, C. Otto, E. Tylaite, N. Majer, E. Schöll, and K. Lüdge, “Optically injected quantum dot lasers: impact of nonlinear carrier lifetimes on frequency-locking dynamics”, *New Journal of Physics* **14**, 053018 (2012).
- [136] E. A. Viktorov, I. Dubinkin, N. Fedorov, T. Erneux, B. Tykalewicz, S. P. Hegarty, G. Huyet, D. Goulding, and B. Kelleher, “Injection-induced, tunable all-optical gating in a two-state quantum dot laser”, *Opt. Lett.* **41**, 3555–3558 (2016).
- [137] G. Sarantoglou, M. Skontranis, and C. Mesaritakis, “All Optical Integrate and Fire Neuromorphic Node Based on Single Section Quantum Dot Laser”, *IEEE Journal of Selected Topics in Quantum Electronics* **26**, 10.1109/JSTQE.2019.2945549 (2020).
- [138] M. Desroches, J. Guckenheimer, B. Krauskopf, C. Kuehn, H. M. Osinga, and M. Wechselberger, “Mixed-mode oscillations with multiple time scales”, *Siam Review* **54**, 211–288 (2012).
- [139] S. Meinecke, B. Lingnau, and K. Lüdge, “Increasing stability by two-state lasing in quantum-dot lasers with optical injection”, in

- Physics and simulation of optoelectronic devices xxv, Vol. 10098, edited by B. Witzigmann, M. Osinski, and Y. Arakawa (International Society for Optics and Photonics, 2017), pages 67–77.
- [140] F. Arecchi, G. Lippi, G. Puccioni, and J. Tredicce, “Deterministic chaos in laser with injected signal”, *Optics communications* **51**, 308–314 (1984).
- [141] D. O’Shea, S. Osborne, N. Blackbeard, D. Goulding, B. Kelleher, and A. Amann, “Experimental classification of dynamical regimes in optically injected lasers”, *Opt. Express* **22**, 21701–21710 (2014).
- [142] A. Gavrielides, V. Kovanis, and T. Erneux, “Analytical stability boundaries for a semiconductor laser subject to optical injection”, *Optics Communications* **136**, 253–256 (1997).
- [143] K. E. Chlouverakis and M. J. Adams, “Stability maps of injection-locked laser diodes using the largest lyapunov exponent”, *Optics Communications* **216**, 405–412 (2003).
- [144] C. Bonatto, J. C. Garreau, and J. A. C. Gallas, “Self-similarities in the frequency-amplitude space of a loss-modulated  $\text{CO}_2$  laser”, *Phys. Rev. Lett.* **95**, 143905 (2005).
- [145] D. O’Brien, S. Hegarty, G. Huyet, J. McInerney, T. Kettler, M. Laemmlin, D. Bimberg, V. Ustinov, A. Zhukov, S. Mikhlin, et al., “Feedback sensitivity of 1.3/spl mu/m inas/gaas quantum dot lasers”, *Electronics Letters* **39**, 1819–1820 (2003).
- [146] D. O’Brien, S. Hegarty, G. Huyet, and A. Uskov, “Sensitivity of quantum-dot semiconductor lasers to optical feedback”, *Optics letters* **29**, 1072–1074 (2004).
- [147] B. Lingnau, M. Dillane, J. O’Callaghan, B. Corbett, and B. Kelleher, “Multimode dynamics and modeling of free-running and optically injected fabry-pérot quantum-dot lasers”, *Phys. Rev. A* **100**, 063837 (2019).
- [148] B. Kelleher, C. Bonatto, P. Skoda, S. P. Hegarty, and G. Huyet, “Excitation regeneration in delay-coupled oscillators”, *Phys. Rev. E* **81**, 036204 (2010).
- [149] D. Bera, L. Qian, T.-K. Tseng, and P. H. Holloway, “Quantum dots and their multimodal applications: a review”, *Materials* **3**, 2260–2345 (2010).
- [150] M. Ziegler, J. W. Tomm, T. Elsaesser, G. Erbert, F. Bugge, W. Nakwaski, and R. P. Sarzała, “Visualization of heat flows in high-power diode

- lasers by lock-in thermography”, *Applied Physics Letters* **92**, 103513 (2008).
- [151] B. Kelleher, D. Goulding, B. Baselga Pascual, S. P. Hegarty, and G. Huyet, “Bounded phase phenomena in the optically injected laser”, *Phys. Rev. E* **85**, 046212 (2012).
- [152] J. Thévenin, M. Romanelli, M. Vallet, M. Brunel, and T. Erneux, “Resonance assisted synchronization of coupled oscillators: frequency locking without phase locking”, *Phys. Rev. Lett.* **107**, 104101 (2011).
- [153] S. Wiczorek, B. Krauskopf, and D. Lenstra, “Multipulse excitability in a semiconductor laser with optical injection”, *Phys. Rev. Lett.* **88**, 063901 (2002).
- [154] M. Abusaa, J. Danckaert, E. A. Viktorov, and T. Erneux, “Intradot time scales strongly affect the relaxation dynamics in quantum dot lasers”, *Phys. Rev. A* **87**, 063827 (2013).
- [155] J. L. Dubbeldam, B. Krauskopf, and D. Lenstra, “Excitability and coherence resonance in lasers with saturable absorber”, *Physical Review E* **60**, 6580 (1999).
- [156] V. Mutneja, “Methods of image edge detection: a review”, *Journal of Electrical Electronic Systems* **04**, 10.4172/2332-0796.1000150 (2015).
- [157] J. Robertson, Y. Zhang, M. Hejda, J. Bueno, S. Xiang, and A. Hurtado, “Image edge detection with a photonic spiking vcsel-neuron”, *Optics Express* **28**, 37526–37537 (2020).
- [158] R. McKenna, D. Mickus, S. Naimi, C. Murphy, M. McDermott, S. Corbett, D. McCloskey, and J. F. Donegan, “Spatially resolved self-heating and thermal impedance of laser diodes using ccd-tr imaging”, *OSA Continuum* **4**, 1271–1281 (2021).
- [159] J. C. Norman, D. Jung, Y. Wan, and J. E. Bowers, “Perspective: the future of quantum dot photonic integrated circuits”, *APL Photonics* **3**, 030901 (2018).
- [160] B. Lingnau, A. H. Perrott, M. Dernaika, L. Caro, F. H. Peters, and B. Kelleher, “Dynamics of on-chip asymmetrically coupled semiconductor lasers”, *Optics letters* **45**, 2223–2226 (2020).